Università degli Studi di
Modena e Reggio Emilia

Dipartimento di Scienze Fisiche, Informatiche e Matematiche

Physics and Nanosciences - School of Graduate Studies

Spin-orbit coupled states in type-I, II and broken gap core-shell nanowires

from a self-consistent k•p approach

Candidate: Andrea Vezzosi

Supervisor: Prof. Guido Goldoni
Co-Supervisor: Dr. Andrea Bertoni

School Coordinator: Prof. Marco Affronte

Cycle: XXXVI

Abstract

Semiconductor nanowires (NWs) manifest unique physical properties ensuing from the reduced dimensionality and represent a promising platform for a wide range of applications in nanotechnology and electronics. NWs can be reliably manufactured in single crystal structures, with precise control of crucial parameters such as chemical composition, dimensions, and doping, enabling to engineer a vast range of devices and integration techniques, including NW-based field-effect-transistors, p-n junctions, light-harvesting and thermoelectric devices. Moreover, the demonstration of NWs with radial material modulation, also referred to as core-shell NWs (CSNWs), paved the way to devices with enhanced performance and new functionalities through wave-function engineering and quantum effects.

Among the theoretical methods used to describe semiconductor nanostructures, the self-consistent $\mathbf{k} \cdot \mathbf{p}$ method, combined with the envelope function approximation, stands out for computational efficiency and predictivity. Of relevance here is the ability to describe the interplay between spin-orbit coupling (SOC) in the underlying compounds, material modulations, and structural parameters. Moreover, considering the impact of built-in electric fields is crucial for describing the nanostructures discussed in this study. For instance, doped NWs inherently demand a self-consistent treatment of the electronic energy levels. Therefore, the thesis project started with the design and deployment of a new and original at-state-of-the-art, object-oriented Python package, where the coupled multiband Schrödinger and Poisson equations are solved by the finite element method; using unstructured and adaptive meshes in self-consistent $\mathbf{k} \cdot \mathbf{p}$ approach keeps the numerical burden and accuracy under control also in strong confinement, high-doping, or low-symmetry regimes. The implemented 8-band $\mathbf{k} \cdot \mathbf{p}$ Hamiltonian is suitable to describe type-I, type-II, and inverted band heterostructures discussed in this thesis.

Modulation doping is a key functionalization technique for high-mobility devices, but relatively less under control in growth processes. Hence, we study how different doping regimes influence the electronic properties of a prototypical high-mobility modulation-doped GaAs/AlGaAs radial heterostructure. We show that high-doping brings about a strong carrier localization towards the core-shell interface, as well as mass inversions and non-trivial changes in the spinorial character of the low-energy valence states. We show by explicit calculations that indications of the band structure's evolution with doping can be exposed in the anisotropy patterns of linearly polarized optical absorption spectra.

Full-shell hybrid NWs –semiconductor NWs embedded in a superconductor– have recently emerged as candidates in the search for Majorana zero modes, possible building-blocks for the implementation of fault-tolerant qubits thanks to their topological nature and ensuing robustness against local disorder. Up to now the primary issue has been the small SOC achieved in typical samples, hindering the possibility to attain a topological superconducting phase. Here, we propose to exploit the inherently strong SOC of the hole valence bands, exploring the potential of InP/GaSb CSNWs in full-shell geometries. Predictive self-consistent $\mathbf{k} \cdot \mathbf{p}$ calculations foresee values of the intrinsic SOC as high as 20 meV·nm, regardless of the electric field or strain at the interface.

InAs/GaSb CSNWs constitute a suitable system for applications in low-power electronics as well as core studies on electron-hole hybridization and topological insulating states. Using self-consistent $\mathbf{k} \cdot \mathbf{p}$ simulations, we identify a new reentrant semimetal state with Weyl dispersion in the hybridization gap of slightly band-inverted NWs, which is triggered by a transverse electric field. Using an effective low-energy Bernevig-Hughes-Zhang model Hamiltonian we show that the semimetallic phase is due to an exact compensation of SOCs and electron-hole interactions. We further rationalize the closure of the indirect gap in terms of the appearance of localized states at both ends of the NW.

Contents

Acronyms

Acronym	Definition
BC	Boundary Condition
BF	Burt-Foreman
BHZ	Bernevig-Hughes-Zhang
CB	Conduction Band
CdGM	Caroli–de Gennes–Matricon
CSNW	Core-Shell Nanowire
EFA	Envelope Function Approximation
EFE	Envelope Function Equation
FEM	Finite Element Method
FET	Field-Effect-Transistor
HH	Heavy Hole
LDOS	Local Density Of States
LH	Light Hole
MOS	Metal-Oxide-Semiconductor
MZM	Majorana Zero Modes
NW	Nanowire
QSH	Quantum Spin Hall
QW	Quantum Well
SC	Superconductor
SO	Spin-Orbit
SOC	Spin-Orbit Coupling
SOFF	Split-Off
SOI	Spin-Orbit Interaction
SM	Semiconductor
TI	Topological Insulator
VB	Valence Band
VLS	Vapor-Liquid-Solid
VS	Vapor-Solid

1

Introduction

Nanowires (NWs) are a class of one-dimensional nano-crystals with diameters in the nanometer range and lengths extending to micrometers. These nanostructures exhibit unique physical, chemical, and electronic characteristics that set them apart from their bulk counterparts, and, during the last 20 years, have been continuously investigated by physicist and engineers in view of promising applications in numerous fields.

The tunable properties of NWs endow them with unique advantages as versatile building blocks in a wide range of applications. Semiconductor NWs made of silicon [1], germanium [2] and III-V semiconductor compounds [3], as well as metallic NWs [4], have been demonstrated and intensively studied for their applications in nano- and opto-electronic devices. Thanks to the recent developments in the area of NW growth, scientists are nowadays able to control the chemical composition [5], shape and diameter of single crystal NWs [6]. Additionally, combination of different materials in hepitaxial NW-based heterostructures [7], have been proven for type-I, type-II, as well as "broken-gap" band alignments [8]. For example, radial variations in composition and doping in so-called core-shell NWs bring about the formation of low-dimensional confinement potentials within the NW, offering opportunities for the design of advanced applications in electronics [9], optoelectronic devices [10], energy harvesting [11], energy transport [12], and light emission or absorption.

Semiconductor NWs provide a platform for the ongoing quest for miniaturization in electronics. As traditional electronics based on two-dimensional metal-oxide-semiconductor (MOS) transistors face a number limitations in scaling down device dimensions, such as the reduction of switching speed caused by short-channel effects [14], NWs offer a novel approach. For example, the implementation of NWs in transistors [15] allows to efficiently implement a three-dimensional electrostatic control of the channel. In such so-called gate-all-around architectures, the gate surrounds the NW from all sides, effectively mitigating short-channel effects, leading to improved switching characteristics, reduced power consumption, and overall optimization of device functionality. A scanning-electron-microscopy image of NW field-effect transistor (FET) with multiple Ω-shaped gates is shown Fig. 1.1[taken from Ref. [13]].

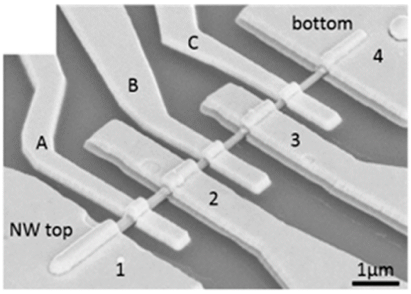

Figure 1.1: Nanowire field-effect-transistor (NW-FET). scanning-electron-microscopy image of a NW-FET with four source-drain contacts labeled 1–4 and three Ω-shaped gates labeled 1–4 A,B and C. Source: Ref.[13]

Due to the reduced dimensionality and high aspect-ratio, NWs have been proposed and demonstrated as high-performance thermoelectric generators [16]. In fact, on the one hand thermal conductivity is reduced by employing NWs, whose dimensions are comparable to the phonon mean free path, on the other hand field-effect modulation of the electrical properties can be exploited to modulate electrical conductivity in order to obtain, ultimately, an increased thermoelectric figure-of-merit. Furthermore, NWs benefit from the high surface-to-volume ratio typical of nanostructures, and the tunability of their surface properties makes them highly sensitive to their environment. This sensitivity can be exploited in applications such as sensors [17] and detectors [18, 19, 20].

At the nanoscale, quantum effects become increasingly prominent. In NWs with a very small cross-section, electronic states form standing waves in the directions of quantized motion. Hence, the three-dimensional band dispersion splits into a series of discrete levels within the conduction and valence bands with one-dimensional dynamics, commonly referred to as energy subbands. Quantum effects can be used to engineer new devices, as for example gate-all-around, NW tunnel FETs [21], promising building blocks for future low-power electronics, which harness the so called band-to-band tunneling [22] as underlying key functioning mechanism.

The tunability of NWs properties is enabled and complemented by the availability of various synthesis techniques, broadly classified into either top-down or bottom-up methodologies. Both approaches have advantages and disadvantages [24]. In the top-down approach, the NW features are sculptured starting from larger-scale solids down to nanoscale dimensions by a combination of lithography, etching and deposition. Top-down techniques offer an advantage in creating NWs with precise, lithographically-defined features at specific locations, facilitating seamless integration into systems [25]. Nevertheless, the use of lithography for patterning introduces surface roughness, which may constitute a significant portion of the overall NW diameter.

Alternatively, bottom-up methods involve the spontaneous growth of NWs in appropriate conditions, starting from a properly synthesized nanoparticle, like the growth of a tree from a small seed, as shown in Fig. 1.2. This often uses the vapor-liquid-solid (VLS) method [26], whereby a set of metal nanoparticles are placed on a substrate (e.g., Au on Si). Each nanoparticle acts as a catalyst for the semiconductor NW growth. The semiconductor precursor (e.g., SiH_4 for silicon) is introduced in vapour phase, while the metal catalyst is heated above the eutectic point of the metal–semiconductor system, enabling absorption of the vapour phase [Fig. 1.2(a)]. As a result, a small droplet of metal–semiconductor alloy, as for example an Au–Si alloy, is formed. When assimilation eventually reaches supersaturation, a solid semiconductor starts to precipitate beneath the droplet [Fig 1.2(b)]. As the process persists, the alloy droplet floats atop of the emerging solid NW, whose

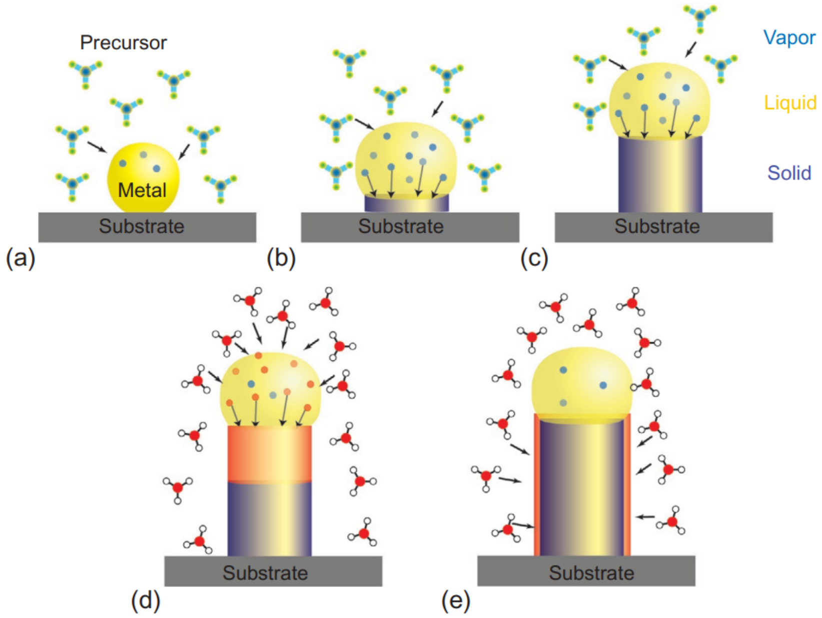

Figure 1.2: Schematic nanowire growth (a-c) Different stages of vapor–liquid–solid (VLS) growth. (d) Growth of an axial heterostructure via the vapor–liquid–solid (VLS) process. (e) Growth of a radial heterostructure via the vapor–solid (VS) process. Source: Ref.[23]

diameter is determined by the size of the alloy nanoparticle [Fig 1.2(c)].

By switching vapour species and growth conditions it is possible to obtain NW heterostructures [27, 28, 29]. If the vapour phase is preferentially absorbed at the surface of the liquid droplet, an axial heterostructure [30] is formed, with material modulation *along* the growth direction [Fig 1.2(d)]. However, the vapour phase can also selectively adsorb on the NW surfaces, a process also referred to as vapor-solid (VS) growth, and the heterostructure will grow in the radial direction [Fig 1.2(e)]. The resulting nanostructure is referred to as core-shell NW (CSNW) [31]. Thanks to easier stress release, epitaxial shell growth is facilitated in NWs even in cases of lattice mismatched materials that would result in incoherent growth for planar heterostructures [32]. Starting from the 1990s, numerous classes of III-V compound semiconductor NWs have been demonstrated with customized dimensions and composition, allowing new forms of band gap engineering at the nanoscale.

Finally, and crucially, from the point of view of scaling and integration, catalyst-free growth methods have also been developed, such as the VS growth [33] and selective-area-epitaxy [34], or self-assisted methods, where a component of the semiconductor NW plays the role of the liquid droplet in the VLS mechanism [35]. This allows to avoid the use of Au, whose unwanted incorporation produces deep levels, especially in silicon [36] and impose severe restrictions to the integration of III-V NWs in Si-based complementary MOS technology. The onset of Au-free growth methods represents a fundamental step towards high-mobility in III-V semiconductor NWs and their future integration in Si-based microelectronics.

Although semiconductor NWs are extremely interesting and flexible systems for future high-speed/low-power electronics, charge carrier mobility in NWs is strongly limited by a number of factors, including surface and impurity scattering. In order to mitigate these effects, radially modulation-doped NW devices have been proposed and demonstrated [37, 38, 39, 40, 13]. However, precise control of

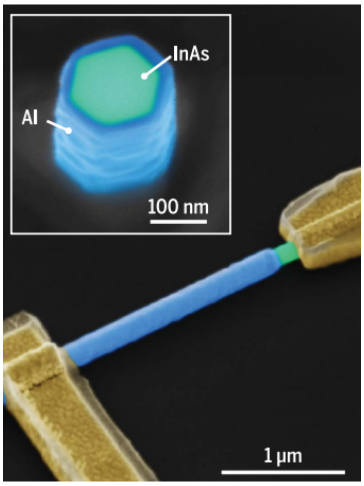

Figure 1.3: Full-shell Majorana nanowire. Colorized electron micrograph of a tunneling device composed of a hybrid nanowire with hexagonal semiconducting InAs core fully coated with a superconducting Al shell. Source: Ref. [43]

dopants incorporation in NWs is still challenging, the ultimate performance in these devices being highly affected by any uncontrolled doping anisotropy. As during the catalyzed growth of III-V NWs dopant incorporation happens either through the catalyst or through the side facets, dopant anisotropy can arise, for example, due the lack of proper coordination between the two incorporation paths, or due to the diffusion of dopants atoms inside the NW core during the growth process. Furthermore, the amphoteric nature of some dopant species, as for example Si in GaAs NWs, represents an additional element to take into account. We contribute to these problems in Ch. 3, where we report on self-consistent calculations of the electronic structure of a prototypical, modulation-doped, GaAs-AlGaAs CSNW [41] for either n- or p-doping. Our calculations show that different doping regimes can be traced in optical anisotropy spectra. Furthermore we identify specific signatures in the anisotropy patterns which distinguish between n- or p-doping. Our results intend to provide a possible characterization technique of the incorporation of dopants in modulation-doped core-shell NWs, the latter being of fundamental importance for their application into commercial products [42].

Semiconductor NWs have emerged as a promising platform in the search for Majorana zero modes (MZMs), quasiparticle excitations that benefit from the topological protection of the underlying phase and, consequently, represent ideal candidates for the realization of fault-tolerant quantum computers. To date, the most promising platform consists of a hybrid system based on a semiconductor NW with strong spin-orbit interaction proximity-coupled to a standard s-wave superconductor within the influence of a longitudinal magnetic field [44, 45]. Majorana-like signatures, e.g., zero-bias anomalies, have been repeatedly measured using transport spectroscopy in partially-coated hybrid systems [46], as well as in the more recent full-shell configuration [43], where a semiconductor core is fully wrapped in a thin superconductor shell [see Fig. 1.3]. An essential concern in this context is to design devices with robust spin-orbit coupling (SOC), as the magnitude of topological energy gap protecting zero-energy Majorana modes is directly proportional to the value of the effective SOC constant [47]. This issue is even more pronounced in the full-shell configuration, where the metallic encapsulation prevents tuning of both the chemical potential and the SOC inside the core by means of large external electric fields. In Ch. 4 we propose and analyze a viable proposal that significantly enhances the performance of full-shell hybrid NWs, thereby facilitating the generation of MZMs. On the one hand, we propose to use a CSNW with a conductive shell and an insulating core [48] for the hybrid's normal core. On the other hand, we make use of the hole bands of III-V compound SMs with intrinsically higher values of SOC with respect to proposals based on the conduction electrons [49].

Majorana bound states are just an example of the broader category of topological phases in condensed matter systems that hold immense potential for qubit applications. In recent years, a new class of topological states has been theoretically predicted [50] and experimentally observed [51], called quantum spin Hall (QSH) states or topological insulators (TI), which, due to the presence of time-reversal symmetry protected, helical edge states, hold promise for application in spin-based electronics and fault-tolerant information processing. While the realization of QSH states in two-dimensional systems, such as inverted InAs-GaSb quantum wells, has been largely investigated both theoretically [52, 53, 54] and experimentally [55, 56, 57], possible signatures of a TI quantum phase transition in the corresponding one-dimensional systems have attracted less attention. In Ch. 5 we study the behaviour of the band structure of InAs-GaSb CSNWs in the presence of a transverse electric field and find that the hybridization gap closes at a critical value of the external field. We show that this new, field controlled, spin-specific semi-metal phase, which can be described as a massless Dirac point, emerges from a subtle compensation of kinetic and spin-orbit couplings. We also connect the vanishing of the gap with the emergence of localized states at both ends of finite length wires describing the fate of such states in the context of an underlying topological transition.

This thesis is concerned with materials and phenomena in which the semiconductor valence states, and, therefore, the spin-orbit interaction, are not only a crucial ingredient for band description, but actually exploited to induce new phenomena. This is particularly interesting in low-dimensional systems as CSNWs, where quantum confinement and external fields combine with appropriate choices of material classes and parameters to allow for SOC engineering [58, 59, 60, 61]. In this context, theoretical methods should be able to describe delicate SOC-related phenomena, such as non-parabolicity, spin splitting, heavy holes and light holes couplings, as well as the kinetic interactions between conduction and valence band states. The $\mathbf{k} \cdot \mathbf{p}$ envelope function theory is often used in literature, as well as in this thesis, since it comes with sustainable computational effort and the required predictive quality in the vicinity of the band gap. This is thoroughly described in Ch. 2. Due to the complexities and low symmetry of the nanomaterials investigated in this thesis, particularly their multilayer nature and the presence of intentional or unintentional free carriers, it is desirable to employ numerical methods built on non-uniform, non-symmetric real-space meshes which can be adapted to the localization of the quantum states. Calculations within this thesis were performed using the `nwkp` package, completely new, highly flexible, object-oriented Python library which has been realized for the purpose of the thesis project. Planning and deployment of the `nwkp` library represent a specific and distinctive outcome of this thesis and is a novel contribution to existing literature. This numerical tool integrates multiband $\mathbf{k} \cdot \mathbf{p}$ methods with the Schrödinger-Poisson approach for nanostructures, within an at-state-of-the-art implementation. The corresponding differential equations are numerically solved using the finite element method [62, 63], an accurate, flexible and largely widespread variational approach which greatly helped in keeping the computational burden under control for very different nanomaterials.

2

Electronic structure of semiconductor nanowires in the $\mathbf{k} \cdot \mathbf{p}$ approach

In this chapter, we summarize the derivation of the $\mathbf{k} \cdot \mathbf{p}$ method in the envelope function approximation (EFA) which is used in this thesis for the quantum mechanical determination of the electronic structure of III-V compound semiconductor nanowires (NWs). Whereas NWs with tens of nm in diameter might involve thousands of atoms per unit cell, requiring enormous computer power with atomistic descriptions, the envelope function approach is a semi-empirical method which approximates the atomic arrangement as a continuum, leading to partial differential equations which can be solved with moderate computational effort using well-founded numerical techniques and with documented predictive quality in the sub-meV energy scale.

We start with the derivation in Sec. 2.1 of the *exact* envelope function equations (EFEs) for an arbitrary heterostructure, including the Pauli spin-orbit interaction (SOI) term. The contents of that section, as well as the related appendices, are based mainly on the work published by Burt in Refs.[64, 65, 66]; here we carefully go through the derivation and clarify some of the most thorny steps. Then, in Sec. 2.2, following in particular Refs. [67, 68, 69], we derive the Burt-Foreman (BF) equations that describe the lowest-energy spectrum of the semiconductor which, for III-V binary compound semiconductors of interest for this work, happens to be at the Γ-point. These equations include the first four spinful bands, namely the topmost three valence band p-like states, also referred to as heavy-holes (HH), light-holes (LH) and split-off (SOFF), and the first s-like conduction band states. Since all these bands are doubly degenerate at the Γ-point, the wave function is actually an eight-component spinor, and the approach goes by the name of 8-band $\mathbf{k} \cdot \mathbf{p}$ approach. Finally, in Sec. (2.3) we make explicit the EFEs for the case of a NW with growth axis directed along an arbitrary crystallographic direction z. By assuming the NW to be of *infinite* length the associated wave vector k_z is a good quantum number. Thus, the EFEs become a set of coupled, two-dimensional partial differential equations which are solved at selected k_z values to obtain the band structure of the NW in proximity of the Γ-point.

In this thesis, we solve the NW's EFEs using the Finite Element Method (FEM) [63, 62]. In essence, it is a variational approach where, in contrast to standard variational methods—in which a trial wave function is defined on the entire simulation domain—the domain is arbitrarily partitioned into small regions, also referred to as *elements*. Within each element, a local polynomial approximation is used to represent the wave function, with coefficients serving as variational parameters. Remarkably, FEM allows for the use of non-uniform, problem-designed real space discretizations. This is particularly handy when dealing with nanostructures, where the wave function may be confined to narrowed regions of the nanodevice due to quantum confinement and/or electrostatic interactions.

In this work we shall consistently consider the effects of non-vanishing distributions of space charges due to ionization of impurity atoms or as charge carriers in terms of free-holes and electrons. Together with external gate voltages from the contacts of the NW, these charges determine an electrostatic potential that can have an important influence on the electronic states. Replacing the exact many-electron potential by an average field (mean-field or Hartree approximation) whose source depends on the wave functions, a self-consistent solution of the coupled multi-band EFEs and Poisson equations is obtained, which is discussed in Sec. (2.4).

The computational scheme has been deployed in-house in an original object-oriented Python library named `nwkp`. At present, `nwkp` appears to be the only library implementing self-consistent solution of EFEs for core-shell nanowires (CSNWs) of arbitrary composition, geometry and doping on non-uniform arbitrary grids by the FEM.

2.1. The envelope function approximation

2.1.1. Derivation of the exact envelope function equations

To describe electron states in presence of external fields[1], or to deal with layered structures, we make use of the envelope function approximation. The starting point is the one-electron Schrödinger equation

$$\left[-\frac{\hbar^2}{2m_0}\boldsymbol{\nabla}^2 + \frac{\hbar}{4m_0^2c^2}(\boldsymbol{\sigma}\times\boldsymbol{\nabla}V)\cdot(-i\hbar\boldsymbol{\nabla}) + V(\boldsymbol{r})\right]\Psi(\boldsymbol{r}) = E\Psi(\boldsymbol{r})\,, \tag{2.1}$$

where $V(\boldsymbol{r}) = V_0(\boldsymbol{r}) + V^e(\boldsymbol{r})$ is the sum of the crystalline, lattice periodic potential V_0 and, possibly, an external potential V^e, while m_0 denotes the free-electron mass, c the velocity of light and $\boldsymbol{\sigma}$ is a vector of Pauli matrices. Note that, due to the presence of SOI, the wave function $\Psi(\boldsymbol{r})$ is a two component spinor.

Let $U_\mu(\boldsymbol{r})$ be a complete set of Bravais lattice periodic functions with normalization

$$\frac{1}{\Omega_0}\int_{u.c.} U_\mu^{*T}\, U_\nu \,\mathrm{d}^3\boldsymbol{r} = \delta_{\mu\nu}\,, \tag{2.2}$$

where $\int_{u.c}$ denotes the integral over the volume Ω_0 of the unit cell of the Bravais lattice. Note that

---

[1] We shall not consider here magnetic fields, but similar arguments can be developed in this case.

the $U_\mu(\boldsymbol{r})$ are spinors as well. Given an arbitrary wave function $\Psi(\boldsymbol{r})$ it can be shown that it exists a set of uniquely defined functions $\psi(\boldsymbol{r})$, called envelope functions, such that

$$\Psi(\boldsymbol{r}) = \sum_\mu \psi_\mu(\boldsymbol{r}) U_\mu(\boldsymbol{r}) \,, \tag{2.3}$$

where the functions $\psi_\mu(\boldsymbol{r})$ are $\mathcal{C}^1$ continuous and are constrained to a plane wave expansion within the first Brillouin zone corresponding to the Bravais lattice used to define the $U_\mu(\boldsymbol{r})$.

We now derive the exact EFEs, including the SOI term

$$\hat{H}_{SO} = \frac{\hbar}{4m_0^2c^2}(\boldsymbol{\sigma} \times \boldsymbol{\nabla} V) \cdot (-i\hbar \boldsymbol{\nabla}) \,. \tag{2.4}$$

The first step is to express the spinor $\langle r|\hat{O}|\Psi\rangle$ in envelope expansion form (2.3), where $|\Psi\rangle$ is a state vector with spinor representative $\Psi(r) = \langle \boldsymbol{r}|\Psi\rangle$ and $\hat{O}$ is an arbitrary operator. We consider a complete set of plane waves (including spin) denoting with $\boldsymbol{G}$ the reciprocal lattice vectors of the crystal Bravais lattice and with $\boldsymbol{k}$ the wave vectors restricted to the corresponding first Brillouin zone. Using the completeness relations we have

$$\langle \boldsymbol{r}|\hat{O}|\Psi\rangle = \sum_{\boldsymbol{k}\boldsymbol{k}'} \sum_{\boldsymbol{G}\boldsymbol{G}'} \langle \boldsymbol{r}|\boldsymbol{k}+\boldsymbol{G}\rangle \left\langle \boldsymbol{k}+\boldsymbol{G}\middle|\hat{O}\middle|\boldsymbol{k}'+\boldsymbol{G}'\right\rangle \left\langle \boldsymbol{k}'+\boldsymbol{G}'\middle|\Psi\right\rangle \,. \tag{2.5}$$

In the spinor notation used above,

$$\langle \boldsymbol{r}|\boldsymbol{k}+\boldsymbol{G}\rangle = \frac{1}{\sqrt{\Omega}} e^{i(\boldsymbol{k}+\boldsymbol{G})\cdot \boldsymbol{r}} \times \mathbb{1}_2 \tag{2.6}$$

and $\left\langle \boldsymbol{k}+\boldsymbol{G}\middle|\hat{O}\middle|\boldsymbol{k}'+\boldsymbol{G}'\right\rangle$ are 2x2 matrices, with $\mathbb{1}_2$ being the 2×2 unit matrix and Ω the volume of the whole crystal. The $\psi_\mu(\boldsymbol{r})$ coefficients and the basis functions $U_\mu(\boldsymbol{r})$ have the Fourier expansions

$$\psi_\mu(\boldsymbol{r}) = \sum_{\boldsymbol{k}} \psi_\mu(\boldsymbol{k}) e^{i\boldsymbol{k}\cdot\boldsymbol{r}} \,, \tag{2.7}$$

$$U_\mu(\boldsymbol{r}) = \sum_{\boldsymbol{G}} U_{\mu\boldsymbol{G}} e^{i\boldsymbol{G}\cdot\boldsymbol{r}} \,. \tag{2.8}$$

Recall that the $U_\mu(\boldsymbol{r})$ are lattice-periodic and the Fourier expansion contains only the reciprocal lattice vectors, while the envelope functions $\psi(\boldsymbol{r})$ have a Fourier expansion limited to the first Brillouin zone.

Using Eqs. (2.8), (2.7), and the fact that

$$\frac{1}{\Omega}\int \mathrm{d}^3\boldsymbol{r}\, e^{i(\boldsymbol{k}-\boldsymbol{k}'+\boldsymbol{G}-\boldsymbol{G}')\cdot\boldsymbol{r}} = \delta_{\boldsymbol{k},\boldsymbol{k}'}\delta_{\boldsymbol{G},\boldsymbol{G}'} \,, \tag{2.9}$$

we have

$$\begin{aligned}
\langle \boldsymbol{k}' + \boldsymbol{G}' | \Psi \rangle &= \int \mathrm{d}^3\boldsymbol{r} \, \langle \boldsymbol{k}' + \boldsymbol{G}' | \boldsymbol{r} \rangle \, \langle \boldsymbol{r} | \Psi \rangle \\
&= \int \mathrm{d}^3\boldsymbol{r} \frac{1}{\sqrt{\Omega}} e^{-i(\boldsymbol{k}'+\boldsymbol{G}')\cdot\boldsymbol{r}} \times \mathbb{1}_2 \sum_\mu \psi_\mu(\boldsymbol{r}) U_\mu(\boldsymbol{r}) \\
&= \sqrt{\Omega} \sum_{\boldsymbol{k}''\boldsymbol{G}''} \underbrace{\frac{1}{\Omega} \int \mathrm{d}^3\boldsymbol{r} e^{i(\boldsymbol{k}''-\boldsymbol{k}'+\boldsymbol{G}''-\boldsymbol{G}')\cdot\boldsymbol{r}}}_{\delta_{\boldsymbol{k}'',\boldsymbol{k}'}\delta_{\boldsymbol{G}'',\boldsymbol{G}'}} \sum_\mu \psi_\mu(\boldsymbol{k}'') U_{\mu\boldsymbol{G}''} \\
&= \sqrt{\Omega} \sum_\mu \psi_\mu(\boldsymbol{k}') U_{\mu\boldsymbol{G}'} \, .
\end{aligned} \tag{2.10}$$

From the completeness of the U_μ functions,

$$\frac{1}{\Omega_0} \sum_\mu |U_\mu\rangle \langle U_\mu| = \mathbb{1}_2 \, , \tag{2.11}$$

we have

$$\begin{aligned}
e^{i\boldsymbol{G}\cdot\boldsymbol{r}} \times \mathbb{1}_2 &= \sqrt{\Omega} \, \langle \boldsymbol{r} | \boldsymbol{G} \rangle \\
&= \frac{\sqrt{\Omega}}{\Omega_0} \sum_\mu \langle \boldsymbol{r} | U_\mu \rangle \, \langle U_\mu | \boldsymbol{G} \rangle \\
&= \frac{\sqrt{\Omega}}{\Omega_0} \sum_\mu U_\mu(\boldsymbol{r}) \int_{u.c.} \mathrm{d}^3\boldsymbol{r}' \, \langle U_\mu | \boldsymbol{r}' \rangle \, \langle \boldsymbol{r}' | \boldsymbol{G} \rangle \\
&= \sum_\mu U_\mu(\boldsymbol{r}) \frac{1}{\Omega_0} \int_{u.c.} \mathrm{d}^3\boldsymbol{r}' U_\mu^{*T}(\boldsymbol{r}') e^{i\boldsymbol{G}\cdot\boldsymbol{r}'} \\
&= \sum_\mu U_\mu(\boldsymbol{r}) U^{*T}_{\mu\boldsymbol{G}} \, .
\end{aligned} \tag{2.12}$$

We now plug Eqs. (2.6), (2.10) and (2.12) in Eq. (2.5) to obtain

$$\langle \boldsymbol{r} | \hat{O} | \Psi \rangle = \sum_{\mu\nu} \sum_{\boldsymbol{k}\boldsymbol{k}'} \sum_{\boldsymbol{G}\boldsymbol{G}'} U_\mu(\boldsymbol{r}) U^{*T}_{\mu\boldsymbol{G}} e^{\;\boldsymbol{k}\cdot\boldsymbol{r}} \left\langle \boldsymbol{k} + \boldsymbol{G} \middle| \hat{O} \middle| \boldsymbol{k}' + \boldsymbol{G}' \right\rangle U_{\nu\boldsymbol{G}'} \psi_\nu(\boldsymbol{k}') \, , \tag{2.13}$$

and finally anti-transform the $\psi_\nu(\boldsymbol{k}')$ using

$$\psi_\nu(\boldsymbol{k}') = \frac{1}{\Omega} \int \mathrm{d}^3\boldsymbol{r}' \psi_\nu(\boldsymbol{r}') e^{-i\boldsymbol{k}'\cdot\boldsymbol{r}'} \tag{2.14}$$

to obtain

$$\langle \boldsymbol{r} | \hat{O} | \Psi \rangle = \sum_{\mu\nu} U_\mu(\boldsymbol{r}) \int \mathrm{d}^3\boldsymbol{r}' O_{\mu\nu}(\boldsymbol{r}, \boldsymbol{r}') \psi_\nu(\boldsymbol{r}') \, , \tag{2.15}$$

with

$$O_{\mu\nu}(\boldsymbol{r}, \boldsymbol{r}') = \frac{1}{\Omega} \sum_{\boldsymbol{k}\boldsymbol{k}'} e^{i\boldsymbol{k}\cdot\boldsymbol{r}} \left(\sum_{\boldsymbol{G}\boldsymbol{G}'} U^{*T}_{\mu\boldsymbol{G}} \left\langle \boldsymbol{k} + \boldsymbol{G} \middle| \hat{O} \middle| \boldsymbol{k}' + \boldsymbol{G}' \right\rangle U_{\nu\boldsymbol{G}'} \right) e^{-i\boldsymbol{k}'\boldsymbol{r}'} \, . \tag{2.16}$$

We now have an expression for the action of an arbitrary operator $\hat{O}$ written in envelope expansion form. The next step is to express the operators of the Schrödinger equation in this form.

When the operator $\hat{O}$ contains derivatives, the matrix element $\left\langle \boldsymbol{k} + \boldsymbol{G} \middle| \hat{O} \middle| \boldsymbol{k}' + \boldsymbol{G}' \right\rangle$ will depend on $\boldsymbol{k}'$. If we express such dependence as a gradient acting on the exponential $e^{-i\boldsymbol{k}'\boldsymbol{r}'}$ in Eq. (2.16), we can bring the gradient operator to act on the envelope function using an integration by parts in Eq. (2.15).

For example, if the operator $\hat{O}$ is the kinetic energy operator, from Eq. (2.16) we have

$$\begin{aligned}\left(\frac{\hat{p}^2}{2m_0}\right)_{\mu\nu}(\boldsymbol{r},\boldsymbol{r}') &= \frac{1}{\Omega}\sum_{\boldsymbol{k}\boldsymbol{k}'} e^{i\boldsymbol{k}\cdot\boldsymbol{r}}\left(\sum_{\boldsymbol{G}\boldsymbol{G}'} U^{*T}_{\mu\boldsymbol{G}}\left\langle\boldsymbol{k}+\boldsymbol{G}\right|\frac{\hat{p}^2}{2m_0}\left|\boldsymbol{k}'+\boldsymbol{G}'\right\rangle U_{\nu\boldsymbol{G}'}\right)e^{-i\boldsymbol{k}'\boldsymbol{r}'}\\ &= \frac{1}{\Omega}\sum_{\boldsymbol{k}\boldsymbol{k}'} e^{i\boldsymbol{k}\cdot\boldsymbol{r}}\left(\sum_{\boldsymbol{G}\boldsymbol{G}'} U^{*T}_{\mu\boldsymbol{G}}\left[\delta_{\boldsymbol{k},\boldsymbol{k}'}\delta_{\boldsymbol{G},\boldsymbol{G}'}\frac{\hbar^2(\boldsymbol{k}'+\boldsymbol{G}')^2}{2m_0}\right]U_{\nu\boldsymbol{G}'}\right)e^{-i\boldsymbol{k}'\boldsymbol{r}'}\\ &= \frac{1}{\Omega}\sum_{\boldsymbol{k}} e^{i\boldsymbol{k}\cdot\boldsymbol{r}}\left(\sum_{\boldsymbol{G}} U^{*T}_{\mu\boldsymbol{G}}\left[-\frac{\hbar^2}{2m_0}\left(\boldsymbol{\nabla}^2-2i\boldsymbol{G}\cdot\boldsymbol{\nabla}-G^2\right)\right]U_{\nu\boldsymbol{G}}\right)e^{-i\boldsymbol{k}\cdot\boldsymbol{r}'}\,.\end{aligned} \tag{2.17}$$

Analogously, when $\hat{O}$ is the Pauli SOI operator, we have

$$\begin{aligned}\left(\hat{H}_{SO}\right)_{\mu\nu}(\boldsymbol{r},\boldsymbol{r}') &= \frac{1}{\Omega}\sum_{\boldsymbol{k}\boldsymbol{k}'} e^{i\boldsymbol{k}\cdot\boldsymbol{r}}\left(\sum_{\boldsymbol{G}\boldsymbol{G}'} U^{*T}_{\mu\boldsymbol{G}}\left\langle\boldsymbol{k}+\boldsymbol{G}\right|\frac{\hbar}{4m_0^2c^2}(\boldsymbol{\sigma}\times\boldsymbol{\nabla}V)\cdot(-i\hbar\boldsymbol{\nabla})\left|\boldsymbol{k}'+\boldsymbol{G}'\right\rangle U_{\nu\boldsymbol{G}'}\right)e^{-i\boldsymbol{k}'\boldsymbol{r}'}\\ &= \frac{1}{\Omega}\sum_{\boldsymbol{k}\boldsymbol{k}'} e^{i\boldsymbol{k}\cdot\boldsymbol{r}}\left(\sum_{\boldsymbol{G}\boldsymbol{G}'} U^{*T}_{\mu\boldsymbol{G}}\left\langle\boldsymbol{k}+\boldsymbol{G}\right|\boldsymbol{v}\left|\boldsymbol{k}'+\boldsymbol{G}'\right\rangle\cdot\hbar(\boldsymbol{k}'+\boldsymbol{G}')U_{\nu\boldsymbol{G}'}\right)e^{-i\boldsymbol{k}'\boldsymbol{r}'}\\ &= \frac{1}{\Omega}\sum_{\boldsymbol{k}\boldsymbol{k}'} e^{i\boldsymbol{k}\cdot\boldsymbol{r}}\left(\sum_{\boldsymbol{G}\boldsymbol{G}'} U^{*T}_{\mu\boldsymbol{G}}\left\langle\boldsymbol{k}+\boldsymbol{G}\right|\boldsymbol{v}\left|\boldsymbol{k}'+\boldsymbol{G}'\right\rangle\cdot(i\hbar\boldsymbol{\nabla}+\hbar\boldsymbol{G}')U_{\nu\boldsymbol{G}'}\right)e^{-i\boldsymbol{k}'\boldsymbol{r}'}\,,\end{aligned} \tag{2.18}$$

where we have defined the spin-orbit velocity operator as

$$\hat{\boldsymbol{v}} = \frac{\hbar}{4m_0^2c^2}(\hat{\boldsymbol{\sigma}}\times\boldsymbol{\nabla}\hat{V})\,. \tag{2.19}$$

We now plug Eq. (2.17) into Eq. (2.15), perform an integration by parts and use the completeness relation

$$\sum_{\boldsymbol{G}} U^{*T}_{\mu\boldsymbol{G}}U_{\nu\boldsymbol{G}} = \delta_{\mu\nu}\,, \tag{2.20}$$

as well as the following definition of the delta distribution function

$$\Delta(\boldsymbol{r}-\boldsymbol{r}') = \frac{1}{\Omega_0}\sum_{\boldsymbol{k}} e^{i\boldsymbol{k}\cdot(\boldsymbol{r}-\boldsymbol{r}')}\,, \tag{2.21}$$

and obtain

$$\langle\boldsymbol{r}|\frac{\hat{p}^2}{2m_0}|\Psi\rangle = \sum_{\mu} U_\mu(\boldsymbol{r})\left(-\frac{\hbar^2}{2m_0}\boldsymbol{\nabla}^2\psi_\mu(\boldsymbol{r}) + \sum_{\nu}\frac{-i\hbar}{m_0}\boldsymbol{p}_{\mu\nu}\cdot\boldsymbol{\nabla}\psi_\nu(\boldsymbol{r}) + \sum_{\nu} T_{\mu\nu}\psi_\nu(\boldsymbol{r})\right)\,, \tag{2.22}$$

where we have also recognized the matrix elements of the momentum operator and the kinetic energy operator between the U_μ functions, respectively

$$\begin{aligned}\boldsymbol{p}_{\mu\nu} &= \frac{1}{\Omega_0}\int_{u.c.}\mathrm{d}^3\boldsymbol{r}\,U^{*T}_{\mu}(\boldsymbol{r})(-i\hbar\boldsymbol{\nabla})U_\nu(\boldsymbol{r}) = \sum_{\boldsymbol{G}\boldsymbol{G}'} U^{*T}_{\mu\boldsymbol{G}}U_{\nu\boldsymbol{G}'}\frac{1}{\Omega_0}\int_{u.c.}\mathrm{d}^3\boldsymbol{r}'e^{-i\boldsymbol{G}\cdot\boldsymbol{r}}(-i\hbar\boldsymbol{\nabla})e^{i\boldsymbol{G}'\cdot\boldsymbol{r}}\\ &= \hbar\sum_{\boldsymbol{G}\boldsymbol{G}'}\boldsymbol{G}'U^{*T}_{\mu\boldsymbol{G}}U_{\nu\boldsymbol{G}'}\frac{1}{\Omega_0}\int_{u.c.}\mathrm{d}^3\boldsymbol{r}\,e^{i(\boldsymbol{G}'-\boldsymbol{G})\cdot\boldsymbol{r}} = \hbar\sum_{\boldsymbol{G}}\boldsymbol{G}U^{*T}_{\mu\boldsymbol{G}}U_{\nu\boldsymbol{G}}\,,\end{aligned} \tag{2.23}$$

$$T_{\mu\nu} = \frac{1}{\Omega_0}\int_{u.c.} \mathrm{d}^3\boldsymbol{r}\, U_\mu^{*T}(\boldsymbol{r})\frac{(-i\hbar\boldsymbol{\nabla})^2}{2m_0}U_\nu(\boldsymbol{r}) = \frac{\hbar^2}{2m_0}\sum_{\boldsymbol{G}} G^2 U_{\mu\boldsymbol{G}}^{*T}U_{\nu\boldsymbol{G}}\,. \tag{2.24}$$

Analogously, for the SOI term we obtain

$$\langle\boldsymbol{r}|\hat{H}_{SO}|\Psi\rangle = \sum_\mu U_\mu(\boldsymbol{r})\left(-i\hbar\sum_\nu\int \mathrm{d}^3\boldsymbol{r}'\,\boldsymbol{v}_{\mu\nu}(\boldsymbol{r},\boldsymbol{r}')\cdot\boldsymbol{\nabla}\psi_\nu(\boldsymbol{r}') + \sum_\nu\int \mathrm{d}^3\boldsymbol{r}'\,H_{\mu\nu}^{SO}(\boldsymbol{r},\boldsymbol{r}')\psi_\nu(\boldsymbol{r}')\right)\,, \tag{2.25}$$

where $\boldsymbol{v}_{\mu\nu}(\boldsymbol{r},\boldsymbol{r}')$ is the matrix element of the spin-orbit velocity operator, given by Eq. (2.16) with $\hat{O}$ replaced by $\hat{\boldsymbol{v}}$, and

$$H_{\mu\nu}^{SO}(\boldsymbol{r},\boldsymbol{r}') = \frac{1}{\Omega}\sum_{\boldsymbol{k}\boldsymbol{k}'} e^{i\boldsymbol{k}\cdot\boldsymbol{r}}\left(\sum_{\boldsymbol{G}\boldsymbol{G}'} U_{\mu\boldsymbol{G}}^{*T}\left\langle \boldsymbol{k}+\boldsymbol{G}\middle|\hat{\boldsymbol{v}}\middle|\boldsymbol{k}'+\boldsymbol{G}'\right\rangle\cdot\hbar\boldsymbol{G}'U_{\nu\boldsymbol{G}'}\right)e^{-i\boldsymbol{k}'\boldsymbol{r}'} \tag{2.26}$$

corresponds to the spin-orbit energy.

Finally, for the potential energy term, we simply have

$$\langle\boldsymbol{r}|\hat{V}|\Psi\rangle = \sum_\mu U_\mu(\boldsymbol{r})\left(\sum_\nu\int \mathrm{d}^3\boldsymbol{r}'\,V_{\mu\nu}(\boldsymbol{r},\boldsymbol{r}')\psi_\nu(\boldsymbol{r}')\right)\,, \tag{2.27}$$

where $V_{\mu\nu}(\boldsymbol{r},\boldsymbol{r}')$, corresponds to Eq. (2.16) with $\hat{O}$ replaced by $\hat{V}$.

Plugging Eqs. (2.22), (2.25) and (2.27) into the Schrödinger equation and equating the ”coefficients” of the U_μ functions, we obtain the following set of *exact EFEs*:

$$\begin{aligned}-\frac{\hbar^2}{2m_0}\boldsymbol{\nabla}^2\psi_\mu(\boldsymbol{r}) + \sum_\nu\frac{-i\hbar}{m_0}\boldsymbol{p}_{\mu\nu}\cdot\boldsymbol{\nabla}\psi_\nu(\boldsymbol{r}) - i\hbar\sum_\nu\int \mathrm{d}^3\boldsymbol{r}'\,\boldsymbol{v}_{\mu\nu}(\boldsymbol{r},\boldsymbol{r}')\cdot\boldsymbol{\nabla}\psi_\nu(\boldsymbol{r}')\\ +\sum_\nu\int \mathrm{d}^3\boldsymbol{r}'\,H_{\mu\nu}(\boldsymbol{r},\boldsymbol{r}')\psi_\nu(\boldsymbol{r}') = E\psi_\mu(\boldsymbol{r})\,,\end{aligned} \tag{2.28}$$

where

$$H_{\mu\nu}(\boldsymbol{r},\boldsymbol{r}') = T_{\mu\nu}\Delta(\boldsymbol{r}-\boldsymbol{r}') + H_{\mu\nu}^{SO}(\boldsymbol{r},\boldsymbol{r}') + V_{\mu\nu}(\boldsymbol{r},\boldsymbol{r}')\,. \tag{2.29}$$

It is worth noting that the above derivation is not restricted to local potentials, as no assumption has been made about the matrix elements $\left\langle \boldsymbol{k}+\boldsymbol{G}\middle|\hat{V}\middle|\boldsymbol{k}'+\boldsymbol{G}'\right\rangle$. More importantly, we see that the third and the fourth terms on the left-hand side of Eq. (2.28) introduce non-locality in the equations even if the potential V is local.

2.1.2. Approximations of the exact envelope function equations

In presence of a local potential V, the non-local contribution to Eq. (2.28) can be safely dropped under the assumption of slowly varying envelope functions. In other words, $V_{\mu\nu}(\boldsymbol{r},\boldsymbol{r}')$ in Eq. (2.29) can be replaced by $V_{\mu\nu}(\boldsymbol{r})\Delta(\boldsymbol{r}-\boldsymbol{r}')$, where $V_{\mu\nu}(\boldsymbol{r})$ is a new function of the position (see App. A.1). The same is true for the spin-orbit velocity $\boldsymbol{v}_{\mu\nu}(\boldsymbol{r})$ and the spin-orbit energy $H_{\mu\nu}^{SO}(\boldsymbol{r})$. The new EFEs become

$$-\frac{\hbar^2}{2m_0}\boldsymbol{\nabla}^2\psi_\mu(\boldsymbol{r}) - \frac{i\hbar}{m_0}\sum_\nu \boldsymbol{\pi}_{\mu\nu}(\boldsymbol{r})\cdot\boldsymbol{\nabla}\psi_\nu(\boldsymbol{r}) + \sum_\nu H_{\mu\nu}(\boldsymbol{r})\psi_\nu(\boldsymbol{r}) = E\psi_\mu(\boldsymbol{r}) \,, \tag{2.30}$$

where

$$H_{\mu\nu}(\boldsymbol{r}) = T_{\mu\nu} + H^{SO}_{\mu\nu}(\boldsymbol{r}) + V_{\mu\nu}(\boldsymbol{r}) \,, \tag{2.31}$$

and we have defined

$$\boldsymbol{\pi}_{\mu\nu} = \boldsymbol{p}_{\mu\nu} + m_0\boldsymbol{v}_{\mu\nu}(\boldsymbol{r}) \,. \tag{2.32}$$

In heterostructures, the EFEs Eq. (2.30) are a good approximation to the exact equations Eq. (2.28) very far away from the interfaces. In fact, far from any interface and in absence of external potentials, it can be shown that (see App. A.2)

$$H_{\mu\nu}(\boldsymbol{r},\boldsymbol{r}') = H^{bulk}_{\mu\nu}\Delta(\boldsymbol{r}-\boldsymbol{r}') \,, \tag{2.33}$$

with

$$H^{bulk}_{\mu\nu} = \frac{1}{\Omega_0}\int \mathrm{d}^3\boldsymbol{r}\, U^{*T}_\mu(\boldsymbol{r})H^{bulk}(\boldsymbol{r})U_\nu(\boldsymbol{r}) \,, \tag{2.34}$$

where $H^{bulk}(\boldsymbol{r})$ is the appropriate potential for the bulk crystal. Note that far away from the interfaces the non-local components of $H_{\mu\nu}(\boldsymbol{r},\boldsymbol{r}')$ vanish without any approximation. Thus, when dealing with an arbitrary heterostructure, if the material interfaces are approximated with abrupt changes, as is often the case, $H_{\mu\nu}(\boldsymbol{r})$ varies from one value of $H^{bulk}_{\mu\nu}$ to another. If $V_{\mu\nu}(\boldsymbol{r})$ also contains a local, slowly varying external potential $V^e(\boldsymbol{r})$, it can be shown that the effective potential for the envelope function becomes (see App. A.3)

$$V^e_{\mu\nu}(\boldsymbol{r},\boldsymbol{r}') = \delta_{\mu\nu}V^e(\boldsymbol{r})\Delta(\boldsymbol{r}-\boldsymbol{r}') \,. \tag{2.35}$$

2.2. Derivation of the effective mass equation

We are typically interested in studying the band structure of a semiconductor in an energy E near the edges of the gap. Thus, we choose a set $\mathcal{S}$ of basis functions $U_{\mu_\mathrm{s}}(\boldsymbol{r})$ such that the corresponding envelope functions $\psi_{\mu_\mathrm{s}}(\boldsymbol{r})$ will be dominant in the envelope expansion (2.3). We denote with $\mathcal{R}$ the set of the remaining basis functions, which we will refer to as $U_{\mu_\mathrm{r}}(\boldsymbol{r})$.

Denoting with s and r the indices running in $\mathcal{S}$ and $\mathcal{R}$, respectively, we set $\mu = \mu_\mathrm{r}$ in Eq. (2.30), and, neglecting the term $\boldsymbol{\nabla}^2\psi_{\mu_\mathrm{r}}$, we obtain

$$\psi_{\mu_\mathrm{r}} = (E - H_{\mu_\mathrm{r}\mu_\mathrm{r}})^{-1}\sum_{\nu_\mathrm{s}}\left(\frac{-i\hbar}{m_0}\boldsymbol{\pi}_{\mu_\mathrm{r}\nu_\mathrm{s}}\cdot\boldsymbol{\nabla}\psi_{\nu_\mathrm{s}}(\boldsymbol{r}) + H_{\mu_\mathrm{r}\nu_\mathrm{s}}\psi_{\nu_\mathrm{s}}(\boldsymbol{r})\right) \,. \tag{2.36}$$

We now plug Eq. (2.36) into Eq. (2.30) with $\mu = \mu_\mathrm{s}$ and obtain

$$-\frac{\hbar^2}{2m_0}\sum_{\nu_s}\boldsymbol{\nabla}\cdot(\gamma_{\mu_\mathrm{s}\nu_\mathrm{s}}\cdot\boldsymbol{\nabla}\psi_{\nu_\mathrm{s}}(\boldsymbol{r})) + \sum_{\nu_\mathrm{s}}\frac{-i\hbar}{m_0}\boldsymbol{\pi}_{\mu_\mathrm{s}\nu_\mathrm{s}}\cdot\boldsymbol{\nabla}\psi_{\nu_\mathrm{s}}(\boldsymbol{r}) + \sum_{\nu_\mathrm{s}}H^{(2)}_{\mu_\mathrm{s}\nu_\mathrm{s}}(E,\boldsymbol{r})\psi_{\nu_\mathrm{s}}(\boldsymbol{r}) = E\psi_{\mu_\mathrm{s}}(\boldsymbol{r}) \,, \tag{2.37}$$

where the effective mass tensor is defined as

$$\gamma_{\mu_s\nu_s}(E,\boldsymbol{r}) = \boldsymbol{I}\delta_{\mu_s\nu_s} + \frac{2}{m_0}\sum_{\mu_r}\boldsymbol{\pi}_{\mu_s\mu_r}\frac{1}{E-H_{\mu_r\mu_r}(\boldsymbol{r})}\boldsymbol{\pi}_{\mu_r\nu_s} \tag{2.38}$$

and

$$H^{(2)}_{\mu_s\nu_s}(E,\boldsymbol{r}) = H_{\mu_s\nu_s}(\boldsymbol{r}) + \sum_{\mu_r}H_{\mu_s\mu_r}(\boldsymbol{r})\frac{1}{E-H_{\mu_r\mu_r}(\boldsymbol{r})}H_{\mu_r\nu_s}(\boldsymbol{r}) \tag{2.39}$$

coincides with the effective potential in second order perturbation theory. The "perturbative" term in Eq. (2.39) represents the interaction between the states in the set of interest $\mathcal{S}$ and the states in the set $\mathcal{R}$ which are traced away.

It is important to note that the first term of Eq. (2.37) takes into account the fact that the band parameters are position dependent in heterostructures, and so they do not commute with the differential operators. This in turn means that the order in which the operators appear with respect to the band parameters matters. Moreover, in writing down Eq. (2.37) we have neglected terms that are appreciable only near interfaces as well as those that lead to contributions to the bulk band structure linear in wave vector [64]. Indeed, the latter contribution, due to the absence of inversion symmetry in the constituent crystalline structure, is generally small for most III-V compound semiconductors.

We now discuss the application of the effective mass equations Eq. (2.37) to a generic multi-layer nanostructure. We make two important assumptions. First, we assume the same basis functions U_μ in all layers. Second, we assume that such basis set approximates the zone-center Bloch functions $u_{\mu 0}$ of all the constituent materials. Then the diagonal elements of $H^{(2)}_{\mu_s\nu_s}(E,\boldsymbol{r})$ represent the appropriate bulk zone-center band profiles to second order in perturbation theory throughout the heterostructure.

In this work the set $\mathcal{S}$ includes the Γ_1 conduction band and the Γ_4 valence band of the semiconductor [70]. It is customary to represent the three Γ_{4v} (valence band) wave functions with $|X\rangle$, $|Y\rangle$ and $|Z\rangle$. The Γ_{1c} (conduction band) wave function is represented as $|S\rangle$. From symmetry arguments, we note that the second term in the LHS of Eq. (2.37) only couples Γ_{1c} with Γ_{4v} states through the interband optical matrix element P:

$$\langle S|\hat{p}_x|X\rangle = \langle S|\hat{p}_y|Y\rangle = \langle S|\hat{p}_z|Z\rangle = i\frac{m_0}{\hbar}P\,. \tag{2.40}$$

When spin-orbit coupling is taken into account it is necessary to include the spin functions into the basis states, leading to an eight-dimensional basis. The matrix elements of the spin-orbit potential energy term are given by Eq. (2.34) with $H^{bulk}(\boldsymbol{r})$ replaced by $\frac{\hbar}{4m_0^2c^2}(\boldsymbol{\sigma}\times\boldsymbol{\nabla}V_0(\boldsymbol{r}))\cdot\boldsymbol{p}$, where $V_0(\boldsymbol{r})$ is the lattice-periodic crystalline potential of the bulk material. We will not consider spin-orbit effects generated by any other external potential, as the dominant contribution to the SOI originates from the atomic core potential $V_0(\boldsymbol{r})$. It can be shown that it exists only one independent matrix element [71]:

$$\langle X|(\boldsymbol{\nabla}V_0\times\boldsymbol{p})_z|Y\rangle \neq 0\,. \tag{2.41}$$

The spin-orbit gap Δ_0 is usually defined as

$$\Delta_0 = \frac{3i\hbar}{4m_0^2c^2}\left\langle X|\partial_x V\,p_y - \partial_y V\,p_x|Y\right\rangle\,. \tag{2.42}$$

We can now compute explicitly the matrix elements of the operator $H^{SO}_{\mu\nu}$ in this basis. For example

$$\langle X|\frac{\hbar}{4m_0^2c^2}(\boldsymbol{\nabla}V_0\times\boldsymbol{p})|Y\rangle\cdot\langle\uparrow|\boldsymbol{\sigma}|\uparrow\rangle = \langle X|\frac{\hbar}{4m_0^2c^2}(\boldsymbol{\nabla}V_0\times\boldsymbol{p})_z|Y\rangle\ \langle\uparrow|\sigma_z|\uparrow\rangle = -i\frac{\Delta_0}{3}\,,$$

and

$$\langle X|\frac{\hbar}{4m_0^2c^2}(\boldsymbol{\nabla}V_0\times\boldsymbol{p})|Z\rangle\cdot\langle\uparrow|\boldsymbol{\sigma}|\uparrow\rangle = \langle X|\frac{\hbar}{4m_0^2c^2}(\boldsymbol{\nabla}V_0\times\boldsymbol{p})_y|Y\rangle\ \langle\uparrow|\sigma_y|\uparrow\rangle = 0\,.$$

One can evaluate in an analogous way the rest of the matrix elements. The result is

$$H^{SO}_{\mu_\mathsf{s}\nu_\mathsf{s}} = \frac{\Delta_{so}}{3}\begin{pmatrix} 0 & 0 & 0 & 0 & 0 & 0 & 0 & 0 \\ 0 & 0 & 0 & 0 & 0 & 0 & 0 & 0 \\ 0 & 0 & 0 & -i & 0 & 0 & 0 & 1 \\ 0 & 0 & i & 0 & 0 & 0 & 0 & -i \\ 0 & 0 & 0 & 0 & 0 & -1 & i & 0 \\ 0 & 0 & 0 & 0 & -1 & 0 & i & 0 \\ 0 & 0 & 0 & 0 & -i & -i & 0 & 0 \\ 0 & 0 & 1 & i & 0 & 0 & 0 & 0 \end{pmatrix}\,. \tag{2.43}$$

From now on, we will neglect the $\boldsymbol{k}$-dependent spin-orbit term $\boldsymbol{v}_{\mu\nu}$, and assume $\boldsymbol{\pi}_{\mu\nu} = \boldsymbol{p}_{\mu\nu}$. As already anticipated, the remaining part of the potential energy term, in absence of strain effects, results in a diagonal matrix containing the position dependent band profiles $E_c(\boldsymbol{r})$ and $E_v(\boldsymbol{r})$ of the conduction and valence bands, respectively. According to Eq. (2.35), the external potential $V^e(\boldsymbol{r})$ is added to the diagonal as well.

To derive an explicit form of the Hamiltonian, one needs to compute the effective mass tensor

$$\gamma^{\alpha\beta}_{\mu_\mathsf{s}\nu_\mathsf{s}} = \delta_{\mu_\mathsf{s}\nu_\mathsf{s}}\delta_{\alpha\beta} + \frac{2}{m_0}\sum_{\mu_\mathsf{r}}\frac{\langle U_{\mu_\mathsf{s}}|p_\alpha|U_{\mu_\mathsf{r}}\rangle\ \langle U_{\mu_\mathsf{r}}|p_\beta|U_{\nu_\mathsf{s}}\rangle}{E - H_{\mu_\mathsf{r}\mu_\mathsf{r}}(\boldsymbol{r})}\,. \tag{2.44}$$

which, in turns, requires the knowledge of each zone-center eigenstate to obtain the dipole matrix elements $\boldsymbol{p}_{\mu\nu}$ and all the matrix elements $H_{\mu_\mathsf{r}\mu_\mathsf{r}}$. This problem is typically circumvented expressing the components $\gamma^{\alpha\beta}_{\mu_\mathsf{s}\nu_\mathsf{s}}$ in terms of existing phenomenological parameters. For the valence band these are the Dresselhaus-Kip-Kittel (DKK) parameters [72] L, M, N^+ and N^-. For the conduction band, the interaction of the first s-like conduction band state with the remote bands gives rise to the electron effective mass through the parameter

$$A_c = \frac{\hbar^2}{2m_0}\left(1 + \frac{2}{m_0}\sum_{\mu_\mathsf{r}}\frac{|\langle S|p_x|U_{\mu_\mathsf{r}}\rangle|^2}{E - H_{\mu_\mathsf{r}\mu_\mathsf{r}}(\boldsymbol{r})}\right)\,. \tag{2.45}$$

Once the various components of the effective mass tensor are matched with the definitions of the parameters DKK parameters and A_c written in terms of the appropriate matrix elements (see Ref. [71]), we can write down the resulting 8×8 Hamiltonian as a sum of three terms:

$$H^{BF}_{\mu\nu}(\boldsymbol{r}) = H^0_{\mu\nu}(\boldsymbol{r}) + H^{SO}_{\mu\nu}(\boldsymbol{r}) + \delta_{\mu\nu}V^e(\boldsymbol{r})\,. \tag{2.46}$$

The first term is given by

$$H^0_{\mu\nu} = \begin{array}{c|cc|ccc|ccc|} & |S\uparrow\rangle & |S\downarrow\rangle & |X\uparrow\rangle & |Y\uparrow\rangle & |Z\uparrow\rangle & |X\downarrow\rangle & |Y\downarrow\rangle & |Z\downarrow\rangle \\ |S\uparrow\rangle & H_c & 0 & \multicolumn{3}{c|}{H_{cv}} & \multicolumn{3}{c|}{0} \\ |S\downarrow\rangle & 0 & H_c & \multicolumn{3}{c|}{0} & \multicolumn{3}{c|}{H_{cv}} \\ \hline |X\uparrow\rangle & & & & & & & & \\ |Y\uparrow\rangle & H_{vc} & 0 & \multicolumn{3}{c|}{H_v} & \multicolumn{3}{c|}{0} \\ |Z\uparrow\rangle & & & & & & & & \\ \hline |X\downarrow\rangle & & & & & & & & \\ |Y\downarrow\rangle & 0 & H_{vc} & \multicolumn{3}{c|}{0} & \multicolumn{3}{c|}{H_v} \\ |Z\downarrow\rangle & & & & & & & & \end{array} \,. \tag{2.47}$$

For the valence band Hamiltonian H_v we have:

$$H_v = \left(E_{v,\text{av}}(\boldsymbol{r}) + \frac{\hbar^2}{2m_0}\hat{\boldsymbol{k}}^2\right)\mathbb{1}_3 + \begin{pmatrix} \hat{k}_xL\hat{k}_x + \hat{k}_yM\hat{k}_y + \hat{k}_zM\hat{k}_z & \hat{k}_xN^+\hat{k}_y + \hat{k}_yN^-\hat{k}_x & \hat{k}_xN^+\hat{k}_z + \hat{k}_zN^-\hat{k}_x \\ \hat{k}_yN^+\hat{k}_x + \hat{k}_xN^-\hat{k}_y & \hat{k}_xM\hat{k}_x + \hat{k}_yL\hat{k}_y + \hat{k}_zM\hat{k}_z & \hat{k}_yN^+\hat{k}_z + \hat{k}_zN^-\hat{k}_y \\ \hat{k}_zN^+\hat{k}_x + \hat{k}_xN^-\hat{k}_z & \hat{k}_zN^+\hat{k}_y + \hat{k}_yN^-\hat{k}_z & \hat{k}_xM\hat{k}_x + \hat{k}_yM\hat{k}_y + \hat{k}_zL\hat{k}_z \end{pmatrix} . \tag{2.48}$$

where $E_{v,\text{av}} = E_v - \Delta_{so}/3$ and $\mathbb{1}_3$ is a 3×3 identity matrix.

Note that the valence band Hamiltonian Eq. (2.48) derived from the exact envelope function theory contains the correct operator ordering, which originates from the non-commutativity of the position-dependent band parameters and the momentum operators. For example, in heterostructures one obtains terms of the form $\hat{k}_xN^+\hat{k}_y + \hat{k}_yN^-\hat{k}_x$, while for a bulk semiconductor one would simply have k_xNk_y, with $N = N^+ + N^-$. Furthermore, since $N^+ \neq N^-$, the operator ordering obtained is said to be *non-symmetrized*. This contrasts with the common practice within the **k** · **p** community before the advent of Burt's exact theory, which involved using a *symmetrized* form, i.e. to set $N^+ = N^- = N/2$, which has been shown to be incorrect for heterostructures [73].

In this work the DKK parameters are calculated from the Luttinger parameters γ_1, γ_2, γ_3 as [67]

$$\begin{aligned} L &= \frac{\hbar^2}{2m_0}(-\gamma_1 - 4\gamma_2 - 1)\,, \\ M &= \frac{\hbar^2}{2m_0}(2\gamma_2 - \gamma_1 - 1)\,, \\ N^+ &= \frac{\hbar^2}{2m_0}(-6\gamma_3 - (2\gamma_2 - \gamma_1 - 1))\,, \\ N^- &= \frac{\hbar^2}{2m_0}(2\gamma_2 - \gamma_1 - 1)\,. \end{aligned} \tag{2.49}$$

The conduction band Hamiltonian H_c is given by

$$H_c = E_c(\boldsymbol{r}) + \hat{k}_x A_c \hat{k}_x + \hat{k}_y A_c \hat{k}_y + \hat{k}_z A_c \hat{k}_z \,. \tag{2.50}$$

The coupling between conduction and valence bands is described by [2]

$$H_{cv} = \begin{pmatrix} iP\hat{k}_x & iP\hat{k}_y & iP\hat{k}_z \end{pmatrix} \tag{2.51}$$

and

$$H_{vc} = \begin{pmatrix} -i\hat{k}_x P \\ -i\hat{k}_y P \\ -i\hat{k}_z P \end{pmatrix} \,. \tag{2.52}$$

The spin-orbit term $H^{SO}_{\mu\nu}$ in given in Eq. (2.43), while the third, diagonal term accounts for the presence of an external potential $V^e(\boldsymbol{r})$.

While in a 6-band **k** · **p** Hamiltonian including only the p-like valence band states all conduction bands are considered to be part of the remote bands set $\mathcal{R}$, in 8-band **k** · **p** theory the lowest s-like conduction band is already included in the **k** · **p** Hamiltonian and not treated as a perturbation anymore. Thus, the material parameters of the valence band Hamiltonian H_v have to be modified accordingly. It can be shown [67] that the required correction term to the DKK parameters is obtained by replacing the bare Luttinger parameters γ_1, γ_2, γ_3 with the modified ones

$$\begin{aligned} \tilde{\gamma}_1 &= \gamma_1 - \frac{E_p}{3E_g}\,, \\ \tilde{\gamma}_2 &= \gamma_2 - \frac{E_p}{6E_g}\,, \\ \tilde{\gamma}_3 &= \gamma_3 - \frac{E_p}{6E_g}\,, \end{aligned} \tag{2.53}$$

being E_g the energy gap of the bulk semiconductor and

$$E_P = \frac{2m_0}{\hbar^2} P^2 \tag{2.54}$$

the Kane energy.

In this work, the parameter A_c is evaluated from the bulk semiconductor band gap and the electron effective mass m_e [75]:

$$A_c = \frac{\hbar^2}{2m_e} - \frac{2}{3}\frac{P^2}{E_g} - \frac{1}{3}\frac{P^2}{E_g + \Delta_{so}} \,. \tag{2.55}$$

For many relevant semiconductors, including the ones we considered in this work, the standard parameters lead to a negative value for A_c. This fact induces spurious solutions [76] that bend within the band gap for large wave vectors. To avoid these unphysical results we set $A_c = 0$ and rescale the E_p parameter (or, equivalently, the parameter P) in order to still get the correct conduction bulk band dispersion [69, 77]:

$$E_P^{\text{rsc}} = \frac{E_g(E_g + \Delta_{so})}{E_g + \frac{2}{3}\Delta_{so}} \left(\frac{m_0}{m_e}\right) \,. \tag{2.56}$$

---

[2] In this work we adopt the common practice in the **k** · **p** literature [67] of neglecting in H_{cv} additional second order terms of the form $k_\alpha B k_\beta$, which are proportional to the inversion asymmetry parameter B [74].

Foreman rigorously showed that this approach is not an approximation and is equivalent to a change of the Bloch basis [78]. Note that the rescaling procedure affects also the valence band Hamiltonian H_v, as the modified Luttinger parameters in the 8-band model depend upon E_P through Eq. (2.53).

2.3. The envelope function approach for nanowires

We now consider the application of the EFEs to compute the electronic states of a NW with growth axis directed along an arbitrary crystallographic direction $[hkl]$.

2.3.1. Rotation of the Burt-Foreman Hamiltonian

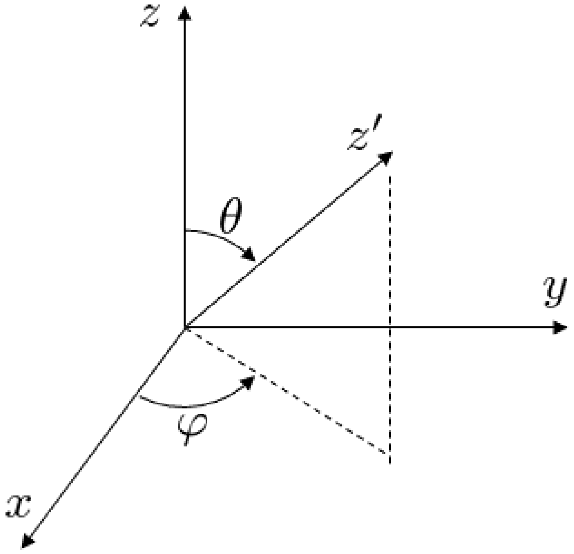

Figure 2.1: Rotation of the coordinate system. The new coordinate system is set with its principal axis z' rotated by an angle (θ,ϕ) with respect to the original coordinate system.

First, we write the BF Hamiltonian Eq. (2.46) in a rotated coordinate system where z' is aligned with the NW's growth direction $[hkl]$. We have that $\boldsymbol{r}' = R\boldsymbol{r}$ and $\hat{\boldsymbol{k}}' = R\hat{\boldsymbol{k}}$ where R is the standard rotation matrix

$$R(\theta,\phi) = \begin{pmatrix} \cos\theta\cos\varphi & \sin\varphi\cos\theta & -\sin\theta \\ -\sin\varphi & \cos\phi & 0 \\ \cos\varphi\sin\theta & \sin\varphi\sin\theta & \cos\theta \end{pmatrix}. \tag{2.57}$$

In this work, to treat NWs with growth axis z' directed along the $[111]$ crystallographic direction, we set the values $\theta = \arccos\left(1/\sqrt{3}\right)$ and $\phi = \pi/4$. We note that the BF Hamiltonian Eq. (2.46) can be written in general terms as

$$H^{BF}_{\mu\nu}(\boldsymbol{r}) = \sum_{\alpha\beta} \hat{k}_\alpha D^{\alpha\beta} \hat{k}_\beta + \sum_{\alpha} \left(F^{\alpha}_{L} \hat{k}_\alpha + \hat{k}_\alpha F^{\alpha}_{R} \right) + G\,, \tag{2.58}$$

where $D^{\alpha\beta}$, $F^{\alpha}_{L(R)}$ and G are 8×8 matrices obtained by collecting terms involving the same powers of the wave vector's component in the Hamiltonian and keeping track of the correct operator ordering. For example, to obtain the matrix D^{xy}, one has to collect all the terms in which the band parameter has $\hat{k}_x$ on the left and $\hat{k}_y$ on the right. Analogously, to obtain F^x_L one has to group all the terms with $\hat{k}_x$ on the right and the band parameter on the left. Note that $D^{\alpha\beta} \neq D^{\beta\alpha}$ and $F^\alpha_L \neq F^\alpha_R$, and that these matrices are not Hermitian. Nevertheless, the sums $D^{\alpha,\beta} + D^{\beta,\alpha}$ and $F^\alpha_L + F^\alpha_R$ are indeed Hermitian.

Using $\hat{\boldsymbol{k}}' = R\hat{\boldsymbol{k}}$ we have

$$H^{BF}_{\mu\nu}(\boldsymbol{r}') = \sum_{\alpha\beta} \hat{k}'_\alpha D^{\alpha\beta}(\theta,\varphi)\hat{k}'_\beta + \sum_\alpha \Big(F^\alpha_L(\theta,\varphi)\hat{k}'_\alpha + \hat{k}'_\alpha F^\alpha_R(\theta,\varphi) \Big) + G \tag{2.59}$$

where the rotated matrices are given by

$$D^{\alpha\beta}(\theta,\varphi) = \sum_{\alpha'\beta'} R_{\alpha\alpha'} D^{\alpha'\beta'} R^{-1}_{\beta'\beta}\,, \tag{2.60}$$

$$F^\alpha_{L/R}(\theta,\varphi) = \sum_{\alpha'} F^{\alpha'}_{L/R} R^{-1}_{\alpha'\alpha}\,. \tag{2.61}$$

From now on we will omit the (θ,φ) dependence for simplicity. To be consistent, we also transform the basis functions $U_\mu(\boldsymbol{r})$ into the rotated frame. Since the basis states are either isotropic (conduction band) or directed along the cartesian axis (valence states), the transformation matrix is simple and it is given by AU, where

$$U = \begin{pmatrix} 1 & & & \\ & 1 & & \\ & & R & \\ & & & R \end{pmatrix} \tag{2.62}$$

is a standard rotation matrix, and

$$A = \begin{pmatrix} \bar{A} & \\ & \bar{A}\otimes I_3 \end{pmatrix}\,, \tag{2.63}$$

with

$$\bar{A} = \begin{pmatrix} e^{-i\varphi/2}\cos\theta/2 & e^{i\varphi/2}\sin\theta/2 \\ -e^{-i\varphi/2}\sin\theta/2 & e^{i\varphi/2}\cos\theta/2 \end{pmatrix}\,, \tag{2.64}$$

rotates the spin. The form of the rotation matrices just given is for a cartesian basis ordered as $\{|S\!\uparrow\rangle, |S\!\downarrow\rangle, |X\!\uparrow\rangle, |Y\!\uparrow\rangle, |Z\!\uparrow\rangle, |X\!\downarrow\rangle, |Y\!\downarrow\rangle, |Z\!\downarrow\rangle\}$, consistently with Eq. (2.47).

Furthermore, we can chose the following symmetry-adapted basis that diagonalizes the SOI term [75]:

$$\begin{aligned}
\left|\frac{1}{2},\frac{1}{2}\right\rangle_{\text{EL}} &= |S'\uparrow'\rangle\,, \\
\left|\frac{1}{2},-\frac{1}{2}\right\rangle_{\text{EL}} &= i\,|S'\downarrow'\rangle\,, \\
\left|\frac{3}{2},\frac{3}{2}\right\rangle_{\text{HH}} &= \sqrt{1/2}\,|(X'+iY')\uparrow'\rangle\,, \\
\left|\frac{3}{2},-\frac{3}{2}\right\rangle_{\text{HH}} &= i\sqrt{1/2}\,|(X'-iY')\downarrow'\rangle\,, \\
\left|\frac{3}{2},\frac{1}{2}\right\rangle_{\text{LH}} &= i\sqrt{1/6}\,|(X'+iY')\downarrow'\rangle - i\sqrt{2/3}\,|Z'\uparrow'\rangle\,, \\
\left|\frac{3}{2},-\frac{1}{2}\right\rangle_{\text{LH}} &= \sqrt{1/6}\,|(X'-iY')\uparrow'\rangle + \sqrt{2/3}\,|Z'\downarrow'\rangle\,, \\
\left|\frac{1}{2},\frac{1}{2}\right\rangle_{\text{SO}} &= \sqrt{1/3}\,(|(X'+iY')\downarrow'\rangle + |Z'\uparrow'\rangle)\,, \\
\left|\frac{1}{2},-\frac{1}{2}\right\rangle_{\text{SO}} &= -i\sqrt{1/3}\,(|(X'-iY')\uparrow'\rangle - |Z'\downarrow'\rangle)\;.
\end{aligned} \tag{2.65}$$

The SOI splits the six-fold degenerate, p-like valence band states into a four-fold degenerate subspace with degenerate eigenvalue $\frac{1}{3}\Delta_{so}$, at energy E_v, and a two-fold degenerate subspace with degenerate eigenvalue $-\frac{2}{3}\Delta_{so}$. Being $E_{v,\text{av}} = E_v - \frac{1}{3}\Delta_{so}$, the two degenerate subspaces are at energies E_v and $E_v - \Delta_{so}$, respectively. The electron states are not affected by spin-orbit coupling. Here we classified the six valence states in terms of the eigenstates $|\boldsymbol{J}, J_z\rangle$ of the total angular momentum $\boldsymbol{J} = \boldsymbol{L} + \boldsymbol{S}$, being J_z its z-component. $\boldsymbol{L}$ is the orbital angular momentum of the Bloch orbit and $\boldsymbol{S}$ is the spin. The four-fold degenerate subspace corresponds to the $J = 3/2$ angular momentum states. The Bloch states with $J_z = \pm 3/2$ are referred to as heavy hole (HH) states, while the ones with $J_z = \pm 3/2$ are referred to as light hole states (LH). The names "heavy" and "light" originate from the smaller curvatures of the energy dispersions for HH bands with respect to LH bands in bulk materials. The two-fold degenerate subspace corresponds instead to the $J = 1/2$ sector, and the corresponding Bloch states are referred to as split-off (SOFF) hole bands.

Note finally that the term "symmetry-adapted" refers to the fact that the total angular momentum $\boldsymbol{J}$ quantization axis is aligned with the growth direction of the NW z'. The transformation matrix from the cartesian basis to the total angular momentum basis is

$$Q = \begin{pmatrix}
1 & 0 & 0 & 0 & 0 & 0 & 0 & 0 \\
0 & i & 0 & 0 & 0 & 0 & 0 & 0 \\
0 & 0 & \frac{1}{\sqrt{2}} & i\frac{1}{\sqrt{2}} & 0 & 0 & 0 & 0 \\
0 & 0 & 0 & 0 & 0 & i\frac{1}{\sqrt{2}} & \frac{1}{\sqrt{2}} & 0 \\
0 & 0 & 0 & 0 & -i\sqrt{\frac{2}{3}} & i\frac{1}{\sqrt{6}} & -\frac{1}{\sqrt{6}} & 0 \\
0 & 0 & \frac{1}{\sqrt{6}} & -i\frac{1}{\sqrt{6}} & 0 & 0 & 0 & \sqrt{\frac{2}{3}} \\
0 & 0 & 0 & 0 & \frac{1}{\sqrt{3}} & \frac{1}{\sqrt{3}} & i\frac{1}{\sqrt{3}} & 0 \\
0 & 0 & -i\frac{1}{\sqrt{3}} & -\frac{1}{\sqrt{3}} & 0 & 0 & 0 & i\frac{1}{\sqrt{3}}
\end{pmatrix}\,. \tag{2.66}$$

If we define $P = QAU$ as the transformation matrix to go from the original cartesian basis to the symmetry-adapted one, the matrices in Eq. (2.59) transform according to (see App. A.4):

$$
\begin{aligned}
D^{\alpha\beta} &\to P^* D^{\alpha\beta} P^T \,, \\
F^{\alpha}_{L/R} &\to P^* F^{\alpha}_{L(R)} P^T \,, \\
G &\to P^* G P^T \,.
\end{aligned}
\tag{2.67}
$$

2.3.2. Infinite nanowires

The translational invariance along z' allows to write the envelope function as

$$
\psi'_\mu(\boldsymbol{r}') = \frac{1}{\sqrt{L}} \psi'_\mu(\boldsymbol{r}'_\perp) e^{i k'_z z'}
\tag{2.68}
$$

where $\boldsymbol{r}'_\perp = \boldsymbol{x}' + \boldsymbol{y}'$ is the in-plane position vector, $\psi'_\mu(\boldsymbol{r}'_\perp)$ is the in-plane envelope function component in the symmetry-adapted basis Eq. (2.65) and k'_z is the free wave vector. If we plug Eq. (2.68) into the transformed EFEs and use $\hat{k}_\alpha = -i\partial_\alpha$ for $\alpha = x, y$, and $\hat{k}_z = k_z$, we obtain an set of coupled, second order, partial differential equations for the in-plane envelope function components $\psi'_\mu(\boldsymbol{r}'_\perp)$. Note that, since k_z is a good quantum number for infinite NWs, the second order terms $-ik_z D^{\alpha z}$ and $-ik_z D^{z\alpha}$ become additional first order differential operators. Analogously, the second order term $k_z^2 D^{zz}$ as well as the first order terms $k_z F^z_R$ and $F^z_L k_z$ become additional zero-th order terms, where no differential operator appears. Explicitly, the Hamiltonian operator reads

$$
\hat{H}^{BF} = \sum_{\alpha,\beta=x',y'} \partial_\alpha \bar{D}^{\alpha\beta} \partial_\beta + \sum_{\alpha=x,y} \left(\bar{F}^\alpha_L \partial_\alpha + \partial_\alpha \bar{F}^\alpha_R \right) + \bar{G} \,,
\tag{2.69}
$$

where

$$
\begin{aligned}
\bar{D}^{\alpha\beta} &= -D^{\alpha\beta} \,, \\
\bar{F}^\alpha_L &= -i(F^\alpha_L + k'_z D^{z\alpha}) \,, \\
\bar{F}^\alpha_R &= -i(F^\alpha_R + k_z D^{\alpha z'}) \,, \\
\bar{G} &= G + k_z^2 D^{z'z'} + k'_z (F^{z'}_R + F^{z'}_L) \,.
\end{aligned}
\tag{2.70}
$$

are the appropriate coefficient matrices for the an infinite NW. While first order and zero-th order matrices gets new terms, as discussed above, each second order matrix for $\alpha, \beta = x', y'$ just gets a minus sign in front, as a result of the product $-i\partial_\alpha D^{\alpha\beta}(-i\partial_\beta) = \partial_\alpha(-D^{\alpha\beta})\partial_\beta$.

2.4. External potential

2.4.1. The Poisson equation

As already stated in Ch. 1, the electronic states of the semiconductor nanostructures studied in this work are subjected to a mesoscopic, external potential $V^e(\boldsymbol{r})$ with several components. First, V^e includes the electron-electron interaction at the mean field level, or Hartree approximation. This amounts to replace the exact many-electron potential by an average one that will be determined by the solution of the Poisson equation

$$\boldsymbol{\nabla}\epsilon(\boldsymbol{r})\boldsymbol{\nabla}\phi(\boldsymbol{r}) = -\frac{\rho(\boldsymbol{r})}{\epsilon_0}\,. \tag{2.71}$$

In Eq. (2.71) $\phi(\boldsymbol{r})$ is the Hartree electrostatic potential, $\rho(\boldsymbol{r})$ is the excess charge density in the nanostructure and $\epsilon(\boldsymbol{r})$ is a position dependent static dielectric constant, while ϵ_0 is the vacuum permittivity. The excess charge density $\rho(\boldsymbol{r})$ originates from the free electrons $n_e(\boldsymbol{r})$, free holes $n_h(\boldsymbol{r})$, as well as ionized donors and acceptors charge concentrations,

$$\rho(\boldsymbol{r}) = e\left[n_h(\boldsymbol{r}) - n_e(\boldsymbol{r}) + \sum_{\boldsymbol{R}_d}\delta(\boldsymbol{r}-\boldsymbol{R}_d) - \sum_{\boldsymbol{R}_a}\delta(\boldsymbol{r}-\boldsymbol{R}_a)\right]\,, \tag{2.72}$$

where $\boldsymbol{R}_d$ and $\boldsymbol{R}_a$ label the position effectively occupied by dopants. We now consider the case of a selectively doped nanowire, of particular interest for this work, i.e. we assume that the impurities are distributed randomly in the z-direction, but have a specific distribution in the (x, y) plane which is determined by the growth process. We split the impurity contributions in two parts [79]. The first part is the spatial average of the impurity potentials

$$n_D(\boldsymbol{r}_\perp) = \frac{1}{\omega}\int_\omega \delta(\boldsymbol{r}-\boldsymbol{R}_d)\mathrm{d}^3\boldsymbol{R}_d\,, \tag{2.73}$$

$$n_A(\boldsymbol{r}_\perp) = \frac{1}{\omega}\int_\omega \delta(\boldsymbol{r}-\boldsymbol{R}_a)\mathrm{d}^3\boldsymbol{R}_a\,, \tag{2.74}$$

where ω is a macroscopic volume that contains many impurities. The second part is the local deviation from this average. Only the first term will be retained in Eq. (2.71). Note that $n_D(\boldsymbol{r}_\perp)$ and $n_A(\boldsymbol{r}_\perp)$ depend on the in-plane position vector $\boldsymbol{r}_\perp$, in order to account for radial heterostructures and selective doping. For infinite NWs, if we neglect the local deviations, the translational invariance along the z-direction is restored and we can write the envelope function as we have done in Sec. 2.3.2. In particular, the external potential in the multiband EFEs becomes $V^e(\boldsymbol{r}_\perp) = -e\phi(\boldsymbol{r}_\perp)$, where $\phi(\boldsymbol{r}_\perp)$ is the solution of a two-dimensional Poisson equation.

The free electron and hole concentrations can be evaluated as, respectively,

$$n_e(\boldsymbol{r}_\perp) = \sum_{n\in\text{c.s.}}\sum_{\nu=1}^{8}\int_{-k_M}^{k_M}\frac{dk}{2\pi}f(E_n(k),\mu,T)\left|\psi_n^\nu(\boldsymbol{r}_\perp,k)\right|^2\,, \tag{2.75}$$

$$n_h(\boldsymbol{r}_\perp) = \sum_{n\in\text{v.s.}}\sum_{\nu=1}^{8}\int_{-k_M}^{k_M}\frac{dk}{2\pi}(1-f(E_n(k),\mu,T))\left|\psi_n^\nu(\boldsymbol{r}_\perp,k)\right|^2\,, \tag{2.76}$$

where the first summation runs over the conduction (valence) subband indices for electrons (holes). Here, $f(E,\mu,T)$ is the Fermi-Dirac distribution function, μ is the chemical potential, T is the temperature and k_B is the Boltzmann constant. The integration in k-space is performed on a uniform grid $[-k_M, k_M]$, where the eigenenergies and wave functions have been determined, being k_M fairly above the Fermi wave vector.

From Eqs. (2.75) and (2.76) we see that the total charge density ρ in Eq. (2.71) depends on the energies E_n and envelope functions ψ_n of the NW. This means that the multi-band EFEs as well as the Poisson equation have to be solved self-consistently. The numerical solution of this problem will be treated in the next section.

2.4.2. Coupled envelope function-Poisson equations

In this section we discuss how to deal with the self-consistent solution of multi-band EFEs and Poisson equations, which are strongly coupled by the quantum free charge density distribution

$$\rho_{\text{free}} = \rho_h + \rho_e = en_h - en_e \tag{2.77}$$

and the electrostatic potential ϕ. Indeed, ϕ enters the EFEs and determines the quantum charge density which in turns enters in the Poisson equation. The solution of the coupled problem involves finding the self-consistent charge density or, alternatively, the electrostatic potential, by an iterative protocol.

The algorithm employed in this work is shown in Algorithm 1. We first solve the Poisson equation without mobile charges, i.e. by setting $\rho_{\text{free}} = 0$, and obtain the initial electrostatic potential $\phi^{(0)}$. At the first iteration we solve the the EFEs with $\phi^{(0)}$, and compute the initial quantum charge density $\rho^{(1)}_{\text{free}}$ from the eigenenergies and wave functions. Then, the Poisson equation is solved with $\rho^{(1)}_{\text{free}}$ and the potential $\phi^{(1)}$ is obtained. At this point one would be tempted to take $\phi^{(1)}$ as the new potential to be inserted into EFEs and iterate the procedure. However, a simple iteration between the two equations runs into convergence problems due to the strong charge oscillation between subsequent steps. To avoid such instability, in this work we rely on the modified second Broyden's method [80, 81, 82, 83, 84] when updating the electrostatic potential at the current iteration. In Algorithm 1 the mixing step is indicated with $\phi^{(i)} = \mathcal{F}_{\text{mix}}(\phi^{(i)}, \phi^{(i-1)}, ..., \phi^{(i-M+1)})$: note that in the Broyden's method, the potential at the next iteration is updated by mixing the potentials of the M previous iterations. Starting from the second iteration ($i \geq 2$), after the new $\rho^{(i)}_{\text{free}}$ has been obtained, we require as exit condition that the electron as well as hole relative densities become stationary, i.e.,

$$\begin{gathered}
\frac{\int_\Omega \mathrm{d}\boldsymbol{r}_\perp \, |\rho_e^{(i)}(\boldsymbol{r}_\perp) - \rho_e^{(i-1)}(\boldsymbol{r}_\perp)|}{\int_\Omega \mathrm{d}\boldsymbol{r}_\perp \, |\rho_e^{(i-1)}(\boldsymbol{r}_\perp)|} < 10^{-3} \,, \\
\frac{\int_\Omega \mathrm{d}\boldsymbol{r}_\perp \, |\rho_h^{(i)}(\boldsymbol{r}_\perp) - \rho_h^{(i-1)}(\boldsymbol{r}_\perp)|}{\int_\Omega \mathrm{d}\boldsymbol{r}_\perp \, |\rho_h^{(i-1)}(\boldsymbol{r}_\perp)|} < 10^{-3} \,.
\end{gathered} \tag{2.78}$$

The number of iterations to converge depends on the specific application. In all the simulations performed for this work convergence is achieved in about 10-20 iteration. If an educated initial guess for the electrostatic potential is available, e.g., from a calculation with slightly different parameters, the number of iterations can be further reduced.

2.5. The Finite Element Method

In this section we summarize the application of FEM to the solution of the EFEs and Poisson equation. Details of the implementation can be found in Refs. [62, 63, 85]. The considerable flexibility of FEM allows a number of optimization strategies in actual calculations of coupled EFEs-Poisson equation for complex nanostructures as the CSNWS investigated in this thesis. Some of such strategies are summarized in Sec. 3.2.1.

Algorithm 1 Coupled envelope function-Poisson iterative solution algorithm.

```
Set $\rho_{\text{free}}^{(0)} = 0$.
Compute $\phi^{(0)}$ from the Poisson equation [Eq. (2.71)] using $\rho_{\text{free}}^{(0)}$.
for $i \geq 1$ do
    Compute wave functions from the EFEs with $\phi^{(i-1)}$.
    Compute $\rho_e^{(i)}$ from the wave functions.
    if $\frac{\int_\Omega |\rho_e^{(i)} - \rho_e^{(i-1)}|}{\int_\Omega |\rho_{\text{free}}^{(i-1)}|} < 10^{-3}$ & $\frac{\int_\Omega |\rho_h^{(i)} - \rho_h^{(i-1)}|}{\int_\Omega |\rho_h^{(i-1)}|} < 10^{-3}$ then        ▷ Check convergence
        break        ▷ Return $\rho_{\text{free}}^{(i)}$ and $\phi^{(i-1)}$
    end if
    Compute $\phi^{(i)}$ from the Poisson equation [Eq. (2.71)] using $\rho_{\text{free}}^{(i)}$.
    Perform Broyden mixing $\phi^{(i)} = \mathcal{F}_{\text{mix}}(\phi^{(i)}, \phi^{(i-1)}, ..., \phi^{(i-M+1)})$.
end for
```

2.5.1. Solution of the envelope function equations

Now we solve the EFEs using FEM [63]. Within FEM, one writes the proper action integral $\mathcal{A}$ that generates the EFEs through a variational procedure. For the multiband EFEs we have

$$\mathcal{A} = \sum_{\mu\nu} \int \mathrm{d}\boldsymbol{r}_\perp \psi_\mu^* \mathcal{L}_{\mu\nu} \psi_\nu \tag{2.79}$$

with the lagrangian density

$$\mathcal{L}_{\mu\nu} = \sum_{\alpha\beta=x,y} -\overleftarrow{\partial}_\alpha \bar{D}_{\mu\nu}^{\alpha\beta} \vec{\partial}_\beta + \sum_{\alpha\beta=x,y} \left(\bar{F}_{L,\mu\nu}^{\alpha} \vec{\partial}_\alpha - \overleftarrow{\partial}_\alpha \bar{F}_{R,\mu\nu}^{\alpha} \right) + \bar{G}_{\mu\nu} - E\,\delta_{\mu\nu}\,, \tag{2.80}$$

where μ and ν refer to the different envelope function components in the multiband problem. Here we drop the prime indices for simplicity, always assuming that the equations are written in the symmetry-adapted basis and the real space coordinate system has z aligned with the growth direction of the NW. We note that the original operator ordering is retained if we take the differential operator $\overleftarrow{\partial}_\alpha$ to act on the left when $\hat{k}_\alpha$ is on the left of the coefficient matrices. Analogously, we have $\vec{\partial}_\alpha$ acting on the right when $\hat{k}_\alpha$ is on the right of the coefficient matrices. It is easy to check that Eq. (2.79) is equivalent to the original eigenvalue problem by performing a functional variation of $\mathcal{A}$ with respect to ψ_μ^* and invoking the principle of least action, namely $\delta\mathcal{A} = 0$ (see App. A.5 for the full derivation). Here, surface terms at the material interfaces arising from the integration by parts can be eliminated using the continuity of the envelope function and of the conservation of the normal component of the probability current [86, 87, 88]. If the wave function is set to zero on the domain boundaries, the outer boundary surface term vanishes too.

The action integral $\mathcal{A}$ is discretized into n_{el} finite elements of the 2D domain,

$$\mathcal{A} = \sum_{i_{el}}^{n_{el}} \mathcal{A}^{(i_{el})}\,. \tag{2.81}$$

The geometrical shape of each element can be arbitrary in principle. Widely used element shapes are the rectangular and triangular ones. In this work we make use only of triangular elements, a shape that allows us to consistently cover the hexagonal section of the simulated NWs. Note, however, that triangles need not to have, and will not have in our calculations, a uniform distribution. The triangular grid should be adjusted to have larger densities where the envelope functions are mostly localized.

The shape of the element defines the number of its geometrical nodes: for a triangle we have three geometrical nodes (four in rectangular elements). The geometrical nodes define the position of each element inside the simulation domain. In our calculations, material modulations in the radial direction, as in CSNWs, are invariably assumed as step-like. Therefore, for simplicity and numerical convenience, we adopt triangulations where the material interfaces always overlap with the elements boundaries. In other words, we build the triangulation in such a way that material interfaces does not intersect any triangular element. Apart from that, the tassellation of the simulation domain with triangular elements, from the point of view of the theoretical formulation of the method, is arbitrary and can be optimized for the problem at hand, as noted above.

Within the i_{el}-th triangular element, each component of the unknown envelope function is approximated using interpolation polynomials [63] $N_j(\boldsymbol{r}_\perp)$ such that

$$\psi_\mu(\boldsymbol{r}_\perp) \simeq \sum_{j=1}^{n_{\text{int}}} \psi_{\mu j} N_j(\boldsymbol{r}_\perp)\,, \tag{2.82}$$

where the sum is performed over the n_{int} interpolation, or nodal points, and the expansion coefficients $\psi_{\mu j}$ represent the value of the μ-th component of the envelope function at the j-th triangle's nodal point. In fact, the interpolation basis functions, by construction, obey the property

$$N_j(x_i, y_i) = \delta_{ij}, \tag{2.83}$$

where (x_i, y_i) are the coordinates of the i-th nodal point. Note that the nodal points can be located on the triangle's vertices, on the triangle's edges or even within the triangle itself. In the former case, the interpolation nodes coincides with the geometrical nodes.

The simplest form of Eq. (2.82) is the case of Lagrange linear interpolation polynomials, where the three interpolation nodes coincide with the geometrical nodes, and the interpolation function are linear functions of the position inside the triangle. Thus, for Lagrange linear elements, we have

$$\psi_\mu(\boldsymbol{r}_\perp) \simeq \sum_{j=1}^{3} \psi_{\mu j} N_j(\boldsymbol{r}_\perp)\,. \tag{2.84}$$

Note that FEM allows to increase the accuracy of the solution by considering higher order interpolation polynomials in each element. For example, if three additional interpolation nodes located at the midpoints of the three sides are defined for each triangular element, second order Lagrange interpolation functions can be employed. The Lagrange polynomial expansion Eq. (2.84) ensures that the envelope function has $\mathcal{C}_0$ continuity throughout the simulation domain. In FEM, one can also ensure the continuity of the envelope function and some of its derivatives at the nodes. For example, to have the continuity of the first derivatives at the nodes, the analogous of Eq. (2.84) is given by

$$\psi_\mu(\boldsymbol{r}_\perp) \simeq \sum_{j=1}^{3} \left(\psi_{\mu j} N_j^H(\boldsymbol{r}_\perp) + \psi'_{\mu j,x} \bar{N}_{j,x}^H(\boldsymbol{r}_\perp) + \psi'_{\mu j,y} \bar{N}_{j,y}^H(\boldsymbol{r}_\perp) \right)\,, \tag{2.85}$$

where the six additional expansion coefficient $\psi'_{\mu j,x}$ and $\psi'_{\mu j,y}$ represent the values of first derivative of the μ-th component of the envelope function at the j-th triangle's nodal point with respect to x and y, respectively, while $N_j^H(\boldsymbol{r}_\perp)$, $\bar{N}_{j,x}^H(\boldsymbol{r}_\perp)$ and $\bar{N}_{j,y}^H(\boldsymbol{r}_\perp)$ are third order interpolation polynomials. The expansion in Eq. (2.85) is referred to as Hermite polynomial interpolation. More details about the Lagrange and Hermite expansions, as well as the actual analytical form of the interpolation polynomials for triangular elements used in this work are given in App. A.6.

To solve the multiband EFEs in this thesis we make use of a mixed polynomial basis, where the s-like conduction band components of the envelope function are represented through Lagrange interpolation polynomials, while the p-like valence band components are represented using the Hermite polynomial expansion. It has been shown in Refs. [76, 89] that such Lagrange-Hermite bases are inherently free form spurious solutions caused by the ill representation of first-order derivatives that plagues generic real-space representation bases of the multiband EFEs.

To simplify the discussion, in the following we assume that linear Lagrange interpolation, Eq. (2.84), is used to represent each component of the envelope function. Plugging Eq. (2.84) into Eq. (2.79) we obtain

$$\begin{aligned}\mathcal{A}^{(i_{el})} &= \sum_{\mu\nu}\sum_{ij=1}^{3}\psi_{\mu i}^{*}\left[\int_{\Omega_{el}} \mathrm{d}\boldsymbol{r}_\perp N_i(\boldsymbol{r}_\perp)\mathcal{L}_{\mu\nu}N_j(\boldsymbol{r}_\perp)\right]\psi_{\nu j} \\ &= \sum_{\mu\nu}\sum_{ij=1}^{3}\psi_{\mu i}^{*}\mathcal{M}_{\mu\nu,ij}^{(i_{el})}\psi_{\nu j}\,,\end{aligned} \tag{2.86}$$

where we have defined the element matrix $\mathcal{M}^{(i_{el})}$ such that

$$\mathcal{M}_{\mu\nu,ij}^{(i_{el})} = \int_{\Omega_{el}} \mathrm{d}\boldsymbol{r}_\perp N_i(\boldsymbol{r}_\perp)\mathcal{L}_{\mu\nu}N_j(\boldsymbol{r}_\perp) \tag{2.87}$$

and Ω_{el} is the area of the i_{el}-th element.

The total action is given by the sum of each element's contribution. This can be written in a very natural manner in matrix form by imposing inter-element continuity through carefully overlaying the element matrices $\mathcal{M}^{(i_{el})}$ [62]. To understand how to construct a global matrix starting from element matrices it is convenient to make a simple example. Let us consider a mesh composed of only two adjacent triangular elements ($i_{el} = 1, 2$) as in Fig. 2.2. In terms of the *global* indices $1 \dots 4$, the first triangle ($i_{el} = 1$) has *local* nodes numbering $i = 1, 2, 3$ while the second triangle ($i_{el} = 1$) has nodes numbering $i = 3, 2, 4$ counted anti-clockwise. The two elements have two nodes (and one edge) in common.

Let us now consider a scalar envelope function ψ. Then, the total action integral for this simple mesh reads

$$\mathcal{A} = \sum_{ij=1}^{3}\psi_i^{(1)*}\mathcal{M}_{ij}^{(1)}\psi_j^{(1)} + \sum_{ij=1}^{3}\psi_i^{(2)*}\mathcal{M}_{ij}^{(2)}\psi_j^{(2)}\,, \tag{2.88}$$

where the summations runs over the local indices for each element, and we used the notation $\psi^{(i_{el})}$ to distinguish the envelope functions in the two elements. Since the two elements share two nodes (the red dots in Fig. 2.2) and we require inter-element continuity, we set $\psi_2^{(1)} = \psi_2^{(2)} = \psi_2$, as the second nodes of the two elements coincides, and we set $\psi_3^{(1)} = \psi_1^{(2)} = \psi_3$, as the third and the first nodes of the first and the second elements, respectively, coincide (see also the table with the node numbering in Fig. 2.2). Using the above conditions, it is possible to rewrite Eq. (2.88) in the global

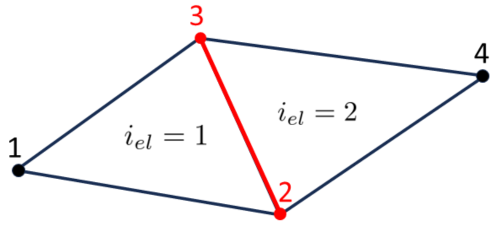

	1^{st} node	2^{nd} node	3^{rd} node
$i_{el} = 1$	1	2	3
$i_{el} = 2$	3	2	4

Figure 2.2: Two adjacent triangular elements. The element label is indicated with a number enclosed in bold parentheses. The global nodes 1 and 4 (black dots) belong to the elements (1) and (2), respectively, while nodes 2 and 3 (red dots) are common to both elements, as well as the edge connecting the two nodes (red edge). Inter-element continuity assume the wave function to be continuous at the nodes 2 and 3, as well as at the common edge.

form

$$\mathcal{A} = \sum_{IJ=1}^{4} \psi_I^* \mathcal{M}_{IJ} \psi_J \,, \tag{2.89}$$

where I and J now stand for global node indices and $\mathcal{M}$ is obtained from $\mathcal{M}^{(1)}$ and $\mathcal{M}^{(2)}$ by summing the contributions from the same nodes and collecting the envelope functions on common vertices. For example, referring to Fig. 2.2, for $I, J = 2, 3$ we have $\mathcal{M}_{IJ} = \mathcal{M}_{IJ}^{(1)} + \mathcal{M}_{IJ}^{(2)}$. The same is true for $I, J = 3, 2$, $I, J = 2, 2$ and $I, J = 3, 3$.

From this example it is now easy to see that the action integral for a multi-component envelope function can be written in its global form as

$$\mathcal{A} = \sum_{\mu\nu} \sum_{IJ}^{n_{glob}} \psi_{\mu I}^* \mathcal{M}_{\mu\nu,IJ} \psi_{\nu J} \,, \tag{2.90}$$

where n_{glob} is the total number of interpolation nodes on the entire domain. We now invoke the principle of stationary action

$$\delta\mathcal{A} = 0 \,, \tag{2.91}$$

and obtain the equations of motion in algebraic form. We vary the action integral with respect to $\psi_{\mu I}^*$ to obtain simultaneous equations for the coefficients $\psi_{\nu J}$,

$$\frac{\delta\mathcal{A}}{\delta\psi_{\mu I}^*} = \sum_{\nu} \sum_{J}^{n_{glob}} \mathcal{M}_{\mu\nu,IJ} \psi_{\nu J} = 0 \,. \tag{2.92}$$

Given the particular form of the lagrangian density $\mathcal{L}_{\mu\nu}$, Eq. (2.80), the above expression results in the generalized eigenvalue problem

$$\sum_{\nu} \sum_{J}^{n_{glob}} \left[\mathcal{H}_{\mu\nu IJ} - E\,\delta_{\mu\nu} \mathcal{S}_{\mu\nu IJ}\right] \psi_{\nu J} = 0 \,. \tag{2.93}$$

Here, $\mathcal{H}_{\mu\nu IJ}$ represents the discretized form of the BF operator $\hat{H}_{\mu\nu}^{BF}$ in Eq. (2.69), while $\mathcal{S}_{\mu\nu IJ}$ is an overlap matrix which is due to the non-orthogonality of the basis functions N_j. From Eq. (2.93) it is clear that the dimension of the problem is given by the number of interpolation nodes n_{glob} in the simulation domain times the number of components of the envelope function.

The problem in Eq. (2.93) can be numerically solved after the inclusion of the proper boundary conditions (BCs). In this work we set each component of the envelope function to zero at the domain external boundaries. This procedure is also referred to as Dirichlet BCs. To do that, we simply cancel the degrees of freedom corresponding to the nodes located on the external boundaries. This can be done by canceling the corresponding rows and columns in the matrix $\mathcal{M}_{\mu\nu,IJ}$. Once the appropriate BCs are introduced, Eq. (2.93) is solved by means of standard library routines.

2.5.2. Solution of the Poisson equation

Consistently with the solution of the EFEs, and with the similar motivation of allowing non-uniform, optimized grids, we solve the 2D Poisson equation using FEM, with the obvious advantage of reusing part of the developed library. Note, however, that the triangular tassellation used to solve the two sets of equations are completely independent and in general are optimized for each equation separately. For example, the electric field extends in regions where the envelope functions vanish and need not be included in the real space description. It is easy, in the self-consistent cycle, to switch between the two grids by interpolation methods.

For the Poisson equation the energy functional to be minimized is given by

$$\mathcal{A} = \int_\Omega \mathrm{d}\boldsymbol{r}_\perp \frac{1}{2}\left[\epsilon(\boldsymbol{r}_\perp)\boldsymbol{\nabla}\phi(\boldsymbol{r}_\perp)\cdot\boldsymbol{\nabla}\phi(\boldsymbol{r}_\perp) - \frac{1}{\epsilon_0}\phi(\boldsymbol{r}_\perp)\rho(\boldsymbol{r}_\perp)\right], \tag{2.94}$$

where Ω is the two dimensional simulation domain, with boundary $\partial\Omega$. We first assume that the potential $\phi(\boldsymbol{r}_\perp)$ is specified at the boundary by the relation $\phi(s) = \phi_0(s)$, where s is a one-dimensional coordinate on the boundary $\partial\Omega$. Then, a functional variation of $\mathcal{A}$ with respect to ϕ followed by an integration by parts gives Eq. (2.71). In fact, the surface terms at the interface between two different materials originating from the integration by parts can be eliminated leveraging the continuity of the normal component of the displacement field $\boldsymbol{D} = \epsilon(\boldsymbol{r}_\perp)\boldsymbol{E}$ at the interface, being $\boldsymbol{E} = -\boldsymbol{\nabla}\phi$. Furthermore, since the potential is fixed at the domain's boundaries, the surface term on $\partial\Omega$ vanishes too. The detailed derivation can be found, for example, in Ref. [62].

If, for a certain fraction $\partial\Omega_n$ of the boundary, the potential $\phi(s)$ is not specified, Neumann BC (i.e., the normal component of the electric field equal to zero) are automatically imposed on $\partial\Omega_n$. In fact, Neumann BC are *natural* BC in the FEM for the Poisson equation. If the boundary potential $\phi(s)$ is left unspecified for the whole boundary $\partial\Omega$, Neumann BC are naturally imposed on the whole boundary, $\phi(s)$ is arbitrary and the solution of the problem $\phi(\boldsymbol{r}_\perp)$ is defined up to a constant. This situation is referred to as *pure* Neumann BC. In this case, to uniquely define the solution of the problem, an additional constrain on the potential ϕ is required. In this thesis, when *pure* Neumann BC are considered, as e.g. in Sec. 5.2 of Ch. 5, we impose the additional constrain

$$\int_\Omega \mathrm{d}\boldsymbol{r}_\perp\, \phi(\boldsymbol{r}_\perp) = 0 \tag{2.95}$$

using the Lagrange multiplier strategy, i.e. by adding the term $c\int_\Omega \mathrm{d}\boldsymbol{r}_\perp\, \phi(\boldsymbol{r}_\perp)$ to action integral Eq. 2.94, where c is a Lagrange multiplier to be sought in $\mathbb{R}$. It is easy to show that the principle of least action for the newly defined action integral gives the Poisson equation with pure Neumann

BC and the zero-mean constrain Eq. 2.95 on the electrostatic potential [63].

As discussed for the multiband EFEs, in FEM the electrostatic potential is approximated in terms of Lagrange linear interpolation polynomials inside each triangular element,

$$\phi(\boldsymbol{r}_\perp) = \sum_{j=1}^{3} \phi_j N_j(\boldsymbol{r}_\perp)\,, \tag{2.96}$$

and following the same procedure described in section 2.5.1, a linear system of n_{glob} equations is obtained:

$$\sum_{J}^{n_{glob}} C_{IJ}\phi_J = b_I\,. \tag{2.97}$$

After the inclusion of proper BCs, Eq. (2.97) is solved with standard library routines.

3

Remotely doped, type-I radial heterostructures

We investigate the electronic band structure of modulation-doped GaAs/AlGaAs core-shell nanowires (CSNWs) for both n- and p-doping. We employ an 8-band Burt-Foreman $\mathbf{k} \cdot \mathbf{p}$ Hamiltonian approach to describe coupled conduction and valence bands in heterostructured nanowires of arbitrary composition, growth directions, and doping. Coulomb interactions with the electron/-hole gas are taken into account within a mean-field self-consistent approach. We map the ensuing multi-band envelope function and Poisson equations to optimized, non-uniform real-space grids by the FEM. Self-consistent charge density, single-particle subbands, density of states and absorption spectra are obtained at different doping regimes. For n-doped samples, the large restructuring of the electron gas for increasing doping results in the formation of quasi-1D electron channels at the core-shell interface. Strong heavy-hole (HH)/light-hole (LH) coupling of hole states leads to non parabolic dispersions with mass inversion, similarly to planar structures, which persist at large dopings, giving rise to direct LH and indirect HH gaps. In p-doped samples the hole gas forms an almost isotropic, ring-like cloud for a large range of doping. Here, as a result of the increasing localization, HH and LH states uncouple, and mass inversion takes place at a threshold density. A similar evolution is obtained at fixed doping as a function of temperature. We show that signatures of the evolution of the band structure can be singled out in the anisotropy of linearly polarized optical absorption.

3.1. Introduction

Among III–V compound semiconductor nanostructures, radially heterostructured nanowires represent an increasingly investigated, silicon-compatible perspective for applications in transistor-based electronic devices [90] and opto-electronic devices [91, 92]. From the point of view of material quality, several issues have already been settled on the route to technological exploitation of nanowires or as a platform for coherent quantum phenomena. These include self-assisted growth [35, 93], order and polytypism [6, 94], high-quality interfaces [95], and multi-layer growth [96]. One critical issue bridging between material science and device nanofabrication is the control of doping, for example in modulation doped heterostructures [97, 38] and radial p-n junctions [98]. This is still a concern in terms of reproducibility between nanowires and homogeneity within each nanowire [42, 39].

As in the realm of planar heterostructures, GaAs-based nanomaterials play a special role also for nanowires. Ultra-high-mobility devices in planar GaAs/AlGaAs heterojunctions build on the modulation doping concept [99]. Here dopants are incorporated in a higher gap AlGaAs layer, physically separated from the lower-gap layers, where carriers are confined, suppressing carrier-ionized impurity scattering. A corresponding, modulation doped radial heterostructure is schematically shown in Fig. 3.1(a) [97], which can be seen as a planar heterojunction with wrapped around layers. Carriers are confined in the GaAs core, while dopants are incorporated in an outer AlGaAs layer. Typically, a thin GaAs capping layer is included to prevent Al oxidation. While mobility is still improving in planar systems [100], where background impurities are the limiting factor, high mobility is more difficult to achieve in core-multi-shell nanowires though [38, 101], and experimental and theoretical characterization is needed.

Due to comparable kinetic and Coulomb energies, in doped core-shell nanowires (CSNWs) electronic states [102] and ensuing response functions [103, 104] are determined by the self-consistent field of free carriers, which, in turn depends on the concentration and type of doping [102], together with the Fermi level pinning at surface states [105, 106]. Hence, different doping regimes may result in distinct charge localization patterns [107]. The ability to predict the band structure in doped CSNWs is therefore a complex task.

Among the methods used, the envelope function approach stands out for its versatility and computational efficiency. Single-band descriptions have been widely used, including non-perturbative electric and magnetic fields [102, 108, 109, 110]. Multi-band $\mathbf{k} \cdot \mathbf{p}$ descriptions, which include spin-orbit coupling arising from valence states that are crucial to describe, e.g., optical properties [111, 112], have been employed for several classes of materials, taking into account composition modulations, crystallographic details and mesoscopic symmetries [113, 114, 115, 8, 68, 116, 86]. Spin-orbit coupling in the conduction band has been evaluated, also in presence of strong magnetic fields [59, 60, 61]. However, a full description of the band structure of doped CSNWs in the different doping regimes including the self-consistent field arising from the free charge is still missing.

In this paper we investigate the electronic band structure of modulation-doped GaAs/AlGaAs CSNWs with n- or p-type doping [117]. We employ the 8-band Burt-Foreman $\mathbf{k} \cdot \mathbf{p}$ Hamiltonian approach developed in Ch. 2, with Coulomb interactions with the electron/hole gas taken into account within a mean-field self-consistent approach. The numerical burden arising from the self-consistent solution of multi-band envelope function and Poisson equations is minimized by the use of the finite element method (FEM) with non-uniform real-space grids, optimized to different doping regimes. Self-consistent charge density, single-particle subbands, density of states and absorption spectra are then obtained. For strong n-doping, quasi-1D channel tend to form at the corners of the core-shell interface. Heavy-hole (HH)/light-hole (LH) couplings lead to non-parabolic dispersions with mass inversion in the valence band, similarly to planar structures, giving rise to direct LH and indirect HH gaps persisting at any doping density. In strongly p-doped samples, on the contrary, the

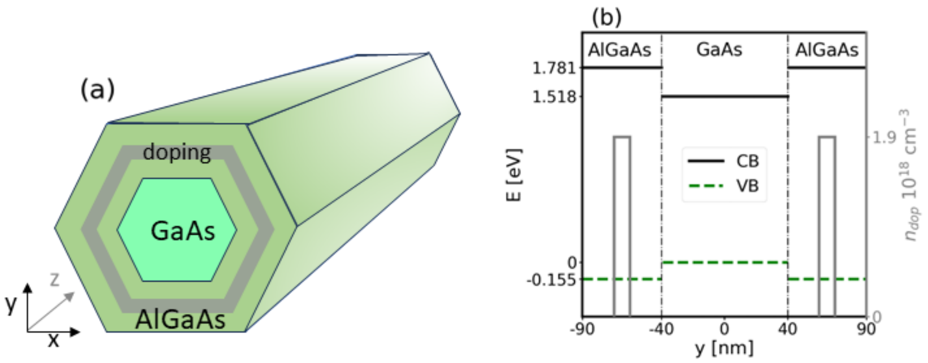

Figure 3.1: (a) Sketch of the section of the simulated CSNWs. The principal axes of the 2D-coordinate system are directed along the $[11\bar{2}]$ and $[\bar{1}10]$ crystallographic directions. (b) bulk band alignment and doping layers

hole gas forms an almost isotropic, ring-like cloud. As a result of the increasing localization, HH and LH states uncouple, and mass inversion takes place at a threshold density. Similar evolutions are obtained at fixed doping as a function of temperature. We suggest that signatures of the evolution of band structure can be traced in the anisotropy of linearly polarized optical absorption.

In Sec. 3.2 we outline the theoretical-computational methods used, largely referring to Ch. 2. Band structures, density of states, projected charge densities and optical anisotropy are discussed in Sec. 3.3, as a function of the doping density, separately for both n- and p-doped samples.

3.2. Model and methods

The electronic structure of the modulation-doped CSNW is obtained using a self-conistent, 8-band $\mathbf{k}\cdot\mathbf{p}$ envelope function approach. We give here a summary of the model used, referencing to Ch. 2 when needed.

We assume the nanowire to be infinite along the z-direction, which coincides with the growth crystallographic axis of the nanowire. Furthermore, we assume that the ionized impurity charges are uniformly distributed along the nanowire and do not break translational invariance along the $z-$direction. Thus, we can write the n-th eigenstate at the in-wire wave-vector k_z as

$$\Psi_n(\boldsymbol{r},k_z)=\frac{1}{\sqrt{L}}\sum_{\nu=1}^{8}e^{ik_zz}\underbrace{\psi_n^\nu(\boldsymbol{r}_\perp,k_z)}_{\substack{\text{Envelope function}\\ \text{component}}}\underbrace{u^\nu(\boldsymbol{r})}_{\substack{\text{Bloch state}\\ |J,J_z\rangle}}\,, \tag{3.1}$$

where $u^\nu(\boldsymbol{r})=\langle\boldsymbol{r}|J,J_z\rangle$ is a Bloch basis function in the symmetry-adapted basis of the angular momentum Eq. (2.65). The coefficients $\psi_n^\nu(\mathbf{r}_\perp,k_z)$ are the ν-th component of the n-th solution of the multi-band envelope-function equation

$$\sum_{\nu=1}^{8}\left[\hat{H}_{\mu\nu}^{BF}(\boldsymbol{r}_\perp,k_z)-e\phi(\boldsymbol{r}_\perp)\delta_{\mu\nu}\right]\psi_n^\nu(\boldsymbol{r}_\perp,k_z)=E_n(k_z)\psi_n^\mu(\boldsymbol{r}_\perp,k_z)\,, \tag{3.2}$$

where $\hat{H}^{BF}$ is the 8×8 Burt-Foreman Hamiltonian operator Eq. (2.46), with material-dependent parameters and including the band offsets, and $\phi(\boldsymbol{r}_\perp)$ represents the electrostatic potential generated by free carriers and fully ionized dopants, which is added to the diagonal of the Hamiltonian operator as derived in App A.3.

Eq. (3.2) represents a set of second order coupled partial differential equations which we numerically solve using FEM on an appropriate two-dimensional grid (see Sec. 2.5.1 and App. A.6) with Dirichlet boundary conditions. The strongly non-parabolic subbands $E_n(k_z)$ and the corresponding envelope functions $\psi_n^\nu(\boldsymbol{r}_\perp, k_z)$ are finally determined on a uniform grid of wave vectors k_z. Since the Hamiltonian is time-reversal symmetric, we need to solve Eq. (3.2) only for positive wave vectors, $k_z \in [0, k_M]$.

From the solutions of Eq. (3.2), we evaluate the total charge density

$$\rho(\boldsymbol{r}_\perp) = e\left[n_h(\boldsymbol{r}_\perp) - n_e(\boldsymbol{r}_\perp) + n_D(\boldsymbol{r}_\perp) - n_A(\boldsymbol{r}_\perp)\right] \,, \tag{3.3}$$

where the free electron and hole densities $n_e(\boldsymbol{r}_\perp)$ and $n_h(\boldsymbol{r}_\perp)$ are calculated from Eqs. (2.75) and (2.76), respectively, and the ionized donor or acceptor 2D profiles $n_D(\boldsymbol{r}_\perp)$ and $n_A(\boldsymbol{r}_\perp)$ are calculated from Eqs. (2.73) and (2.74), respectively.

The electrostatic potential $\phi(\boldsymbol{r}_\perp)$ is the solution of the 2D Poisson equation, Eq. (2.71) with a material dependent dielectric constant $\epsilon(\boldsymbol{r}_\perp)$, with the source term given by the charge density in Eq. (3.3). Again, the Poisson equation is solved using FEM on a 2D grid with Dirichlet boundary conditions. The potential at the outer boundary of the CSNW is fixed to zero at the six edges of the outer layer of the structure. The computational protocol does not imply any symmetry and allows to include arbitrary voltages at gates surrounding the nanowire [16], although we will not investigate this configuration here. The above steps are iterated self-consistently until convergence as described in Sec. 2.4.2 using Algorithm 1.

To characterize bands states, a k_z-dependent spinorial analysis is useful. The contribution to each state of any of the component of the envelope function can be estimated as

$$C_n^\nu(k_z) = \int |\psi_n^\nu(\boldsymbol{r}_\perp, k_z)|^2 \mathrm{d}\boldsymbol{r}_\perp \,, \tag{3.4}$$

with the normalization condition

$$\sum_{\nu=1}^{8} C_n^\nu(k_z) = 1 \,,$$

at each subband index n and wave-vector k_z. When analysing electronic states, we shall classify states in terms of EL, HH, LH characters [see also Eq. (2.65)], which are computed as

$$\begin{aligned} C_{\mathrm{EL}}(k_z) = &\quad C_n^1(k_z) + C_n^2(k_z) \,, \\ C_{\mathrm{HH}}(k_z) = &\quad C_n^3(k_z) + C_n^4(k_z) \,, \\ C_{\mathrm{LH}}(k_z) = &\quad C_n^5(k_z) + C_n^6(k_z) \,. \end{aligned} \tag{3.5}$$

We shall also plot the projected probability distributions at $k_z = 0$, defined as

$$\begin{aligned}
\phi_{\mathsf{EL}}(\boldsymbol{r}_\perp) &= \sum_{\nu\in\{1,2\}} C_n^\nu(0)\frac{|\psi_n^\nu(\boldsymbol{r}_\perp,0)|^2}{\xi_n^\nu}\,,\\
\phi_{\mathsf{HH}}(\boldsymbol{r}_\perp) &= \sum_{\nu\in\{3,4\}} C_n^\nu(0)\frac{|\psi_n^\nu(\boldsymbol{r}_\perp,0)|^2}{\xi_n^\nu}\,,\\
\phi_{\mathsf{LH}}(\boldsymbol{r}_\perp) &= \sum_{\nu\in\{5,6\}} C_n^\nu(0)\frac{|\psi_n^\nu(\boldsymbol{r}_\perp,0)|^2}{\xi_n^\nu}\,,
\end{aligned} \tag{3.6}$$

where

$$\xi_n^\nu = \max_{\boldsymbol{r}_\perp} |\psi_n^\nu(\boldsymbol{r}_\perp,0)|^2\,.$$

Additionally, we compute the projected density of states (PDOS) for any given component ν of the wave function,

$$g_\nu(E) = \frac{1}{N}\sum_n^{subbands}\sum_k C_n^\nu(k)\delta(E-E_n(k))\,, \tag{3.7}$$

where N is the total number of points in k-space considered in the summation. Furthermore, for n/p-doped samples we evaluate the self-consistent linear charge density of electrons/holes as

$$\rho_{\mathsf{lin}} = \int n_{e/h}(\boldsymbol{r}_\perp)\mathsf{d}\boldsymbol{r}_\perp\,. \tag{3.8}$$

The calculation of the optical anisotropy proceeds as follows. In the dipole approximation, the interband absorption intensity of photons with energy $\hbar\omega$ and light polarization vector ε reads:

$$I_{\boldsymbol{\varepsilon}}(\hbar\omega) \propto \sum_{n\in\mathsf{v.s.}}\sum_{m\in\mathsf{c.s.}}\sum_k |M^\varepsilon_{n\to m,k}|^2\,\left[f(E_n(k))-f(E_m(k))\right]\delta[E_m(k)-E_n(k)+\hbar\omega]\,, \tag{3.9}$$

where $M^\varepsilon_{n\to m,k}$ is the interband optical matrix element, [79]

$$M^{\boldsymbol{\varepsilon}}_{n\to m,k_z} \simeq \sum_{\mu\nu=1}^{8}\langle u^\mu|\boldsymbol{\varepsilon}\cdot\boldsymbol{p}|u^\nu\rangle\int \mathsf{d}\boldsymbol{r}_\perp \psi_m^{\mu^*}(\boldsymbol{r}_\perp,k_z)\psi_n^\nu(\boldsymbol{r}_\perp,k_z)\,. \tag{3.10}$$

Summations are extended to convergence on a sufficiently large number of valence subbands (v.s.) n, conduction subbands (c.s.) m, and wave vectors up to k_M.

Note that doping, in addition to determine the envelope functions via the self-consistent field, enters Eq. (3.9) through Fermi-Dirac distributions, which account for band filling effects when electron/hole subband edges approach the Fermi energy due to doping. For undoped structures the Fermi energy is well within the gap, and this term is almost equal to unity. In heavily doped structures, however, it inhibits interband transitions to the lowest subbands which may be non-negligibly occupied.

Finally, we compute the relative optical anisotropy β between linearly polarized light along the wire axis, I_{ε_z}, and perpendicular to it along the x direction, I_{ε_x}:

$$\beta = \frac{I_{\varepsilon_z}-I_{\varepsilon_x}}{I_{\varepsilon_z}+I_{\varepsilon_x}}\,. \tag{3.11}$$

3.2.1. Numerical implementation details

The above self-consistent 8-band $\mathbf{k} \cdot \mathbf{p}$ equations may result in a computationally intensive task, but a number of strategies can be implemented to keep the computational burden low and avoid the use of massively parallel architectures. Most of the strategies mentioned below take advantage of the flexibility of FEM which allows the use of non-uniform grids, which we generate by the `Free FEM` library [118].

The $\mathbf{k} \cdot \mathbf{p}$ Hamiltonian is represented on a 2D hexagonal domain, partitioned in a D_6 symmetry-compliant, unstructured mesh of triangular elements. Since at different doping levels the charge density forms substantially dissimilar localization patterns [102], different density-optimized grids are used at different doping levels. A typical grid used for a high density regime is shown in Fig. 3.2, showing that the grid is denser where charge density is localized.

We emphasize that the use of centro-symmetric grid is critical to correctly reproduce the degeneracies expected in an hexagonal, centro-symmetric nanowire, without the need of extremely dense grids. Breaking the inversion symmetry of the grid would not only artificially split the *orbital* degeneracy expected in the conduction band [119], but also split the *spin* degeneracy, particularly in the strongly spin-orbit coupled valence band [120]. The need to maintain the inversion symmetry discourages the use of standard automatic adaptive grid methods. Hence, we use fixed, although optimized, non-uniform grids. To partition the hexagonal domain in a D_6 symmetry-compliant way, we make use of a customized `Free FEM` procedure.

In CSNWs which are at stage here, the charge density is confined to the GaAs core (although in a non trivial manner) and rapidly goes to zero inside the shell material; therefore, we use larger elements inside the shell with respect to the core and we require the envelope function to vanish somewhere inside the shell, typically at the doping layer. A typical grid used in the calculations is shown in Fig. 3.2. Finally, we found it convenient to use coarser grids during the self-consistent cycle, with optimized, finer grid used only in the last iterations.

For the 8-band $\mathbf{k} \cdot \mathbf{p}$ model the bound states of interest around the gap correspond to interior eigenvalues of the Hamiltonian matrix. To compute the charge density via Eqs. (2.75), (2.76) the sum is restricted to few tens of subbands (usually n_{max}=60 for the electrons and n_{max}=100 for holes), and iterative methods are preferable. We use the Arnoldi method [121], implemented in the `ARPACK` library [122], together with the shift-and-invert approach, where the original problem is recast to target the largest eigenvalues. This approach provides faster convergence and enables the search for n_{max} eigenvalues around an energy value E_{search}. Thus, since for both n- and p-doping the occupation of the minority carrier is negligible, during the self-consistent cycle one needs to solve only for the conduction or the valence band structure, respectively, by properly choosing E_{search} [1]. The full band structure is then calculated only in the final converged self-consistent potential.

The Poisson equation is solved on a single specific mesh extending over the entire 2D domain of the heterostructure. To go back-and-forth between the grids of the envelope function and Poisson solver, as well as between different grids used during the self-consistent cycle, we make use of 2D

---

[1] Note that the convergence of the diagonalization is affected by the actual value of E_{search} [123]. For this reason, computational times can be further reduced by using the minimum (maximum) conduction (valence) band eigenvalue at $E_n^{min}(k_z)$ ($E_n^{max}(k_z)$) as E_{search} for the next diagonalization at $k_z + \Delta k_z$.

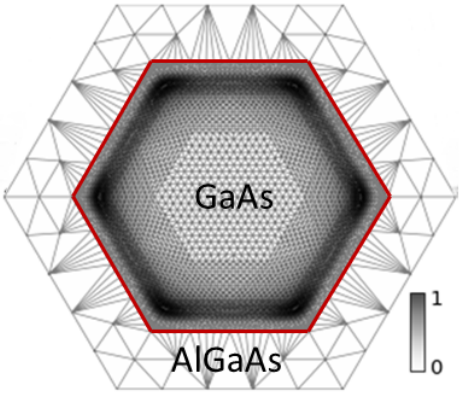

Figure 3.2: Typical finite element grid and charge density distribution. The FEM allows for the use of unstructured, non-uniform and optimized real space discretization. In this example, the number of triangular elements concentrates at the interface between the two materials, where the charge density (in grey scale) localizes, and coarsen elsewhere.

linear interpolation. As discussed in Sec. 2.4.2, to achieve the convergence of the self-consistent protocol we rely on the modified second Broyden's method [82]. The inverse Jacobian is updated using the information from $M = 8$ previous iterations. We fixed the weight corresponding to the first iteration to $w_0 = 0.01$, while all the other weights w_m, with $m = 1, ..., M-1$, are computed as suggested in Ref. [81]. The simple mixing parameter β_{mix} is fixed to 0.05.

Before the simulation starts, the mesh is processed through a bandwidth reduction procedure leveraging the reverse Cuthill–McKee algorithm [124] implemented within the `SciPy` library [125]. This is done in order to obtain tightly banded sparse matrices from the FEM discretization.

The above self-consistent numerical protocol and ancillary calculations have been performed by the in-house developed `python` library `nwkp`. A typical run uses a grid of about 7000 triangular elements and 3500 nodes for the $\mathbf{k} \cdot \mathbf{p}$ problem and 10-20 self-consistent iterations. A run on a single node architecture equipped with 16 2.60 GHz Intel Xeon E5-2670 processor cores takes about 6 hours CPU time.

3.3. Results

We simulate a typical modulation-doped structure [38] consisting of a GaAs hexagonal core with an edge-to-edge distance of 80 nm surrounded by a 50-nm-wide Al$_{0.3}$Ga$_{0.7}$As shell and a GaAs capping layer of thickness 10 nm. The 2D-coordinate system has the x- and y-axes directed along the $[11\bar{2}]$ and $[\bar{1}10]$ crystallographic directions, respectively, while the z-axis coincides with the growth direction of the nanowire, namely, the $[111]$ crystallographic direction. Buried inside the shell, at a distance of 20 nm from the core-shell interface, a 10-nm-thick layer is doped at a constant density n_D of donors or n_A of acceptors. A slice of the bulk band edges CB (conduction band) and VB (valence band) and of the selective doping profile along the edge-to-edge direction (y-axis) is shown in Fig. 3.1(b)[2] All calculations discussed below are performed at $T = 20$ K, except in Sec. 3.3.4. The chemical potential μ is fixed at the mid-gap value of GaAs [106]. The bulk band parameters of the 8-band model for GaAs and AlGaAs as well as the interface band offsets used in the simulations

---

[2] The 10-nm wide GaAs capping layer is not shown here, but is considered in the numerical simulations.

	GaAs		Al$_{0.3}$/Ga$_{0.7}$/As
E_g [eV]	1.518		1.936
ΔE_c [eV]		0.263	
ΔE_v [eV]		0.155	
Δ_{so} [eV]	0.341		0.323
E_p / E_p^{rsc} [eV]	28.8 / 20.9		26.5 / 18.0
m_e	0.067		0.092
γ_1 / $\tilde{\gamma}_1$	6.98 / 2.39		6.01 / 2.91
γ_2 / $\tilde{\gamma}_2$	2.06 / -0.235		1.69 / 0.138
γ_3 / $\tilde{\gamma}_3$	2.93 / 0.635		2.48 / 0.928
ϵ_r	13.18		12.24
a_{lc} [nm]	0.56		

Table 3.1: Material parameters used in the simulations at $T = 20$ K. E_g is the energy gap, ΔE_c, ΔE_v are the conduction and valence band offset values at the GaAs/Al$_{0.3}$Ga$_{0.7}$As interface, Δ_{so} is the split-off energy, E_p is the bare Kane energy, E_p^{rsc} the rescaled Kane energy (Eq. 2.56), m_e is the effective conduction electron mass, γ_i are the bare Luttinger parameters, $\tilde{\gamma}_i$ are the modified values (Eq. 2.53), ϵ_r is the relative dielectric constant and a_{lc} is the lattice constant. The band structure parameters are taken from Ref. [126] except for the band offset values. The latter have been determined assuming an offset ratio of $\Delta E_c : \Delta E_v = 63 : 37$, as recommended in Ref. [127].

are reported in Tab. 3.1.

3.3.1. Band structure of the undoped nanowire

As a reference for calculations of the band structure of doped CSNWs to be discussed in the next sections, we first consider an undoped sample and analyze the conduction and valence bands subbands, which are shown in Fig. 3.3 (left), together with the corresponding PDOSs (right). These are best analyzed together with the projected probability distributions of the EL, HH, and LH spinor components [see Eqs. (3.4), (3.6)] at $k_z = 0$, which are shown separately in Fig. 3.4[3].

We first consider conduction states. Due to the large gap of GaAs, which disentangles conduction and valence bands in the **k** · **p** Hamiltonian, conduction subbands [Fig. 3.3(a)] show an almost pure EL character with parabolic dispersion and ensuing $1/\sqrt{\text{energy}}$ PDOS typical of 1D systems [Fig. 3.3(b)]. In a system with D_{6h} symmetry, assuming a perfectly isotropic band structure, we expect the ground state to be non degenerate, while the second/third and fourth/fifth doublets are degenerate [119]. Here, anisotropic residual interactions with the valence band remove the degeneracies by $\sim 10^{-3}$meV, a quantity which cannot be distinguished in Fig. 3.3[4]. Indeed, the single/-double degeneracy of the levels is easily recognized in the height of the peaks of the PDOS.

As shown in Fig. 3.4(left column), the lowest conduction state is $1s$-like in the center, while the nearly degenerate doublets are ring-like states with an increasing modulation in the corners of the hexagonal confining potential. The 6-th state is again a non-degenerate state with a $2s$ character. Higher levels (not shown here) have maxima on the corners of the hexagon and nodes along the facets or vice versa [119, 128].

The valence subbands [Fig. 3.3(c)] are of course denser in energy than conduction subbands, due

---

[3] The SO component for these states is negligible and it is not shown here.

[4] As discussed in Sec. 3.2, the almost exact double degeneracy can be taken as a quality indicator of the grid. As in our FEM implementation the elements are triangular, the symmetry of the system can be reproduced by a symmetry-compliant, though non-uniform, grid at moderate grid densities.

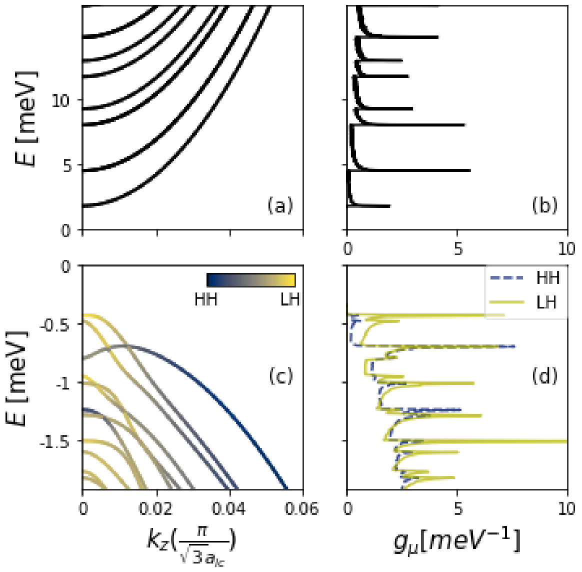

Figure 3.3: Band structure of the undoped nanowire. Conduction (a) and valence (c) subbands of an undoped GaAs/AlGaAs CSNW with core width equal to 80 nm and shell width of 50 nm. In (c) the hue/color represents the spinorial character in terms of HH and LH, according to Eqs. (3.4). Conduction (b) and valence (d) PDOS [Eq. (3.7)] for different spinor components. The zero of the energy in each panel is taken at the bulk band edge of GaAs for conduction and valence band, respectively.

to the larger mass of holes. The LH-HH mixing, which is small but finite also at Γ, leads to a strongly non-parabolic dispersion of the subbands with k_z. As shown by the color code of the lines, the two highest subbands have a predominant LH character at Γ, which is also shown by the corresponding distribution functions in Fig. 3.4(center and right columns) [5]. In between several subbands in Fig. 3.3(c) pointing downward and with a strong LH character at Γ, we recognize a mixed character state (the 3rd subband) and an almost HH subband (the 6-th state) (see also Fig. 3.4). These two subbands strongly couple at finite wave vectors (note from the hue that these two subbands exchange their HH-LH character), causing a strong camel's back dispersion of the third subband and a corresponding peak in the PDOS at $\sim$ -0.54 meV with 50% character of either HH and LH components. All in all, the LH character dominates the PDOS, which agrees with Ref. [68]. Note that band crossings of the third subband can be traced to states belonging to different irreducible representations of the C_{3v} double symmetry group of [111] oriented nanowires with hexagonal cross-section [129, 130, 131].

The probability distributions of HH and LH states shown in Fig. 3.4 are either s-like or ring-like (arising from a quadrupolar symmetry of the real/imaginary parts of the envelope functions), similarly to corresponding conduction states, although of course the ordering is different, as HH- and LH-like states interlace. No orbital degeneracies are expected, since the strongly anisotropic bulk valence band structure does not share the hexagonal symmetry of the confinement.

We finally note that all electronic states are doubly spin-degenerate, due to the centro-symmetric symmetry of the system (which is carefully preserved by the FEM grid), which will hold true in all calculations throughout [6].

---

[5] Note that the quantization axis of the total angular momentum **J** is chosen along the free direction, i.e., the nanowire axis z, not along the confinement direction, as usually done in quantum wells; hence, the HH/LH labelling of the highest valence state is opposite to the quantum well case, see, e.g., [75]

[6] It should be noted that our $\mathbf{k} \cdot \mathbf{p}$ model has an higher symmetry with respect to an atomistic Hamiltonian due to lack of

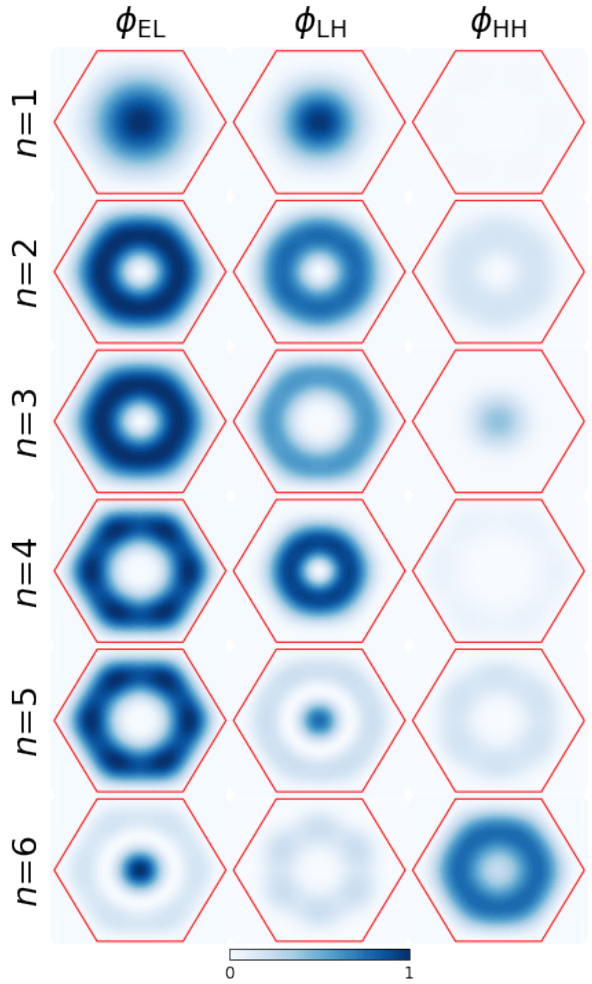

Figure 3.4: Projected probability distributions [Eqs. (3.6)] of the six lowest conduction band (1st column) and six highest valence band states (2nd and 3rd column) at Γ for the undoped material of Fig. 3.3.

3.3.2. n-doping

We now consider n-doped samples with increasing doping density n_D, up to high-doping regimes. As shown in Fig. 3.5(a), the self-consistent linear charge density [Eq. (3.8)] increases almost linearly for large doping, while an increasing number of conduction subbands fall below the Fermi energy [Fig. 3.5(b)]. The evolution of the (unoccupied) valence band states at Γ is also shown in Fig. 3.5(c).

The evolution of the localization of the self-consistent charge density and the corresponding electrostatic potential, shown in Fig. 3.6(left), is not trivial. With increasing doping, the charge density evolves from a small, isotropic charge distribution in the core of the structure to a larger, ring-like charge density distribution, and finally to a charge density which is primarily located in the corners of the core, as can be inferred by comparing the edge-to-edge and corner-to-corner profiles in Fig. 3.6. This is in agreement with single-band self-consistent calculations [102, 132], as expected from the nearly pure EL character of conduction subbands.

Conduction subbands retain a trivial parabolic dispersion regardless of the doping level (and type),

---

bulk inversion symmetry (BIA) in III-V materials. This would remove the double degeneracy of our $\mathbf{k}\cdot\mathbf{p}$ subbands with tiny spin-splittings in the micro-eV range [130].

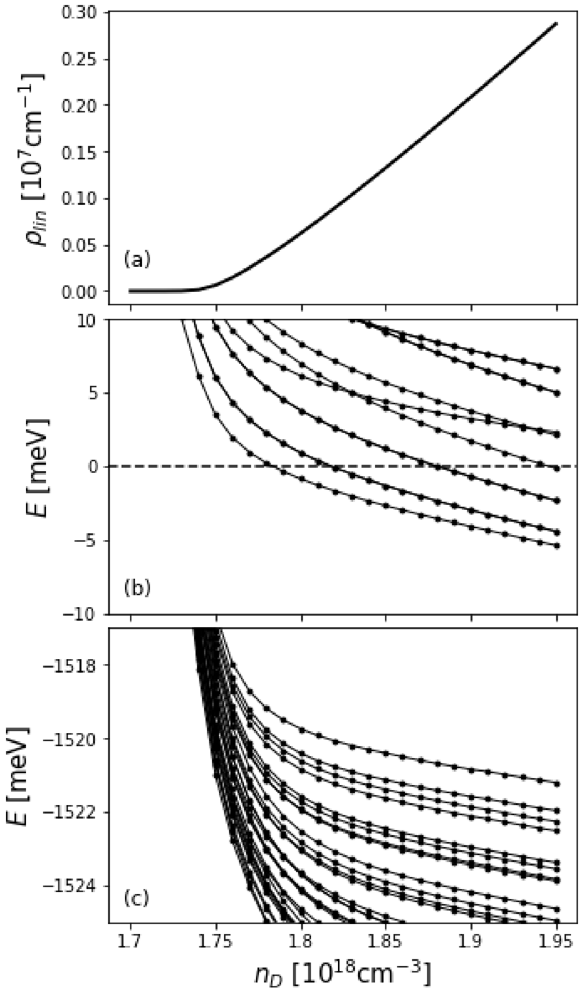

Figure 3.5: (a) Linear free charge density [Eq. (3.8)], (b) conduction subband energies at $k_z = 0$, and (c) valence subband energies at $k_z = 0$ as a function of the doping density n_D. Energies are referred to the Fermi level.

which is therefore not shown here. However, it is still interesting to consider the evolution of the localization of the conduction envelope functions shown in terms of the projected density distribution $\phi_{\text{EL}}(\boldsymbol{r}_\perp)$ in Fig. 3.7 (left columns in each panel), with increasing doping (panels from left to right). For each of the seven lowest levels, the larger the doping, the more localized is $\phi_{\text{EL}}(\boldsymbol{r}_\perp)$ at the core-shell interface. For the largest doping shown here, all subbands feature a clear six-fold symmetry induced by the heterostructure confining potential. Note that the ordering of the levels in terms of symmetry depends on the level of doping, as seen from the “exchange” of the 6-th and 7-th levels with increasing doping.

Although for n-doping the charge density is determined by conduction band states, the valence band structure does have an evolution as well, due to the restructuring of the free charge density and ensuing change in the self-consistent confining electrostatic potential shown in Fig. 3.6. The valence band structure shown in Fig. 3.6 (second column) shows a downward shift of the subbands and an increase of the inter-subband gaps, due to the increased localization energy at the core-shell interface. The $k_z = 0$ character (Fig. 3.6, right column) at low doping is $\sim 10 \div 30\%$ LH for most states, except for the ground level which is almost completely LH, and two states which stand out with a strong HH character. Increasing doping increases the gaps, but does not change much the

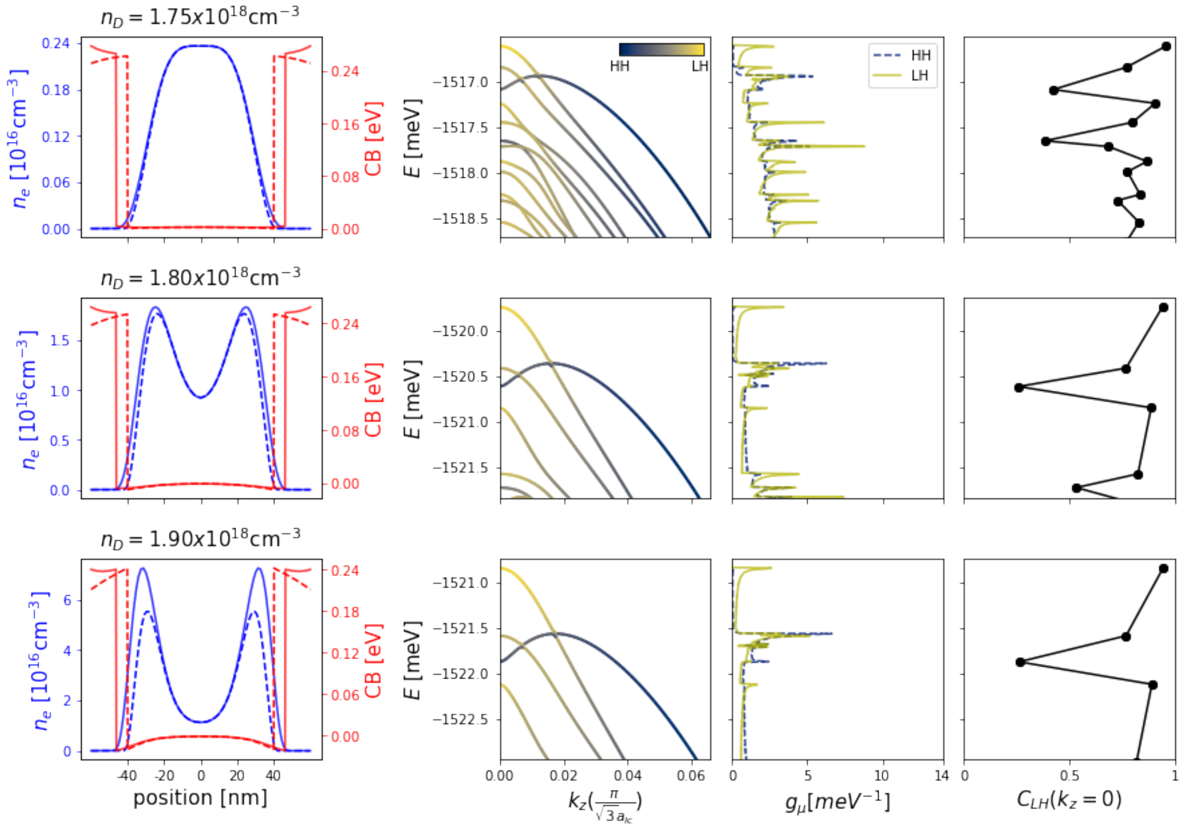

Figure 3.6: Left column: free charge density distribution n_e (blue) and self-consistent conduction-band profile CB (red) shown along the edge-to-edge (dashed line) and corner-to-corner (full line) directions of the CSNW section for $T = 20$ K at selected values of n_D, as indicated. Doping increases from top to bottom. Middle left and middle right columns: valence subbands and PDOS, respectively, corresponding to the doping density and self-consistent potential of the left panels. The hue/color represents the spinorial character in terms of HH and LH, according to Eqs. (3.4). Right column: LH-character of each subband at Γ.

subband dispersions. At the largest doping shown here, the PDOS is dominated by i) a LH peak near the gap, and ii) two overlapping peaks, one arising from a LH band and one from a HH band. Note, however, that the latter HH peak arises from the camel's back subband with a maximum at a finite k_z and, therefore, an indirect gap with the conduction band.

Figure 3.7 shows that as doping increases holes tend to be more localized in the center, with a mostly isotropic distribution. This contrasts with conduction states which move towards the GaAs/AlGaAs interface at larger doping densities, and it is due to the opposite sign of the electrostatic energy. Note that, as already noted for EL states, also for HH and LH states the order in terms of symmetry is not preserved as doping is swept. For example the 7-th level changes both character and orbital symmetry as n_D moves from 1.75 to 1.80 10^{18} cm^{-3}.

3.3.3. p-doping

We next discuss the results for p-doped materials, focusing on the effects of an increasing acceptor density n_A on the band structure and the hole charge density localization.

Figure 3.8(a) shows a linear increase of the free charge density after a threshold density of dopants.

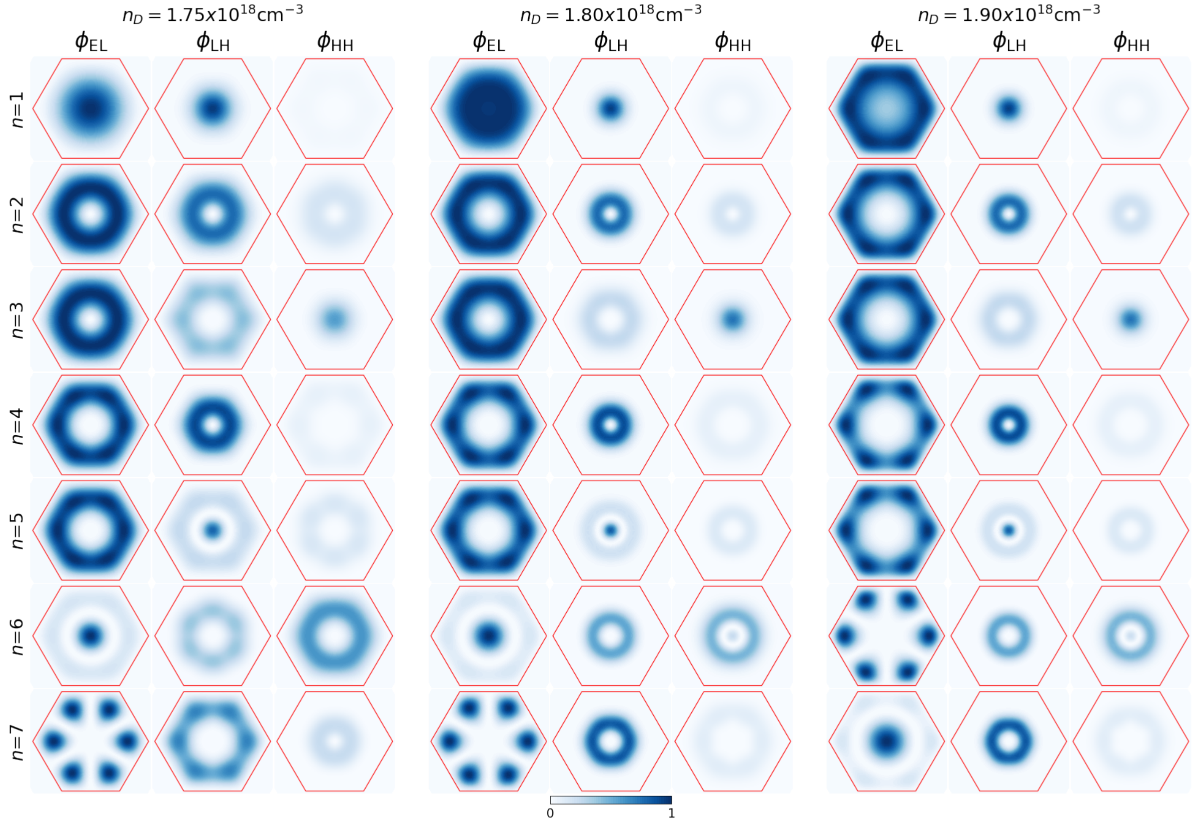

Figure 3.7: Projected probability distributions [Eqs. (3.6)] for the seven lowest conduction and seven highest valence subbands at the same selected doping densities of Fig. 3.6, as indicated. Each column corresponds to the EL, LH, HH component, as indicated.

Note that the range of densities is similar with respect to the n-doping case, despite the very different parameters and, as we shall see below, charge localization. Indeed, the free charge n_h, shown in Fig. 3.9(left) at selected values of the acceptor density n_A, shows a dip in the center already at weak doping, which is consistent with the larger mass and lower confinement energy of holes with respect to conduction electrons. As the acceptor doping density n_A increases, the charge progressively moves toward the interfaces to minimize Coulomb energy, in analogy with the n-doping case, but in contrast with the latter case, the hole gas remains remarkably isotropic, a seen by comparing the edge-to-edge and corner-to-corner profiles which nearly coincide in Fig. 3.9(left). In other words, the hole charge forms a uniform gas with a cylindrical shape and little resemblance to the host hexagonal confining potential up to these doping densities.

As n_A is swept, the conduction levels [Fig. 3.8(b)] shift in energy with respect to the Fermi level and finally stabilize, while an increasing number of hole subbands approach the Fermi energy and contribute to the free charge. Note that at large dopings, hole levels separate in a low-energy and a high-energy branch, which correspond to increasingly LH- and HH-like levels, respectively.

In contrast to the n-doping case, the hole band structure is strongly affected by p-doping, as exemplified in Fig. 3.9. This is due to the different localization energies of HHs and LHs in the increasingly localizing self-consistent potential. A prominent effect can be seen by comparing Figs. 3.9 and 3.10. The only strongly HH level (the 6-th level in Fig. 3.10, left panel) moves to lower energy due to the light mass. As a result, HH-LH mixing and related anticrossings are removed, the mass of the

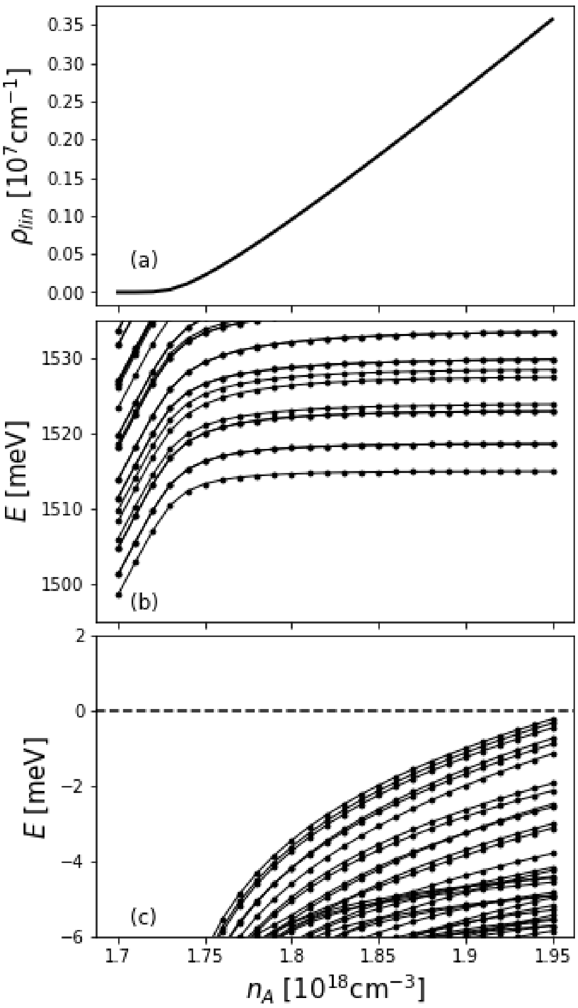

Figure 3.8: (a) Linear free charge density [Eq. (3.8)], (b) conduction subband energies at $k_z = 0$, and (c) valence subband energies at $k_z = 0$ as a function of the doping density n_A. Energies are referred to the Fermi level.

camel's back subband changes sign, and all bands point downward with a small mass at the large densities. Note that the PDOS at large doping is dominated by far by LH states. Furthermore, as a consequence of the reduced $\mathbf{k} \cdot \mathbf{p}$ coupling in the valence band at high doping densities, the hole energy levels at Γ tend to group in 6-fold clusters [see Fig. 3.8(c)] separated by gaps that increase with increasing n_A [119].

Figure 3.10 shows that all highest valence subbands become strongly localized at the interfaces at high doping. Contrary to conduction electrons, however, which always tend to localize at the six corners, holes alternate subbands localized at the corners and at the facets, which is again in agreement with single-band calculations in Ref. [102]. Since the charge density is a convolution of these levels, the isotropy of the hole cloud noted above is justified.

We also note that, as doping is increased, there is no definite order of LH- and HH-like levels in term of symmetry/localization, due to the increasing hole confinement energy towards the core-shell interface which is different for HH and LH components.

Finally, we note that, similarly to n-doped samples, minority carriers localize in the opposite direction,

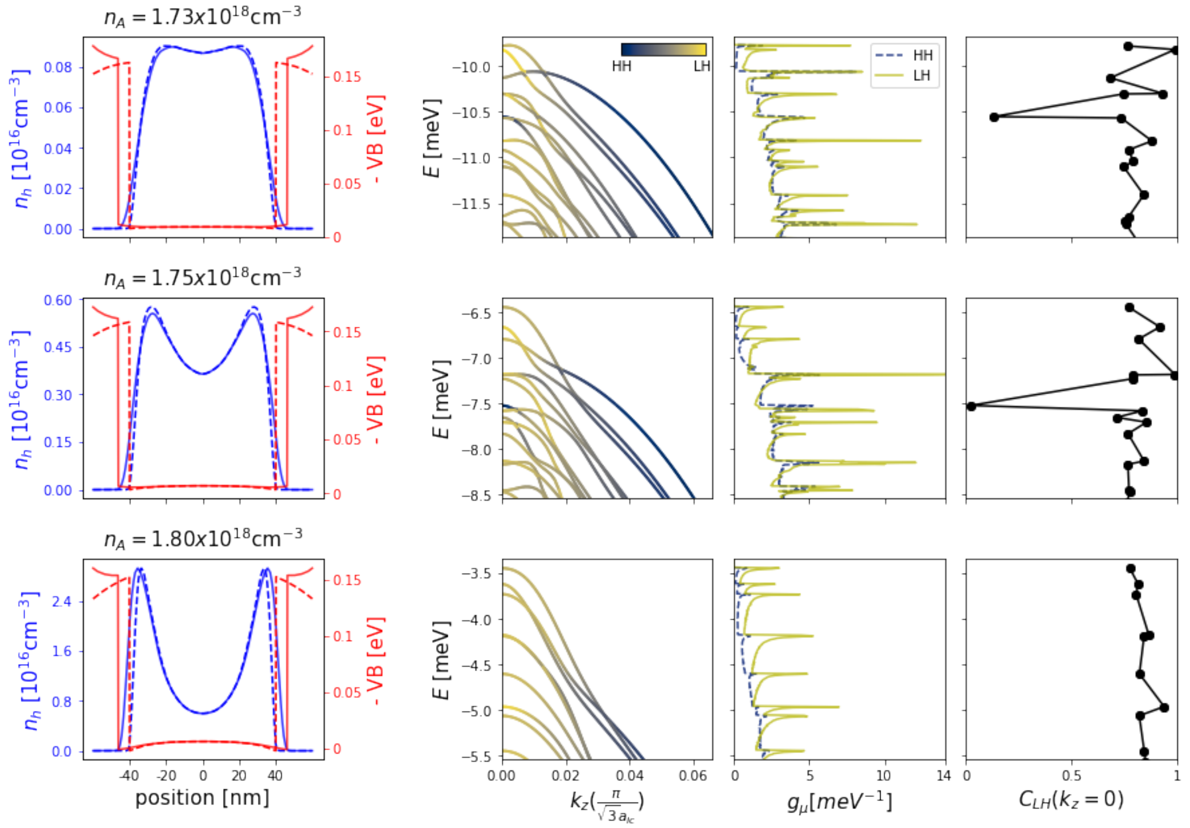

Figure 3.9: Left column: free charge density distribution n_h (blue) and self-consistent valence-band profile VB (red) shown along the edge-to-edge (dashed line) and corner-to-corner (full line) directions of the CSNW section for $T = 20$ K at selected values of n_A, as indicated. Doping increases from top to bottom. Middle left and middle right columns: valence subbands and PDOS, respectively, corresponding to the doping density and self-consistent potential of the left panels. The hue/color represents the spinorial character in terms of HH and LH, according to Eqs. (3.4). Right column: LH-character of each subband at Γ.

due to the opposite sign of the self-consistent potential. However, conduction electrons are much more rigid and stable due to the light mass, hence showing little evolution with doping density, and in particular no symmetry inversion takes place.

3.3.4. Temperature dependence

The electronic states discussed above are the result of the competition between comparable energy scales in the meV range. As temperatures of ~ 10 K are in the same energy range, we expect that small changes in temperature at this scale may bring about strong restructuring of the electronic system. As we shall see below, in general the effect of a temperature variation on the free-carrier charge density and the valence band structure are qualitatively analogous to the effects of a varying doping density.

In Fig. 3.11 we consider an n-doped sample with donor density $n_D = 1.76 \times 10^{18}$ cm^{-3} at $T = 10$ K (top row) and $T = 30$ K (bottom row), which are above and below the temperature used in Sec. 3.3.2. Such temperature variations respectively increase or decrease the bulk-band gap values of 1 meV with respect to the values in Tab. 3.1 for both the core and the shell materials. As a result, the band-offset are unchanged, while the band structure parameters that are affected by a rescaling procedure

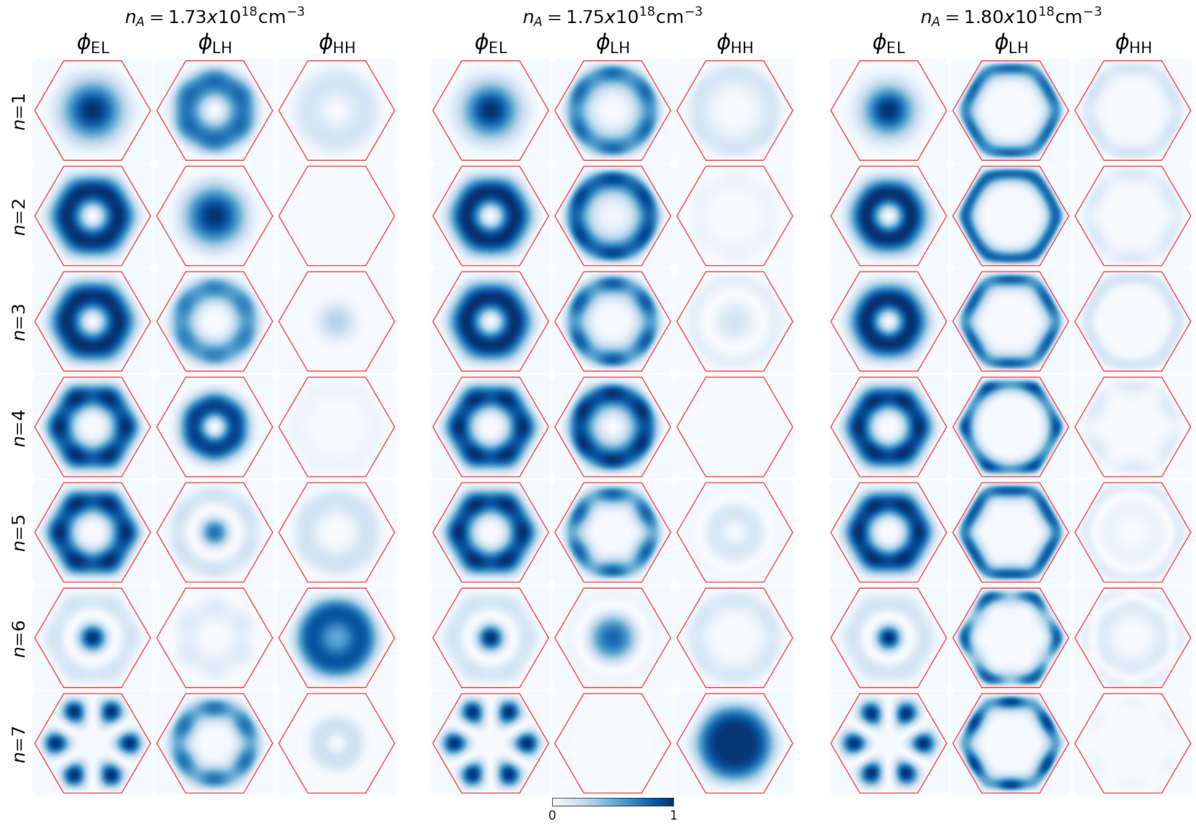

Figure 3.10: Projected probability distributions [Eqs. (3.6)] for the seven lowest conduction and seven highest valence subbands at the same selected doping densities of Fig. 3.9, as indicated. Each column corresponds to the EL, LH, HH component, as indicated.

are slightly modified. Starting at the lower temperature, the electronic charge density (left column) evolves from an isotropic charge density centered in the core to a ring-like density. This is similar to the effect of increasing doping, as in Fig. 3.6, as the occupation probability of the levels above the chemical potential increases with temperature, and more charge populates the nanowire. Consistently with Fig. 3.6, the valence band structure and PDOS are little affected by temperature in this range. However, the subbands are shifted in the opposite direction with respect to Fig. 3.6.

In Fig. 3.12 we consider a p-doped sample with acceptor density $n_A = 1.75 \times 10^{18}$cm^{-3} at the same two temperature as above. Again, increasing the temperature results in a greater hole charge density and a more pronounced charge depletion in the center due to the Coulomb interaction. Clearly, valence band states are more sensitive to changes in the charge density for p-doping. Indeed, Fig. 3.12 shows that as temperature is increased, HH-like states move to lower energies, while HH-like subbands change their curvature downward. As a consequence, the PDOS undergoes a substantial restructuring, as all main features are LH-like. Note that in contrast to the case of a doping density variation, the valence band structure is shifted downward when the temperature increases.

3.3.5. Optical anisotropy

Optical absorption in quasi-one-dimensional systems is dominated by excitonic and polarization effects induced by Coulomb interactions, not included in Eqs. (3.9),(3.10) [133, 134]. However, the

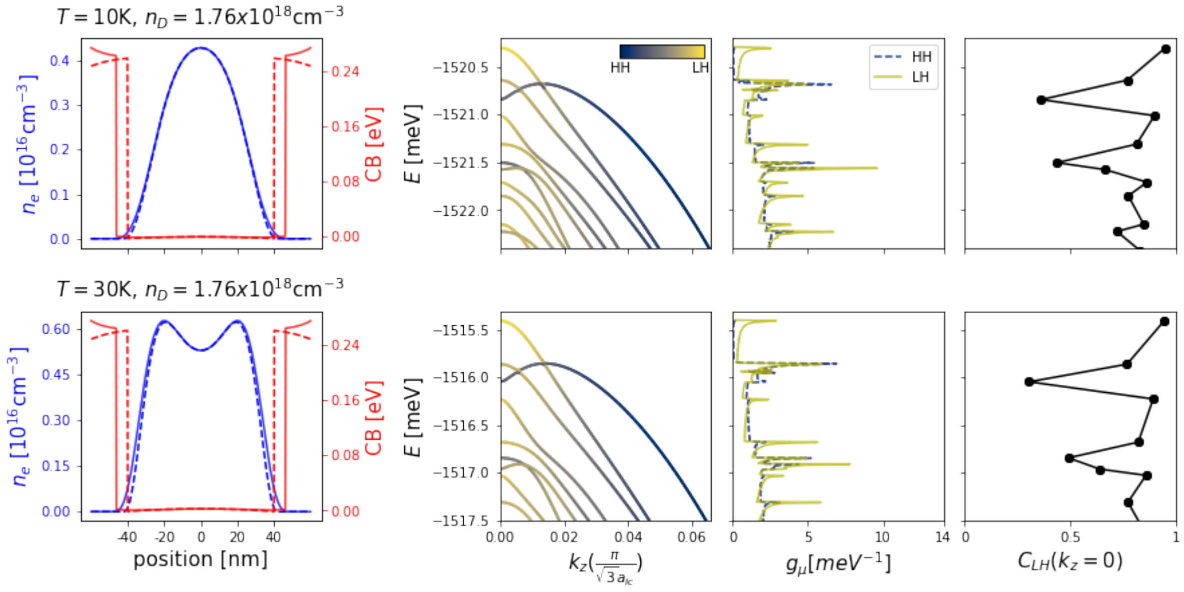

Figure 3.11: Left column: free charge density distribution n_e (blue) and self-consistent conduction-band profile CB (red) shown along the edge-to-edge (dashed line) and corner-to-corner (full line) directions of the CSNW section for $T = 10$ K (top row) and $T = 30$ K (bottom row) at the single doping density $n_D = 1.76 \times 10^{18}$ cm^{-3}. Middle left and middle right columns: valence subbands and PDOS, respectively, corresponding to the doping density, temperature and self-consistent potential of the left panels. The hue/color represents the spinorial character in terms of HH and LH, according to Eqs. (3.4). Right column: LH-character of each subband at Γ.

optical anisotropy between linearly polarized light along and transverse the nanowire axis, should be less sensitive to Coulomb effects [111, 112]. On the other hand, while x-polarized light couples to HH states [see Eq. (2.65)], z-polarized light does not. Hence, β is a sensitive probe of the orbital composition of valence band states [111].

In Fig. 3.13 we show the calculated relative optical anisotropy β [Eq. (3.11)] at selected doping concentrations for n- (left) and p-doped (right) samples, respectively. Doping concentration increases from top to bottom in both panels. To emphasize the anisotropy of the more intense absorption peaks, the line darkness is modulated with the intensity of the absorption spectrum at the given photon energy. For reference, we also show in the inset single-particle absorption spectra in the two polarizations (for the undoped sample) with optical transitions from the n-th valence state to the m-th conduction state labelled *(mn)*.

As a reference, we shall first describe the spectral anisotropy of the undoped sample [top panels in Figs. 3.13(a),(b)]. The first positive structure, labelled $\boxed{\text{a}}$, arises from the fundamental optical transition ⑪ [see inset of Fig. 3.13(a)] which involves the almost purely LH state. This is also an intense transition due to the overlapping envelope functions components (see Fig. 3.4, first row). The positive anisotropy is $\beta \simeq 3/5$, which is expected from the ratio between the momentum matrix element in the z and x directions,

$$\left|\left\langle S,\pm\frac{1}{2}\middle|p_z\middle|\frac{3}{2},\pm\frac{1}{2}\right\rangle\right|^2 = 4\left|\left\langle S,\pm\frac{1}{2}\middle|p_x\middle|\frac{3}{2},\pm\frac{1}{2}\right\rangle\right|^2,$$

hence $\beta = \frac{4-1}{4+1}$.

The next two negative dips in the anisotropy structure $\boxed{\text{a}}$ involve the $m = 1$ EL subband, and arise

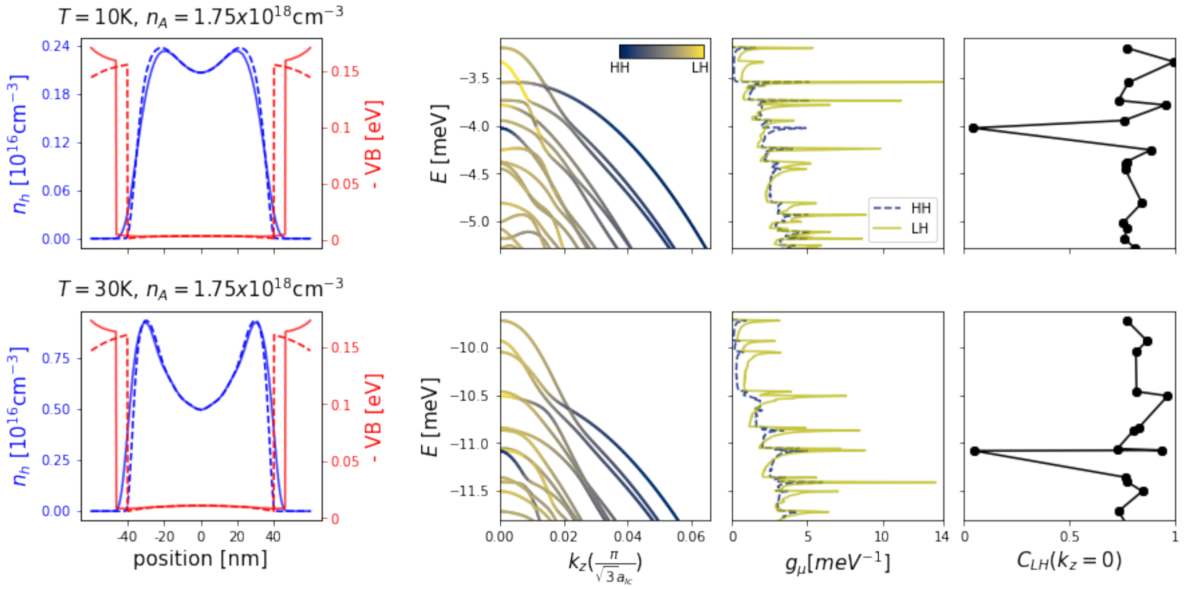

Figure 3.12: Left column: free charge density distribution n_h (blue) and self-consistent valence-band profile VB (red) shown along the edge-to-edge (dashed line) and corner-to-corner (full line) directions of the CSNW section for $T = 10$ K (top row) and $T = 30$ K (bottom row) at the single doping density $n_A = 1.75 \times 10^{18}$ cm^{-3}. Middle left and middle right columns: valence subbands and PDOS, respectively, corresponding to the doping density, temperature and self-consistent potential of the left panels. The hue/color represents the spinorial character in terms of HH and LH, according to Eqs. (3.4). Right column: LH-character of each subband at Γ.

from the HH components of transitions *(13)* and *(16)* (see Fig. 3.4, third and sixth row). As HH components do not couple to EL states for light linearly polarized along z, we indeed expect the anisotropy to be negative for these optical transitions.

A second, positive anisotropy set of structures at higher photon energies, labelled $\boxed{\text{b}}$, involves transitions to the $m = 2$ conduction subband with predominantly LH initial states, namely *(22)* and *(24)* transitions (see also Fig. 3.4, second and fourth row).

As the optical anisotropy discriminates specific transitions, it is interesting to discuss how the anisotropy spectra evolves with doping concentration. As seen in Figs. 3.13(a),(b) in both n- and p-doped samples the absorption edge experiences a red-shift with increasing doping, due to band gap renormalization. In Fig. 3.14 we compare the energy difference ΔE between the ground state energy of the conduction and the valence band, respectively, showing that the effective energy gap decreases almost linearly for both kind of samples in the range of a few meV as doping concentration rises.

In n-doped samples, Fig. 3.13(a), the absorption intensity of the lowest transitions gradually vanishes with doping, which is due to two concomitant effects, i) band-filling due to electron subbands falling below the Fermi level, which inhibits inter-band absorption to these levels, and ii) optical matrix element reduction, which is due to Coulomb repulsion: the free charge distribution in the occupied band tends to localize towards the core-shell interfaces as doping concentration is increased, while confining states in the center in the other band, lessening the optical matrix element between initial and final states [Eq. (3.10)]. Both effects contribute to suppress low-energy absorption at high-doping, finally moving the absorption edge to the strongly anisotropic structure $\boxed{\text{c}}$, originated by transitions to the $m = 7$ EL subband, namely *(71)*, mainly LH with positive anisotropy, and *(73)*, mainly

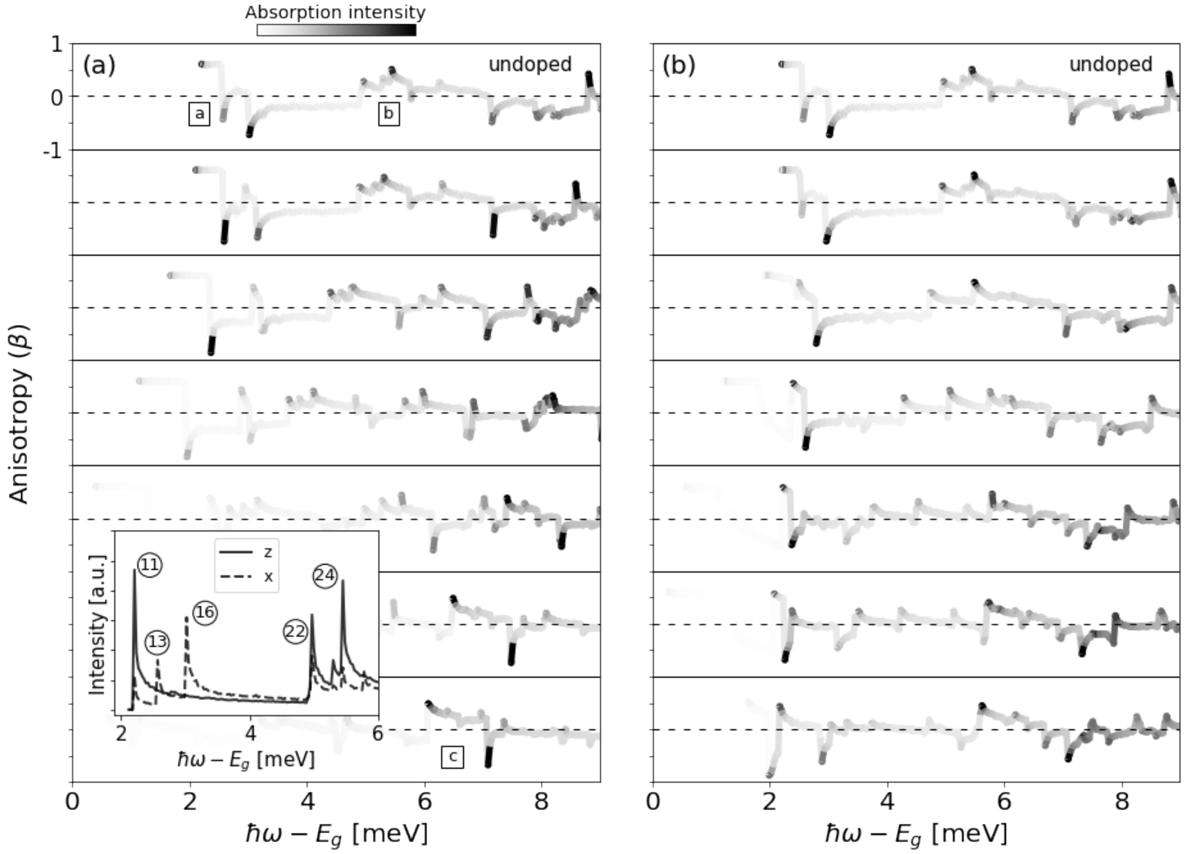

Figure 3.13: (a) Optical anisotropy β [Eq. (3.11)] for n-doped samples at different donor concentrations. From top to bottom: undoped, 1.75, 1.77, 1.79, 1.82, 1.87, 1.90 $\times 10^{18}$ cm^{-3}. Horizontal dashed lines indicate the zero reference, each panel extends vertically from -1 to +1. The gray hue represents the intensity of the corresponding absorption spectrum [Eq. (3.9)] at the given photon energy. E_g=1.518 eV is the band gap of GaAs at $T = 20$ K. Inset: calculated absorption spectra of the undoped structure for linearly polarized light. Peaks are labelled with (mn), where m is the index of the final conduction subband and n the index of the initial valence subband involved in the optical transition. (b) Same as panel (a) but for p-doped samples. From top to bottom: undoped, 1.73, 1.75, 1.77, 1.79, 1.80, 1.82 $\times 10^{18}$ cm^{-3}.

HH, hence with negative anisotropy.

For p-doped samples, see Fig. 3.13(b), the band-filling effect is less pronounced within the examined range of doping. In fact, even at the highest acceptor density shown in Fig. 3.13(b), the highest valence subband does not cross the Fermi level (see Fig. 3.8). Here, the suppression of the absorption intensity with positive anisotropy at $\boxed{\text{a}}$ is mainly due to reduction of the initial and the final states' overlap, due to an increasing localization towards the core-shell interfaces of the hole ground state envelope function (see Fig. 3.10, first row). The first negative dip gradually disappears because the third valence subband loses its HH character with increasing doping (see Fig. 3.10, third row and Fig. 3.9, second column). The opposite occurs for the second negative anisotropy peak, which persists at high doping, due to the increasing HH character of the sixth hole subband with doping, as already pointed out in Sec. 3.3.3, which in turn increases the optical matrix element for x-polarized light.

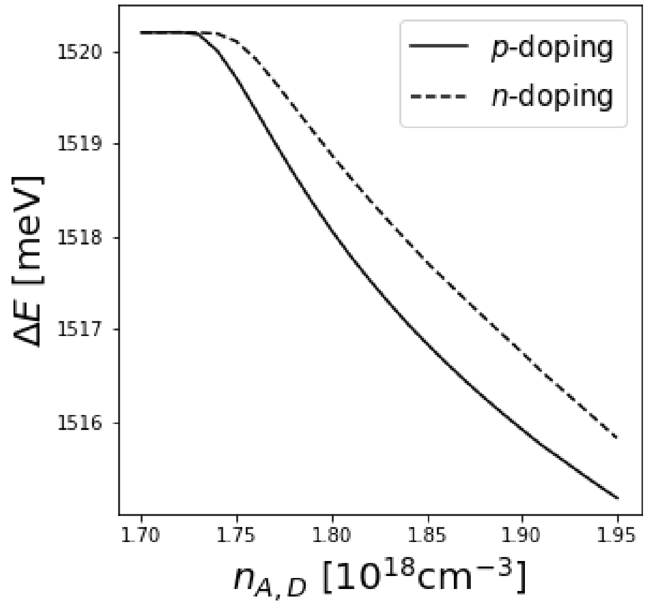

Figure 3.14: Effective energy gap ΔE as a function of doping concentration for n- and p-doped samples.

3.4. Conclusions

We have thoroughly investigated the band structure of doped GaAs-based CSNWs, with an emphasis on the evolution of spin-orbit coupled valence band states with doping, either of n- or p-type [117]. This is an important piece of information for the characterization of such materials, where doping is still an issue.

Our calculations, performed with a state-of-the-art Burt-Foreman 8-band $\mathbf{k} \cdot \mathbf{p}$ description, treat many-body effects at the mean-field level, and extend previous investigations to realistic descriptions of doped materials. The use of a flexible FEM approach, which allows to use non-uniform grids, proved to be numerically efficient at different doping levels. This is clearly an advantage in view of multi-parameter optimization, e.g., by stochastic methods [135, 136, 86].

In particular, we have investigated a proto-typical CSNW with remote doping. As in corresponding planar heterojunctions, the conduction subbands feature a parabolic in-wire dispersion, while hole subbands have a complex dispersion, with inverted masses, which has been rationalized in terms of HH-LH mixing. In large core nanowires, with small confinement energies, increasing doping density moves the majority carriers to the core-shell interface in order to reduce the Coulomb energy. Correspondingly, the states of the minority carrier band are confined to the core by the self-consistent electrostatic field, and in general the overlap of conduction and valence states decreases. While this is qualitatively true for both types of dopings, our calculations allow to identify several differences between the two type of samples which may have an impact, in particular, on optical absorption. In particular, for p-doping the valence band structure is strongly reshaped by confinement of holes at the core-shell interface, and all low energy excitations have a strong LH character.

It may be expected that band structure affects optical absorption and, in particular, optical anisotropy for light polarized along or normal to the nanowire axis. Hence, we have evaluated the doping-density dependent optical anisotropy, which is able to distinguish the spin-orbital character of the transition. In addition to the expected band-filling effects, specific signatures can be identified in the anisotropy patterns which distinguish between n- and p-doping.

4

Full-shell tubular-core hybrid nanowires with hole bands: a practical proposal for Majorana zero modes

Full-shell hybrid nanowires, structures comprising a superconductor shell that encapsulates a semiconductor core, have attracted considerable attention in the search for Majorana zero modes (MZMs). The main caveats of this platform, however, are that the predicted spin-orbit coupling (SOC) is too small to achieve substantial topological minigaps and that the MZMs typically coexist with a finite background of trivial subgap states. In order to overcome both problems, we explore the potential of utilizing core-shell hole-band nanowires within the superconductor full-shell, forming a concentric trilayer heterostructure with an i) insulating core, an ii) intermediate semiconductor layer, and iii) an outer superconductor shell. This tubular-core nanostructure is specially suitable for the creation of protected MZMs in full-shell geometries because it minimizes the presence of other detrimental subgap states and therefore enables the development of true sizeable topological minigaps. We propose particularly InP/GaSb core-shell nanowires and exploit the unique characteristics of the III-V compound semiconductor valence bands. We show that they exhibit a robust hole SOC that depends on the semiconductor layer radius and thickness, with magnitudes around 20 meV·nm. Interestingly, we find that this enhanced coupling is intrinsic and thus does not rely on electric fields, which are non-tunable in a hybrid full-shell geometry.

4.1. Introduction

Hybrid superconductor-semiconductor (SC-SM) heterostructures are probably the most analyzed platform [137] for the creation of one-dimensional (1D) topological superconductivity [138, 45] and the search of Majorana zero modes [139] (MZMs). MZMs offer immunity to local noise and possess non-trivial braiding statistics [140], making them promising building-blocks of future fault-tolerant quantum computers [141, 142, 143]. In conventional Majorana nanowires [138, 45] (NWs), a SM NW with strong spin-orbit coupling (SOC) and g-factor is partially covered by an s-wave SC and subject to a Zeeman field [144, 145, 146, 147]. A popular choice of materials is Al for the SC and n-type III-V compound SMs such as InAs or InSb, although other possibilities are also studied [148, 149, 150]. In spite of the tremendous advancement of this field in the last decade, the experimental demonstration and manipulation of MZMs remain challenging due to a number obstacles [151], including the presence of various types of disorder [152, 153, 154, 155, 156, 157], metallization effects exerted by the parent SC on the SM parameters [158, 159, 160], or the need to subject the hybrid system to strong magnetic fields [161, 162].

An alternative nanowire design that alleviates some of the problems that conventional Majorana NWs face was recently proposed. It is called a full-shell hybrid NW [43], and consists of a SM core fully wrapped in a SC shell, instead of only partially covered by the SC. The encapsulation of the core by the metallic shell should shield the NW from the electrostatic environment, and reduce disorder created by surface reconstruction of the NW facets exposed to air in partial-shell NWs. Moreover, conventional partial-shell NWs are predicted to undergo a topological phase transition for a sufficiently strong Zeeman field [45, 44], which typically requires strong magnetic fields B that degrade the parent superconducting state [163] before the topological transition can occur [59, 164]. In full-shell NWs, however, the topological driving mechanism is a magnetic-field mediated orbital effect when the SC is threaded by an odd number of fluxoids [43]. The topological phase transition and thus the appearance of MZMs are in this case predicted at much smaller B values. Additionally, these NWs can operate with small or zero g-factor.

Full-shell NWs present also some disadvantages, most notably the impossibility to gate tune the chemical potential inside the core due to the metallic encapsulation. Furthermore, using microscopic simulations in realistic Al/InAs full-shell wires, the electron SOC has been predicted to be too small to provide substantial topological protection [49]. This Rashba SOC appears due to the radial electric field that is produced by the SM conduction-band bending at the SM-SC interface in III-V compound SMs. As the chemical potential, the electrostatic potential profile and thus the SOC are also not tunable by external gating.

Full-shell hybrid NWs present another challenge. For the parameter regions for which Majorana states are predicted to appear, these zero modes typically coexist with a number of trivial subgap states that disperse with flux, cross zero energy, and give rise to a dense local density of states (LDOS) background around them. These subgap states have been dubbed Caroli–de Gennes–Matricon (CdGM) analogs [165], and their presence is due to the doubly-connected geometry of the SC shell and the non-zero winding of the SC pairing phase in the presence of a magnetic flux. A recent study [166] that thoroughly examines the phenomenology of these hybrid NWs has established that MZMs free from CdGM analogs for a certain flux interval, and thus with true topological minigaps, are possible in tubular-core NWs. These are structures with a core in the form of a tube of a certain thickness, wrapped in the SC shell.

In view of these arguments, in this chapter we make a specific and practical proposal that substantially improves the performance of full-shell hybrid NWs and thus facilitates the creation of protected MZMs. On the one hand, we propose to use a core-shell insulator-SM NW for the hybrid's core. Note that typical core-shell NWs have a SM core and an insulating shell, as the reason of the shell is normally to protect the semiconducting interior. Here, we propose to do the opposite, we want to place the active SM layer outside, confining and pushing the wave function closer to the SC-SM interface by means of an insulating core. In this chapter, we will refer to this part of the hybrid wire as the tubular-core SM to avoid any confusion with the SC full-shell covering. On the other hand, we propose to make use of the *hole* bands of III-V compound SMs as we want to harness the spin-orbit coupled nature of the valence bands (VBs).

Our proposal centers around a specific material configuration, tubular-core InP/GaSb NWs, with GaSb acting as the SM shell and InP as the insulating core, see Fig. 4.1(b). This NW should have the Fermi level placed at the VBs, close to the band edge [167, 168], which is convenient for the topological phase when proximitized with the SC. In our analysis, we first examine the SO coupling of GaSb/InP NWs for different GaSb radii and thicknesses. We find substantial values, of the order of 20 meV·nm[1], that do not rely on external factors like electric fields or strain.

Subsequently, we consider a trilayer structure by proximitizing the InP/GaSb tubular core with a SC shell. Different SCs could in principle be considered[2]. Being Al the most tested one in full-shell hybrids, we perform specific numerical simulations for Al/X/GaSb/InP, where “X” here stands for a possible insulating layer between the SC and the SM that controls the coupling between both materials. Apart from tuning the system into the topological phase, this insulating layer has been proposed to reduce disorder and metallization effects. We analyze the topological phase diagram and the local density of states (LDOS) at the end of a semi-infinite full-shell tubular-core NW. We find extended regions in parameter space where the system is topological and the MZMs display a measurable topological minigap of the order of 30 μeV (more than 10% of the parent SC gap). This is possible thanks to a combination of factors: the SOC of the hole bands, the tubular nature of the core and the increased carrier mass of holes as compared to wires based on the SM CB.

To the best of our knowledge, this type of trilayer hybrid nanostructures has not yet been grown and analyzed experimentally. Apart from its obvious application for topological superconductivity, it offers a new playground for the study of superconducting proximity effect and SOC in both n-type and p-type nanostructures.

This chapter is organized as follows. In Sec. 4.2 we analyze the tubular-core SM. We first present our model, focused on the description of the VBs of III-V SM NWs. We use a microscopic approach that employs a self-consistent Schrödinger-Poisson equation within a multi-band k·p Hamiltonian framework. Subsequently, we elucidate the origin and strength of the SOC in an InP/GaSb geometry. With this knowledge, we derive an effective Hamiltonian that accurately describes the lowest-energy subbands. In Sec. 4.3 we turn to the complete structure, the full-shell tubular-core hybrid. Leveraging the effective Hamiltonian and using the realistic parameters for the NW obtained in the previous section, we analyze the topological phase diagram and the LDOS. We conclude in Sec. 4.4. More details about the methods can be found in the related appendices.

---

[1] This number for the SOC should be compared to values of $2-4$ meV·nm found in Ref. [49] for similar geometries.

[2] For example, Al [169], Pb [170], Ta [171], V [172] or Sn [173]. This is nevertheless a material science problem and should be investigated experimentally.

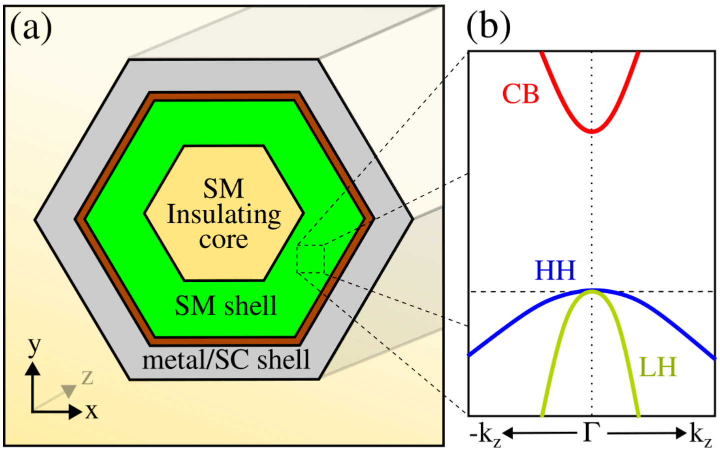

Figure 4.1: Sketch of the nanodevice. (a) Full-shell tubular-core hybrid nanowire (NW). This heterostructure is composed of a semiconductor (SM) core-shell NW made of an insulating core (yellow) and an active SM layer (green). We call this part the *tubular-core SM*. The NW is coated all around by a thin superconductor (SC) shell (grey). An additional insulating layer (brown) may be placed between the SM and SC to regulate the coupling between both materials. This composite system can host a topological superconducting phase when an axial magnetic flux is applied. (b) Typical band structure of a bulk III-V compound SM. For some specific materials, like the GaSb/InP tubular-core NWs studied here, the Fermi level may lie at the valence bands close to the band edge (LH and HH stands for light and heavy-hole bands, and CB for conduction band).

4.2. Tubular-core hole-band semiconductor

4.2.1. Model and methods

We look for a SM tubular-core heterostructure whose Fermi level lies at the VBs of shell and close to the VB maximum, see Fig. 4.1(b). The core must be insulating at these energies, since we seek to empty the wire's center and push the charge wave function towards the outer part of the NW, as explained in the introduction. In this sense, type-II ”broken gap” SM heterostructures are not helpful, as the valence and conduction bands in different layers overlap. Only type-I and type-II are thus useful. There are several material combinations that could be analyzed, being the lattice mismatch between the two materials an important factor to determine whether the heterostructure is viable. It would be interesting to study both theoretically and experimentally how quantitative and even qualitative details vary between different choices. For the sake of concreteness, we propose to use type-II heterostructures based on Sb compounds because they have hole carriers at the Fermi level more commonly [174]. Particularly, for our numerical simulations we will consider InP/GaSb core-shell NWs. To avoid any confusion with the full-shell hybrid, we rename it GaSb/InP tubular-core NW. To the best of our knowledge, these have not yet been grown and analyzed experimentally, but they appear to be feasible. In this regard, high quality and relaxed GaSb layers grown directly on InP(001) substrates using solid source molecular beam epitaxy have been reported [175, 176]. Furthermore, InAs-InP-GaAsSb core-dual-shell NWs have been recently grown using catalyst-free chemical beam epitaxy [177].

InP-GaSb heterostructures exhibit a type-II band alignment with a wide gap of ~ 0.5 eV. Specifically, the VB maximum of GaSb lies within the energy gap of InP, as schematically illustrated in Fig. 4.2(a). Furthermore, we assume that the Fermi level is placed close to the VB edge of GaSb, as observed in Ref. [175]. Partial control over the wire's overall doping could be achieved through the incorporation of chemical impurities within the InP core during the growth process [178, 175, 179]. Given that the

Table 4.1: Material parameters used in the 8-band k·p model at temperature $T = 4$ K. The energy gap E_g, the conduction and valence band offsets ΔE_c and ΔE_v at the InP/GaAs interface, the split-off energy Δ_{so}, the Kane energy E_p, the conduction electron effective mass m_e and the Luttinger parameters γ_i are taken from Ref. [126]. E_p^{rsc} is the rescaled Kane energy Eq. (2.56) and $\tilde{\gamma}_i$ are the modified values Eq. (2.53). ϵ_r refers to the relative dielectric constant of each material.

	InP		GaSb
E_g [eV]	1.4236		0.812
ΔE_c [eV]		0.514	
ΔE_v [eV]		0.91	
Δ_{so} [eV]	0.108		0.76
E_p / E_p^{rsc} [eV]	20.7 / 18.3		27 / 24.8
m_e	0.0795		0.039
γ_1 / $\tilde{\gamma}_1$	5.08 / 0.79		13.4 / 3.2
γ_2 / $\tilde{\gamma}_2$	1.60 / -0.55		4.7 / -0.39
γ_3 / $\tilde{\gamma}_3$	2.10 / -0.047		6.0 / 0.9
ϵ_r	11.77		15.7

InP core primarily acts as an insulator in this context, it is reasonable to assume that these dopants would exert a minimal influence on the electronic properties of the wire, aside from their impact on the Fermi level position.

We note that group IV SMs integrated into heterostructures, such as Ge/Si heterostructures, are more popular platforms to exploit the hole-bands of SMs [180]. These materials are well-established and widely adopted in SM qubit platforms [181, 182, 183, 184] as their valence bands exhibit strong SO coupling [185, 186, 187, 188] and electrically tunable g-factors [189, 190, 191]. Moreover, they can be proximitized by a SC as well [192, 193, 194, 195, 196, 197]. However, these favorable properties stem from the strain introduced at the Ge/Si heterostructure interface [198, 199, 200], which imposes specific design constraints. Firstly, the wires or stackings must be thin enough to homogeneously induce the required degree of strain in the hole NW or layer. Secondly, strain may induce further disorder and, while this concern is not relevant in qubits based on QDs, it becomes problematic in quasi-1D systems [201, 202, 155], especially for thin wires/layers. Still, several theoretical works have proposed and analyzed nanodevices based on these heterostructures for the creation and manipulation of 1D MZMs [203, 204, 205]. And even though they do not consider the effect of disorder, either they find very narrow topological windows as a result of the small g-factors [205], or tiny minigaps as a consequence of the necessary strong confinement [204].

We start with the analysis of the band structure of holes in GaSb-InP tubular-core NWs with hexagonal cross section and assumed to be translational invariant along its growth axis (z-direction). We obtain the energy spectrum of the NW through a self-consistent solution of the coupled Envelope Function-Poisson equations, employing the 8-band Burt-Foreman Hamiltonian developed in Ch. 2, which accurately describes the lowest energy states of NWs made out of III-V compound SMs around the Γ point [206, 71] and thus provides reliable estimations for the SOC [207]. The parameters of used for the simulations in this chapter are reported in Tab. 4.1. All these calculations are performed through the Python library `nwkp`, as discussed in Ch. 2, which is developed in-house.

A typical NW energy spectrum is shown in Fig. 4.2(b), displaying several subbands that arise due to the confinement imposed by the finite wire's cross section. The color represents the light hole (LH) and heavy hole (HH) character of each state, as in Eqs. (3.4). E_0 indicates the top of the highest energy subband at Γ. Due to the presence of both time reversal symmetry and inversion symmetry, each subband is doubly degenerate.

The subbands in Fig. 4.2(b) presents several noteworthy aspects. First, the subband dispersion is negative, as expected for the VBs. No camel's back structure, typical of hole bands in heterostructure, is present, due to the strong confinement in the narrow shell which strongly separates HHs from LHs. Second, all subbands have a hybrid LH and HH character that depends on k_z. Remarkably, the LH character predominates in the higher energy subbands, i.e. close to the Fermi level. This means that these states have a lighter mass in the $z-$direction, which is the quantization axis of the total angular momentum of the Bloch states. On the other hand, being the lowest energy transverse modes, these states have a heavier mass in the confinement plane. On the contrary, lower energy subbands (with higher kinetic energy) have a larger HH character in the $z-$direction and lower effective mass in the confinement plane. In any case, LH-HH coupling is the essential ingredient, as we shall demonstrate, to provide a strong SOC to the different subbands, and it is ultimately regulated by the strength of the lateral confinement.

In Fig. 4.2(c) we show an example of the self-consistent charge density distribution corresponding to the spectrum computed in Fig. 4.2(b). It shows the hole concentration throughout the cross section of the CSNW (solid black lines represent the interfaces). Although no specific symmetry is implied in the calculation, the charge density has a ring-like distribution centered at the GaSb-shell average radius, with negligible presence within the InP core. The nearly perfect cylindrical symmetry of this charge distribution arises from the finite thickness w of the SM shell and the occupation of the lowest angular momentum states.

In a NW with cylindrical symmetry and within the axial approximation, the total angular momentum component J_z commutes with the Hamiltonian, hence m_j is a good quantum numbers which takes the values $m_j \in (\mathbb{Z}+1/2)$. In Fig. 4.2(b) we calculate projection C_{m_j} of the different states onto the value $m_j = 1/2$, represented by the size of the dots at discrete values of k_z. Specifically, we project the nanowire eigenstates onto the eigenstates of the total angular momentum operator $\hat{J}_z$ with corresponding eigenvalue $m_j = 1/2$. The reader can refer to appendix B.1 for more details about how we obtain the C_{m_j} coefficients. We are interested in this particular total angular momentum quantum number because, in the presence of superconductivity in a full-shell geometry, these states will be able to give rise to MZMs. It is noteworthy that in Fig. 4.2(b) the two higher energy subbands predominantly correspond to the $m_j = 1/2$ sector, meaning that a cylindrical approximation [208] is justified for them. The use of the cylindrical approximation to treat the eigenstates of the hexagonal wire remains in general justified as long as the shell thickness w is larger than approximately 5 nm. Only for very small values of w, the charge distribution tends develop an hexagonal shape due to the hybridization with higher angular harmonics $m_j + 6n$ for integer n.

To complement our investigation, we present the electrostatic potential energy profile $-e\phi(r)$ for the same parameters in Fig. 4.2(d). It is computed self-consistently taking into account the potential generated by the hole charges within the NW. We set the boundary condition as $\phi_\mathrm{b} = 0$ at the wire facets, assuming that there is a surrounding metal that is grounded. Consequently, the potential energy is zero in proximity to the interface and becomes progressively negative towards the core. This implies that holes tend to feel attracted towards the outer interface. It is important to note that if the metallic shell is superconducting, $\phi_\mathrm{b} \neq 0$ even if it is grounded. This is due to the Ohmic SM-SC contact that produces a SM band bending at the interface as a result of the work-function differ-

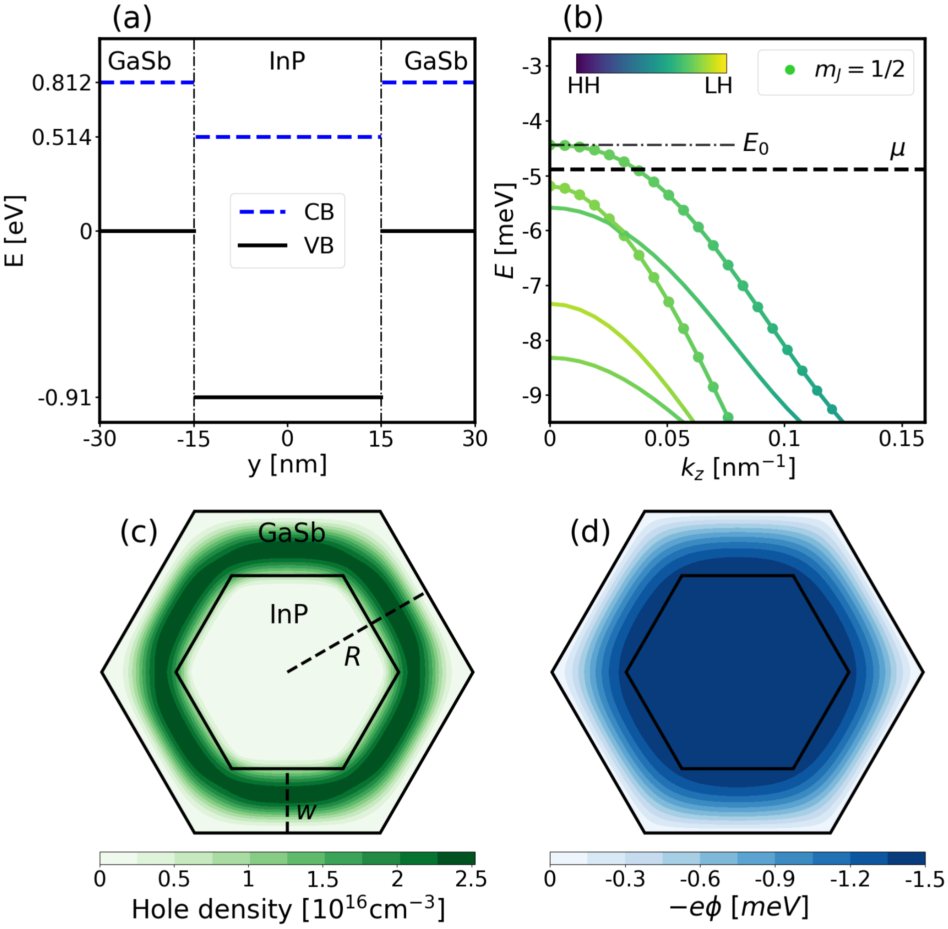

Figure 4.2: GaSb/InP tubular-core Nws. (a) Schematic representation of the band alignment of a InP/GaSb heterostructure. This type-II SM heterostructure features the GaSb valence band (VB) maximum positioned within the energy gap of InP. We assume that the Fermi level lies close to the GaSb VB maximum. (b) Typical energy spectrum of GaSb/InP NWs near the Γ point as a function of the axial wave vector k_z. The colorbar denotes the weight of each state on the light-hole (LH) and heavy-hole (HH) bulk bands. Due to confinement effects, the highest energy subbands exhibit primarily a LH character, albeit with a degree of hybridization between LH and HH states. μ is the chemical potential and E_0 is the VB edge energy. (c) Charge density distribution of holes within the tubular-core nanowire, corresponding to the spectrum presented in (b). The wire geometry is defined by its radius R and shell thickness w. (d) Electrostatic potential profile for the same simulation. For these simulations $R = 30$ nm and $w = 15$ nm.

ence between both materials. The precise magnitude and shape of this band-bending depends on chemical details that have not yet been studied for this heterostructure. In general, it is reasonable to assume that it will create a negative potential energy at the outer interface, pushing holes away from it and towards the inner interface. This might be very convenient for our full-shell hybrid nanowire proposal as this might decrease metallization effects from the SC while still preserving the necessary proximity effect due to the finite thickness of the SM layer.

4.2.2. Spin-orbit coupling

We now proceed to study the SOC in these InP-GaSb, tubular-core NWs. Using the lowest energy hole subbands and wave functions, calculated from the 8-band **k** · **p** model, we derive both the SOC α and the effective mass m^* (see App. B.2 for the rather elaborate method). In Fig. 4.3(a), we present the SOC constant α of the highest-energy state, i.e., the closest to the band edge, as a function of the

NW shell thickness w for different NW radii R, each represented by a different color. We extract the SOC when the chemical potential is located halfway between the two subbands of the first m_j=1/2 subbands pair. We consider realistic values [3] for R and w, ranging from $R = 15$ nm to $R = 40$ nm, and from $w = 5$ nm to $w = R - 10$ nm. For these tubular-core NWs, we obtain SOCs in the range of 15 to 30 meV·nm. These numbers are larger by a factor of ~ 4 than the largest SOCs found in Ref. [49] for solid-core NWs based on CB electrons and equivalent radius R. As in the case of Ref. [49], we find that the α increases with R. In our case, moreover, for a fixed R, α also increases with w.

In Fig. 4.3(b) we show the behavior of the SOC constant with the doping level of the wire, considering different shell thicknesses w for a fixed radius $R = 30$ nm. Notably, the SOC remains almost constant with μ, what suggests that the hole bands are essentially insensitive to the built-in electric field inside the wire. This is in sharp contrast to what happens to the CB of these materials, where the sole contribution to the (Rashba) SOC arises from the electric field [206].

Both the observations that, for a fixed R, α increases with w and is essentially independent of the electric field, point to the intrinsic nature of the hole-band SOC of III-V compound semiconductors. To further understand this behavior and unravel the underlying origin of the SOC, in Fig. 4.3(d) we conduct a comparative analysis by selectively omitting certain contributions. In blue we present the results derived from the complete 8-band model, which are the same as the blue curve in Fig. 4.3(a). First, we want to test whether the interaction between the HH-LH bands of GaSb and either the split-off bands or the CBs of both GaSb or InP, do influence the SOC. To explore this, we set either the split-off gaps Δ_β to exceedingly large value or the coupling with the CBs P_β to zero. We recompute the energy spectrum and SOC under each assumption, and plot the results in Fig. 4.3(d) with different colors. Notice that none of these bands contribute significantly to the hole SOC as all the curves lie almost on top of each other.

Next, we consider whether the SOC arises from the inversion asymmetry generated by the core-shell interface [60]. Specifically, we investigate whether the non-commutativity of the Kane parameters with momentum at the interface plays an important role. To test this, we set all Kane parameters (excluding the gaps) of InP to be identical to those of GaSb. Remarkably, the results depicted in grey in Fig. 4.3(d) reveal that the interfacial effects do not have a significant influence on the SOC of the GaSb hole bands.

These results lead us to conclude that the origin of the SOC is an inherent property of GaSb, rooted in the symmetry of the crystal structure of this tetravalent SM. Furthermore, as InP plays a negligible role, we can assume that the core serves as a generic wide band-gap insulator in our simulations, and that could be replaced by other insulator. Nevertheless, the particular chemical properties of the core are still relevant to determine the Fermi level within the hole bands of GaSb.

---

[3] Regarding w, the minimum thickness of 5 nm ensures that the shell can be grown with sufficient homogeneity, while we fix $w = R - 10$ nm for the maximum since the minimum core radius that is typically grown nowadays is approximately 10 nm. For R, although larger radii are certainly possible experimentally, the methodology that we employ to extract the value of α ceases to be valid for $R \gtrsim 50$ nm.

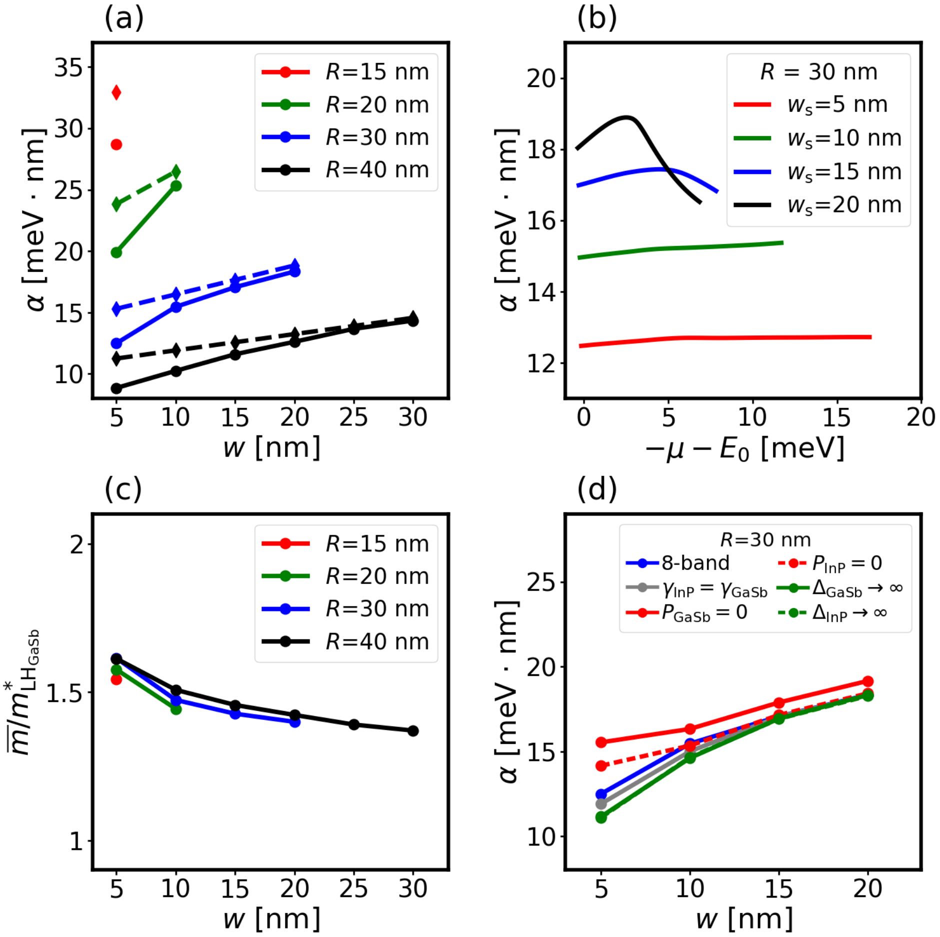

Figure 4.3: SOC of GaSb/InP tubular-core NWs. (a) SOC α of the highest-energy subband pair as a function of GaSb shell thickness w for different wire radii R, each represented by a different color. α decreases with R and increases with w. Solid lines corresponds to the 8-band model numerical results while dashed lines to results obtained analytically with Eq. (4.4). α decreases with R and increases with w. (b) α vs chemical potential of the wire ($-\mu$) for $R = 30$ nm and various w. The negative sign of $-\mu$ stems from the occupation of the VB. Notably, there is a weak dependence on doping and, consequently, on the electric field inside the nanostructure. (c) Harmonic mean effective mass $\bar{m}$ [see Eq. (B.4)] of the same subbands as in (a) divided the light-hole bulk effective mass of GaSb $m^*_{\text{LH}_{\text{GaSb}}} = m_0/(\gamma_1 + 2\gamma_2) = 0.0439 m_0$, being m_0 the free electron mass. $\bar{m}$ does not change substantially with w. (d) α vs shell thickness w for a core-shell NW of $R = 30$ nm, considering various scenarios: infinite split-off gaps for GaSb (solid green) or InP (dashed green), zero coupling between CBs and VBs for GaSb (solid red) or InP (dashed red), and identical Kane parameters (except for the gaps) for InP and for GaSb (grey). The results computed with the full 8-band model are also shown for comparison (blue). Other parameters as in the red curve of (a). The different curves lie almost on top of each other. This suggests an intrinsic origin of the SOC of the GaSb hole bands.

4.2.3. Effective Hamiltonian

Given the previous observations, it is justified to describe the NW through the Luttinger-Kohn (LK) Hamiltonian in axial approximation that only involves the two spinful LH and HH bands of GaSb,

$$H_{\mathsf{LK}} = \left(\gamma_1 + \frac{5}{2}\gamma_{\mathsf{s}}\right)\frac{p^2}{2m_0} - \frac{\gamma_{\mathsf{s}}}{m_0}\left(\boldsymbol{p}\cdot\boldsymbol{S}\right)^2 \,, \tag{4.1}$$

where $\boldsymbol{p} = -i\hbar\boldsymbol{\nabla}$ is the momentum operator, $\boldsymbol{S}$ is the vector of spin-3/2 matrices and γ_1 and $\gamma_s = (\gamma_2 + \gamma_3)/2$ are the Luttinger parameters of GaSb, while m_0 is the free electron mass. In App. B.3 we show that starting from H_{LK} it is possible to derive a 2×2 effective Hamiltonian that describes the the two highest-energy subbands, given by

$$H_{\mathsf{eff}} = \left(E_{\mathsf{mean}} + \frac{\hbar^2 k_z^2}{2\bar{m}}\right)\sigma_0 + \left(\frac{\delta E}{2} + \frac{\hbar^2 k_z^2}{2\widetilde{m}}\right)\sigma_z + \alpha_{\mathsf{eff}} k_z \sigma_y \,. \tag{4.2}$$

Here, σ_i are the standard Pauli matrices, E_{mean} is the mean energy of the two subbands, δE the subband splitting and $\bar{m}$ and $\widetilde{m}$ are the harmonic mean effective mass and its dispersion, respectively. Particularly, for the effective mass and the SOC we have

$$\bar{m} = \frac{2m_1 m_2}{m_1 + m_2}\,, \tag{4.3}$$

$$\alpha_{\mathsf{eff}} = \frac{\gamma_s}{m_0}\hbar^2\sqrt{3}\,\chi\left(\frac{1}{R} + \frac{w}{2R^2}\right)\,, \tag{4.4}$$

where m_i is the effective mass of each subband. In Eq. (4.4) χ is an overlap factor that depends on the degree of LH/HH hybridization of the two subbands.

To asses the validity of the effective Hamiltonian of Eq. (4.2) we compute α_{eff} analytically using Eq. (4.4) and tabulated values for γ_i and χ [126]. We show the results in Fig. 4.3(a) with dashed lines for comparison with the numerical results. Even though the agreement is not perfect, it is fairly good. This is important in light of the various approximations made to derive the effective Hamiltonian of Eq. (4.2). This attests the overall validity of the analytical approach.

Notice that, in accordance with our numerical 8-band model simulations, the effective SOC of Eq. (4.4) is independent of the electric field, decreases with R, and increases with w. Moreover, α_{eff} also increases with the degree of LH/HH hybridization χ, which is ultimately regulated by the degree of confinement of the wave function. This supports again that the origin of the SOC in this case is not an electric field, as it happens for the CB, but is rather an orbital effect imposed by the confinement of the wave function. In a cylinder, α_{eff} thus points towards the radial direction, along which the spatial symmetry is broken. This property is crucial in order to have a gapped topological superconducting phase, as shown in Ref. [166], and it naturally happens in our tubular-core NW. We note that in a conventional full-shell NW that leverages the properties of the conduction band, this is unlikely to happen as the electric field of the heterostructure forces the Rashba to point towards the core instead.

Since larger w provides larger SOCs, the reader might question the necessity of the InP core in our setup. There are three essential reasons that underline its importance. Firstly, an insulating core serves to mitigate the impact of disorder stemming from impurities introduced during the NW (core) growth process. Secondly, it's worth noting that, in contrast to the electrons in the CB, the band-bending typically observed in the SM at the SM/SC interface tends to push holes away from the interface, effectively suppressing the superconducting proximity effect. Consequently, an insulator becomes indispensable to counteract this effect, pushing the holes back toward the SC interface. Thirdly, a very thick shell can introduce CdGM states with different and unpredictable dispersions under the influence of a magnetic field. These states may reduce the size of the minigap and, what is more, have the potential to disrupt the topological superconducting phase. In Ref. [166], we show that this can be partially avoided as long as $w \lesssim 30$ nm.

4.3. Full-shell tubular-core NWs

4.3.1. Model

We now delve into the examination of the full-shell hybrid configuration. As explained in the introduction, when a SM with strong SOC is fully wrapped by a SC film, MZMs may emerge at the ends of the NW when subjected to a magnetic flux. To investigate this phenomenon, we study a system like the one depicted in Fig. 4.1, wherein the outer layer is now a SC inducing superconductivity through proximity effect. Following the methodology of Ref. [166], we describe the proximity effect through the incorporation of a self-energy term, stemming from the diffusive SC, into the effective Hamiltonian described by Eq. (4.2). For the SM, we use the values of α extracted in this work, and we set $m_1 = m_2 = 0.2\, m_0$. For the SC we use the parameters for Al, a commonly utilized material in conventional full-shell NWs. It is worth noting that achieving epitaxial growth of Al on GaSb may pose challenges due to significant lattice mismatch between the two materials. Alternatively, SCs like Sn [209, 210] or Nb [211, 212], which have been grown in other III-V compound SMs, posses lattice constants similar to GaSb with comparable superconducting gaps. Another strategy involves depositing a thin layer of an insulating ternary SM, such as InGaSb, between GaSb and Al, effectively assimilating lattice constants. This approach further helps to regulate the metallization effects. Since an exhaustive consideration of all interface intricacies is beyond the scope of this study, we explore the system's behavior with respect to the tunneling ratio Γ between the SC and the tubular SM. This constant is inherently tied to the transparency of the interface and the (normal) density of states of the SC.

From this Hamiltonian, we describe in Ref. [166] the extensive methodology used in order to extract key topological properties of the system. These include the local density of states (LDOS) at the end of the NW, the topological invariant, and the localization length of the MZMs. These three serve as key indicators for comprehending the extension and robustness of the topological superconducting phase.

4.3.2. Results

We focus our study on a NW with $R = 30$ nm, $w = 10$ nm and a thickness of the SC layer of $d = 10$ nm. This configuration ensures a robust SO coupling and a limited number of CdGM states. In Fig. 4.4(a), we present the topological phase diagram, depicting the dependence on two key parameters: the

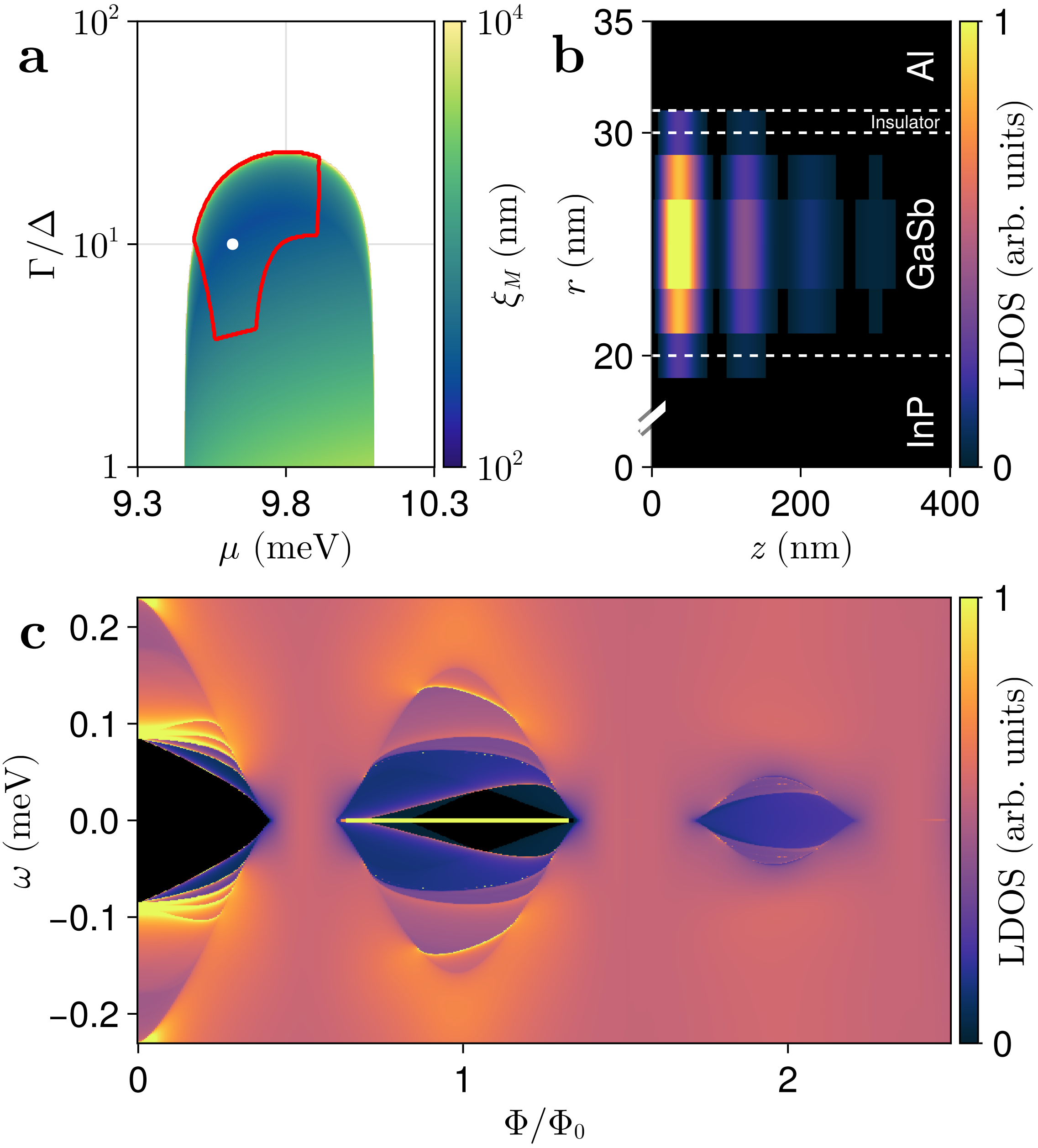

Figure 4.4: Topological properties of the full-shell tubular-core hybrid NW. (a) Topological phase diagram of the full-shell tubular-core NW as a function of the tunneling ratio Γ between the SC and the tubular SM (normalized to the parent gap Δ) and the chemical potential μ. The colored (white) area corresponds to the topological (trivial) region. The color scale represents the Majorana localization length $\xi_{\rm M}$. (b) LDOS at the end of a semi-infinite full-shell tubular-core NW along the longitudinal (z) and radial (r) directions, for the topological state identified with a white dot in (a). (c) LDOS for the same topological state as a function of energy ω and magnetic flux Φ (normalized to the superconducting flux quantum $\Phi_0 = h/2e$). Parameters: $R = 30$ nm, $w = 10$ nm, SC layer thickness $d = 10$ nm, $\Delta = 0.23$ meV, diffusive superconducting coherence length $\xi_{\rm d} = 70$ nm, g-factor of the NW $g = 2$, and $\alpha = 15$ meV·nm. Moreover, for (a) $\Phi = 0.71\Phi_0$; and for (b,c) $\mu = 9.62$ meV, $\Gamma/\Delta_0 = 10$ [marked in white in (a)]. For (b) $\Phi = 1.1\Phi_0$. We use a discretization constant of $a_0 = 2$ nm for these simulations. In (a) ξ_M is evaluated at $\Phi = 0.71\Phi_0$. In (b) $\Phi = 1.1\Phi_0$.

tunneling strength Γ, normalized to the parent superconducting gap $\Delta = 0.23$meV, and the chemical potential μ. The colored region indicates a non-trivial topological phase, with color encoding the Majorana localization length. We observe an extensive topological phase in parameter space, yielding Majorana zero modes MZMs for $\Gamma < 20\Delta$ and within a chemical potential range of $\Delta\mu \simeq 0.5$ meV. The Majorana localization length spans from 0.1 to 1 μm, indicating that a few μm-long NW should be sufficient to host truly zero-energy Majorana states. The red contour in Fig. 4.4(a) delineates the region with a genuine minigap where there are no CdGM states compromising the MZMs. This region constitutes 1/3 of the overall topological region.

For a deeper understanding of the measurable characteristics of the NW, we depict in Fig. 4.4(c) the LDOS at one of the wire's end vs energy ω and magnetic flux, for specific (Γ, μ) values corresponding to the white dot in panel (a). In the tunneling regime, a standard conductance measurement between a normal lead and the NW should be directly proportional to this LDOS. Notably, we observe the conventional Little-Parks oscillations of the superconducting gap as a function of magnetic flux, which is completely destroyed when the SC steps into a different quantized flux Φ_0. As expected, the zeroth-lobe exhibits no subgap states, while the first-lobe hosts a extended MZM with a sizeable topological minigap of 30 μeV. This magnitude surpasses typical thermal energies in experimental setups, rendering the topological state easily measurable. To complement this analysis, we show in Fig. 4.4(b) the LDOS along the longitudinal (z) and radial (r) directions of the NW, for the MZM state identified in (c). As expected, this state localizes predominantly at one end of the wire, exhibiting an exponential decay into the wire with some oscillations, together with a localization within the GaSb tubular SM, with a minor penetration into the SC Al layer.

4.4. Conclusions

In this chapter we have studied the VBs of tubular-core GaSb/InP NWs and their potential as a platform for topological superconducting phases, particularly in full-shell geometries where the NW is fully-covered by a SC shell. First, we have studied the strength and origin of the SOC in the tubular-core SM, a key attribute to sustain a topological superconducting phase as well as to provide long coherence times in some other qubit proposals. Our investigations unveiled that tubular-core GaSb/InP NWs boast a robust SOC, with values approximately around 20 meV·nm, that does not depend on the electric field or strain at the interface. These crucial features eliminate the necessity of tuning the electric field inside the NW or using ultra-thin NWs, what imposes severe device constrictions. In fact, we observe that the SOC in our tubular-core NWs increases with increasing shell thickness, as opposed to Ge/Si heterostructures, where strain plays the major role [200]. Although our simulations do not account for strain effects, we estimate in App. B.4 that they introduce a small deviation to the SOC of $\sim 20\%$ close to the GaSb/InP interface. Consequently, GaSb/InP heterostructures exhibit promising potential as a competitor of Ge/Si in the realm of SM qubits. Nevertheless, it's worth noting that other properties, such as the g-factor, warrant further exploration.

We have also uncovered that our hole-band tubular-core NWs demonstrate promise in hosting a topological superconducting phase when proximitized with a superconducting material. Unlike previous proposals reliant on the CB of III-V compound SMs, which suffer from reduced SOC in full-shell geometries [49], our GaSb/InP platform circumvents this limitation as it does not depend on the electric field. Additionally, the insulating nature of the InP core serves to mitigate the impact of disorder stemming from impurities introduced during the NW growth process. It also counters band-bending effects that tend to expel holes from the SC interface, thereby enhancing the proximity effect. And in addition, the thin thickness of the tubular GaSb SM ensures that no CdGM states spoil the topological phase, thus providing a true topological minigap [166]. We obtain MZMs for extended regions in parameter space, providing typical minigaps of $30\ \mu$eV.

We have explored several materials and NW geometries, although not all are presented in this context. Our investigations indicate that combinations such as GaSb/InP or GaAsSb/GaSb are promising, as they likely position the Fermi level close to the VB edge while maintaining the insulating nature of the core. In terms of geometry, we observe that nanowires with a radius R not exceeding 40 nm and a SM shell thickness w smaller than 15 nm, consistently exhibit the most favorable topological minigaps and more extended topological phases. These material choices and geometries are deemed realistic and hold significant potential for practical implementation. However, it is crucial to acknowledge that a more in-depth investigation is essential concerning the SC/SM interface. While it is evident that a SC, be it Al or Sn, can be epitaxially grown on top of GaSb (or GaAsSb) to induce superconductivity, the specific details of this proximity effect on the VBs of the SM remain unclear. This aspect demands a more thorough analysis in future research that necessarily needs from experimental support, being beyond the scope of this work and opening a new venue of research.

5

A Weyl semimetal state in inverted gap semiconductor nanowires induced by an electric field

This chapter deals with the hybridization gap in InAs-GaSb core-shell nanowires, an inverted gap system. First, we develop a self-consistent prediction of the low-energy states of these nanowires, including the charge transfer between the layers. Then, we study the behaviour of the hybridization gap in the presence of a transverse electric field. We identify a new semi-metal state with Weyl dispersion which can be switched by the electric field. Using a laterally confined Bernevig-Hughes-Zhang model describing a four-band, low-energy Hamiltonian, we connect the observed reentrant semi-metal transition with the topological transition in inverted gap quantum wells and we investigate the behaviour and fate of localized end states at both extrema of a long, but finite wire with respect to the applied electric field and disorder.

5.1. Introduction

Topological insulators (TI) in quantum wells (QWs) represent a cutting-edge frontier, where the interplay of topology and quantum mechanics has the potential for revolutionizing electronics and quantum computing [213, 214]. At their core, they are quasi-2D materials characterized by an insulating interior and conductive one-dimensional states at the edges of the sample. Such spin-momentum locked states are ”protected” from scattering from disorder or defects, if time-reversal symmetry is preserved, leading to extraordinary robustness in electron spin transport, a phenomenon termed Quantum Spin Hall (QSH) effect [215]. In other words, in a TI phase, *helical* modes [216] appear at the edges of the 2D sample, characterized by spin-up traveling in one direction and the spin-down traveling in the opposite direction without back-scattering as long as time-reversal symmetry is preserved. However, if a scattering potential that breaks time-reversal symmetry, as for example the one generated by a magnetic impurity, is present, back-scattering becomes possible and deviations from perfect transmission are observed in experiments [217, 218].

The QSH insulator was first theoretically predicted in 2006 by Bernevig, Hughes, and Zhang [50] and experimentally observed [51] in HgTe/CdTe QWs. Here, the unusual inverted ordering with conduction s-states laying below valence p-states leads to a topologically non-trivial semi-metal state. Transition to the normal insulating states, i.e. with normal ordering of conduction and valence states, takes place when HgTe is sandwiched between CdTe layers, which is a normal insulator, when the thickness of the QW falls below $\sim$6 nm and the quantum confinement shifts s-states above p-states, i.e. to the normal ordering. In other words, quantum confinement allows to fine-tune the gap in order to trigger the topological transition. A further proposal for the QSH state includes ”broken-gap” type-II InAs/GaSb/AlSb QWs [219]. Also in this case the topological phase is due to the inverted alignment of the valence and conduction bands of the two materials, with the GaSb valence band lying above the InAs conduction band. Similarly to HgTe-CdTe QWs, quantum confinement may induce a transition to a normal ordering and to a normal insulator, but in contrast to HgTe-CdTe QWs, in InAs/GaSb QWs electrons and holes are hosted in different layers, and the band inversion can be easily tuned by external gate fields [52].

Nanowires (NWs) have also been investigated in the search for topological states and proposed as building blocks for topological quantum gates, e.g. in superconductor proximitized nanostructures [220, 144, 221] (see Ch. 4). Based on the topological properties in the corresponding QW structures, InAs-GaSb core-shell NWs (CSNWs) represent an attracting system for the study of topological states of matter in 1D. The electronic structure and the effective gap of InAs-GaSb CSNWs have been studied using the cylindrical approximation [114] as well as the more realistic hexagonal section [222], as a function of the structural parameters of the system, such as core radius and shell thickness. For a fixed core radius, a band-inverted fundamental gap exists in a finite range of intermediate shell thicknesses, with maximum values around $\sim$3.5 meV. This naturally raises the question about the possible realization of a one-dimensional TI phase in these wires.

In principle, this is excluded by the low symmetry of the system. InAs-GaSb CSNWs, as well as 2D InAs-GaSb QWs, belong to the symmetry class AII [223]. Systems in this symmetry class obey time-reversal symmetry, with $\mathcal{T}^2 = -1$, being $\mathcal{T}$ the time reversal operator, but not particle-hole or chiral symmetry, with $\mathcal{P}$ and $\mathcal{C}$ being the corresponding anti-unitary operators, respectively. The symmetry class AII for dimensionality D=2 is characterized by a $\mathbb{Z}_2$ topological invariant, which describes 2D QSH insulators as HgTe-CdTe and InAs-GaSb QW. However, the class AII lacks a topological phase in 1D, rendering, in principle, InAs-GaSb CSNWs topologically trivial.

However, let us consider an ideal, band-inverted InAs-GaSb CSNW where the lowest energy conduction subband and the highest energy valence subband, i.e. the ones forming the inverted hybridization gap, have the same band dispersion shape (but opposite curvature, obviously). In such an ideal system the existence of the 1D topological state could be possible, as both time-reversal and particle-hole symmetries are present [222]. In fact, such system would be either in the symmetry class CII ($\mathcal{P}^2$ = -1) or DIII ($\mathcal{P}^2$ = 1), with $2\mathbb{Z}$ and $\mathbb{Z}_2$ topological invariants in one dimension, respectively [223]. In a real CSNW, particle-hole symmetry is normally broken, due to the complexity of the band structures in the materials. For example, electrons and holes have different effective masses even in bulk semiconductors. Additionally, in nanostructures, the spin splitting induced by a structure inversion asymmetry of the confining potential—originating from, for instance, an external electric field—differs for electrons and holes [224]. However, if this symmetry breaking is sufficiently small, it could be considered as a perturbation and the system could display a 1D topological phase as long as the hybridization gap remains finite [222].

Indeed, it was theoretically predicted in Ref. [225] that finite-length, InAs-GaSb CSNW can host localized states at the wire extremes, even if these so called end states were shown to be not topologically protected against a time-reversal symmetry preserving potential axial disorder in a model cylindrical CSNW.

Here, we investigate the electronic structure of InAs-GaSb CSNWs using a self-consistent, 8-band $\mathbf{k}\cdot\mathbf{p}$ approach (see Ch. 2) which takes full account of the symmetry and crystallographic directions of the nano-crystal and external electric fields. We are particularly interested in the fundamental band gap of the system, the hybridization gap which results from the anticrossing of the inverted electron and hole subbands. To make our calculation, in Sec. 5.2 we first discuss the charge transfer effects in InAs-GaSb CSNWs. To include such self-consistent effects we extended and implemented previously proposed approaches in the context of InAs-GaSb QWs, exposing the substantial effect of the corresponding built-in electric field on the fundamental band gap of the system, which were neglected in previous investigations [116].

In Sec. 5.3 we consider InAs-GaSb CSNWs with a transverse electric field. The combined effect of a symmetry-breaking external field $E_\perp$ and the spin-orbit interaction (SOI) in the valence band of the semiconductors removes the spin-degeneracy of the energy subbands, a phenomenon commonly referred to as structural inversion asymmetry (SIA) spin splitting [206]. Starting from a CSNW with with a slightly inverted ordering of the first electron and hole subbands, we find that $E_\perp$ can induce a Dirac-like dispersion of two spin-polarized subbands, with vanishing mass at a critical electric field $\widetilde{E}_\perp$. At this field the fundamental gap of the NW vanishes at a large system-dependent wave vector k_0, and the system passes through a semimetallic phase with Weyl dispersion and weakly broken electron-hole symmetry. When the electric field is further increased beyond $\widetilde{E}_\perp$ the gap opens again, and the system returns to a semiconducting phase.

To understand the nature of the semimetallic transitions, in Sec. 5.4 we use the Bernevig, Hughes, and Zhang (BHZ) 2D model Hamiltonian first introduced in Ref. [50] to describe the QSH phase in HgTe-CdTe QWs, and we obtain an effective Hamiltonian that reproduces the low-energy spectrum of the CSNW in the vicinity of the field-induced Dirac point. Using this low-energy theory, we elucidate that the crossing of the two subbands arises due to a compensation between the Rashba SOI, modulated by the electric field, and the $\mathbf{k}\cdot\mathbf{p}$ electron-hole interaction.

Finally, we investigate finite-length CSNWs. We show that localized end states form and survive in presence of the electric field up to the critical value $\widetilde{E}_\perp$, where the fundamental gap closes. As the field is increased beyond $\widetilde{E}_\perp$ the end states disappear, merging into the electron and hole subbands which, at the same time, return to normal ordering. Hence, the semimetal transition is interpreted as an electric field induced transition between topologically different phases. We also investigate the stability of these states against potential disorder along the axial direction and asymmetric electron-hole Rashba couplings.

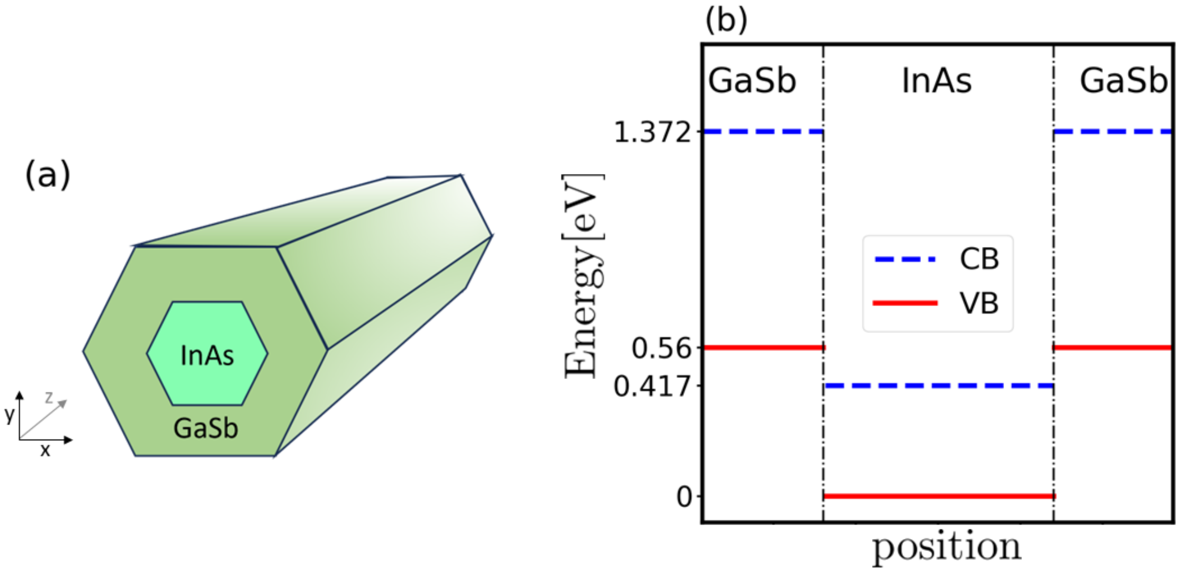

Figure 5.1: Broken-gap InAs-GaSb nanowires.(a) Sketch of the simulated hexagonal InAs-GaSb CSNW. (b) Bulk conduction band (CB, dashed blue line) and valence band (VB, full red line) profiles of InAs-GaSb heterostructures. The InAs lowest conduction band falls approximately 0.14 eV below the topmost valence band of GaSb, a band alignment usually referred to as type-II broken-gap.

5.2. Self-consistent effects in broken-gap nanowires

In Fig. 5.1(a) we sketch an InAs-GaSb CSNW grown along the [111] crystallographic axis. As already mentioned in Ch. 1, InAs/GaSb interfaces form a type-II broken-gap band alignment, that is, the conduction band edge of one bulk material falls below the highest valence band of the adjacent layer.

In particular, as shown in Fig. 5.1(b), the InAs conduction band edge is $\sim$ 0.14 eV below the GaSb valence band edge. This results in a significant coupling between conduction bands pointing upward and valence bands pointing downward, and results in a gap opening at a finite wave vector, the so-called hybridization gap. This is fully taken into account by the use of our 8-band $\mathbf{k}\cdot\mathbf{p}$ approach (see Ch. 2), which includes the lowest energy Γ_6 conduction bands, as well as the top-most Γ_8 and Γ_7 valence states.

Similarly to QW systems, in a CSNW of appropriate geometrical parameters quantum confinement can raise the lowest electron subband edge e_0 above the highest hole subband edge h_0, restoring the conventional subbands alignment of a trivial insulator. This situation is depicted in Fig. 5.2(a). In this scenario, the effective band gap $E_g = e_0 - h_0$ occurs at the Γ point. In InAs-GaSb CSNWs this situation happens for small values of core radius R_c and shell thickness w (typically R_c, $w < 5$ nm).

For larger R_c and w confinement energies are lowered, and the positions of e_0 and h_0 are reversed, as depicted in in Fig. 5.2(b). Here, the subband extrema e_0 and h_0 are exchanged, and the effective band gap occurs at $k_z \neq 0$. Furthermore, we expect a spontaneous charge transfer from one material to the other to occur when the chemical potential is within the effective gap, as required by the charge neutrality condition. This concept is again schematically represented in Fig. 5.2(b): filled blue circles and red open circles indicate occupied electron states and unoccupied hole states, respectively. The former create negative charge contributions, while the latter create positive charge con-

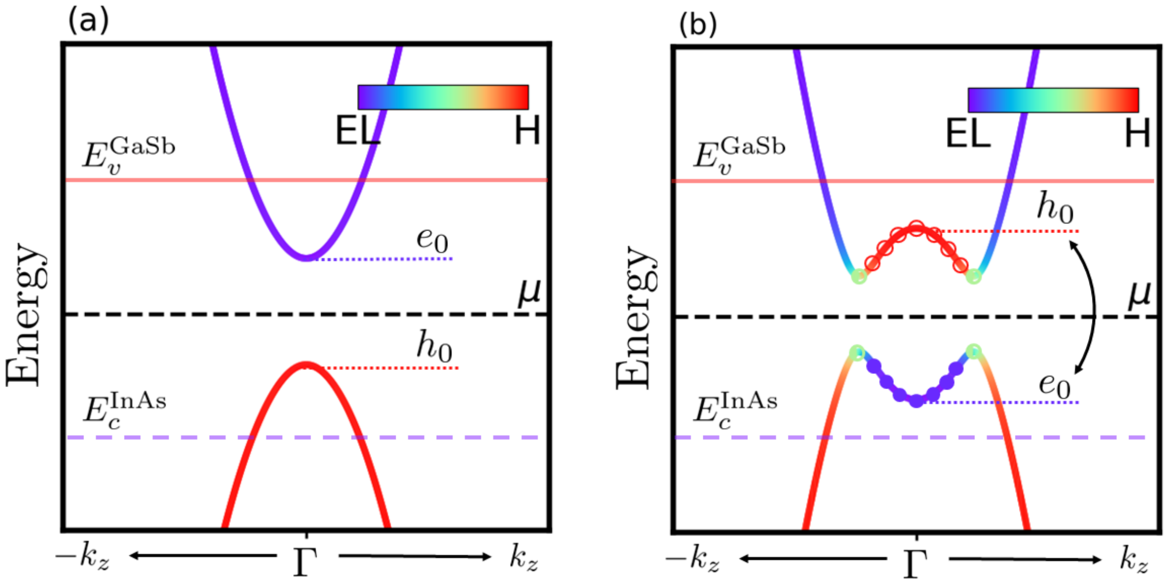

Figure 5.2: Schematic band structure of InAs-GaSb core-shell nanowires. (a) Typical band structure of InAs-GaSb CSNW in the normal semiconducting regime. The color coded EL/H character is calculated according to Eqs. (5.1),(5.2). Even if the (bulk) InAs conduction band (dashed, light-blue line) lies below the (bulk) GaSb valence band (dashed, red line), the lowest electron subband edge (e_0) and the highest hole subband edge (h_0) follow the conventional ordering of semiconducting materials due to a strong quantum confinement imposed in CSNWs with sufficiently small core radii and shell thicknesses. In this regime, if the chemical potential μ lies within the gap no charge transfer occurs at zero temperature. Furthermore, electron-hole hybridization is negligible, as shown by the almost pure spinorial character of the subbands, encoded in the colorbar. (b) Typical band structure of InAs-GaSb CSNW in the inverted regime. For larger structural parameters, quantum confinement is lowered, causing e_0 and h_0 to invert with respect to panel (a). Because of electron-hole kinetic interactions an hybridization gap opens. When the chemical potential lies within the this gap, contrary to panel (a), charge transfer between the InAs and the GaSb region occurs. States of the e_0 subband (blue dots) contribute with a negative charge density within the InAs region, while the states of the h_0 subband (red circles) contribute with a positive charge density within the GaSb region. States located at the anticrossings between the two subbands (green circles), as a result of electron-hole hybridization, are expected to contribute to the negative as well as to the positive charge density in the respective regions.

tributions. Since the electron states originate from the InAs conduction bands, a negative charge density is expected to form within the core of the NW. On the contrary, since hole states originate from the GaSb valence bands, a positive charge density is likely to form within the shell of the NW. As a result of the charge transfer between different layers, band bending in both layers takes place, affecting the electronic structure of the system.

What about the green, half-filled dots in Fig. 5.2(b)? As the color refers to the bulk electron or hole character of the wave-function, these are strongly hybridized states, and form the extrema of the effective band gap, which is usually referred to as the hybridization gap. Thus, we expect those states to have non-zero probability density in both the core and the shell of the NW, and to contribute with both positive and negative charge density distributions.

While for purely electron and hole states (filled blue dots and open red circles) we can in principle use Eqs. (2.75) and (2.76) to evaluate the charge density contributions, the case of overlapping hole and electron states (green half filled dots) is more difficult to deal with, as it is not possible to occupy independently electron and hole states as prescribed by the multi-band envelope function approach (EFA).

Self-consistent electronic structure calculations exist for InAs-GaSb, broken-gap QWs and 2D superlattices. In Ref. [226] the authors employ a single-band approach, which neglects the **k** · **p** coupling between conduction and valence bands and therefore circumvents any ambiguity in the definition of the charge densities. Typical self-consistent multi-band models only considered narrow layer widths, where the standard prescription for the calculation of the charge density still applies [227]. For situations where the standard multiband EFA fails, a self-consistent multi-band approach was used for the first time in Ref. [228]. In that paper, the proposed method is to occupy only certain components of the electronic states, according to their bulk spinorial character. In a more recent work [229], a self-consistent 8-band **k** · **p** model has been used to study the semimetal–semiconductor transition in InAs-GaSb QWs under external electric fields, even if the details of the method used to evaluate the charge density are not explicitly specified. Remarkably, from the paper, one can infer that the electron and hole densities are computed separately.

A conceptually different technique has been instead proposed in Ref. [230], under the name of ”full-band” EFA. Here the classification into electron and hole states is avoided and the charge density is evaluated within the electron picture. The authors apply their method to the calculation of optical transition energies of intrinsic InAs-GaSb superlattices in a band inverted regime, and found good agreement with experimental data. The main limitation for the extension of this method to NWs is that one is forced to compute the entire spectrum of the Hamiltonian. For an 8-band model and a typical real space discretization on the order of 10^3 nodes one has to compute *all* the eigenvalues and eigenvectors of a matrix of dimension $10^4 \times 10^4$, a computationally prohibitive task for a direct diagonalization method [1].

In this work we designed an *ad-hoc* method for the evaluation of the charge density in broken-gap NWs, properly aimed to reproduce the expected charge transfer effects in inverted-gap situations as in Fig. 5.2(b). Our method is very close to the ones used in Refs. [228] and [229], in the sense that it calculates the positive and negative charge density contributions separately. Furthermore, being a

---

[1] Note that the use of direct diagonalization methods does not take advantage of the sparsity structure of the matrices generated by the real space discretization with FEM.

modified EFA, it only involves the calculation of a reduced number lowest energy eigenstates around the chemical potential, and not the entire spectrum.

First, we define the electron EL and hole H character of each state from

$$\mathsf{EL} = \int \mathrm{d}\boldsymbol{r}_\perp \sum_\mu |\psi_\mu(\boldsymbol{r}_\perp)|^2 \Theta_{\mathsf{InAs}}(\boldsymbol{r}_\perp)\,, \tag{5.1}$$

$$\mathsf{H} = \int \mathrm{d}\boldsymbol{r}_\perp \sum_\mu |\psi_\mu(\boldsymbol{r}_\perp)|^2 \Theta_{\mathsf{GaSb}}(\boldsymbol{r}_\perp)\,, \tag{5.2}$$

where the Heaviside Θ functions are

$$\Theta_{\mathsf{InAs}}(\boldsymbol{r}_\perp) = \begin{cases} 1 & if \quad \boldsymbol{r}_\perp \in \text{InAs core} \\ 0 & if \quad \text{otherwise} \end{cases}\,, \tag{5.3}$$

$$\Theta_{\mathsf{GaSb}}(\boldsymbol{r}_\perp) = \begin{cases} 1 & if \quad \boldsymbol{r}_\perp \in \text{GaSb shell} \\ 0 & if \quad \text{otherwise} \end{cases}\,. \tag{5.4}$$

These numbers can be evaluated for each subband s and for each wave-vector k_z.

The total charge density can be written as[2]

$$\rho(\boldsymbol{r}_\perp) = e \sum_{s \in \text{subbands}} \int_{-k_M}^{k_M} \frac{dk}{2\pi} \left(-n_s(\boldsymbol{r}_\perp, k_z) + p_s(\boldsymbol{r}_\perp, k_z)\right) \tag{5.5}$$

To calculate n_s and p_s, we define two character ”threshold” values, $\mathsf{EL}_{\mathsf{min}} \in [0,1]$ and $\mathsf{H}_{\mathsf{min}} \in [0,1]$, and we compute the negative charge in the NW according to the following rule:

$$n_s(\boldsymbol{r}_\perp, k_z) = \begin{cases} n_s^{\mathsf{EFA}}(\boldsymbol{r}_\perp, k) & if \quad \mathsf{EL} > \mathsf{EL}_{\mathsf{min}} \\ n_s^{\mathsf{MEFA}}(\boldsymbol{r}_\perp, k) & if \quad (\mathsf{EL} < \mathsf{EL}_{\mathsf{min}} \quad \text{and} \quad \mathsf{H} < \mathsf{H}_{\mathsf{min}}) \end{cases}\,, \tag{5.6}$$

where n_s^{EFA} refers to the standard EFA for the conduction band

$$n_s^{\mathsf{EFA}}(\boldsymbol{r}_\perp, k) = \sum_\mu f(E_s(k), \mu, T)\, |\psi_\mu^s(\boldsymbol{r}_\perp, k)|^2, \tag{5.7}$$

and n_s^{MEFA} refers to a modified EFA for the conduction band

$$n_s^{\mathsf{MEFA}}(\boldsymbol{r}_\perp, k) = \sum_\mu f(E_s(k), \mu, T)\, |\psi_\mu^s(\boldsymbol{r}_\perp, k)|^2 \Theta_{\mathsf{InAs}}(\boldsymbol{r}_\perp)\,. \tag{5.8}$$

Analogous equations hold for the positive charge density. Explicitly, we have

$$p_s(\boldsymbol{r}_\perp, k_z) = \begin{cases} p_s^{\mathsf{EFA}}(\boldsymbol{r}_\perp, k) & if \quad \mathsf{H} > \mathsf{H}_{\mathsf{min}} \\ p_s^{\mathsf{MEFA}}(\boldsymbol{r}_\perp, k) & if \quad (\mathsf{H} < \mathsf{H}_{\mathsf{min}} \quad \text{and} \quad \mathsf{EL} < \mathsf{EL}_{\mathsf{min}}) \end{cases}\,, \tag{5.9}$$

---

[2] In this chapter we refer for convenience to the free electron and hole concentrations using the symbols n and p, respectively, instead of the symbol n_e and n_h used to refer to the same quantities in Chs. 2 and 3.

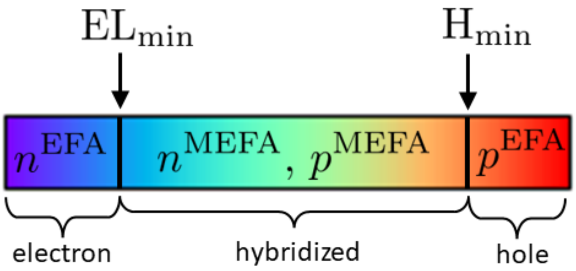

Figure 5.3: Modified EFA approach. Schematic visualization of the approach used in this work to calculate the charge densities of electrons and holes in inverted-gap InAs-GaSb CSNWs. Basically, each one of the calculated electronic states is assigned to either the "electron", "hybridized" or "hole" class according to its spinorial character. States whose character is above (below) the threshold character $\mathrm{EL}_{\mathrm{min}}$ ($\mathrm{H}_{\mathrm{min}}$) are classified as "electron" ("hole") and the corresponding charge density is evaluated using the standard EFA approach. Otherwise, the state occupation is evaluated using the modified EFA approach: the part of the wave function that overlaps with the InAs (GaSb) region contributes to the negative (positive) charge according the the standard EFA approach. Note that states that belong to the "hybridized" class can contribute with a charge density of both signs.

where p_s^{EFA} refers to the standard EFA approach for the valence band,

$$p_s^{\mathrm{EFA}}(\boldsymbol{r}_\perp, k) = \sum_\mu (1 - f(E_s(k), \mu, T))\ |\psi_\mu^s(\boldsymbol{r}_\perp, k)|^2, \tag{5.10}$$

and p_s^{MEFA} refers to a modified EFA approach for the valence band

$$p_s^{\mathrm{MEFA}}(\boldsymbol{r}_\perp, k) = \sum_\mu (1 - f(E_s(k), \mu, T))\ |\psi_\mu^s(\boldsymbol{r}_\perp, k)|^2 \Theta_{\mathrm{GaSb}}(\boldsymbol{r}_\perp). \tag{5.11}$$

Figure 5.3 aims at clarifying schematically our modified EFA. The two threshold values are used to select between the standard EFA and the modified one. If the electron character EL, Eq. (5.1), is larger than $\mathrm{EL}_{\mathrm{min}}$ the standard EFA for the conduction band in Eq. (5.7) is used to compute the negative charge contribution. Otherwise, if $\mathrm{EL}<\mathrm{EL}_{\mathrm{min}}$ and $\mathrm{H}>\mathrm{H}_{\mathrm{min}}$ only the InAs layer contributes to the negative charge [see Eq. (5.8)]. For the positive charge contribution an analogous approach follows. If the hole character H, Eq. (5.2) is larger than $\mathrm{H}_{\mathrm{min}}$ the standard EFA approach in Eq. (5.10) for the valence band is used to compute the positive charge contribution. Otherwise, if $\mathrm{H}<\mathrm{H}_{\mathrm{min}}$ and $\mathrm{EL}>\mathrm{EL}_{\mathrm{min}}$ only the GaSB layer contributes to the positive charge [see Eq. (5.11)].

In practice, we assign each state to one of the three regions outlined in Fig. (5.3), namely "electron", "hole" or "hybridized". States that belong to the "electron" and "hole" classes contribute to the negative and positive charge respectively in both layers. States that belong to the "hybridized" class, contribute to both the negative charge (only within the InAs layer) and the positive charge (only within the GaSb layer). For example, half-filled green dots in Fig. 5.2(b) belong to the "hybridized" class. Those that are above the chemical potential, will contribute to the positive charge in the GaSb layer through the hole component of the probability density. On the other hand, those below the chemical potential, will contribute to the negative charge in the InAs layer through the electron component of the probability density.

It seems natural to ask why we don't simply take all states to fall into the "hybridized" class and add the corresponding charge according to their H or EL character. The answer is that, although energetically the states well above or well below the band-inverted gap are naturally regarded as pure conduction band and pure valence band states, respectively, in the 8-band $\mathbf{k}\cdot\mathbf{p}$ approach

Table 5.1: Material parameters used in the 8-band k·p model at temperature $T = 4$ K for InAs-GaSb CSNWs. The energy gap E_g, the conduction and valence band offsets ΔE_c and ΔE_v at the InAs-GaSb interface, the split-off energy Δ_{so}, the Kane energy E_p, the conduction electron effective mass m_e and the bare Luttinger parameters γ_i are taken from Ref. [126]. E_p^{rsc} is the rescaled Kane energy Eq. (2.56) and $\tilde{\gamma}_i$ are the modified values Eq. (2.53). ϵ_r refers to the relative dielectric constant of each material. EL_{min} and H_{min} are the threshold values introduced in our modified EFA approach, and have been heuristically determined using insights from the numerical simulations of the specific nanostructure.

	InAs		GaSb
E_g [eV]	0.417		0.812
ΔE_c [eV]		0.955	
ΔE_v [eV]		0.56	
Δ_{so} [eV]	0.39		0.76
E_p / E_p^{rsc} [eV]	21.5 / 19.1		27 / 24.8
m_e	0.026		0.039
γ_1 / $\tilde{\gamma}_1$	20 / 4.7		13.4 / 3.2
γ_2 / $\tilde{\gamma}_2$	8.5 / 0.86		4.7 / -0.39
γ_3 / $\tilde{\gamma}_3$	9.2 / 1.6		6.0 / 0.9
ϵ_r	15.5		15.7
EL_{min}		0.8	
H_{min}		0.95	

they always carry some degree of electron-hole hybridization, even at large wave vectors k_z [222]. In particular, the EL character never converges to one, for increasing k_z. Therefore, calculating the charge according to the EL or H character would run into convergence issues. For example we would have negative charge contributions from states deeply located in the valence band, or positive charge contributions from states deeply located in the conduction band. Apart from being an unphysical result, this would force us to take into account also eigenstates that are very far away from the chemical potential.

We now use this self-consistent $\mathbf{k}\cdot\mathbf{p}$ protocol to study the band structure of free-standing InAs-GaSb CSNWs. The band parameters are reported in Tab.5.1. The position of the Fermi level is determined by charge neutrality condition $n = p$. We used pure Neumann boundary conditions (BCs) for the Poisson equation (see Sec. 2.4.1) in order to set the electric field to zero at the outer surface of the wire.

In Fig. 5.4(a) we show the two-dimensional map of the charge density of an InAs-GaSb CSNW with core radius $R_c = 7$ nm and shell width $w = 7.32$ nm calculated using our self-consistent protocol: a hole gas is formed in the shell, mostly originating from the GaSb valence band states, while an electron gas, originating from the InAs conduction band states, is found within the core.

The calculated charge density distribution can be explained qualitatively by considering the character of the calculated subbands in Fig. 5.4(a). Here, the color corresponds to the electron or hole character, according to Eqs. (5.1) and (5.2). As expected, the system is in an inverted regime [as in Fig. 5.2(b)], with three valence subbands above the lowest electron subband subband. The main contribution to the positive charge density in the GaSb shell comes from hole states above the chemical potential, here labelled with open red circles in the first subband. On the other hand, the negative charge in the InAs core mostly comes from the occupied electron states in the fourth subband, here indicated with filled blue dots. Furthermore, hybridized states, as for example the states in the second subband indicated with circles, contribute to the charge density of both layers. The states that are not indicated with dots, do not contribute significantly to the charge density. For ex-

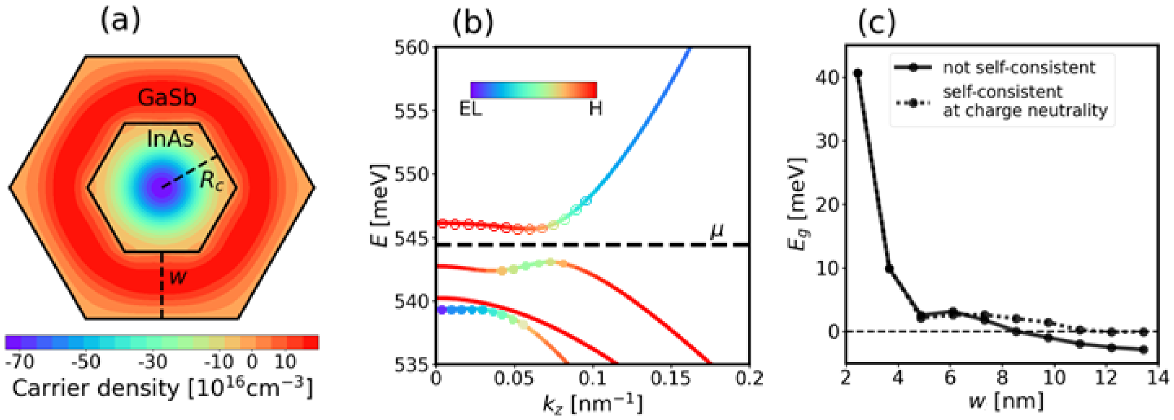

Figure 5.4: Self-consistent band structure of broken-gap, InAs-GaSb nanowires. (a) Charge density of an InAs-GaSb CSNW with InAs core radius $R_c = 7$ nm and GaSb shell thickness $w = 7.32$ nm at charge neutrality, obtained using our self-consistent, modified EFA approach. Our method correctly yields a positive charge density in the GaSb shell and a negative charge distribution in the InAs core. (b) Electronic structure corresponding to panel (a). The color refers the electron (EL) or hole (H) character of the different subband states, calculated from the wave function localization in the InAs and GaSb layer, respectively [see Eqs. (5.1) and (5.2)]. States indicated with dots are those contributing to the charge density in panel (a): occupied electron states in the fourth subband (filled blue dots) participate to the negative charge density, while unoccupied hole states in the first subband (red circles) participate to the positive charge distribution. Furthermore, states in the second subband between $k_z = 0.05$ and 0.1 nm^{-1} (green dots) contribute to the charge distribution in both materials. The position of the Fermi level is determined by the charge neutrality condition. (c) Effective energy gap E_g of a CSNW with $R_c = 7$ nm for different values of the GaSb shell thickness w with (dashed line) and without (full line) including self-consistent effects, at charge neutrality.

ample, the states in the first subband for $k_z > 0.1$ nm^{-1} fall within the "electron" class according to their spinorial character. As a consequence, these states are occupied using Eq. (5.7), which rapidly goes to zero after a few k_bT away from the chemical potential μ, as dictated by the Fermi distribution function $f(E, \mu, T)$. The same is true for electron states found at higher energy, not shown in Fig. 5.2(b). A perfectly analogous reasoning holds for hole states.

Systematic studies of the effective band gap of InAs-GaSb NWs as a function of the structural parameters have been performed for both cylindrical [114] and hexagonal geometries [222] using 8-band models. However, up to now, the influence of charge transfer and self-consistent effects in InAs-GaSb NW has been neglected in the literature. In Fig. 5.4(c) we consider a NW with $R_c = 7$ nm and we calculate the effective energy gap E_g of the system as a function of the shell width w, In particular, we compare the results obtained with and without the inclusion of charge transfer effects. The self-consistent calculations are indicated with a dashed black line, while the full black line is obtained neglecting charge transfer effects. For small values of w, being the system in the normal semiconducting regime [Fig. 5.2(a)], charge transfer does not occur, and the two curves are superimposed [3]. However, starting from $w \sim 6$ nm, the self-consistent result departs from the non-self-consistent one, as charge transfer starts to play a role. In particular, when a charge distribution is present inside the wire, band bending is expected to occur and to influence the band structure and the effective energy gap. Importantly, for experimentally achievable structures with $w > 8.32$ nm, the non self-consistent model predicts a semimetallic phase ($E_g < 0$) where the self-consistent model predicts a semiconducting behaviour ($E_g > 0$).

---

[3] Note that in the normal regime no charge is present in the system according to the standard EFA. Thus, we also have a proof that in the normal regime our modified EFA gives the same results as the standard EFA.

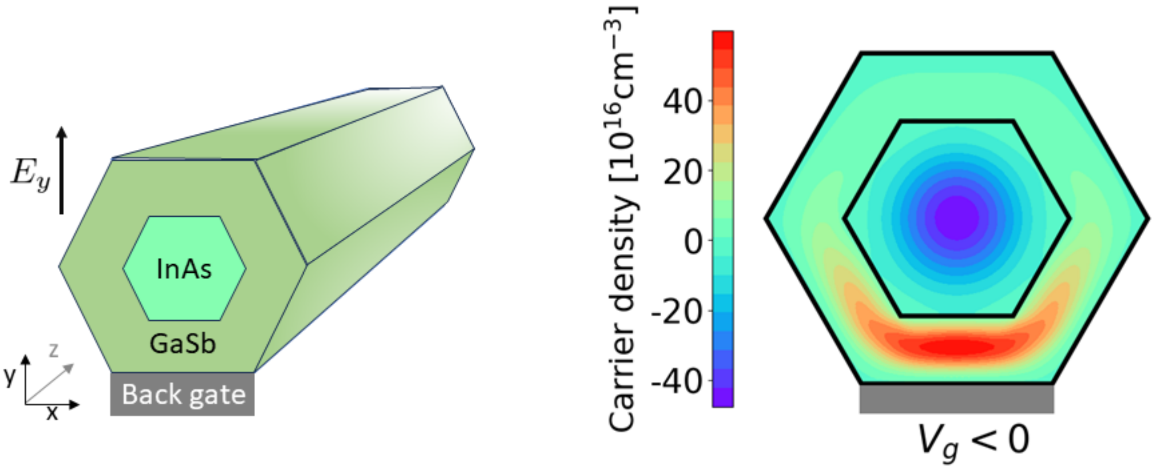

Figure 5.5: Transverse electric field. Sketch of the simulated InAs-GaSb CSNW. A back-gate located below the NW induces a transverse electric field directed along the y-direction. The chemical potential is assumed to be fixed by a second gate attached to the NW, and is a free parameter in our simulations. (b) Typical charge density distribution in the nanodevice for a negative back gate potential $V_g < 0$, obtained using our self-consistent approach. This situation is modeled by a positive electric field in the y-direction $E_y > 0$ in the simulations. Holes are attracted to the bottom edge of the NW hexagonal cross section. In principle, electrons are pushed in the opposite direction, even if hardly visible from the figure. The electrostatic potential is fixed to zero at the bottom edge of the wire, while Neumann BCs are used for the remaining five edges. Parameters: $R_c = 7$ nm, $w = 4.88$ nm, $\mu = 539.14$ eV, $E_y = 1.285$ V/μm.

5.3. Effects of a transverse electric field

We now consider InAs-GaSb CSNWs in the presence of a transverse electric field. We assume a constant electric field E_y directed along the y-direction, as schematically depicted in Fig. 5.5(a). Furthermore, we fix the potential to zero at the bottom edge of the wire and impose Neumann BCs for the remaining edges. This configuration intends to reproduce the effects of a back gate voltage V_g placed below the NW. We will assume that the chemical potential can be tuned by a second gate connected to the NW. In Fig. 5.5(b) we show a typical, calculated charge density map in inverted-gap, InAs-GaSb CSNW when $V_g < 0$, a situation which we simulate using $E_y > 0$. In this case, holes are attracted towards the bottom edge of the hexagonal section. Electrons, having opposite charge with respect to holes, are weakly pushed towards the top edge.

In Fig. 5.6 we show the band structure for a NW with with $R_c = 7$ nm, $w = 4.88$ nm, $\mu = 539.14$ eV and $E_y = 1$ V/μm. The CSNW parameters are chosen so to realize a slightly inverted gap, with only one electron-like subband below one hole-like subband. The subbands are degenerate at $k_z = 0$ due to time-reversal symmetry. The size of the arrows in Fig. 5.6 is proportional to the modulus $|S_x|$ of the x-component of the vector spin operator $\hat{\boldsymbol{S}}$, that we evaluate as $S_x = \langle\Psi|\hat{S}_x|\Psi\rangle$ as a function of the wave vector k_z for each subband eigenstate $|\Psi\rangle$. Upwords (downwards) pointing arrows indicates a positive (negative) sign of S_x. At $k_z \neq 0$ each subband splits in two subbands with opposite spin component S_x, due to the SIA induced by the electric field braking inversion symmetry along the y-direction. It should be noted that SIA spin splitting is present only if we have both a macroscopic electric field, that breaks inversion symmetry, and a microscopic electric field from the atomic cores, that is responsible for the matrix elements of the microscopic spin-orbit interaction $H^{SO}_{\mu\nu}$ [206]. We note that the spin splitting in the valence subbands is more pronounced with respect to the electron subbands. This is expected, since it originates from the "direct" SOI between p-like states in the valence band. In the conduction states, which are s-like, there is no direct SOI and the splitting

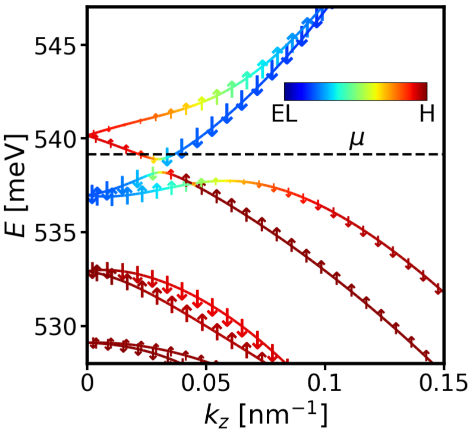

Figure 5.6: Energy bands with transverse electric field. Energy bands of the InAs-GaSb CSNW in presence of a transverse electric field E_y=1 V/μm directed along the y-direction. At $k_z \neq$0 each subband splits in two subbands with opposite spin component S_x: the modulus $|S_x|$ of the x-component of the vector spin operator $\hat{\boldsymbol{S}}$ calculated as $S_x = \langle\Psi|\hat{S}_x|\Psi\rangle$ is represented by the size of the arrows. Upwords pointing arrows indicates a positive sign of S_x, while downwards pointing arrows indicates a negative sign of S_x.

ensues from the coupling with the valence band [231].

In Fig. 5.7(a) we show the same band structure as in Fig. 5.6 but concentrating in a narrow region around the gap. The four subbands interact between each other in a complex way, as a result of the interplay between electron-hole kinetic interactions, regulated by the optical matrix element P, and SOI. Qualitatively, we identify two anticrossings: the first is between subbands ”1” and ”4”, the second between subbands ”2” and ”3”, with clearly different couplings. The latter defines the effective gap of the system, and is an hybridization gap, as it stems from the anticrossing between a conduction subband and a valence subband.

Interestingly, increasing the value of the electric field E_y the system undergoes a transition through a semimetallic phase, where the effective gap of the system vanishes. The gap closing is shown in Fig. 5.7(b), for an electric field $E_y = 1.285$ V/μm. Here two opposite spin, electron and hole subband cross at $k_z \neq 0$. Furthermore, the crossing subbands show a linear dispersion describing massless Dirac particles in one dimension near a degeneracy point $k_0 \neq 0$. Clearly, an identical behaviour is obtained in the negative branch of k_z, not shown here, due to Kramers degeneracy, with a gap closing at $-k_0$. Consistently with the closing gap, the crossing subbands show a pure electron and hole character. If the electric field is further increased, the two subbands anticross again, and the energy gap reopens, as shown in Fig. 5.7(c).

In Fig. 5.7(d), we systematically study the effective gap of the same NW as a function of the the electric field E_y and the chemical potential μ. While the former is generated by a back-gate voltage below the NW, the latter can be tuned by contacts directly attached to to it. Note that self-consistent charge transfer is included here, as explained in Sec. 5.2. We find that the for each value of μ in the explored range the gap closes at two values of the electric field. In particular, the three dots refer to the sequence Fig. 5.7(a),(b) and (c), as indicated. The gap closing point is represented by the red dot. The corresponding gap closing point at negative electric field is is non-symmetric with respect to $E_y = 0$. This is due to the fact that the presence of the back-gate voltage attached to the NW breaks inversion symmetry with respect to the $x = 0$ plane, making the form of the self-consistent potential (thus of the screening-effects), to depend on the sign of the electric field.

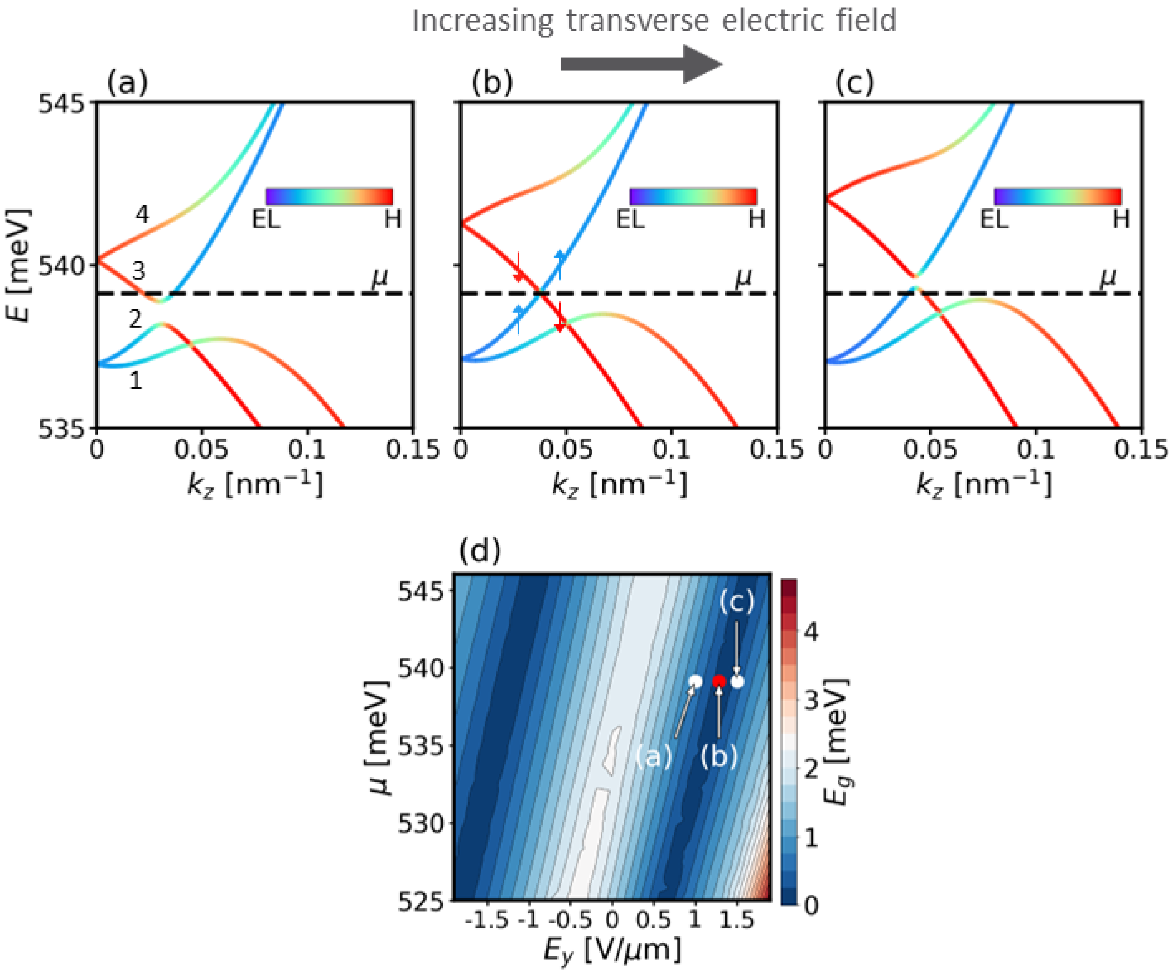

Figure 5.7: Semimetal state induced by and electric field. Evolution of the energy band structure of the InAs-GaSb CSNW in presence of increasing values of the transverse electric field E_y, specifically (a) $E_y = 1$ V/μm, (b) $E_y = 1.285$ V/μm and (c) $E_y = 1.5$ V/μm. The system undergoes a transition through a semimetallic phase in (b), where the energy gap vanishes. (d) Phase diagram of the nanowire as a function of chemical potential μ and electric field E_y. For each value of μ, a semimetallic state as in panel (b) occurs at two values of the electric field E_y, one negative and one positive. The sequence in panels (a), (b) and (c) is highlighted with dots as indicated, the red one corresponding the the gap closing point.

5.4. An effective low-energy model

In this section we delve deeper into the understanding of the occurrence of the semimetallic phase induced by the electric field. We will show below that the intimate physical reason underneath the energy crossing of the two opposite spin, electron and hole subbands is a compensation of SOI with the electron-hole **k** · **p** interaction.

To show this we use the BHZ model, a 2D model Hamiltonian that was first introduced in Ref. [50] to describe the topological quantum phase transition between the conventional insulating phase and the phase exhibiting the QSH effect in HgTe-CdTe semiconductor QWs, which form a type-III heterostructure, i.e., a QW with band inverted well material. Indeed, HgTe has an inverted band ordering whereby the first s-like, Γ_6 band lies below the first p-like band with symmetry Γ_8. On the contrary, the barrier material (CdTe) has a normal band ordering, with the Γ_6 band above the Γ_8 band.

The BHZ Hamiltonian can be obtained from general symmetry considerations and the standard **k** · **p** theory for a quasi-2D QW grown along the z direction with the in-plane wave vector $\boldsymbol{k} = (k_x, k_y)$. It has the form

$$H_{\text{BHZ}} = \begin{pmatrix} h(\boldsymbol{k}) & 0 \\ 0 & h^*(-\boldsymbol{k}) \end{pmatrix}, \tag{5.12}$$

with

$$h(\boldsymbol{k}) = h_0(\boldsymbol{k})\tau_0 + \sum_{i=x,y,z} h_i(\boldsymbol{k})\tau_i\,, \tag{5.13}$$

where τ_i are the standard Pauli matrices and τ_0 is the identity matrix. The lower block is related to the upper one by time-reversal symmetry, here represented by the operator $\mathcal{T} = i\tau_y K$, where K stands for complex conjugation. The above Hamiltonian is written in the basis of the first spin-up and spin-down (±) electron-like and (heavy) hole-like subbands ($|\text{EL}+\rangle$,$|\text{H}+\rangle$,$|\text{EL}-\rangle$,$|\text{H}-\rangle$) of the HgTe-CdTe QW at the Γ point. It can be shown (see [206]) that, with J_z quantized along the QW growth direction, at $\boldsymbol{k} = 0$ the $|\text{EL}\pm\rangle$ states are linear combinations of the bulk s-like states $\left|\Gamma_6^-, J_z = \pm\frac{1}{2}\right\rangle$ and p-like states $\left|\Gamma_8^+, J_z = \pm\frac{1}{2}\right\rangle$ (LHs), while the $|\text{H}\pm\rangle$ states consist of the bulk states $\left|\Gamma_8^+, J_z = \pm\frac{3}{2}\right\rangle$ (HHs). From the parity under inversion of the Bloch states $P\left|\Gamma_8^+, J_z = \pm\frac{3}{2}\right\rangle = \left|\Gamma_8^+, J_z = \pm\frac{3}{2}\right\rangle$, $P\left|\Gamma_8^+, J_z = \pm\frac{1}{2}\right\rangle = \left|\Gamma_8^+, J_z = \pm\frac{1}{2}\right\rangle$ and $P\left|\Gamma_6^-, J_z = \pm\frac{1}{2}\right\rangle = -\left|\Gamma_6^-, J_z = \pm\frac{1}{2}\right\rangle$, one obtains that the electron-like subbands states $|\text{EL}\pm\rangle$ and the hole-like ones $|\text{H}\pm\rangle$ have opposite parity, i.e. $P\,|\text{EL}\pm\rangle = -\,|\text{EL}\pm\rangle$ and $P\,|\text{H}\pm\rangle = |\text{H}\pm\rangle$. As a result, the matrix elements h_0 and h_z must be even under P (as they connect states with the same parity eigenvalue), while the matrix elements the matrix elements h_x and h_y must be odd (as they connects states with opposite parity eigenvalue). Taking into account time-reversal, inversion, and crystal symmetry, a Taylor expansion near $\boldsymbol{k} = 0$ gives the functional form of the matrix matrix elements h_i [50]:

$$\begin{aligned} h_0(\boldsymbol{k}) &= C - D(k_x^2 + k_y^2)\,, \\ h_x(\boldsymbol{k}) &= \mathcal{A}k_x\,, \\ h_y(\boldsymbol{k}) &= -\mathcal{A}k_y \\ h_z(\boldsymbol{k}) &= M - B(k_x^2 + k_y^2)\,. \end{aligned} \tag{5.14}$$

The parameters C, D, $\mathcal{A}$, B and M depend on the materials involved as well as the structural parameters of the QW, as for example the QW thickness. The parameter C sets the zero of energy.

The parameter $\mathcal{A}$ regulates the strength of the kinetic electron-hole interaction. B and D regulates in-plane dispersion of the energy bands and can be related to the effective masses m_e and m_h of electrons and holes respectively by the relation $D \pm B = -\hbar^2/2m_{e/h}$, or

$$D = -\frac{\hbar^2}{2}\left(\frac{1}{m_e} + \frac{1}{m_h}\right) , \tag{5.15}$$

$$B = -\frac{\hbar^2}{2}\left(\frac{1}{m_e} - \frac{1}{m_h}\right) . \tag{5.16}$$

Note that $m_e > 0$ while $m_h < 0$. As a consequence D is proportional to the difference between the inverse absolute values of the effective masses, while B will be proportional to their average.

The critical quantity is the gap parameter M, with $2M$ being the energy difference between the EL and H levels at the Γ point. Remarkably, when the ratio $\frac{M}{B}$ changes sign a band inversion occurs. In HgTe-CdTe QWs, this ratio is experimentally controllable through the width of the HgTe QW. As shown in Ref. [50], band inversion, via closing of the bulk gap, leads the system to the topological insulator (TI) phase which exhibits QSH edge states due to bulk-boundary correspondence.

The QSH state has been predicted in InAs-GaSb QWs as well. As already noted in Sec. 5.2 InAs-GaSb heterostructures can be in an inverted band regime for proper values of structural parameters, i.e. the width of the InAs and GaSb layers. Furthermore, electron-hole kinetic interactions provide a finite bulk insulating gap in the inverted regime. Therefore, the inverted regime of InAs-GaSb QWs should be a topologically nontrivial QSH phase protected by the bulk gap [219]. Nevertheless, we emphasize the fundamental distinction between HgTe-CdTe and InAs-GaSb QWs; in the former the band inversion takes place only in the HgTe well, while in the latter electrons and holes are confined in distinct materials (electron in the InAs layer and holes in the GaSb layer) and the full heterostructure is in the inverted band regime.

The BHZ model discussed above for HgTe-CdTe QWs has been used to describe the topological transition in asymmetric InAs-GaSb QWs, although in this case the BHZ Hamiltonian must include additional terms to account for the effect of SIA induced by the fact that the QW is asymmetric along the growth direction. However, these terms only modify the location of the phase transition between the QSH and the trivial insulating phases (phase boundary in the parameter space) [216]. On the other hand, a major advantage of asymmetric InAs-GaSb QW with respect to HgTe-CdTe QWs is their much larger sensitivity to external gate voltages ensuing from the spatial separation of electrons and holes in different asymmetric layers.This enable the possibility to drive the system to the inverted regime, hence into the TI phase, by means of electrical gating [232].

In Ref. [233] an extension of the BHZ model in presence of an inversion breaking potential generated by an electric field in the z direction was derived. The authors use **k** $\cdot$ **p** theory and derive an effective 4$\times$4 Hamiltonian through third-order Löwdin perturbation theory, using the unperturbed basis of the eigenstates of the 6$\times$6 Kane Hamiltonian at $\boldsymbol{k} = 0$. The k-dependent part of the Kane Hamiltonian as well as the electrostatic potential $V(z) = -eE_z z$ are treated as a perturbation. The result is an

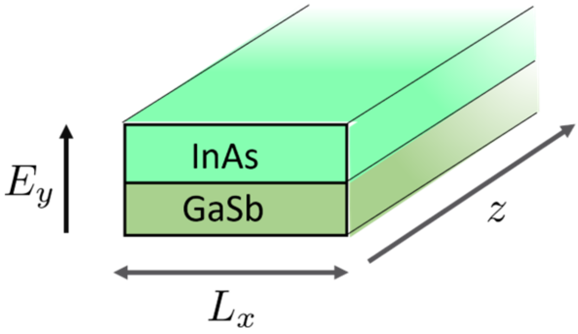

Figure 5.8: Sketch of the BHZ model for InAs-GaSb core-shell nanowires. A simple model for for InAs-GaSb CSNWs in presence of a transverse electric field can be obtained starting from a two-dimensional InAs-GaSb quantum well with growth axis along y, and considering a short strip of length L_x along the x-direction. The translationally invariant direction z then represents the nanowire growth axis.

extended BHZ Hamiltonian

$$H_{\mathsf{BHZ}} = \epsilon(k)\mathbb{1}_4 + \begin{pmatrix} \mathcal{M}(k) & \mathcal{A}k_+ & 0 & -S_0k_-^2 \\ \mathcal{A}k_- & -\mathcal{M}(k) & S_0k_-^2 & 0 \\ 0 & S_0k_+^2 & \mathcal{M}(k) & -\mathcal{A}k_- \\ -S_0k_+^2 & 0 & -\mathcal{A}k_+ & -\mathcal{M}(k) \end{pmatrix}, \tag{5.17}$$

where $k_\pm = k_x \pm ik_y$, $k^2 = k_x^2 + k_y^2$, $\mathcal{M} = M - Bk^2$, $\varepsilon(k) = C - Dk^2$ and $\mathbb{1}_4$ is a 4×4 identity matrix. The parameter S_0 is a linear function of the electric field, or $S_0 =$ const $\times$ E_z, being the constant of proportionality material and structure dependent, while the definitions of the other the parameters are the same as the ones of Eq. (5.14). With respect to Eq. (5.12) we note the presence of SIA terms, proportional to S_0 and hence induced by the electric field, coupling electron states to hole states that belong to different spin blocks. The linear Stark shift term, which is a first order correction term, is absent because the envelope functions of the unperturbed basis have a well defined parity under spatial inversion. Nevertheless, the electric field enters in the Hamiltonian through the terms $\pm S_0 k_\pm^2$, which originates from the second order correction in perturbation theory. It should be noted that the Hamiltonian of Ref. [233] includes additional Rashba terms that couples electron and hole states with opposite spin, respectively. Since these terms do not alter the conclusions of this section, we will neglect them for now to easy our analysis. Their effect will be considered in Sec.5.5.2.

The critical observation is that, as the electric field breaks the symmetry in the y direction and induces the localization of holes in the GaSb layer near the gate [see Fig. 5.5 (right panel)], the system appears approximately as a laterally confined GaSb/InAs QW. Hence, to model the energy dispersion of the NW, we use the extended BHZ model Eq. (5.17), which simulates a 2D system, adding a lateral confinement. Specifically, we write the Hamiltonian in Eq. (5.17) in the zx plane by relabeling $(k_x, k_y) \to (k_z, k_x)$ and consider a *short* strip along the x direction by replacing $k_x \to -i\frac{\partial}{\partial x}$. A schematic picture of the *short* strip model is shown in Fig 5.8. Assuming open BCs at the strip edges, we project H_{BHZ} onto the following real space basis

$$\psi_n(x) = \sqrt{\frac{2}{L_x}} \sin\left(\frac{n\pi}{L_x}\left(x - \frac{L_x}{2}\right)\right). \tag{5.18}$$

If we consider only $n = 1$, which is justified for sufficiently narrow strips (we shall consider $L_x = 16.5$

nm hereafter), after the projection we obtain a 4×4 Hamiltonian

$$\begin{aligned} H_4(k_z) = \varepsilon'(k_z) I + \mathcal{M}'(k_z)\sigma_0\tau_z \\ + \mathcal{A}k_z\sigma_z\tau_x + S_0\left(k_z^2 - \frac{\pi^2}{L_x^2}\right)\sigma_y\tau_y \end{aligned}, \tag{5.19}$$

where

$$\varepsilon'(k_z) = C - D\left[(\pi/L_x)^2 + k_z^2\right] \,, \tag{5.20}$$

$$\mathcal{M}'(k_z) = M - B\left[(\pi/L_x)^2 + k_z^2\right] \,, \tag{5.21}$$

and $\tau_{x,y,z}$ and $\sigma_{0,x,y,z}$ are Pauli matrices acting on the electron-hole and pseudospin subspaces, respectively.

To support the validity of the Hamiltonian $H_4(k_z)$, in App. C.1 we considered a cylindrical InAs-GaSb CSNW and derived a effective 4-band Hamiltonian describing the two spinful, lowest-energy electron and hole subbands of the system. We used first order perturbation theory and we did not consider the interaction with other subbands apart from the four ones that we considered explicitly. Despite these approximations, we found that the form of the 4-band Hamiltonian obtained in this way is exactly equivalent, apart from the term to proportional to $k_z^2\sigma_y\tau_y$, to the form of the effective Hamiltonian $H_4(k_z)$ in Eq. (5.19) obtained starting from the laterally confined two-dimensional QW model. Importantly, the Hamiltonian obtained starting from the CSNW model with cylindrical symmetry, contains the term proportional to $\sigma_y\tau_y$, which is expected to dominate at small k_z, and is essential to reproduce the field-induced gap closure observed in the numerical simulation, as we shall demonstrate.

By inspection from the numerical diagonalization of $H_4(k_z)$, we infer that the degenerate subspace at $k_z = k_0$ is spanned by the following eigenvectors:

$$|\psi_1\rangle = \frac{1}{\sqrt{2}}\begin{pmatrix} 1 \\ 0 \\ 1 \\ 0 \end{pmatrix} \qquad |\psi_2\rangle = \frac{1}{\sqrt{2}}\begin{pmatrix} 0 \\ -1 \\ 0 \\ 1 \end{pmatrix}. \tag{5.22}$$

For $|\psi_{1,2}\rangle$ to be eigenvectors with degenerate eigenvalue E_0 at $k_z = k_0$ we find that the following two conditions must hold:

$$\mathcal{M}'(k_0) = 0\,, \tag{5.23a}$$

$$\mathcal{A}k_0 + S_0\left(k_0^2 - \frac{\pi^2}{L_x^2}\right) = 0\,. \tag{5.23b}$$

From the first condition Eq. (5.23a) one obtains the wave vector at the crossing point

$$k_0 = \sqrt{\frac{M}{B} - \frac{\pi^2}{L_x^2}}\,, \tag{5.24}$$

which does not depend on the value of the electric field E_y. Furthermore we have that the energy at which the gap closes is given by

$$E_0 = \varepsilon'(k_0) = C - \frac{D}{B}M\,. \tag{5.25}$$

$\mathcal{A}$ [nm eV]	31.8 $\times$ 10^{-3}
B [nm^2 eV]	-1.052
D [nm^2 eV]	-0.0436
M [eV]	-38 $\times$ 10^{-3}
C [eV]	537.5 $\times$ 10^{-3}
$S_0/(eE_y)$ [nm^3]	27.016
L_x [nm]	16.5

Table 5.2: Parameters of the BHZ model Hamiltonian Eq. (5.17). The parameter $\mathcal{A}$ regulates the strength of the electron-hole kinetic interaction. B is proportional to the average between the effective masses $m_{e/h}$, while D is proportional to the difference between the two. $2M$ is the value of the inverted-gap. C is a constant energy shift. S_0 regulates the strength of the Rashba electron-hole, opposite-spin interaction. L_x is the *short* strip length used to model the energy states of the nanowire.

The second condition Eq. (5.23b), that is fulfilled for a specific value of the electric field E_y, shows that, *at the degeneracy point $k_z = k_0$, the same-spin electron-hole kinetic interaction is suppressed by the opposite-spin electron-hole Rashba term proportional to S_0.*

The effective Hamiltonian with the parameters of Tab. 5.2 indeed reproduces very well the exact **k** $\cdot$ **p** energy spectrum in proximity of the band crossing at k_0 and energy E_0, where fitting is enforced, but it is very accurate for the two crossing subbands down to Γ, as shown in Fig. 5.9(a). The fitting is performed as follows. The values of k_0, E_0 and E_y are extracted from the numerical results in Fig. 5.7(b). We also assume a fixed value of $\mathcal{A}$ (see Tab.5.2) close to the value employed in Ref.[225]. Thus, from Eq. (5.23) we obtain the value of S_0. Eventually, from Eqs. (5.24) and Eqs. (5.25) we eliminate the parameters B and D in favour of M and C, which now represent the remaining two fitting parameters used in order to reproduce the band structure in Fig. 5.7(b).

Using the laterally confined BHZ Hamiltonian H_4 with the parameters in Tab. 5.2, in Fig. 5.9(b) we plot the fundamental energy gap E_g (blue) of the energy spectrum of the Hamiltonian H_4 and the condition in Eq. 5.23b (red) as a function of the electric field E_y. The fundamental energy gap E_g closes and reopens as a function of the electric field E_y, a feature we already obtained in the numerical simulations of Fig 5.7. Furthermore, as already stated, the gap closes at the specific value of electric field that fulfills the condition in Eq. (5.23b).

Starting from Eq. (5.19) it is possible and instructive to derive an effective 2×2 Hamiltonian close to k_0. To do that we write the wave vector as $k_z = k_0 + k$ where k is the distance wave vector calculated from the degeneracy point. Thus, we can write the Hamiltonian in Eq. (5.19) as

$$H_4(k) = H_0 + H(k)\,, \tag{5.26}$$

where $H_0 = H(k = 0) = H(k_0)$ is the Hamiltonian $H_4(k_z)$ calculated at the degeneracy point, while $H(k)$ is treated as a perturbation. At first order in perturbation theory, we project the Hamiltonian $H_4(k_z)$ onto the degenerate subspace spanned by $|\psi_1\rangle$ and $|\psi_2\rangle$ while keeping only linear terms in k. The resulting 2×2 Hamiltonian is given by

$$\begin{aligned} H_2(k) = E_0\sigma_0 &- 2k_0\left(B\sigma_z + D\sigma_0\right)k \\ &- \left(\mathcal{A} + 2S_0k_0\right)\sigma_x k \end{aligned}. \tag{5.27}$$

Furthermore, we can rotate the coordinate system using the rotation operator $U = e^{-i\frac{\pi}{2}\sigma_x}$ and obtain

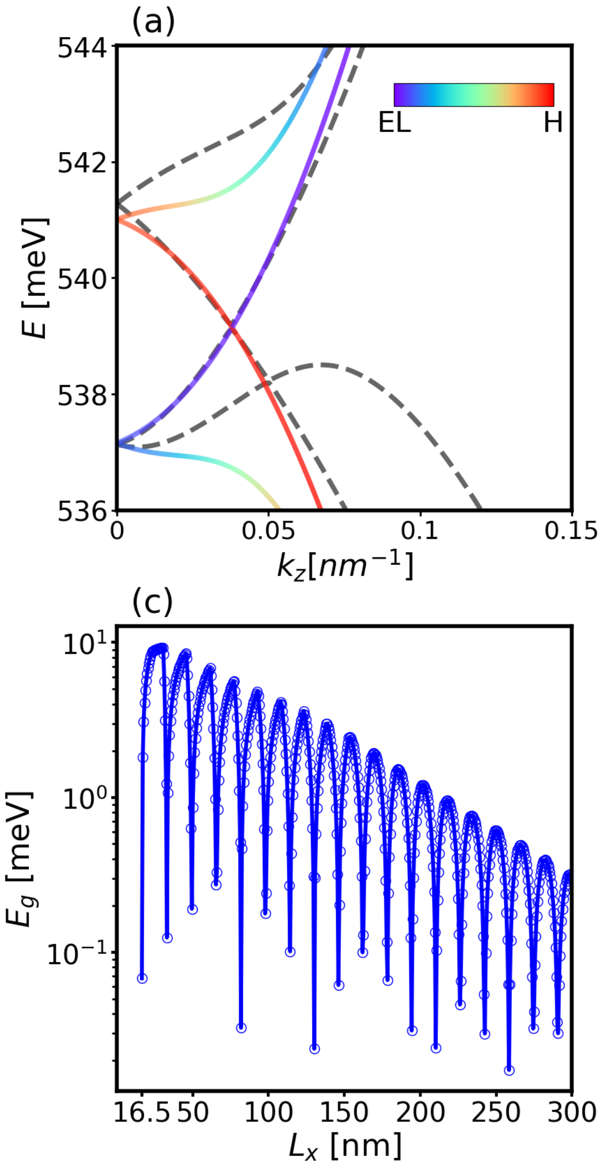

Figure 5.9: BHZ model results. (a) Energy spectrum of the short strip BHZ model (full line) superimposed with the energy bands of the core-shell nanowire [Fig 5.7(b)] for the gap closing point, or semimetallic state. The low-energy model well describes the energy spectrum of the nanowire in the vicinity if the crossing point. (b) Energy gap of the short strip BHZ model (blue line) and gap closing condition Eq. (5.23) as a function of the electric field E_y. When the gap closing condition is satisfied, the energy gap goes to zero. (c) Energy gap as a function of the strip length L_y at a fixed electric field $E_y = 1.285$ V$/\mu$m, showing multiple gap closing point. (d) Energy band structure for $L_y = 210.8$ nm, exhibiting topologically protected edge states.

the rotated Hamiltonian $\widetilde{H}_2(k) = U^\dagger H_2(k) U$, namely

$$\widetilde{H}_2(k) = E_0\sigma_0 - 2k_0 D\sigma_0 k - 2k_0 B\sigma_y k - (\mathcal{A} + 2S_0 k_0)\,\sigma_x k\,. \tag{5.28}$$

The spectrum of $\widetilde{H}_2(k)$ is given by a linear dispersion relation of the form

$$E_\pm(k) = E_0 + \hbar v_\pm k\,, \tag{5.29}$$

with

$$v_\pm = \frac{1}{\hbar}\left(-2k_0 D \pm \sqrt{4k_0^2(S_0^2 + B^2) + 4S_0 k_0 \mathcal{A} + \mathcal{A}^2}\right)\,. \tag{5.30}$$

With the effective parameters in Tab 5.2 we obtain $v_+ = 1.326 \times 10^5$m/s and $v_- = -1.226 \times 10^5$m/s Note that the two velocities at the crossing of the two subbands have slightly different absolute values, or in other words, the two crossing linear bands are slightly rotated counterclockwise. This is a consequence of the second term in Eq. (5.28), which is proportional to the identity matrix σ_0 and the parameter D. The latter would zero if the absolute values of the effective masses $|m_{el}|$ and $|m_h|$ of the two subbands were equal. In this case, the two velocities would be exactly opposite, as the effective Hamiltonian $H_4(k_z)$ would possess exact particle-hole symmetry. In fact, it is easy to show that the Hamiltonian $H_4(k_z)$ with $D = 0$ satisfies chiral symmetry, as $\mathcal{C}H\mathcal{C}^\dagger = -H$ [4] with $\mathcal{C} = \sigma_y\tau_x$, as well as time-reversal symmetry, as already noted. Since $H_4(k_z)$ has both chiral and time reversal symmetry, particle-hole symmetry is also implied. Note also that due to Kramer's degeneracy, an analogous semimetal phase occurs at $-k_0$, with opposite spins of the two subbands, and the opposite velocity asymmetry. The latter, indeed, is possible because the crossing occurs at a finite wave vector. In QSH states the velocity must be equal by symmetry, since the degeneracy occurs at the Γ point and spin degeneracy must occur.

Before delving more deeply into the nature of the semimetal transition in the next section, we answer to the natural question about the relationship between the field-induced semimetal phase at a finite wave vector k_0 discussed above and the expected Dirac point at Γ in topological QWs. Therefore, we studied how the spectrum of H_4 changes when we consider increasing larger values of the strip length L_x, including a sufficiently large number of basis states (5.18). In Fig. 5.9(c) we show the evolution of the fundamental energy gap of the system as a function of the strip length L_x at a finite field. The energy gap shows an oscillatory exponential decay, corresponding to multiple gap closings at specific values of L_x. This is similar to what has been reported in Ref. [234] for stripes of increasing width at zero-field. However, while in the latter case a gap closing requires careful tuning of the heterostructure parameter, in the present case at each length one could find an appropriate electric field at which the gap vanishes. Note also that as L_x is increased, at each gap closing the degeneracy wave vector k_0 moves further towards the Γ point. This is exemplified in Fig. 5.9(d) where we show the energy spectrum at a specific length $L_x = 210.8$ nm, showing a gap closing near the topologically protected edge states of a purely 2D system. In conclusion, the field-induced semimetal phase in a band-inverted CSNW at a critical field and finite wave vector appears as a natural evolution of the TI phase at zero field for band-inverted QWs.

---

[4] This is strictly true if also $C = 0$, but this is always possible by redefining the zero of the energy.

5.5. End states

As discussed in Sec. 5.1, from the topological point of view an InAs/GaSb CSNWs lacks a topological invariant in 1D and does not support topologically protected states, analogous of the edge states in QSH phases. However, a band inverted NW can host localized end states [225]. We show next that these states may appear in the hybridization gap with an electric field modulating the gap, but do not survive the closing of the gap at the the critical value of electric field $\widetilde{E}_\perp$, which brings the system back to the normal s-p ordering.

To investigate end states in our band inverted NW by the full **k** · **p** approach for a finite, but long sample would be numerically inconvenient. However, we can assume that the laterally confined BHZ model (5.19), which has been fitted to provide a good description of the states at fields near the degeneracy point, also provides a qualitatively correct band structure at low field. Hence, we start from the *short* strip model Hamiltonian $H_4(k_z)$ and consider a long but finite length L_z along the z direction, by replacing $k_z \to -i\frac{\partial}{\partial z}$. Again, we project the Hamiltonian onto a real space basis $\psi_n(z)$ with the same form of Eq. (5.18), but directed along z, satisfying open BCs at the wire ends $-L_z/2$ and $L_z/2$, including a sufficiently high number N_s of basis functions. Typically convergence is achieved with $N_s \simeq 100$ for $L_z = 1000$ nm and $N_s \simeq 200$ for $L_z = 4000$ nm.

In Figs. 5.10(a), (b) we show the energy eigenvalues of the finite length NW Hamiltonian for $L_z = 1000$ nm and $L_z = 4000$ nm, respectively, as a function of the transverse electric field E_y. For a finite length NW k_z is not a good quantum number, of course, and a set of discrete states appear at each field, ensuing from the discretization of k_z in the axial direction. Clearly, as L_z is increased, the discrete states become denser. When the electric field is below the critical value for the infinitely long NW, here at $\widetilde{E}_\perp = 1.285\,$, V/m, the system is gapped and in the inverted regime, with a set of s-like states below, and well separated from, a set of p-like states, as shown by the hue in the figures. Direct inspection shows that these states are extended along the NW. However, a four-fold degenerate state also appear at the energy E_0 [see Eq. 5.25]. For these states, we plot in Figs. 5.10(c), (d) the squared modulus of the wave function (normalized to its maximum at each field) as a function of E_y. We clearly see that these mid-gap states are localized at the ends of the NW.

Figures 5.10(a), (b) show that, as the electric field approaches the critical value $\widetilde{E}_\perp$, i.e. the field at which the "bulk" gap vanishes, the end states start to split in two distinct Kramers degenerate doublets. Of course, for a finite system the gap never vanishes exactly. However, above the critical value, where the "bulk" gap opens again, the end states approach the continuum of bulk states. As seen in Figs. 5.10(a), (b), the s-like states now lay above the p-like states. In other words, consistently with the disappearance of the end states, the system has passed from an inverted to a normal band ordering. This can also be seen from the evolution of the localization shown in Figs. 5.10(c), (d): end states delocalize from the extrema to the bulk of the NW when crossing the critical field $\widetilde{E}_\perp$. As one may expect, while for the shorter NW with $L_z = 1000$ nm the end states appearance/disappearance is less clear-cut, since the gap of the continuum is not closing completely, for the longer NW of $L_z = 4000$ nm the transition is very sharp. We note finally from Figs. 5.10(a), (b) that the two Kramers pairs are symmetrically located in energy with respect to E_0. Correspondingly they have identical localization, as seen comparing Figs. 5.10(c), (d) with Figs. 5.10(e), (f), as one should expect from the fact that particle-hole symmetry is only *perturbatively broken* in the effective Hamiltonian by a small difference in the effective masses, which is contained in the parameter D.

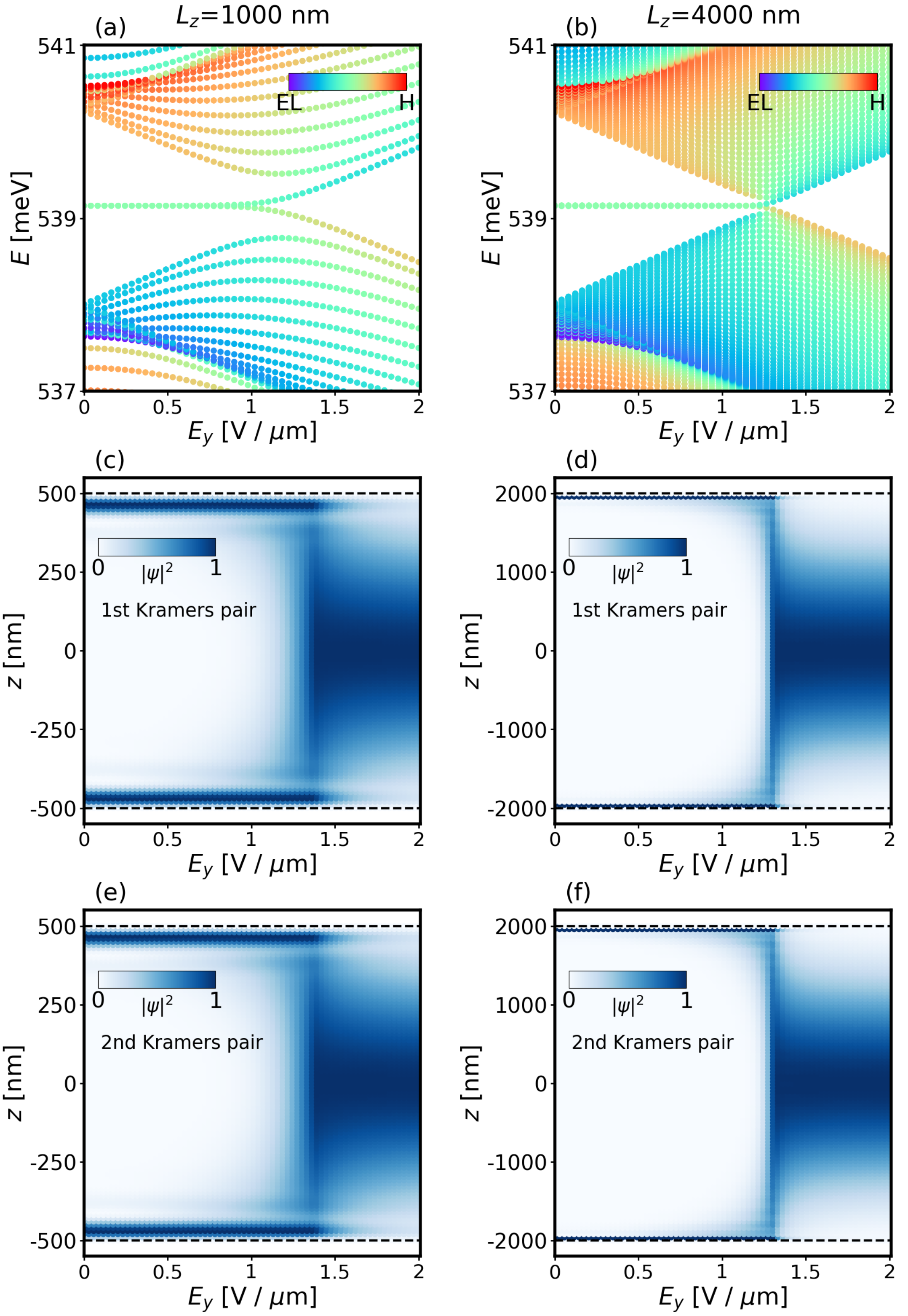

Figure 5.10: End states of the core-shell nanowire. Energy spectra and end states localization for NWs with finite lengths (a,c) $L_z = 1000$ nm and (b,d) $L_z = 4000$ nm versus electric field E_y obtained using the discretized BHZ Hamiltonian with hard-wall boundary conditions at the wire ends, indicated by dashed black lines. In (a) and (b) the color represents the electron/hole contribution of each state, while in (c) and (d) it represents the modulus square of the wave function normalized to its maximum.

Note that, as already anticipated, we have neglected additional Rashba terms which would be present in the extended BHZ Hamiltonian H_{BHZ} in Eq. (5.17). These terms, which will be included in a subsequent section, are usually different for electrons and holes. The difference between the two Rashba couplings, analogously to the difference between the effective masses, represents a further particle-hole symmetry breaking term in the Hamiltonian.

To summarize, we found that starting from a NW in the topological insulating phase at zero field, the electric field has the effect to move the conduction states upward and the valence states downward until a transition to a trivial insulator occurs through a semimetal phase at a finite field and wave vector. Correspondingly, localized end states suddenly delocalize and merge in the bulk band states. This is clearly reminiscent of the topological insulator transition predicted in InAs-GaSb QWs and to the fate of edge states which form in 2D topological systems due to the bulk-edge correspondence, which discriminate between the trivial and topological phase. Hence, end states can be seen as parents of the edge states in a 2D system when one of the in-plane direction is strongly confined to form a narrow stripe. Interestingly, *the transition to the trivial phase obtained after the critical value of electric field in InAs/GaSb CSNW happens without altering the sign of the inverted gap at* Γ. Contrary to previous investigations in 2D systems, therefore, where the transition in induced by crossing spin-degenerate s- and p- like states at Γ, here the transition is only due to the compensation between off-diagonal $\mathbf{k} \cdot \mathbf{p}$ and SOC terms induced by the field between opposite-spin subbands.

As already noted, one of the advantages of the InAs/GaSb heterostructures, with respect to Hg/Te ones, is the possibility to drive the system to a topological insulating phase by means of an external electric field. In this perspective, a sufficiently strong field is used to change the band ordering at Γ [52]. In our system, on the contrary, we start from the outset with a band-inverted material, by carefully choosing the nanostructure parameters. The field does not close the gap at Γ, and actually this gap is slightly enhanced by the field, as seen comparing Figs. 5.7(a–c), driving the system to an even more inverted regime. The vanishing of the gap discussed above, instead, occurs at a finite wave vector and it has not been observed before. In Ref. [235] the authors explored the dependence of the hybridization gap in InAs/GaSb QWs as a function of external electric fields, and showed that when the system is tuned to more inverted regime by a gate voltage (a larger inverted gap at Γ), the hybridization gap decreases. However, gap closure for a critical electric field was not investigated. In Ref. [232] the authors considered a similar system and showed the occurrence of electric field-induced gap oscillations in the non-trivial phase. However, even if the gap closes and re-opens multiple times after the transition, the end states do not disappear, although their localization length increases with the electric field, while the system stays in the topological phase.

5.5.1. Axial disorder

Even if localized states, reminiscent of the topological edge states in 2D systems, are present at both ends of the wire, it remains to evaluate the degree of topological protection against disorder. In Ref. [225], the authors noted that in a cylindrical model NW the end states (at zero field) are not topologically protected against axial disorder. We expect this to be true also in our model.

To check this, we introduce an axial disorder in the Hamiltonian as in Ref. [225]. We add to H_4 the following disorder Hamiltonian

$$H_{dis}(z) = a(z) V_{dis} I_{4\times 4} \tag{5.31}$$

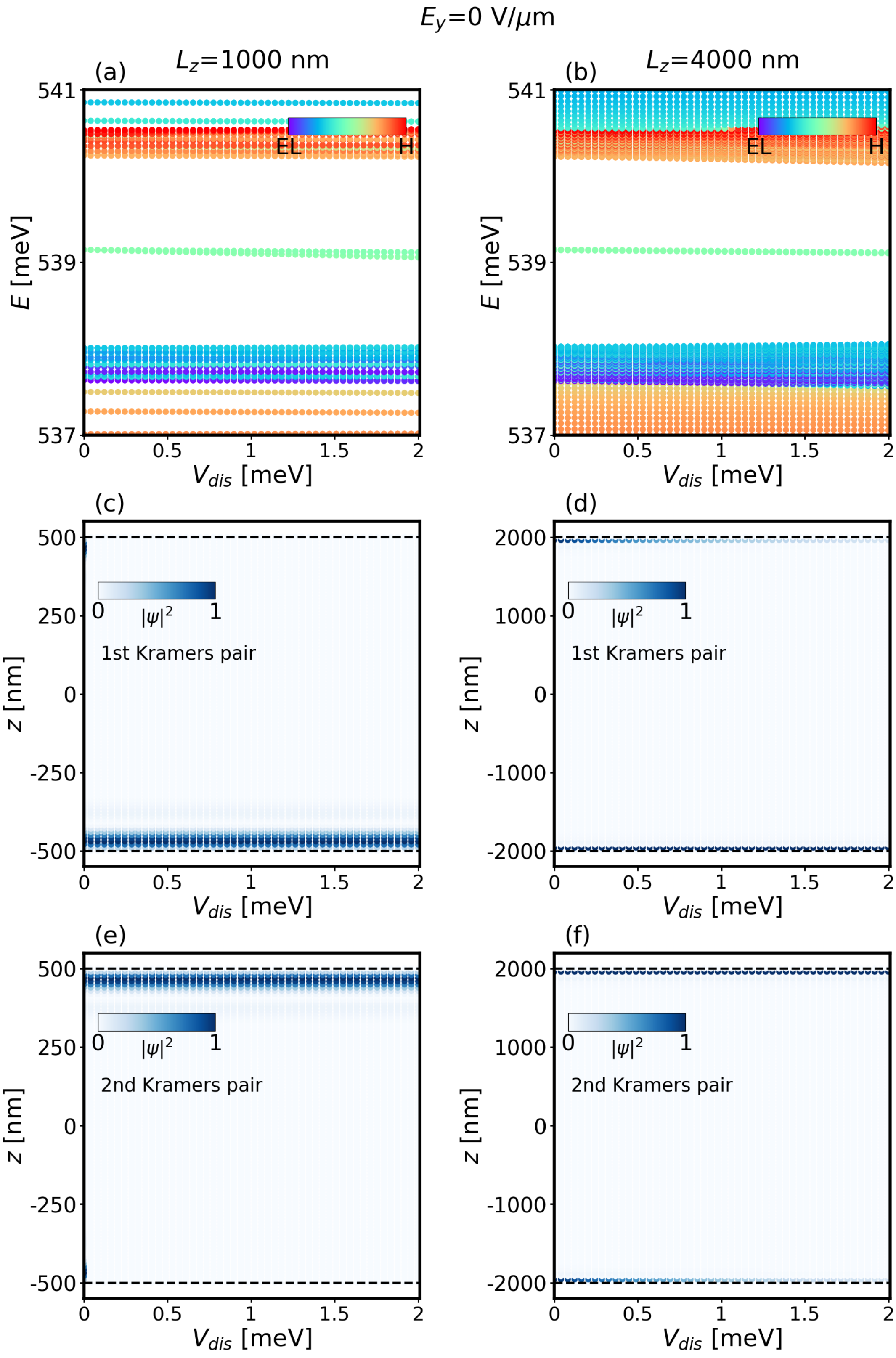

Figure 5.11: End states vs axial disorder at zero electric field. Energy spectra and end states localization for both Kramer pairs for nanowires with finite lengths (a,c,e) $L_z = 1000$ nm and (b,d,f) $L_z = 4000$ nm versus axial disorder intensity V_{dis} obtained using the discretized BHZ Hamiltonian with hard-wall boundary conditions at the wire ends, indicated by dashed black lines. In (a) and (b) the color represents the electron/hole contribution of each state, while in (c),(d),(e) and (f) it represents the modulus square of the wave function normalized to its maximum.

where $a(z)$ is a random number from a uniform distribution in the interval [-1,1] and V_{dis} is the disorder intensity. The disorder distribution $a(z)$ is a step-constant function with step length given by $d = 5$ nm. The corresponding matrix element is

$$H_{dis}^{nm} = V_{dis}\mathbb{1}_{4\times 4}\int \mathrm{d}z\,\psi_n^*(z)a(z)\psi_m(z)\,. \tag{5.32}$$

First, we investigate how axial disorder affects the energy states of the finite length NW model in absence of the electric field. In Fig. 5.11(a) and (b) we show the energy eigenvalues of the for $L_z = 1000$ nm and $L_z = 4000$ nm, respectively, as a function of the axial disorder intensity V_{dis}. For both values of L_z, the four-fold degenerate state at energy E_0 split in two doubly degenerate Kramers pairs. The latter phenomenon is enhanced for the shorter NW with respect to the longer one, where the energy splitting is hardly visible even at the highest disorder intensity of 2 meV.

In Fig. 5.11(c) and (d) we plot the squared modulus of the wave function normalized to its maximum as a function of V_{dis} for the first (c) and the second (d) Kramer pair of the shorter NW with $L_z = 1000$ nm. We see that when $V_{dis} \neq 0$ the two states remains localized at opposite ends of the NW. The same happens to Kramers pairs of the longer NW with $L_z = 4000$ nm represented in Fig. 5.11(d) and (f), even if in this case, the full localization at opposite ends of the wire sets in at larger values of V_{dis}.

As already noted in Ref. [225], the energy splitting is a clear signature of the lack of topological protection of the end states. In fact, the splitting between the two states cannot be attributed to the wave function overlap due to finite wire length, as the two states remains localized at opposite ends of the NW for $V_{dis} \neq 0$.

In Fig. 5.12 we repeat a similar analysis, but considering a fixed value of $V_{dis} = 1.5$ meV and studying how axial disorder affects the end states as a function of the electric field E_y. From Fig. 5.12 (a), (b) we see that the energy splitting induced by disorder persists at small values of electric field. As the electric field reaches the critical value, the end states disappear and merge into the continuum of bulk states, as already seen in absence of axial disorder. From Fig. 5.12(c),(e) and (d), (f), we see that the wave functions of both Kramers pair remains localized at the wire ends up to the critical value, where the end states disappear and the wave function delocalizes throughout the wire length. Interestingly, close to the critical field, the wave functions of the Kramers pairs seem to become symmetric with respect to $z = 0$, as in Figs. 5.10(c) and (d) without axial disorder.

5.5.2. Rashba terms

In this section include additional Rashba terms that are present in the Hamiltonian of Ref. [233] and that we have neglected up to now:

$$H_{\mathrm{R}} = \begin{pmatrix} 0 & 0 & -iR_0k_- & 0 \\ 0 & 0 & 0 & iT_0k_-^3 \\ iR_0k_+ & 0 & 0 & 0 \\ 0 & -iT_0k_+^3 & 0 & 0 \end{pmatrix}\,. \tag{5.33}$$

Here, both R_0 and T_0 are linear functions of the electric field E_z. The term proportional to R_0 originates from the second order correction in perturbation theory and couples the basis states $|\mathrm{EL}\uparrow\rangle$

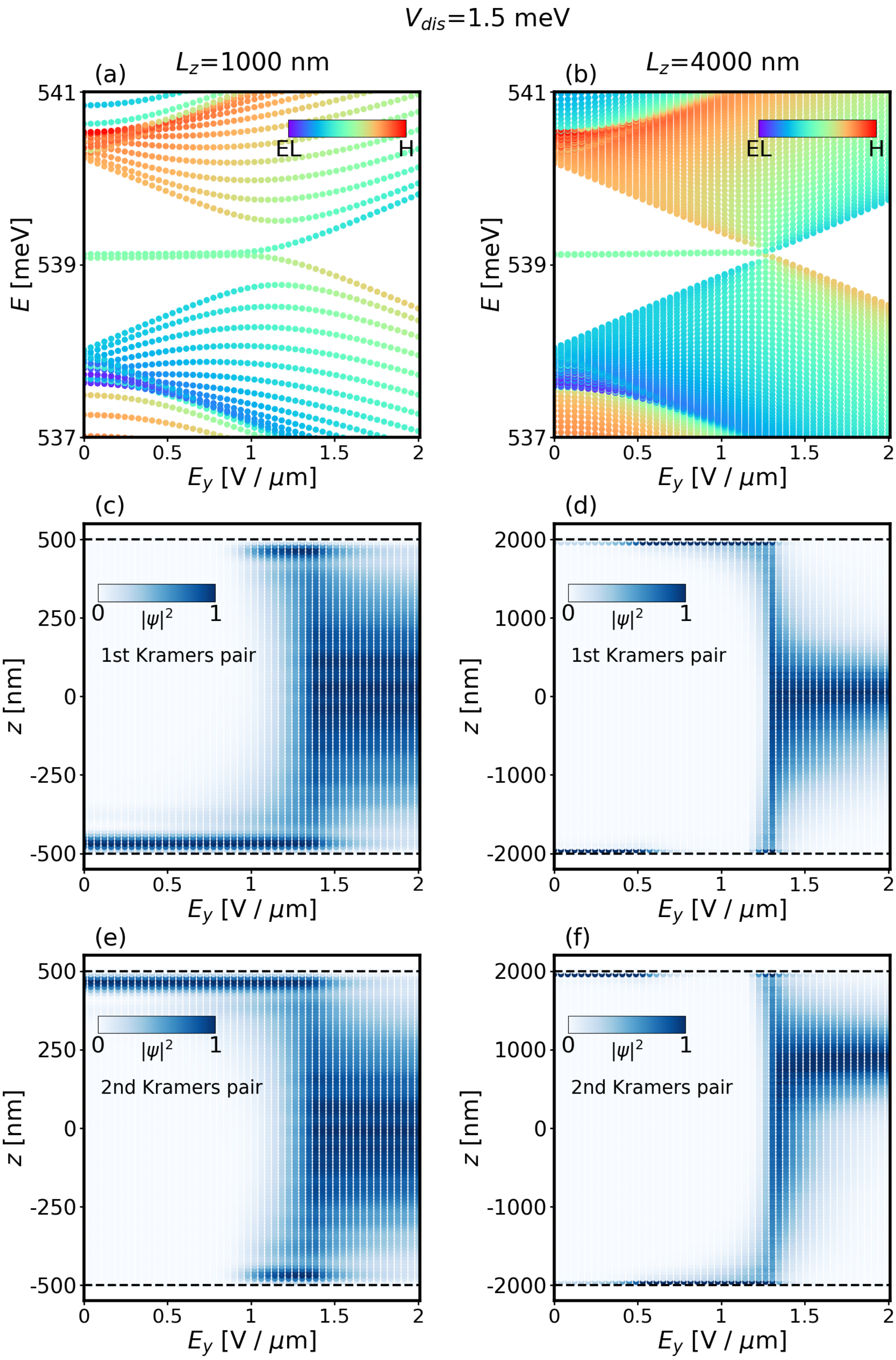

Figure 5.12: End states vs electric field with axial disorder. Energy spectra and end states localization for both Kramer pairs for NWs with finite lengths (a,c,e) $L_z = 1000$ nm and (b,d,f) $L_z = 4000$ nm versus electric field E_y in presence of axial disorder with intensity $V_{dis} = 1.5$ meV obtained using the discretized BHZ Hamiltonian with hard-wall boundary conditions at the wire ends, indicated by dashed black lines. In (a) and (b) the color represents the electron/hole contribution of each state, while in (c),(d),(e) and (f) it represents the modulus square of the wave function normalized to its maximum.

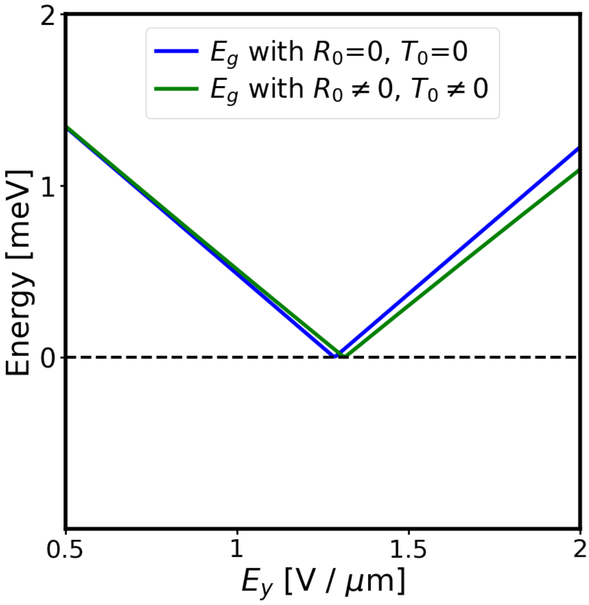

Figure 5.13: Gap closure with and without Rashba terms. Energy gap of the short strip BHZ model with (blue line) and without (green) the Rashba term H_{R} in Eq. (5.33) as a function of the electric field E_y. The energy gap goes to zero for a given critical electric field in both cases.

and $|\mathrm{EL}\downarrow\rangle$, while the term proportional to T_0 couples $|\mathrm{H}\uparrow\rangle$ with $|\mathrm{H}\downarrow\rangle$ and is a third order term. In particular, we considered $R_0/(eE_y) = 5$ nm^2 and $T_0/(eE_y) = 50$ nm^4. The derivation of the effective low energy model including H_{R} is straightforward. After the projection onto the real space basis in Eq. (5.18) with $n = 1$, we obtain H_4 given by Eq. (5.19) plus the additional term

$$H_{\mathrm{R},4} = \begin{pmatrix} 0 & H_{\mathrm{R},2} \\ H^{\dagger}_{\mathrm{R},2} & 0 \end{pmatrix} \tag{5.34}$$

where

$$H_{\mathrm{R},2} = \begin{pmatrix} -iR_0k_z & 0 \\ 0 & -3iT_0\left(\frac{\pi}{L_x}\right)^2 k_z + iT_0k_z^3 \end{pmatrix} . \tag{5.35}$$

Again, we first consider infinite length NWs. In Fig. 5.13 we show that even in presence of the Rashba terms introduced by H_{R} the gap closes and reopens as a function of the electric field. However, it is not easy to guess the form of the degenerate eigenvectors Eq. (5.22) in this case. Thus we are not able to find the corresponding gap closing conditions analogous to Eq. (5.23). By comparing the two curves in Fig. 5.13, however, we see that value of the critical field that closes the gap is only slightly displaced when we include Rashba terms.

As a final step, in Fig. 5.14 we repeated the analysis of the end state formation in finite length NWs in presence of Rashba terms. Figs. 5.14(a), (b) clearly show that the end states below the critical electric field split in two Kramers pairs. For electric fields well below the critical value, the energy splitting between the two states slightly increases. As the critical value is approached the two Kramers pair seem to come closer to each other and finally merge with the corresponding continuum, similarly to the case without the Rashba term. However, several difference can be noticed. First, merging is not complete, and the two doublets remain slightly in the gap, separated by the continuum, this effect being larger for holes in the valence states. Second, and consistent with this observation, although at the critical field the wave functions delocalize throughout the length of the NW, when the critical field is overcome, the wave function of both pairs tend to re-localize at the both ends of the wire, see Figs. 5.14(d), (f), but the localization length is field dependent and is very different from the localization of the end states.

Hence, the semimetal phase at $\widetilde{E}_\perp$ discriminates between topological mid-gap end states with field independent localization and trivial in-gap states near the top and bottom of the valence and conduction states, respectively, which appear as trivial defect states induced by the breaking of the translational symmetry of a normal insulator.

5.6. Conclusions

In this chapter we investigated the lowest-energy states of inverted gap InAs-GaSb CSNWs. These are dominated by the hybridization of s- and p-like states which, when inverted in the valence-conduction band ordering, lead to finite wave vector hybridization gaps. Since this results from a delicate balance of internal fields and material parameters, we have extended previous calculations [116] to include the unavoidable charge transfer between the upper hole states and the lower electron states. *A posteriori*, this proved to be an essential contribution for predictive calculations and extends the parameter range for the stability of the semiconducting phase with respect to the semimetallic one.

Using our self-consistent $\mathbf{k} \cdot \mathbf{p}$ calculations, we have investigated the effect of a transverse electric field, as generated for example by a back-gate placed beneath the CSNW, on the hybridization gap. Assuming a *slightly inverted* CSNW, where only two subbands are inverted, we obtained spin splitted subbands, as a result of the combination of SOC and the removal of the inversion symmetry. In this configuration, electron and hole subbands couple in pair and with opposite spin. For each pair the coupling is increased or decreased, and the hybridization gap depends on the field and, possibly, the chemical potential.

Hence, We investigated the phase diagram of the fundamental hybridization gap of the system as a function of chemical potential μ and electric field E_y in the range of a few tens of meV around the fundamental gap and a few V/μm, for the chemical potential and the field, respectively. Interestingly, for each value of the chemical potential μ, the *effective gap of the system vanishes* at two, nearly opposite, critical values of the electric field $\widetilde{E}_y$. This gap closing happens as a 1D Dirac point located at a field- and structure dependent wave vector, far from the Γ point, and it has been apparently unnoticed in the literature.

We have then adapted a low-energy effective analytical Hamiltonian, which has been devised and used to study topological transitions in 2D systems, to describe the dispersion of the crossing subbands and the occurrence of the semimetal state, which turns out to be due to an exact compensation between the electron-hole kinetic interaction and the electron-hole Rashba coupling. The BHZ Hamiltonian has also been used to study the end states in finite CSNWs, localized at both ends of the wire, which appear in the hybridization gap for electric fields below the critical value $\widetilde{E}_y$. The presence of end-states in the inverted phase, already noted in previous studies, can be ascribed to the approximate particle-hole symmetry present in the model Hamiltonian. However, we find that these states do not survive the closing of the ”bulk” hybridization gap at $\widetilde{E}_y$, which, indeed, brings the system back to the normal s-p ordering. Being the extinction of the end states after the closing

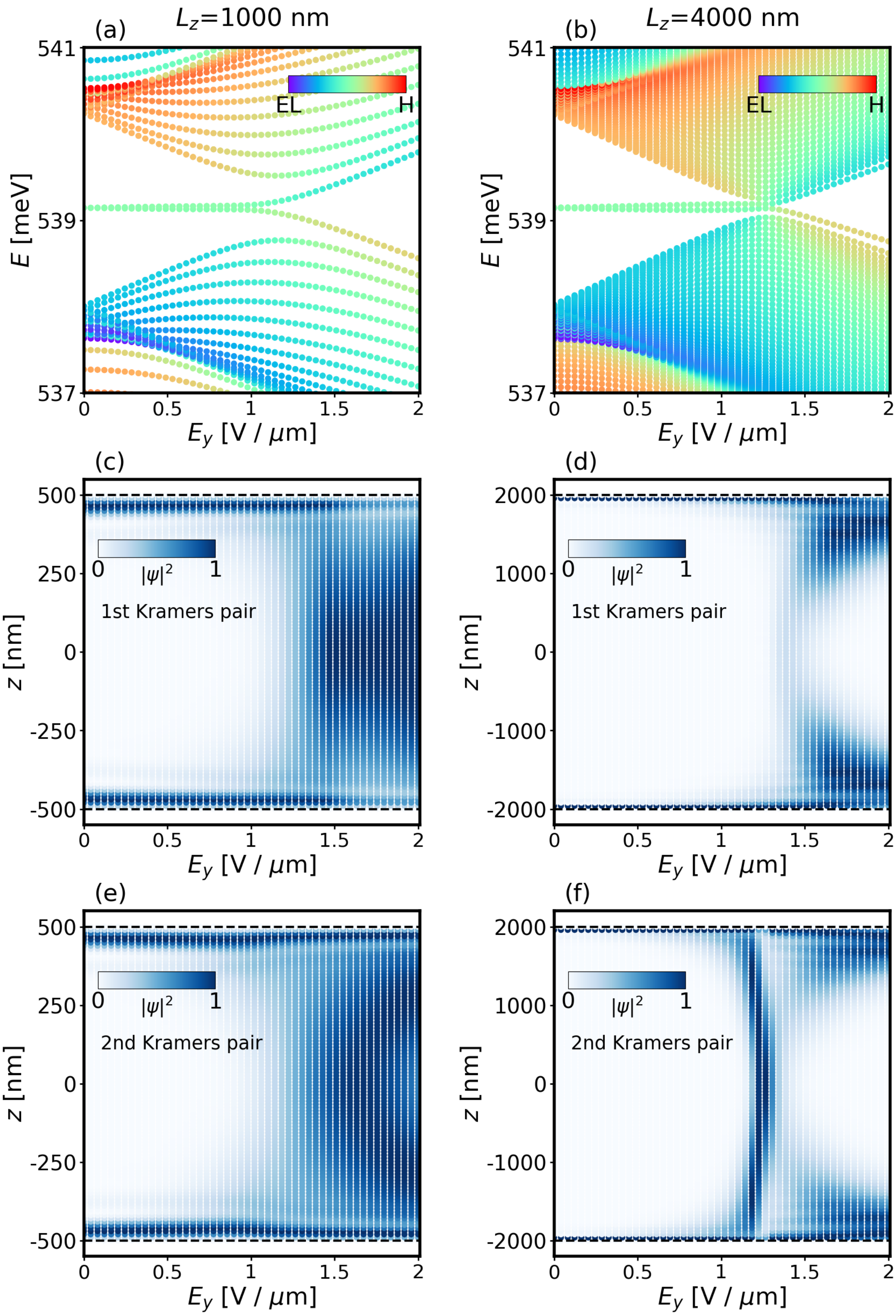

Figure 5.14: End states vs electric field with Rashba terms. Energy spectra and end states localization for both Kramer pairs for NWs with finite lengths (a,c,e) $L_z = 1000$ nm and (b,d,f) $L_z = 4000$ nm versus electric field E_y in presence of Rashba terms $R_0 = 5$ nm^2 and $T_0 = 50$ nm^4 obtained using the discretized BHZ Hamiltonian with open BCs at the wire's ends, indicated by dashed black lines. In (a) and (b) the color represents the electron/hole contribution of each state, while in (c),(d),(e) and (f) it represents the modulus square of the wave function normalized to its maximum.

of the ”bulk” gap a common signature of a topological transition, we speculate that the critical field $\widetilde{E}_y$ discriminates between two distinct topological phases in the system.

A key aspect for possible applications in quantum coherent devices is the degree of protection from disorder of such end states. These states cannot be exactly decoupled from disorder, since the system does not have exact electron-hole symmetry, in addition to time-reversal symmetry. However, symmetry removal is small in the investigated regime, and we made preliminary investigation of the effect of axial disorder. We also considered the inclusion of additional Rashba terms in the effective model and their effect on the end states. We find that slightly asymmetric, electron/hole Rashba interaction terms introduce additional particle-hole symmetry breaking terms and consequently the end state gap out with increasing electric field below $\widetilde{E}_y$.

While our investigation of end states is performed by a simplified model Hamiltonian which captures the topological aspects, it does not contain the full complexity of the quantum states of the system as a $\mathbf{k} \cdot \mathbf{p}$ calculation would do. In particular, the electric field does not affect localization, which in the BHZ Hamiltonian is frozen by the choice of the parameters. A full $\mathbf{k} \cdot \mathbf{p}$ calculation would be very inconvenient for a very long but finite CSNW. An alternative is to use a $\mathbf{k} \cdot \mathbf{p}$ description and, by means of the Green’s function matrix of a semi-infinite system, calculate the corresponding surface local density of states [236, 237], in order to confirm the presence and stability of end states in the gap from zero field up to the critical field. From an experimental point of view, we speculate that end states could be probed by, for example, tunnel spectroscopy between adjacent NWs.

6

Summary and outlook

In this thesis, we have made contributions to several scientific domains where III-V semiconductor core-shell nanowires, and, in particular, the role of spin-orbit coupling, are the essential ingredients enabling advancements in the development of novel electronic and quantum devices.

For example, we have contributed to the field of nanoelectronics. In particular, in Ch. 3 we have investigated a high-mobility, modulation-doped, GaAs-AlGaAs core-shell nanowire, a promising building block for the development of faster and more energy-efficient electronic devices operating at the nanoscale. Our calculations provided a thoughtful and systematic analysis of the band structure of these nanowires as a function of dopants concentration. As doping influences the electronic structure, and, crucially, the spin-orbital character of the highest energy valence band states of the nanowire, we showed that optical anisotropy spectra are able to distinguish between different doping regimes, as well as between n- and p-doped samples. Our results suggest a yet-unexplored, rapid characterization method of dopants incorporation in semiconductor nanowires, to be compared with the most widely used optical doping characterization techniques, as e.g. photoluminescence and Raman spectroscopy.

In Ch. 4, we have contributed to the search of new platforms for the generation of Majorana zero modes in condensed matters systems, a promising basis for obtaining topologically protected qubits. In particular, our study has focused on the valence bands of type-II InP/GaSb core-shell nanowires and assessed their potential in the quest to obtain topological superconductivity in full-shell, hybrid nanowire heterostructures. Crucially, our calculations unveiled a strong and intrinsic spin-orbit coupling, stemming from the spin-orbit coupled nature of the valence bands of the nanowire. This key factor, as well as the insulating-core/conductive-shell configuration, has the potential to relax some of the most prohibitive device constrictions of the full-shell nanowire proposal configuration. While certain aspects of our proposal, such as the specific details of the proximity effect on the valence bands, demand further theoretical and experimental investigation, our calculations aim to draw attention to this area and advance the field of full-shell Majorana nanowires, particularly towards core-shell, hole-based platforms.

Motivated by the reported topological insulating behavior in InAs-GaSb quantum wells, In Ch. 5 we studied the electronic structure of the corresponding one-dimensional nanostructures, namely, InAs-GaSb core-shell nanowires, in the search for topologically non-trivial states stemming from the inverted gap phase of the system. First, we reported a methodological contribution, i.e. the development of a modified envelope function approach, able to deal with the electron-hole hybridized nature of the energy levels, which hinders the separate occupation of electron and hole states when calculating the charge carrier densities. Then, we investigated the effect of a transverse electric field on slightly inverted core-shell nanowires, where only two subbands are inverted. We found that the spin-split subbands dispersion, as well as the formation of the hybridization gap, results from a non-trivial interplay between kinetic electron-hole and Rashba spin-orbit interactions. Moreover, we observed a critical electric field at which the two interactions mutually suppress each other, leading to gap closure. Finally, using an effective, low-energy Hamiltonian, we study finite length wires, and find that localized end states at the wire ends are present below the critical field, but vanish as the ”bulk” gap closes. Given the approximate particle-hole symmetry present in the model Hamiltonian, this feature could be ascribed to a (field-mediated) topological transition. However, it is important to acknowledge that our simplified model Hamiltonian, while capturing the topological aspects, disregards the full complexity of the quantum states of the system. In this regard, a more in-depth investigation, as e.g. a full $\mathbf{k} \cdot \mathbf{p}$ calculation complemented with the calculation of the local density of states of a semi-infinite system, is essential and will be object of near future work.

A

Appendices for chapter 2

A.1. The local approximation for the potential term

The effective potential for the envelope function is

$$V_{\mu\nu}(\boldsymbol{r},\boldsymbol{r}') = \frac{1}{\Omega}\sum_{\boldsymbol{k}\boldsymbol{k}'} e^{i\boldsymbol{k}\cdot\boldsymbol{r}} \left(\sum_{\boldsymbol{G}\boldsymbol{G}'} U^{*T}_{\mu\boldsymbol{G}} \left\langle \boldsymbol{k}+\boldsymbol{G}\middle|\hat{V}\middle|\boldsymbol{k}'+\boldsymbol{G}'\right\rangle U_{\nu\boldsymbol{G}'}\right) e^{-i\boldsymbol{k}'\boldsymbol{r}'} . \tag{A.1}$$

If the bare $\hat{V}$ is local and the envelope functions are slowly varying, the effective potential $V_{\mu\nu}(\boldsymbol{r},\boldsymbol{r}')$ can be separated into a local and a non-local component. The Fourier coefficient of the potential $\hat{V}$ are

$$\begin{aligned}\left\langle \boldsymbol{k}+\boldsymbol{G}\middle|\hat{V}\middle|\boldsymbol{k}'+\boldsymbol{G}'\right\rangle &= \frac{1}{\Omega}\int \mathrm{d}^3 r\, V(\boldsymbol{r}) e^{-i(\boldsymbol{k}-\boldsymbol{k}'+\boldsymbol{G}-\boldsymbol{G}')\cdot\boldsymbol{r}} \\ &= \frac{1}{\Omega}\int \mathrm{d}^3 r\, V(\boldsymbol{r}) e^{-i(\boldsymbol{k}_1+\boldsymbol{G}-\boldsymbol{G}'-\boldsymbol{G}_1)\cdot\boldsymbol{r}} , \\ &= \tilde{V}_{\boldsymbol{G}-\boldsymbol{G}'-\boldsymbol{G}_1}(\boldsymbol{k}_1)\end{aligned} \tag{A.2}$$

where $\boldsymbol{k}_1 = \boldsymbol{k}-\boldsymbol{k}'+\boldsymbol{G}_1$ is within the first Brillouin zone and $\boldsymbol{G}_1$ is a reciprocal lattice vector. Replacing $\boldsymbol{k}$ in favour of $\boldsymbol{k}_1$ we get

$$V_{\mu\nu}(\boldsymbol{r},\boldsymbol{r}') = \frac{1}{\Omega}\sum_{\boldsymbol{k}_1\boldsymbol{k}'} e^{i(\boldsymbol{k}_1+\boldsymbol{k}'-\boldsymbol{G}_1)\cdot\boldsymbol{r}} \left(\sum_{\boldsymbol{G}\boldsymbol{G}'} U^{*T}_{\mu\boldsymbol{G}} \tilde{V}_{\boldsymbol{G}-\boldsymbol{G}'-\boldsymbol{G}_1}(\boldsymbol{k}_1) U_{\nu\boldsymbol{G}'}\right) e^{-i\boldsymbol{k}'\boldsymbol{r}'} . \tag{A.3}$$

The local approximation is obtained for $\boldsymbol{G}_1 = 0$. In fact,

$$V^{(loc)}_{\mu\nu}(\boldsymbol{r},\boldsymbol{r}') = V_{\mu\nu}(\boldsymbol{r})\Delta(\boldsymbol{r}-\boldsymbol{r}') , \tag{A.4}$$

where

$$V_{\mu\nu}(\boldsymbol{r}) = \sum_{\boldsymbol{k}_1} \left(\sum_{\boldsymbol{G}\boldsymbol{G}'} U^{*T}_{\mu\boldsymbol{G}} \tilde{V}_{\boldsymbol{G}-\boldsymbol{G}'}(\boldsymbol{k}_1) U_{\nu\boldsymbol{G}'}\right) e^{i\boldsymbol{k}_1\boldsymbol{r}} . \tag{A.5}$$

A similar equation can be obtained for the spin-orbit velocity $\boldsymbol{v}_{\mu\nu}$. For the spin-orbit energy one obtains

$$H^{SO\,(loc)}_{\mu\nu}(\boldsymbol{r},\boldsymbol{r}') = H^{SO}_{\mu\nu}(\boldsymbol{r})\Delta(\boldsymbol{r}-\boldsymbol{r}')\,, \tag{A.6}$$

with

$$H^{SO}_{\mu\nu}(\boldsymbol{r}) = \sum_{\boldsymbol{k}_1}\left(\sum_{\boldsymbol{G}\boldsymbol{G}'} U^{*T}_{\mu\boldsymbol{G}}\tilde{\boldsymbol{v}}_{\boldsymbol{G}-\boldsymbol{G}'}(\boldsymbol{k}_1)\cdot\hbar\boldsymbol{G}' U_{\nu\boldsymbol{G}'}\right)e^{i\boldsymbol{k}_1\boldsymbol{r}}\,, \tag{A.7}$$

We note that $\boldsymbol{G}_1 \neq 0$ only when $\boldsymbol{k}-\boldsymbol{k}'$ is outside the first Brillouin zone. Since for slowly varying envelope functions both $\boldsymbol{k}$ and $\boldsymbol{k}'$ are close the zone center, the local approximation is justified in this case.

A.2. Asymptotic form of the potential term far from the interface

Starting from Eq. (A.1) and using

$$\big\langle \boldsymbol{k}+\boldsymbol{G}\big|\hat{V}\big|\boldsymbol{k}'+\boldsymbol{G}'\big\rangle = \frac{1}{\Omega}\int \mathrm{d}^3r''\,V(\boldsymbol{r}'')e^{-i(\boldsymbol{k}-\boldsymbol{k}'+\boldsymbol{G}-\boldsymbol{G}')\cdot\boldsymbol{r}''}\,, \tag{A.8}$$

we have

$$V_{\mu\nu}(\boldsymbol{r},\boldsymbol{r}') = \sum_{\boldsymbol{G}\boldsymbol{G}'} U^{*T}_{\mu\boldsymbol{G}}U_{\nu\boldsymbol{G}'}\int \mathrm{d}^3r''\,\Delta(\boldsymbol{r}-\boldsymbol{r}'')V(\boldsymbol{r}'')e^{-i(\boldsymbol{G}-\boldsymbol{G}')\cdot\boldsymbol{r}''}\Delta(\boldsymbol{r}''-\boldsymbol{r}')\,. \tag{A.9}$$

The integrand is appreciably different from zero only around $\boldsymbol{r}$ and $\boldsymbol{r}'$. Thus, for $\boldsymbol{r}$ and $\boldsymbol{r}'$ away from any interface, one can replace $V(\boldsymbol{r}'')$ with the appropriate bulk potential $V^{bulk}(\boldsymbol{r}'')$. The bulk potential has the periodicity of the crystal lattice, and we can write down its plane wave expansion as

$$V^{bulk}(\boldsymbol{r}) = \sum_{\boldsymbol{G}} V^{bulk}_{\boldsymbol{G}}e^{i\boldsymbol{G}\cdot\boldsymbol{r}}\,, \tag{A.10}$$

and one has

$$\begin{aligned}\big\langle \boldsymbol{k}+\boldsymbol{G}\big|\hat{V}^{bulk}\big|\boldsymbol{k}'+\boldsymbol{G}'\big\rangle &= \sum_{\boldsymbol{G}''} V^{bulk}_{\boldsymbol{G}''}\frac{1}{\Omega}\int \mathrm{d}^3r\,e^{-i(\boldsymbol{k}-\boldsymbol{k}'+\boldsymbol{G}-\boldsymbol{G}'-\boldsymbol{G}'')\cdot\boldsymbol{r}}\\ &= \sum_{\boldsymbol{G}''} V^{bulk}_{\boldsymbol{G}''}\frac{1}{\Omega}\int \mathrm{d}^3r\,e^{-i(\boldsymbol{k}_1-\boldsymbol{G}_1+\boldsymbol{G}-\boldsymbol{G}'-\boldsymbol{G}'')\cdot\boldsymbol{r}}\,,\end{aligned} \tag{A.11}$$

where $\boldsymbol{k}_1 = \boldsymbol{k}-\boldsymbol{k}'+\boldsymbol{G}_1$ is within the first Brillouin zone and $\boldsymbol{G}_1$ is a reciprocal lattice vector. Let $\boldsymbol{G}'' \to \boldsymbol{G}''-\boldsymbol{G}_1$ (as $\boldsymbol{G}''$ is a dummy variable) and obtain:

$$\begin{aligned}\big\langle \boldsymbol{k}+\boldsymbol{G}\big|\hat{V}^{bulk}\big|\boldsymbol{k}'+\boldsymbol{G}'\big\rangle &= \sum_{\boldsymbol{G}''} V^{bulk}_{\boldsymbol{G}''}\frac{1}{\Omega}\int \mathrm{d}^3r\,e^{-i(\boldsymbol{k}_1+\boldsymbol{G}-\boldsymbol{G}'-\boldsymbol{G}'')\cdot\boldsymbol{r}}\\ &= \sum_{\boldsymbol{G}''} V^{bulk}_{\boldsymbol{G}''}\delta_{\boldsymbol{k}_1,\boldsymbol{0}}\delta_{\boldsymbol{G}'',\boldsymbol{G}-\boldsymbol{G}'}\\ &= V^{bulk}_{\boldsymbol{G}-\boldsymbol{G}'}\delta_{\boldsymbol{k},\boldsymbol{k}'}\,.\end{aligned} \tag{A.12}$$

Substituting this expression into the effective potential gives

$$V_{\mu\nu}(\boldsymbol{r},\boldsymbol{r}') = V_{\mu\nu}^{bulk}\Delta(\boldsymbol{r}-\boldsymbol{r}')\,, \tag{A.13}$$

where

$$\begin{aligned} V_{\mu\nu}^{bulk} &= \sum_{\boldsymbol{G}\boldsymbol{G}'} U_{\mu\boldsymbol{G}}^{*T} V_{\boldsymbol{G}-\boldsymbol{G}'}^{bulk} U_{\nu\boldsymbol{G}'} \\ &= \frac{1}{\Omega_0}\int \mathrm{d}^3r\, U_\mu^{*T}(\boldsymbol{r}) V^{bulk}(\boldsymbol{r}) U_\nu(\boldsymbol{r})\,. \end{aligned} \tag{A.14}$$

A similar expressions holds for the spin-orbit velocity term

$$\boldsymbol{v}_{\mu\nu}(\boldsymbol{r},\boldsymbol{r}') = \boldsymbol{v}_{\mu\nu}^{bulk}\Delta(\boldsymbol{r}-\boldsymbol{r}')\,, \tag{A.15}$$

with

$$\boldsymbol{v}_{\mu\nu}^{bulk} = \frac{1}{\Omega_0}\int \mathrm{d}^3r\, U_\mu^{*T}(\boldsymbol{r})\frac{\hbar^2}{4m_0^2c^2}(\boldsymbol{\sigma}\times\boldsymbol{\nabla}V^{bulk}(\boldsymbol{r}))U_\nu(\boldsymbol{r})\,. \tag{A.16}$$

For the spin-orbit energy we have

$$H_{\mu\nu}^{SO}(\boldsymbol{r},\boldsymbol{r}') = H_{\mu\nu}^{SO\,bulk}\Delta(\boldsymbol{r}-\boldsymbol{r}') \tag{A.17}$$

with

$$H_{\mu\nu}^{SO\,bulk} = \frac{1}{\Omega_0}\int \mathrm{d}^3r\, U_\mu^{*T}(\boldsymbol{r})\frac{\hbar^2}{4m_0^2c^2}\left(\boldsymbol{\sigma}\times\boldsymbol{\nabla}V^{bulk}(\boldsymbol{r})\right)\cdot\boldsymbol{p}\,U_\nu(\boldsymbol{r})\,. \tag{A.18}$$

A.3. Inclusion of local, slowly varying, external potentials

Consider a local, slowly varying external potential $V^e(\boldsymbol{r})$. Under this assumption, $V^e(\boldsymbol{r})$ has appreciable Fourier components only close to $k\sim 0$:

$$V^e(\boldsymbol{r}) = \sum_{\boldsymbol{k}} \tilde{V}^e(\boldsymbol{k})e^{i\boldsymbol{k}\cdot\boldsymbol{r}}\,. \tag{A.19}$$

Using the local approximation and Eq. (A.5) with

$$\tilde{V}^e_{\boldsymbol{G}-\boldsymbol{G}'}(\boldsymbol{k}) = \tilde{V}^e(\boldsymbol{k})\delta_{\boldsymbol{G},\boldsymbol{G}'}\,, \tag{A.20}$$

we obtain

$$\begin{aligned} V^e_{\mu\nu}(\boldsymbol{r},\boldsymbol{r}') &= \sum_{\boldsymbol{k}}\left(\sum_{\boldsymbol{G}\boldsymbol{G}'} U_{\mu\boldsymbol{G}}^{*T}\tilde{V}^e(\boldsymbol{k})\delta_{\boldsymbol{G},\boldsymbol{G}'}U_{\nu\boldsymbol{G}'}\right)e^{i\boldsymbol{k}\cdot\boldsymbol{r}}\Delta(\boldsymbol{r}-\boldsymbol{r}') \\ &= \sum_{\boldsymbol{k}}\tilde{V}^e(\boldsymbol{k})e^{i\boldsymbol{k}\cdot\boldsymbol{r}}\sum_{\boldsymbol{G}} U_{\mu\boldsymbol{G}}^{*T}U_{\nu\boldsymbol{G}}\Delta(\boldsymbol{r}-\boldsymbol{r}') \\ &= \delta_{\mu\nu}V^e(\boldsymbol{r})\Delta(\boldsymbol{r}-\boldsymbol{r}')\,. \end{aligned} \tag{A.21}$$

A.4. Envelope function equations under a change of basis

In the exact envelope function theory the wave function is expanded according to Eq. (2.3). Let P be the unitary matrix that describes the transformation of the basis set U_μ into a new basis set $\widetilde{U}_\mu$:

$$\widetilde{U}_\mu = \sum_\nu P_{\mu\nu} U_\nu \,. \tag{A.22}$$

Since the transformation matrix is unitary ($P^{-1} = P^\dagger$), the inverse transformation reads

$$\begin{aligned} U_\mu &= \sum_\nu \left(P^{-1}\right)_{\mu\nu} \widetilde{U}_\nu \\ &= \sum_\nu \left(P^\dagger\right)_{\mu\nu} \widetilde{U}_\nu \\ &= \sum_\nu P^*_{\nu\mu} \widetilde{U}_\nu \,. \end{aligned} \tag{A.23}$$

To obtain the envelope expansion in the new basis, we plug Eq. (A.23) into Eq. (2.3),

$$\begin{aligned} \Psi &= \sum_{\mu\nu} P^*_{\nu\mu} \widetilde{U}_\nu \psi_\mu \\ &= \sum_\mu \widetilde{U}_\mu \sum_\nu P^*_{\mu\nu} \psi_\nu \\ &= \sum_\mu \widetilde{U}_\mu \widetilde{\psi}_\mu \,, \end{aligned} \tag{A.24}$$

where we have defined the transformed envelope function component $\widetilde{\psi}_\mu$ as

$$\widetilde{\psi}_\mu = \sum_\nu P^*_{\mu\nu} \psi_\nu \,, \tag{A.25}$$

and in going from the first to the second line in Eq. (A.24) we have simply interchanged the dummy indices μ and ν. By comparing Eq. (A.22) with Eq. (A.25) we see that if P is the unitary matrix that transforms the U_μ functions to the new basis, the envelope functions ψ_μ instead transforms to the new basis through the complex conjugated matrix P^*.

As a result, as the BUrt-Foreman Hamiltonian Eq. (**??**) acts on the envelope functions ψ_μ, it transforms as

$$\begin{aligned} \widetilde{H}^{BF} &= P^* H^{BF} (P^*)^\dagger \\ &= P^* H^{BF} P^T \,, \end{aligned} \tag{A.26}$$

where P^T denotes the transpose of the matrix P.

A.5. Functional variation of the multiband action integral

In this section we show that a functional variation of the action integral

$$\mathcal{A} = \sum_{\mu\nu} \int \mathrm{d}\boldsymbol{r}_\perp \psi^*_\mu \mathcal{L}_{\mu\nu} \psi_\nu \,, \tag{A.27}$$

with the lagrangian density

$$\mathcal{L}_{\mu\nu} = \sum_{\alpha\beta=x,y} \Big(-\overleftarrow{\partial}_\alpha \bar{D}^{\alpha\beta}_{\mu\nu} \overrightarrow{\partial}_\beta \; + \bar{F}^{\alpha}_{L,\mu\nu} \overrightarrow{\partial}_\alpha - \overleftarrow{\partial}_\alpha \bar{F}^{\alpha}_{R,\mu\nu} \Big) + \bar{G}_{\mu\nu} - E\,\delta_{\mu\nu} \,, \tag{A.28}$$

gives the multiband envelope function equations after invoking the principle of least action

$$\delta\mathcal{A} = 0 \,. \tag{A.29}$$

Given a generic functional $\mathcal{F}$ of the wave function ψ and its derivatives,

$$\mathcal{F} = \mathcal{F}\left(\psi, \psi^*, \frac{\partial \psi}{\partial x}, \frac{\partial \psi^*}{\partial x}, \ldots \right) \,, \tag{A.30}$$

we define the functional variation of $\mathcal{F}$ with respect to ψ^* as

$$\delta_{\psi^*}\mathcal{F} = \frac{\partial \mathcal{F}}{\partial \psi^*}\delta\psi^* + \frac{\partial \mathcal{F}}{\partial\left(\frac{\partial\psi^*}{\partial x}\right)} \delta\left(\frac{\partial \psi^*}{\partial x}\right) + \ldots \tag{A.31}$$

The functional $\mathcal{A}$ is a sum of terms that contain both first order and second order differential operators, as well as homogeneous terms. First, we consider the variation of second order term with $\alpha = x$ and $\beta = y$. We have

$$\begin{aligned} \delta\left(\int \mathrm{d}x\mathrm{d}y \, \frac{\partial \psi^*_\mu}{\partial x} D^{xy}_{\mu\nu} \frac{\partial \psi_\nu}{\partial y} \right) &= \int \mathrm{d}x\mathrm{d}y \, \frac{\partial(\delta\psi^*_\mu)}{\partial x} D^{xy}_{\mu\nu} \frac{\partial \psi_\nu}{\partial y} \\ &= -\int \mathrm{d}x\mathrm{d}y \, \delta\psi^*_\mu \partial_x D^{xy}_{\mu\nu} \partial_y \psi_\nu + \oint \delta\psi^*_\mu D^{\alpha\beta}_{\mu\nu} \partial_y \psi_\nu \mathrm{d}y \\ &= -\int \mathrm{d}x\mathrm{d}y \, \delta\psi^*_\mu \partial_x D^{xy}_{\mu\nu} \partial_y \psi_\nu + \oint \delta\psi^*_\mu D^{xy}_{\mu\nu} \partial_y \psi_\nu \cos(\theta)\mathrm{d}S \,, \end{aligned} \tag{A.32}$$

where integration by parts in two dimension has been used in going from the first line to the second line. In going from the second line to the third one we have used the fact that $\mathrm{d}y = \cos(\theta)\mathrm{d}S$, where $\mathrm{d}S$ represent the differential arc length on the boundary S, and θ is the angle that $\vec{n}$, i.e. the unit normal vector to the boundary S, forms with the x-axis of a cartesian reference system. The direction of the path of the contour integral is performed such that the domain is always located on the left and $\vec{n}$ is always oriented outside the integration domain.

Analogous equations hold for the remaining second order terms:

$$\delta\left(\int \mathrm{d}x\mathrm{d}y \, \frac{\partial \psi^*_\mu}{\partial y} D^{yx}_{\mu\nu} \frac{\partial \psi_\nu}{\partial x} \right) = -\int \mathrm{d}x\mathrm{d}y \, \delta\psi^*_\mu \partial_y D^{yx}_{\mu\nu} \partial_x \psi_\nu + \oint \delta\psi^*_\mu D^{yx}_{\mu\nu} \partial_x \psi_\nu \sin(\theta)\mathrm{d}S \,, \tag{A.33}$$

$$\delta\left(\int \mathrm{d}x\mathrm{d}y \, \frac{\partial \psi^*_\mu}{\partial x} D^{xx}_{\mu\nu} \frac{\partial \psi_\nu}{\partial x} \right) = -\int \mathrm{d}x\mathrm{d}y \, \delta\psi^*_\mu \partial_x D^{xx}_{\mu\nu} \partial_x \psi_\nu + \oint \delta\psi^*_\mu D^{xx}_{\mu\nu} \partial_x \psi_\nu \cos(\theta)\mathrm{d}S \,, \tag{A.34}$$

$$\delta\left(\int \mathrm{d}x\mathrm{d}y\,\frac{\partial\psi_\mu^*}{\partial x}D_{\mu\nu}^{yy}\frac{\partial\psi_\nu}{\partial x}\right) = -\int \mathrm{d}x\mathrm{d}y\,\delta\psi_\mu^*\partial_y D_{\mu\nu}^{yy}\partial_y\psi_\nu + \oint \delta\psi_\mu^* D_{\mu\nu}^{yy}\partial_y\psi_\nu\,\mathrm{sin}(\theta)\mathrm{d}S\,. \tag{A.35}$$

For the first order terms we have

$$\delta\left(\int \mathrm{d}x\mathrm{d}y\,\psi_\mu^* F_{L,\mu\nu}^{x}\frac{\partial\psi_\nu}{\partial x}\right) = \int \mathrm{d}x\mathrm{d}y\,\delta\psi_\mu^* F_{L,\mu\nu}^{x}\frac{\partial\psi_\nu}{\partial x}\,, \tag{A.36}$$

$$\delta\left(\int \mathrm{d}x\mathrm{d}y\,\psi_\mu^* F_{L,\mu\nu}^{x}\frac{\partial\psi_\nu}{\partial x}\right) = \int \mathrm{d}x\mathrm{d}y\,\delta\psi_\mu^* F_{L,\mu\nu}^{x}\partial_x\psi_\nu\,, \tag{A.37}$$

$$\delta\left(\int \mathrm{d}x\mathrm{d}y\,\psi_\mu^* F_{L,\mu\nu}^{y}\frac{\partial\psi_\nu}{\partial y}\right) = \int \mathrm{d}x\mathrm{d}y\,\delta\psi_\mu^* F_{L,\mu\nu}^{y}\partial_y\psi_\nu\,, \tag{A.38}$$

$$\delta\left(\int \mathrm{d}x\mathrm{d}y\,\frac{\partial\psi_\mu^*}{\partial x}F_{R,\mu\nu}^{x}\psi_\nu\right) = -\int \mathrm{d}x\mathrm{d}y\,\delta\psi_\mu^*\partial_x F_{R,\mu\nu}^{x}\psi_\nu + \oint \delta\psi_\mu^* F_{R,\mu\nu}^{x}\psi_\nu\,\mathrm{cos}(\theta)\mathrm{d}S\,, \tag{A.39}$$

$$\delta\left(\int \mathrm{d}x\mathrm{d}y\,\frac{\partial\psi_\mu^*}{\partial y}F_{R,\mu\nu}^{y}\psi_\nu\right) = -\int \mathrm{d}x\mathrm{d}y\,\delta\psi_\mu^*\partial_y F_{R,\mu\nu}^{y}\psi_\nu + \oint \delta\psi_\mu^* F_{R,\mu\nu}^{y}\psi_\nu\,\mathrm{sin}(\theta)\mathrm{d}S\,. \tag{A.40}$$

Let us first assume that the integration domain consists only of one region, as it happens for example for single material nanowires. In this case, if we assume Dirichlet boundary conditions at the outer boundary, the surface terms vanish there. In fact, if we fix the value of ψ_μ at the outer boundary, any arbitrary variation $\delta\psi_\mu^*$ will be zero there.

Let us consider instead a multi-convex domain, where the integration domain consists of two or more regions, as it happens for example in core-shell nanowires, where different regions corresponds to different materials. In this case, we face two kinds of boundary surfaces: the interfaces between two different materials and the outer surface. As in the case of single material nanowires, if we assume that the wave function is fixed at the outer boundary, the surface terms vanish there. On the contrary, the surface terms at any material interface do not vanish *a priori*. Anyway, it can be shown that setting all these leftover surface terms to zero is equivalent to the conservation of the probability current across the material interfaces. In other words, the probability current conservation is naturally included in the problem by simply setting all the surface terms to zero.

To show that this is true, we evaluate the probability current vector components J_x and J_y as in Ref. [86], i.e., we substitute $\psi_\nu \to e^{i\Lambda(x,y)}\psi_\nu$ in Eq. (A.27) and perform a functional variation of the Lagrangian with respect to the gauge function $\Lambda(x,y)$. We have

$$\begin{aligned}\mathrm{J}_x = \frac{1}{\hbar}\left(\frac{\delta\mathcal{L}_{\mu\nu}}{\delta(\partial_x\Lambda)}\right)\Bigg|_{\Lambda=0} &= \frac{i}{\hbar}[-\psi_\mu^* D_{\mu\nu}^{xx}\partial_x\psi_\nu + (\partial_x\psi_\mu^*)D_{\mu\nu}^{xx}\psi_\nu - \psi_\mu^* D_{\mu\nu}^{xy}\partial_y\psi_\nu + (\partial_y\psi_\mu^*)D_{\mu\nu}^{yx}\psi_\nu \\ &+ \psi_\mu^* F_{L,\mu\nu}^{x}\psi_\nu - \psi_\mu^* F_{R,\mu\nu}^{x}\psi_\nu]\,,\end{aligned} \tag{A.41}$$

$$\begin{aligned}\mathrm{J}_y = \frac{1}{\hbar}\left(\frac{\delta\mathcal{L}_{\mu\nu}}{\delta(\partial_y\Lambda)}\right)\Bigg|_{\Lambda=0} &= \frac{i}{\hbar}[-\psi_\mu^* D_{\mu\nu}^{yy}\partial_y\psi_\nu + (\partial_y\psi_\mu^*)D_{\mu\nu}^{yy}\psi_\nu - \psi_\mu^* D_{\mu\nu}^{yx}\partial_x\psi_\nu + (\partial_x\psi_\mu^*)D_{\mu\nu}^{xy}\psi_\nu \\ &+ \psi_\mu^* F_{L,\mu\nu}^{y}\psi_\nu - \psi_\mu^* F_{R,\mu\nu}^{y}\psi_\nu]\,.\end{aligned} \tag{A.42}$$

Thus, following Ref. [86], the conservation of the normal component of the probability current requires the continuity of the following quantity across any material interface:

$$\begin{aligned}&D^{xx}_{\mu\nu}\partial_x\psi\,\mathsf{cos}(\theta) + D^{yy}_{\mu\nu}\partial_y\psi\,\mathsf{sin}(\theta)\\ &+ D^{xy}_{\mu\nu}\partial_y\psi\,\mathsf{cos}(\theta) + D^{yx}_{\mu\nu}\partial_x\psi\,\mathsf{sin}(\theta)\\ &+ F^{x}_{R,\mu\nu}\psi\,\mathsf{cos}(\theta) + F^{y}_{R,\mu\nu}\psi\,\mathsf{sin}(\theta) = \text{continuous}\,.\end{aligned} \tag{A.43}$$

Note that the condition in Eq. (A.43) exactly cancels the contributions of the interface terms in the variation of the action integral. To see that this is the case, we can consider the example of a core-shell nanowire with two different materials for the core and the shell regions, respectively. In this case, if we set the wave function to zero at the outer boundary, we are left with the surface terms originated just by the interface between these two different materials. The direction of the path of the contour integral at the interface is clockwise for the core region and anticlockwise for the shell region. As a result, one is left with the difference between the surface terms calculated for one material minus the ones calculated for the other material. It easy to see from the above equations that setting this difference to zero coincides with the probability current continuity condition in Eq. (A.43).

Eventually, the functional variation of the action integral $\mathcal{A}$ reads

$$\delta_{\psi^*_\mu}\mathcal{A} = \int \mathsf{d}x\mathsf{d}y\,\delta\psi^*_\mu \sum_\nu \left(\sum_{\alpha,\beta=x',y'} \partial_\alpha \bar{D}^{\alpha\beta}_{\mu\nu}\partial_\beta + \sum_{\alpha=x,y} \left(\bar{F}^{\alpha}_{L,\mu\nu}\partial_\alpha + \partial_\alpha \bar{F}^{\alpha}_{R,\mu\nu}\right) + \bar{G}_{\mu\nu} - E\delta_{\mu\nu} \right)\psi_\nu\,. \tag{A.44}$$

Since the variation $\delta\psi^*_\mu$ is arbitrary, the principle of least action Eq. (A.29) requires the integrand of Eq. (A.44) to identically vanish, which gives the envelope function equations

$$\sum_\nu H^{BF}_{\mu\nu}\psi_\nu = E\psi_\nu\,, \tag{A.45}$$

with H^{BF} given in Eq. (2.69).

A.6. Finite elements: implementation details

In this appendix we explain how to implement the finite element method (FEM) for the multiband envelope function equations (EFEs) and the Poisson equation. As already discussed in Sec. 2.5.1, the FEM discretization of the EFEs lead to a generalized eigenvalue problem of the form of Eq. (2.93). The solution of Eq. (2.93) gives the unknown coefficients $\psi_{\mu I}$ of an expansion of the form of Eq. (2.84).

The Hamiltonian matrix $\mathcal{H}_{\mu\nu IJ}$ as well as the overlap matrix $\mathcal{S}_{\mu\nu IJ}$ are constructed through an element-wise assembly procedure. For each element i_{el} of the simulation domain, we first evaluate the corresponding element matrix from Eq. (2.87). Explicitly, given the form of the Lagrangian density op-

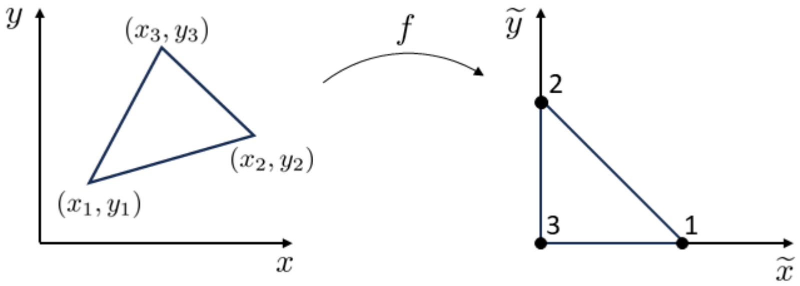

Figure A.1: The real element (left) and its mapping to the reference triangle (right).

erator in Eq. (2.80), we need to evaluate the following quantity

$$\begin{aligned}\mathcal{H}^{(i_{el})}_{\mu\nu,ij} = &-\int_{\Omega_{i_{el}}} \mathrm{d}\boldsymbol{r}_\perp \sum_{\alpha\beta=x,y} (\partial_\alpha N_i(\boldsymbol{r}_\perp))\bar{D}^{\alpha\beta}_{\mu\nu}(\boldsymbol{r}_\perp)(\partial_\beta N_j(\boldsymbol{r}_\perp)) \\ &+\int_{\Omega_{i_{el}}} \mathrm{d}\boldsymbol{r}_\perp \sum_{\alpha=x,y} N_i(\boldsymbol{r}_\perp)\bar{F}^{\alpha}_{L,\mu\nu}(\boldsymbol{r}_\perp)(\partial_\alpha N_j(\boldsymbol{r}_\perp)) \\ &-\int_{\Omega_{i_{el}}} \mathrm{d}\boldsymbol{r}_\perp \sum_{\alpha=x,y} (\partial_\alpha N_i(\boldsymbol{r}_\perp)\bar{F}^{\alpha}_{R,\mu\nu}(\boldsymbol{r}_\perp)N_j(\boldsymbol{r}_\perp) \\ &+\int_{\Omega_{i_{el}}} \mathrm{d}\boldsymbol{r}_\perp N_i(\boldsymbol{r}_\perp)\bar{G}_{\mu\nu}(\boldsymbol{r}_\perp)N_j(\boldsymbol{r}_\perp)\end{aligned} \tag{A.46}$$

for the Hamiltonian operator, while for the overlap matrix we have

$$\mathcal{S}^{(i_{el})}_{\mu\nu,IJ} = \int_{\Omega_{i_{el}}} \mathrm{d}\boldsymbol{r}_\perp N_i(\boldsymbol{r}_\perp)\delta_{\mu\nu}N_j(\boldsymbol{r}_\perp)\,. \tag{A.47}$$

Note that the matrices $\bar{D}^{\alpha\beta}_{\mu\nu}(\boldsymbol{r}_\perp)$, $\bar{F}^{\alpha}_{L,\mu\nu}(\boldsymbol{r}_\perp)$, $\bar{F}^{\alpha}_{R,\mu\nu}(\boldsymbol{r}_\perp)$ and $\bar{G}_{\mu\nu}(\boldsymbol{r}_\perp)$ can in principle depend on the position vector $\boldsymbol{r}_\perp$ inside each element i_{el}. A common approach in FEM is to perform the two-dimensional integrals in Eq. (A.46), defined on the *real* element $\Omega_{i_{el}}$, in the so called *standard or reference* element $\widetilde{\Omega}_{i_{el}}$ instead. For simplicity, let us consider the case of triangular elements used in this work. The real element, with coordinates (x_i, y_i) with $i = 1, 2, 3$ in the global coordinate system, is mapped to a unique reference triangle in the $\widetilde{x}, \widetilde{y}$ plane through an affine transformation f. In this work, the mapping f is defined by the relation

$$\begin{pmatrix} x - x_3 \\ y - y_3 \end{pmatrix} = \mathbf{J}\begin{pmatrix} \widetilde{x} \\ \widetilde{y} \end{pmatrix} , \tag{A.48}$$

where

$$\mathbf{J} = \begin{pmatrix} x_1 - x_3 & x_2 - x_3 \\ y_1 - y_3 & y_2 - y_3 \end{pmatrix} = \begin{pmatrix} \frac{\partial x}{\partial \widetilde{x}} & \frac{\partial x}{\partial \widetilde{y}} \\ \frac{\partial y}{\partial \widetilde{x}} & \frac{\partial y}{\partial \widetilde{y}} \end{pmatrix} . \tag{A.49}$$

The determinant $|\mathbf{J}|$ of the matrix $\mathbf{J}$ is the Jacobian of the transformation from the area element dxdy to d$\widetilde{x}$d$\widetilde{y}$. The labeling of the nodes in the real element as well as in the reference element are shown in Fig. (A.1). In particular, we see that the mapping f transforms the node with coordinates (x_i,y_i) of the real element into the point labelled with i in the reference element.

The differential operators ∂_x and ∂_y in Eq. (A.46) transform to the reference triangle as

$$\frac{\partial}{\partial x} = \frac{\partial \widetilde{x}}{\partial x}\frac{\partial}{\partial \widetilde{x}} + \frac{\partial \widetilde{y}}{\partial x}\frac{\partial}{\partial \widetilde{y}}\,, \tag{A.50}$$

$$\frac{\partial}{\partial y} = \frac{\partial \widetilde{x}}{\partial y}\frac{\partial}{\partial \widetilde{x}} + \frac{\partial \widetilde{y}}{\partial y}\frac{\partial}{\partial \widetilde{y}}\,, \tag{A.51}$$

where [62]

$$\frac{\partial \widetilde{x}}{\partial x} = \frac{1}{|\mathbf{J}|}\frac{\partial y}{\partial \widetilde{y}}\,, \tag{A.52}$$

$$\frac{\partial \widetilde{y}}{\partial x} = -\frac{1}{|\mathbf{J}|}\frac{\partial y}{\partial \widetilde{x}}\,, \tag{A.53}$$

$$\frac{\partial \widetilde{x}}{\partial y} = -\frac{1}{|\mathbf{J}|}\frac{\partial x}{\partial \widetilde{y}}\,, \tag{A.54}$$

$$\frac{\partial \widetilde{y}}{\partial y} = \frac{1}{|\mathbf{J}|}\frac{\partial x}{\partial \widetilde{x}}\,. \tag{A.55}$$

Thus, Eq. (A.46) transferred to the reference element reads

$$\begin{aligned}
\mathcal{H}^{(i_{el})}_{\mu\nu,ij} = &-\int_{\widetilde{\Omega}_{i_{el}}} \mathrm{d}\widetilde{\boldsymbol{r}}_\perp \sum_{\alpha\beta=x,y} \left(\sum_{\widetilde{\alpha}=\widetilde{x},\widetilde{y}} \frac{\partial\widetilde{\alpha}}{\partial\alpha}\partial_{\widetilde{\alpha}} N_i(\widetilde{\boldsymbol{r}}_\perp)\right) \bar{D}^{\alpha\beta}_{\mu\nu}(\widetilde{\boldsymbol{r}}_\perp) \left(\sum_{\widetilde{\beta}=\widetilde{x},\widetilde{y}} \frac{\partial\widetilde{\beta}}{\partial\beta}\partial_{\widetilde{\beta}} N_j(\widetilde{\boldsymbol{r}}_\perp)\right) |\mathbf{J}| \\
&+\int_{\widetilde{\Omega}_{i_{el}}} \mathrm{d}\widetilde{\boldsymbol{r}}_\perp \sum_{\alpha=x,y} N_i(\widetilde{\boldsymbol{r}}_\perp)\bar{F}^{\alpha}_{L,\mu\nu}(\widetilde{\boldsymbol{r}}_\perp) \left(\sum_{\widetilde{\alpha}=\widetilde{x},\widetilde{y}} \frac{\partial\widetilde{\alpha}}{\partial\alpha}\partial_{\widetilde{\alpha}} N_j(\widetilde{\boldsymbol{r}}_\perp)\right) |\mathbf{J}| \\
&-\int_{\widetilde{\Omega}_{i_{el}}} \mathrm{d}\widetilde{\boldsymbol{r}}_\perp \sum_{\alpha=x,y} \left(\sum_{\widetilde{\alpha}=\widetilde{x},\widetilde{y}} \frac{\partial\widetilde{\alpha}}{\partial\alpha}\partial_{\widetilde{\alpha}} N_i(\widetilde{\boldsymbol{r}}_\perp)\right) \bar{F}^{\alpha}_{R,\mu\nu}(\widetilde{\boldsymbol{r}}_\perp) N_j(\widetilde{\boldsymbol{r}}_\perp)|\mathbf{J}| \\
&+\int_{\widetilde{\Omega}_{i_{el}}} \mathrm{d}\widetilde{\boldsymbol{r}}_\perp N_i(\widetilde{\boldsymbol{r}}_\perp)\bar{G}_{\mu\nu}(\widetilde{\boldsymbol{r}}_\perp)N_j(\widetilde{\boldsymbol{r}}_\perp)|\mathbf{J}|\,,
\end{aligned} \tag{A.56}$$

while Eq. (A.47) becomes

$$\mathcal{S}^{(i_{el})}_{\mu\nu,ij} = \int_{\widetilde{\Omega}_{i_{el}}} \mathrm{d}\widetilde{\boldsymbol{r}}_\perp N_i(\widetilde{\boldsymbol{r}}_\perp)\delta_{\mu\nu}(\widetilde{\boldsymbol{r}}_\perp)N_j(\widetilde{\boldsymbol{r}}_\perp)|\mathbf{J}|\,. \tag{A.57}$$

The integrals in Eqs. (A.46) and (A.47) can be evaluated using Gauss quadrature in two dimensions [62]. Once the element matrices $\mathcal{H}_{\mu\nu,ij}$ and $\mathcal{S}_{\mu\nu,ij}$ are obtained for each element of the mesh, the corresponding global matrices $\mathcal{H}_{\mu\nu,IJ}$ and $\mathcal{S}_{\mu\nu,IJ}$ are obtained by carefully overlaying the single element matrices, as explained in Sec. 2.5.1.

For the Poisson equation, the finite element discretization lead to the linear system in Eq. (2.97) for the electrostatic potential $\phi(\boldsymbol{r}_\perp)$. The element matrix for the stiffness term is given by

$$C^{(i_{el})}_{ij} = \int_{\Omega_{i_{el}}} \epsilon(\boldsymbol{r}_\perp) \sum_{\alpha=x,y} \partial_\alpha N_i(\boldsymbol{r}_\perp)\partial_\alpha N_j(\boldsymbol{r}_\perp)\,, \tag{A.58}$$

while for the mass term we have

$$b^{(i_{el})}_i = \int_{\Omega_{i_{el}}} N_i(\boldsymbol{r}_\perp)\frac{\rho(\boldsymbol{r}_\perp)}{\epsilon_0}\,. \tag{A.59}$$

Again, when the integrals are performed within the reference element we have

$$C_{ij}^{(i_{el})} = \int_{\widetilde{\Omega}_{i_{el}}} \epsilon(\widetilde{\boldsymbol{r}}_\perp) \sum_{\alpha=x,y} \left(\sum_{\widetilde{\alpha}=\widetilde{x},\widetilde{y}} \frac{\partial\widetilde{\alpha}}{\partial\alpha} \partial_{\widetilde{\alpha}} N_i(\widetilde{\boldsymbol{r}}_\perp) \right) \left(\sum_{\widetilde{\alpha}=\widetilde{x},\widetilde{y}} \frac{\partial\widetilde{\alpha}}{\partial\alpha} \partial_{\widetilde{\alpha}} N_j(\widetilde{\boldsymbol{r}}_\perp) \right) |\mathbf{J}| \tag{A.60}$$

for the stiffness element matrix, and

$$b_i^{(i_{el})} = \int_{\widetilde{\Omega}_{i_{el}}} N_i(\widetilde{\boldsymbol{r}}_\perp) \frac{\rho(\widetilde{\boldsymbol{r}}_\perp)}{\epsilon_0} |\mathbf{J}| \tag{A.61}$$

for the load vector.

In this work we always assume constant bulk band parameters for a given material region, as well as heterostructures with abrupt interfaces that coincide with the finite elements boundaries. In this case, the coefficient matrices that enter the Hamiltonian operator are always constant in each element, and we can bring them outside the integrals in Eqs. (A.46) and (A.47). So, the remaining integrals only depend on the coordinates of the element and on the shape functions $N(\widetilde{\boldsymbol{r}}_\perp)$. This means that, in the actual self-consistent band structure calculations for nanowires, we evaluate this set of integrals once for all, i.e. independently of the value of the free wave vector k_z and only at the first iteration of the self-consistent cycle. Since $\epsilon(\boldsymbol{r}_\perp)$ is also constant within each element of the mesh, an analogous reasoning holds for the Poisson equation when dealing with the integral in Eq. (A.60).

On the contrary the element matricx corresponding to the electrostatic potential $\phi(\boldsymbol{r}_\perp)$ in the EFEs,

$$\mathcal{V}_{\mu\nu,ij}^{(i_{el})} = -e \int_{\widetilde{\Omega}_{i_{el}}} \mathrm{d}\widetilde{\boldsymbol{r}}_\perp N_i(\widetilde{\boldsymbol{r}}_\perp) \delta_{\mu\nu} \phi(\widetilde{\boldsymbol{r}}_\perp) N_j(\widetilde{\boldsymbol{r}}_\perp) |\mathbf{J}| \,,$$

and the mass term in the Poisson equation, Eq. (A.61), are evaluated at each iteration of the self-consistent cycle. Note that both the electrostatic potential $\phi(\boldsymbol{r}_\perp)$ and the charge density $\rho(\boldsymbol{r}_\perp)$ are allowed to vary within each finite element and can not be factorized outside of the integrals.

Up to now we have assumed that the wave function inside each element is approximated using an expansion of the form in Eq. (2.84), i.e. a Lagrange polynomial expansion of a given order. If instead the wave function is approximated inside each element using the Hermite polynomial expansion in Eq. (2.85), the above equations are slightly modified. To simplify the notation, we can write Eq. (2.85) in a more compact form by introducing an additional index to keep into account that at each node of the mesh the solution of the problem has now three nodal degrees-of-freedom, i.e. the value of the wave function and its first derivatives. Thus, we have

$$\psi_\mu(\boldsymbol{r}_\perp) \simeq \sum_{j=1}^{3} \sum_{\gamma=1}^{3} \psi_{\mu j\gamma} N_{j\gamma}^{H}(\boldsymbol{r}_\perp) \,, \tag{A.62}$$

where $\gamma = 1$ corresponds to the value of the function, while $\gamma = 2$ and $\gamma = 3$ corresponds to the first derivatives with respect to x and y, respectively. Correspondingly, the element matrix in Eq. (2.87) becomes

$$\mathcal{M}_{\mu\nu,ij,\gamma\delta}^{(i_{el})} = \int_{\Omega_{el}} d\boldsymbol{r}_\perp N_{i\gamma}(\boldsymbol{r}_\perp) \mathcal{L}_{\mu\nu} N_{j\delta}(\boldsymbol{r}_\perp) \tag{A.63}$$

The dimension of each element matrix is given by the number of nodes in each element n_{nod} times the number of component of the multiband problem n_{dof} times the number of degrees-of-freedom per node n_{comp}. Thus, for the 8-band $\mathbf{k}\cdot\mathbf{p}$ envelope function equations, if we use the Hermite interpolation on a mesh composed of triangular elements, each element matrix has dimension $8 \times 3 \times 3 = 72$. Eventually, the Hamiltonian and overlap element matrices for the Hermite elements are given by Eqs. (A.46) and (A.47) where the shape functions have now an additional index accounting for the presence of multiple degrees-of-freedom on each node.

With Hermite interpolation, the representation of the wave function $\psi_\mu(\boldsymbol{r}_\perp)$ in terms of interpolation functions defined on the reference element requires a further step. In order to reproduce reproduces $\frac{\partial\psi_\mu(\boldsymbol{r}_\perp)}{\partial x}=\psi'_{\mu j,x}$ and $\frac{\partial\psi_\mu(\boldsymbol{r}_\perp)}{\partial y}=\psi'_{\mu j,y}$ when $\boldsymbol{r}_\perp=(x_j,y_j)$ we need to use a modified form of the Hermite expansion Eq. (A.62), i.e.

$$\psi_\mu(\boldsymbol{r}_\perp) \simeq \sum_{j=1}^{3}\sum_{\gamma=1}^{3} \psi_{\mu j\gamma}\widetilde{N}^H_{j\gamma}(\widetilde{\boldsymbol{r}}_\perp)\,, \tag{A.64}$$

where

$$\begin{aligned}
\widetilde{N}^H_{j1}(\widetilde{\boldsymbol{r}}_\perp) &= N^H_{j1}(\widetilde{\boldsymbol{r}}_\perp)\,,\\
\widetilde{N}^H_{j2}(\widetilde{\boldsymbol{r}}_\perp) &= \mathbf{J}_{11}N^H_{j2}(\widetilde{\boldsymbol{r}}_\perp) + \mathbf{J}_{12}N^H_{j,3}(\widetilde{\boldsymbol{r}}_\perp)\,,\\
\widetilde{N}^H_{j3}(\widetilde{\boldsymbol{r}}_\perp) &= \mathbf{J}_{21}N^H_{j2}(\widetilde{\boldsymbol{r}}_\perp) + \mathbf{J}_{22}N^H_{j3}(\widetilde{\boldsymbol{r}}_\perp)
\end{aligned} \tag{A.65}$$

are the modified shape functions in the reference element.

A.6.1. Lagrange and Hermite triangular elements

Here we report the analytical expressions of the interpolation functions used in this work.

Lagrange linear elements
Three interpolation nodes that coincide with the triangle's vertices.

$$\begin{aligned}
\widetilde{N}_1 &= \widetilde{x}\\
\widetilde{N}_2 &= \widetilde{y}\\
\widetilde{N}_3 &= 1 - \widetilde{x} - \widetilde{y}
\end{aligned} \tag{A.66}$$

Lagrange quadratic elements
Six interpolation nodes. $j = 1,2,3$ coincide with the triangle's vertices. $j = 4,5,6$ are mid-side located on the edges 2-3, 3-1, 1-2, respectively, where the edge i-j connects the triangle's vertices i and j.

$$\begin{aligned}
\widetilde{N}_1 &= -\widetilde{x} + 2\widetilde{x}^2\\
\widetilde{N}_2 &= -\widetilde{y} + 2\widetilde{y}^2\\
\widetilde{N}_3 &= 1 - 3\widetilde{x} - 3\widetilde{y} + 2\widetilde{x}^2 + 4\widetilde{x}\widetilde{y} + 2\widetilde{y}^2\\
\widetilde{N}_4 &= 4\widetilde{y} - 4\widetilde{x}\widetilde{y} - 4\widetilde{y}^2\\
\widetilde{N}_5 &= 4\widetilde{x} - 4\widetilde{x}\widetilde{y} - 4\widetilde{x}^2\\
\widetilde{N}_6 &= 4\widetilde{x}\widetilde{y}
\end{aligned} \tag{A.67}$$

Hermite cubic elements

Three interpolation nodes that coincide with the triangle's vertices, with three degrees-of-freedom per node (the value of the function and its first derivatives with respect to x and y)

$$
\begin{aligned}
\widetilde{N}^H_{11} &= \widetilde{x}^2(3-2\widetilde{x}) + 2\widetilde{x}\widetilde{y}\,(1-\widetilde{x}-\widetilde{y})\\
\widetilde{N}^H_{21} &= \widetilde{y}^2(3-2\widetilde{y}) + 2\widetilde{x}\widetilde{y}\,(1-\widetilde{x}-\widetilde{y})\\
\widetilde{N}^H_{31} &= (1-\widetilde{x}-\widetilde{y})^2\,(3-2\,(1-\widetilde{x}-\widetilde{y})) + 2\widetilde{x}\widetilde{y}\,(1-\widetilde{x}-\widetilde{y})\\
\widetilde{N}^H_{12} &= \widetilde{x}^2(\widetilde{x}-1.) - \widetilde{x}\widetilde{y}\,(1-\widetilde{x}-\widetilde{y})\\
\widetilde{N}^H_{22} &= \widetilde{x}\widetilde{y}^2 + \frac{1}{2}\widetilde{x}\widetilde{y}\,(1-\widetilde{x}-\widetilde{y})\\
\widetilde{N}^H_{32} &= \widetilde{x}\,(1-\widetilde{x}-\widetilde{y})^2 + \frac{1}{2}\widetilde{x}\widetilde{y}\,(1-\widetilde{x}-\widetilde{y})\\
\widetilde{N}^H_{13} &= \widetilde{x}^2\widetilde{y} + \frac{1}{2}\widetilde{x}\widetilde{y}\,(1-\widetilde{x}-\widetilde{y})\\
\widetilde{N}^H_{23} &= \widetilde{y}^2(\widetilde{y}-1) - \widetilde{x}\widetilde{y}\,(1-\widetilde{x}-\widetilde{y})\\
\widetilde{N}^H_{33} &= \widetilde{y}\,(1-\widetilde{x}-\widetilde{y})^2 + \frac{1}{2}\widetilde{x}\widetilde{y}\,(1-\widetilde{x}-\widetilde{y})
\end{aligned}
\tag{A.68}
$$

B

Appendices for chapter 4

B.1. Angular momentum projections

In order to obtain the projections of the different states onto the value $m_j = 1/2$ we employ the following procedure. First, we consider the following eigenvalue equation:

$$\hat{J}_z \left|\Phi\right\rangle = m_j \left|\Phi\right\rangle \,, \tag{B.1}$$

where $\hat{J}_z = \left(\hat{L}_z \otimes \mathbb{1}_{\text{spin}}\right) \oplus \left(\mathbb{1}_{\text{orb}} \otimes \hat{S}_z\right)$ and $\langle \boldsymbol{r}|\Phi\rangle = \sum_{\nu=1}^{8} \phi^{\nu}(\boldsymbol{r}_\perp) \left|S, S_z\right\rangle e^{ik_z z}$, being $\left|S, S_z\right\rangle$ an eigenstate of the total pseudospin angular momentum $\boldsymbol{S}$ in symmetry adapted basis Eq. (2.65). In the position representation the z-component of the orbital angular momentum operator is written as $\hat{L}_z = -i\hbar(x\partial_y - y\partial_x)$. We then solve Eq. (B.1) using FEM on the hexagonal domain and obtain a set of $n_{dof} \times 8$ eigenvalues end eigenvectors, being n_{dof} the total number of vertices in the mesh. Since the equation is solved on an hexagonal domain (thus braking cylindrical symmetry) we find a continuous distribution of the eigenvalues of $\hat{J}_z$ along the real axis. However, we find that the density of eigenvalues is tightly peaked around half-integer values $(2l-1)\hbar/2$ with $l \in \mathbb{Z}$. To quantify the projections of each eigenstate of the nanowire (NW) Hamiltonian $\left|\Psi\right\rangle$ onto a single $\widetilde{m}_j$ sector we evaluate the following quantity for each value of the wave vector k_z:

$$C_{\widetilde{m}_j} = \frac{\displaystyle\sum_{\pm m_j \in I_{\widetilde{m}_j}} \left|\left\langle \Phi_{m_j} \middle| \Psi \right\rangle\right|^2}{N} \,, \tag{B.2}$$

where $\langle \boldsymbol{r}|\Psi\rangle = \sum_{\nu=1}^{8} \psi^{\nu}(\boldsymbol{r}_\perp) \left|S, S_z\right\rangle e^{ik_z z}$ and the sum is performed considering the set of eigenvalues m_j that fall within an given interval $I_{\widetilde{m}_j}$ centered around $\widetilde{m}_j$ and $N = \sum_{m_j} \left|\left\langle \Phi_{m_j} \middle| \Psi \right\rangle\right|^2$ is a normalization factor which is required since the two set of eigenstates we are projecting onto each other are not orthonormal.

B.2. Extraction of SOC and effective mass values

In this section we show how we obtain the values of the spin-orbit coupling (SOC) coefficient and effective mass values of the highest-energy subband pair of the hexagonal NW. We actually used the same fitting approach of Ref. [49] with minor adjustments. As anticipated in the main text, the highest energy hole states of the NW are well described by the following 2×2 fitting Hamiltonian

$$H_{\text{fit}} = \left(E_{\text{mean}} + \frac{\hbar^2 k_z^2}{2\bar{m}} \right) \sigma_0 + \left(\frac{\delta E}{2} + \frac{\hbar^2 k_z^2}{2\widetilde{m}} \right) \sigma_z + \alpha \sigma_y k_z \,, \tag{B.3}$$

where E_{mean} is the mean energy of the two subbands at $k_z = 0$, δE is the energy splitting at $k_z = 0$ between the two states, and $\bar{m}$ is the harmonic mean of the effective masses m_1 and m_2 of the two subbands, i.e.,

$$\bar{m} = \frac{2 m_1 m_2}{m_1 + m_2} \,, \tag{B.4}$$

and

$$\frac{1}{\widetilde{m}} = \frac{m_2 - m_1}{2 m_1 m_2} \,. \tag{B.5}$$

Here, σ_i are Pauli matrices for an *effective* spin-$1/2$ degree of freedom. Note that, in contrast to the case of spin-$1/2$ electrons in semiconductor NWs, the highest-energy hole subband pair has contributions from both states with spin projection $\pm 3/2$ (HHs) and $\pm 1/2$ (LHs). We will show this explicitly, and how Eq. (B.3) can be derived from the Luttinger-Kohn Hamiltonian, in the next Section.

The fitting Hamiltonian H_{fit} has the spectrum:

$$E_{\pm}\left(k_z\right) = \left(E_{\text{mean}} + \frac{\hbar^2 k_z^2}{2\bar{m}} \right) \pm \left(\frac{\delta \widetilde{E}(k_z)}{2} \right) \sqrt{1 + \frac{4 \alpha^2 k_z^2}{\delta \widetilde{E}(k_z)^2}} \,, \tag{B.6}$$

being

$$\delta \widetilde{E}(k_z) = \delta E + \frac{\hbar^2 k_z^2}{\widetilde{m}^*} \,. \tag{B.7}$$

Using Eq. (B.6) one can in principle fit the numerical results of the 8-band $\mathbf{k} \cdot \mathbf{p}$ model and extract the coefficients α, $\bar{m}$ and $\widetilde{m}$. However, as was already noted in Ref. [49], the effect of the SOC is dominated by the energy splitting δE, and thus a fitting cannot resolve it. To overcome this issue we basically follow the solution proposed in the supplementary material of Ref. [49], with a minor adjustment. The numerical diagonalization of the envelope function equations for hexagonal NWs gives access only to a subset of eigenstates close the a predefined energy region of interest. In this case we only calculate a few subbands close to the valence band edge of GaSb. On the contrary, the authors in Ref. [49] assume that the entire spectrum has been obtained after the numerical diagonalization of the 8-band Hamiltonian. This is probably numerically accessible in that work, as the NWs are modeled in a cylindrical approximation, and only the radial (thus one dimensional) envelope function equations have to be solved.

Anyway, even if we only know a reduced subset of low energy eigenstates from the numerical diagonalization, the proposed approach is still applicable with a few clarifications. First, we diagonalize the 8-band $\mathbf{k} \cdot \mathbf{p}$ Hamiltonian $H_{n_{dof} \times n_{dof}}$ at $k_z = 0$, and write the q lowest energy eigenvectors in the columns of the rectangular matrix $X_{n_{dof} \times q}$. The matrix X diagonalizes the Hamiltonian H, such that $X^\dagger H X = \Lambda$, where Λ is an $q \times q$ matrix containing the eigenvalues λ_i ($i = 1, ..., q$) on the diagonal.

Now we construct the matrix $\widetilde{\Lambda} = \text{diag}(-\frac{\delta E}{2}, +\frac{\delta E}{2}, 0, ..., 0)$. The matrix $\widetilde{\Lambda}$ is then used to shift the two subbands of the first subband pair such that the two states have the same energy at $k_z = 0$. To implement the energy shifting technique, we compute the matrix $\delta H = OX\widetilde{\Lambda}X^\dagger O^\dagger$, where O is an overlap matrix such that $X^\dagger O X = \mathbb{1}_{q\times q}$, and diagonalize the Hamiltonian $\widetilde{H}(k_z) = H(k_z) + \delta H$ as a function of k_z. In the perturbed spectrum $\delta E \simeq 0$ and the spin-orbit effect is now pronounced, and α can be fit with much improved certainty. Although we included the parameter $\widetilde{m}$ in the fitting procedure, to keep into account that the two subbands can have different effective masses, in Fig. 4.3 of the main text we show only results for the harmonic mean effective mass $\bar{m}$ of the subband pair (as in Ref. [49]). The reason is that $1/\widetilde{m}$ is in general very small and, in any case, the extracted values or α are essentially independent of $\widetilde{m}$. Note that $\bar{m}$ is extracted from the band structure of the original Hamiltonian $H(k_z)$.

B.3. Effective two-band Hamiltonian for holes

As justified in the main text, the low-energy physics the GaSb-InP tubular-core NW can be described through a four-band Luttinger-Kohn (LK) Hamiltonian with cylindrical symmetry. In the eigenbasis of the spin-3/2 angular momentum operator $\{|S_z = +3/2\rangle, |S_z = +1/2\rangle, |S_z = -1/2\rangle, |S_z = -3/2\rangle\}$, the LK Hamiltonian can be written as

$$H_{\text{LK}} = \left(\gamma_1 + \frac{5}{2}\gamma_{\text{s}}\right)\frac{p^2}{2m_0} - \frac{\gamma_{\text{s}}}{m_0}\left(\boldsymbol{p}\cdot\boldsymbol{S}\right)^2 \,, \tag{B.8}$$

where $\boldsymbol{p} = \hbar\boldsymbol{k} = -i\hbar\boldsymbol{\nabla}$ is the momentum operator, γ_1 and $\gamma_s = (\gamma_2 + \gamma_3)/2$ are the Luttinger parameters of GaSb and m_0 is the free electron mass. Since $(\gamma_3 - \gamma_2)/\gamma_1 \ll 1$ in GaSb, anisotropic corrections to the LK Hamiltonian are small and the isotropic approximation is well justified. In this section we show that how to derive a 2×2 effective Hamiltonian that describes the highest-energy subbands pair starting from Eq.B.8.

To account for cylindrical symmetry we rotate the Hamiltonian to a cylindrical coordinate system using the unitary operator $U = e^{-iS_z\varphi}$, which acts on the operators as:

$$U^\dagger \boldsymbol{p} U = \boldsymbol{p} - \boldsymbol{e}_\varphi \hbar S_z, \tag{B.9}$$

$$U^\dagger \boldsymbol{S} U = \boldsymbol{e}_r S_x + \boldsymbol{e}_\varphi S_y + \boldsymbol{e}_z S_z, \tag{B.10}$$

$$U^\dagger p^2 U = p_r^2 - \frac{i\hbar}{r}p_r + \frac{p_\varphi^2 - 2\hbar p_\varphi S_z + \hbar^2 S_z^2}{r^2} + p_z^2, \tag{B.11}$$

$$\begin{aligned} U^\dagger(\boldsymbol{p}\cdot\boldsymbol{S})^2 U &= \left(p_r S_x - \frac{i\hbar S_x}{r} + \frac{p_\varphi S_y}{r} - \frac{\hbar S_z S_y}{r} + p_z S_z\right)^2 \\ &= p_r^2 S_x^2 - \frac{2i\hbar}{r}p_r S_x^2 - \frac{\hbar}{r}p_r\left\{S_x, S_z S_y\right\} + \frac{i\hbar^2}{r^2}S_z S_y S_x + \frac{\hbar^2}{r^2}(S_z S_y)^2 \\ &+ \frac{p_\varphi}{r}p_r\left\{S_x, S_y\right\} - \frac{i\hbar}{r^2}p_\varphi S_y S_x + \frac{p_\varphi^2}{r^2}S_y^2 - \frac{\hbar}{r^2}p_\varphi\left\{S_z S_y, S_y\right\} + \frac{p_\varphi}{r}p_z\left\{S_y, S_z\right\} \\ &+ p_r p_z\left\{S_z, S_x\right\} - \frac{\hbar}{r}p_z\left\{S_z S_y, S_z\right\} - \frac{i\hbar}{r}p_z\left\{S_x, S_z\right\} + p_z^2 S_z^2 \,. \end{aligned} \tag{B.12}$$

where $p_r = -i\hbar\partial_r$, $p_\varphi = -i\hbar\partial_\varphi$, $p_z = -i\hbar\partial_z$, and

$$\boldsymbol{e}_r = \cos(\varphi)\boldsymbol{e}_x + \sin(\varphi)\boldsymbol{e}_y \,, \tag{B.13}$$

$$\boldsymbol{e}_\varphi = -\sin(\varphi)\boldsymbol{e}_x + \cos(\varphi)\boldsymbol{e}_y \,. \tag{B.14}$$

In performing these calculations, we have made use of the commutation relations $[p_\varphi, \boldsymbol{e}_{\boldsymbol{\varphi}}] = i\hbar\boldsymbol{e}_r$, $[p_\varphi, \boldsymbol{e}_r] = -i\hbar\boldsymbol{e}_\varphi$ and $\left[k_r, r^{-1}\right] = ir^{-2}$. Now we rewrite the above expressions in terms of the hermitean radial momentum

$$p_r = -i\hbar\left(\frac{\partial}{\partial r} + \frac{1}{2r}\right) \,. \tag{B.15}$$

To do that one simply needs to perform the replacements:

$$\begin{aligned} p_r &\to p_r + \frac{i\hbar}{2r} \\ p_r^2 &\to p_r^2 + \frac{i\hbar}{r}\left(-i\hbar\frac{\partial}{\partial r}\right) - \frac{\hbar^2}{4r^2} \,. \end{aligned} \tag{B.16}$$

Making the above substitution one gets

$$U^\dagger p^2 U = p_r^2 - \frac{\hbar^2}{4r^2} + \frac{p_\varphi^2 - 2\hbar p_\varphi S_z + \hbar^2 S_z^2}{r^2} + p_z^2 \tag{B.17}$$

$$\begin{aligned} U^\dagger(\boldsymbol{p}\cdot\boldsymbol{S})^2 U = {} & p_r^2 S_x^2 + \frac{\hbar^2}{4r^2}S_x^2 - \frac{i\hbar}{r}p_r S_x^2 - \frac{\hbar}{r}p_r\left\{S_x, S_z S_y\right\} + \frac{i\hbar^2}{2r^2}\left[S_z S_y, S_x\right] + \frac{\hbar^2}{r^2}(S_z S_y)^2 \,, \\ & + \frac{p_\varphi}{r}p_r\left\{S_x, S_y\right\} + \frac{i\hbar}{2r^2}p_\varphi\left[S_x, S_y\right] + \frac{p_\varphi^2}{r^2}S_y^2 - \frac{\hbar}{r^2}p_\varphi\left\{S_z S_y, S_y\right\} + \frac{p_\varphi}{r}p_z\left\{S_y, S_z\right\} \\ & + p_r p_z\left\{S_z, S_x\right\} - \frac{i\hbar}{2r}p_z\left\{S_z, S_x\right\} - \frac{\hbar}{r}p_z\left\{S_z S_y, S_z\right\} + p_z^2 S_z^2. \end{aligned} \tag{B.18}$$

We can now write down the rotated Hamiltonian $\widetilde{H}_{\mathsf{LK}} = U^\dagger H_{\mathsf{LK}} U$ using the standard representation of the 4×4 angular momentum matrices $\boldsymbol{S}$ for a spin $3/2$ system. The matrix elements of this Hamiltonian are

$$
\begin{aligned}
\left(\widetilde{H}_{\mathsf{LK}}\right)_{11} &= \frac{\hbar^2}{2m_0}\left\{(\gamma_1+\gamma_s)\left(k_r^2+\frac{k_\varphi^2-3k_\varphi+2}{r^2}\right)+(\gamma_1-2\gamma_s)k_z^2\right\},\\
\left(\widetilde{H}_{\mathsf{LK}}\right)_{22} &= \frac{\hbar^2}{2m_0}\left\{(\gamma_1-\gamma_s)\left(k_r^2+\frac{k_\varphi^2-k_\varphi}{r^2}\right)+(\gamma_1+2\gamma_s)k_z^2\right\},\\
\left(\widetilde{H}_{\mathsf{LK}}\right)_{33} &= \frac{\hbar^2}{2m_0}\left\{(\gamma_1-\gamma_s)\left(k_r^2+\frac{k_\varphi^2+k_\varphi}{r^2}\right)+(\gamma_1+2\gamma_s)k_z^2\right\},\\
\left(\widetilde{H}_{\mathsf{LK}}\right)_{44} &= \frac{\hbar^2}{2m_0}\left\{(\gamma_1+\gamma_s)\left(k_r^2+\frac{k_\varphi^2+3k_\varphi+2}{r^2}\right)+(\gamma_1-2\gamma_s)k_z^2\right\},\\
\left(\widetilde{H}_{\mathsf{LK}}\right)_{12} &= -\frac{\gamma_s}{m_0}\hbar^2\sqrt{3}\,k_z\left(k_r-\frac{i(k_\varphi-1)}{r}\right),\\
\left(\widetilde{H}_{\mathsf{LK}}\right)_{13} &= -\frac{\gamma_s}{m_0}\frac{\sqrt{3}}{2}\hbar^2\left(k_r^2-\frac{i(2k_\varphi-1)}{r}k_r-\frac{k_\varphi^2-2k_\varphi}{r^2}\right),\\
\left(\widetilde{H}_{\mathsf{LK}}\right)_{14} &= \left(\widetilde{H}_{\mathsf{LK}}\right)_{23}=0,\\
\left(\widetilde{H}_{\mathsf{LK}}\right)_{24} &= -\frac{\gamma_s}{m_0}\frac{\sqrt{3}}{2}\hbar^2\left(k_r^2-\frac{i(2k_\varphi+1)}{r}k_r-\frac{k_\varphi^2-1}{r^2}\right),\\
\left(\widetilde{H}_{\mathsf{LK}}\right)_{34} &= -\frac{\gamma_s}{m_0}\hbar^2\sqrt{3}\,k_z\left(-k_r+\frac{i(k_\varphi+1)}{r}\right).
\end{aligned}
\tag{B.19}
$$

where $k_r=-i(\partial_r+1/2r)$ and $k_\varphi=-i\partial_\varphi$. The rest of the elements can be derived taking into account that $\widetilde{H}_{\mathsf{LK}}$ must be hermitian[1].

We note that total angular momentum $J_z=p_\varphi+\hbar S_z$ in the original coordinate system transforms as $U^\dagger J_z U=p_\varphi$ in the rotated frame. As a consequence, p_φ is a good quantum number and each eigenstate of the Hamiltonian is also an eigenstate $|\pm l\rangle$ of the total angular momentum with eigenvalue $\hat{p}_\varphi\,|\pm l\rangle=\pm\hbar(l-1/2)\,|\pm l\rangle$, being $l\in\mathbb{N}$. In the same way, k_z is also a good quantum number, as the NW is translationally invariant along the NW's axis.

Now we obtain a 2×2 Hamiltonian that describes the first subband pair with total angular momentum $m_j=1/2$. To do that, we first split the Hamiltonian $\widetilde{H}_{\mathsf{LK}}$ in two parts as

$$
\widetilde{H}_{\mathsf{LK}}=H_0+H'\,, \tag{B.20}
$$

where $H_0=\widetilde{H}_{\mathsf{LK}}(k_z=0)$ is the zero-order Hamiltonian, while $H'=\widetilde{H}_{\mathsf{LK}}(k_z)-H_0$ is treated as a perturbation. Since we are interested in the first subband pair with total angular momentum $m_j=1/2$, we can focus on the $m_j=1/2$ sector only, and replace k_φ with $k_\varphi=1/2$ in Eq. (B.19). Now we can, in principle, numerically diagonalize the Hamiltonian H_0 and obtain a finite set of eigenstates $|i\rangle$ with the eigenergies E_i such that $H_0\,|i\rangle=E_i\,|i\rangle$. Each eigenstate $|i\rangle$ can be expressed as

$$
|i\rangle=\sum_\beta f_{i,\beta}(r)\,|\beta\rangle\,|l=1\rangle \tag{B.21}
$$

where $f_{i,\beta}$ is a radial envelope function component of the i-the subband eigenstate with $\beta=1,2,3,4$ corresponding to the basis states $\{|S_z=+3/2\rangle\,,|S_z=+1/2\rangle\,,|S_z=-1/2\rangle\,,|S_z=-3/2\rangle\}$, and $|l=1\rangle$

---

[1] When taking the hermitean conjugates of the above matrix elements, we make use of the commutator $[k_r,r^{-1}]=i/r^2$.

is an eigenstate of the total angular momentum operator with eigenvalue $\hat{p}_\varphi \left|l=1\right\rangle = \hbar(1/2)\left|l=1\right\rangle$. It easy to note from the matrix elements in Eq. (B.19) that at k_z=0 the LK Hamiltonian H_0 separates in two disconnected blocks: one block couples the states $\left|S_z=+3/2\right\rangle$ with $\left|S_z=-1/2\right\rangle$, while the other block couples the states $\left|S_z=-3/2\right\rangle$ with $\left|S_z=+1/2\right\rangle$. As a result, the eigenstates of the first subband pair with $m_j=1/2$ can be written as

$$\begin{aligned}\left|\text{LH1}\right\rangle &= \left(f_{\text{LH1},1}(r)\left|1\right\rangle + f_{\text{LH1},3}(r)\left|3\right\rangle\right)\left|l=1\right\rangle \\ \left|\text{LH2}\right\rangle &= \left(f_{\text{LH},2}(r)\left|2\right\rangle + f_{\text{LH},4}(r)\left|4\right\rangle\right)\left|l=1\right\rangle\end{aligned}\ , \tag{B.22}$$

At the lowest order in perturbation theory, we can obtain an effective Hamiltonian for these two states by projecting the full Hamiltonian $\widetilde{H}_{\text{LK}} = H_0 + H'$ onto the basis $\{\left|\text{LH1}\right\rangle, \left|\text{LH2}\right\rangle\}$. The matrix elements of H_0 in this basis yield the eigenenergies of the two subbands at the Γ point E_{LH1} and E_{LH2} separated by an energy splitting $\delta E = E_{\text{LH2}} - E_{\text{LH1}}$ while the matrix elements of H' have to be computed as

$$\langle i|H'|j\rangle = \int_0^R \mathrm{d}r\, r \sum_{\beta,\beta'}^{4} f^*_{i,\beta} H'_{\beta\beta'} f_{j,\beta'} \tag{B.23}$$

where R indicates the total radius of the nanowire, and we have implicitly assumed that the angular integration in dφ between the two eigenstates of the total angular momentum gives 1, i.e.

$$\langle l=1|l=1\rangle = \frac{1}{2\pi}\int_0^{2\pi} \mathrm{d}\varphi\, e^{-i(1/2)} e^{i(1/2)} = 1\,. \tag{B.24}$$

Explicitly, we obtain

$$\begin{aligned}\langle \text{LH1}|H'|\text{LH2}\rangle = &-\frac{\gamma_s}{m}\hbar^2\sqrt{3}\,k_z \int_0^R \mathrm{d}r\, r f^*_{\text{LH1},1}(r)\left(k_r + \frac{i}{2r}\right) f_{\text{LH2},2}(r) \\ &-\frac{\gamma_s}{m}\hbar^2\sqrt{3}\,k_z \int_0^R \mathrm{d}r\, r f^*_{\text{LH1},3}(r)\left(-k_r + \frac{3i}{2r}\right) f_{\text{LH2},4}(r)\,,\end{aligned} \tag{B.25}$$

$$\langle \text{LH1}|H'|\text{LH2}\rangle = \frac{\hbar^2 k_z^2}{2m}\left(\gamma_1 + 2\gamma_s(|c_{\text{LH1},3}|^2 - |c_{\text{LH1},1}|^2)\right)\ , \tag{B.26}$$

$$\langle \text{LH2}|H'|\text{LH2}\rangle = \frac{\hbar^2 k_z^2}{2m}\left(\gamma_1 + 2\gamma_s(|c_{\text{LH2},2}|^2 - |c_{\text{LH2},4}|^2)\right)\ , \tag{B.27}$$

where we defined

$$|c_{i,\beta}|^2 = \int_0^R \mathrm{d}r\, r|f_{i,\beta}(r)|^2\,, \tag{B.28}$$

with the normalization condition

$$\sum_\beta |c_{i,\beta}|^2 = 1 \quad \forall i\,. \tag{B.29}$$

Note that the Hamiltonian H_0 is real and symmetric, thus we can chose the envelope functions $f_{i,\beta}(r)$ to be real. As a result, being $k_r = -i(\partial_r + 1/2r)$, the off-diagonal matrix element in Eq. (B.25) is purely imaginary. The obtained effective 2×2 Hamiltonian can be eventually written a more compact form as

$$H_{\text{eff}} = \left(E_{\text{mean}} + \frac{\hbar^2 k_z^2}{2\bar{m}}\right)\sigma_0 + \left(\frac{\delta E}{2} + \frac{\hbar^2 k_z^2}{2\widetilde{m}}\right)\sigma_z + \alpha_{\text{eff}}\sigma_y k_z\,, \tag{B.30}$$

where E_0 and δE are the mean energy and the energy splitting at $k_z=0$ between the two subbands, respectively, $\bar{m}$ is given my Eq. (B.4) with m_1 and m_2 replaced by

$$m_{\text{LH1}} = \frac{m_0}{\gamma_1 + 2\gamma_s(c_{\text{LH1},3} - c_{\text{LH1},1})} \tag{B.31}$$

and

$$m_{\text{LH2}} = \frac{m_0}{\gamma_1 + 2\gamma_s(c_{\text{LH2},2} - c_{\text{LH2},4})}\,, \tag{B.32}$$

respectively, while

$$\frac{1}{\tilde{m}} = \frac{m_{\text{LH2}} - m_{\text{LH1}}}{2m_{\text{LH1}}m_{\text{LH2}}}\,. \tag{B.33}$$

Note that the Hamiltonian in Eq. (B.30) is completely analogous to Eq. (B.3) with the effective SOC coefficient given by

$$\begin{aligned} \alpha_{\text{eff}} =& \frac{\gamma_s}{m_0}\hbar^2\sqrt{3}\int_0^R \mathrm{d}r\, r f_{\text{LH1},1}(r)\left(-ik_r + \frac{1}{2r}\right) f_{\text{LH2},2}(r) \\ +& \frac{\gamma_s}{m_0}\hbar^2\sqrt{3}\int_0^R \mathrm{d}r\, r f_{\text{LH1},3}(r)\left(ik_r + \frac{3}{2r}\right) f_{\text{LH2},4}(r)\,. \end{aligned} \tag{B.34}$$

As already noted, the envelope functions $f_{i,\beta}$ can be found through a numerical diagonalization of the Hamiltonian H_0. An alternative, analytical approach is to assume a reasonable functional form for the $f_{i,\beta}$ and integrate out the radial degrees of freedom. The results of the 8-band $\mathbf{k}\cdot\mathbf{p}$ calculations in Ch. 4 show that the charge density of the nanowire is almost completely confined in the GaSb shell. Thus, it is reasonable to expand the radial wave function onto the the following basis states [200]

$$\psi_n(r) = \sqrt{\frac{2}{w\,r}}\sin\left(\frac{n\pi}{w}\left(r - R_{\text{av}} - \frac{w}{2}\right)\right), \tag{B.35}$$

where $n \in \mathbb{N}$ stems for different radial subbands and $\psi_n(r)$ satisfies hard-wall boundary conditions at $R_{\text{av}} \pm w/2$, being $R_{\text{av}} \equiv R - w/2$ an average effective radius.

For the states $|\text{LH1}\rangle$ and $|\text{LH2}\rangle$, which correspond to the first radial mode, we can consider only $n = 1$ in the expansion. Explicitly, we have

$$\begin{aligned} |\text{LH1}\rangle &= \psi_1(r)\left(c_{\text{LH1},1}|1\rangle + c_{\text{LH1},3}|3\rangle\right)|l=1\rangle \\ |\text{LH2}\rangle &= \psi_1(r)\left(c_{\text{LH},2}|2\rangle + c_{\text{LH},4}|4\rangle\right)|l=1\rangle \end{aligned}\,. \tag{B.36}$$

By plugging Eq. (B.36) into Eq. (B.34), and using the fact that $\langle\psi_1|k_r|\psi_1\rangle = 0$, we can obtain an analytical expression for the effective SOC coefficient, i.e.

$$\begin{aligned} \alpha_{\text{eff}} &= \frac{\gamma_s}{m_0}\hbar^2\sqrt{3}\left(\frac{\chi_{12} + 3\chi_{34}}{2}\right)\int_0^R \mathrm{d}r\,\psi_1^2(r) \\ &= \frac{\gamma_s}{m_0}\hbar^2\sqrt{3}\left(\frac{\chi_{12} + 3\chi_{34}}{2}\right)\left(\frac{-2\mathcal{I}}{w}\right) \end{aligned} \tag{B.37}$$

where

$$\mathcal{I} = \int_0^\pi \frac{\sin^2(x)}{(x-a)}\mathrm{d}x\,, \tag{B.38}$$

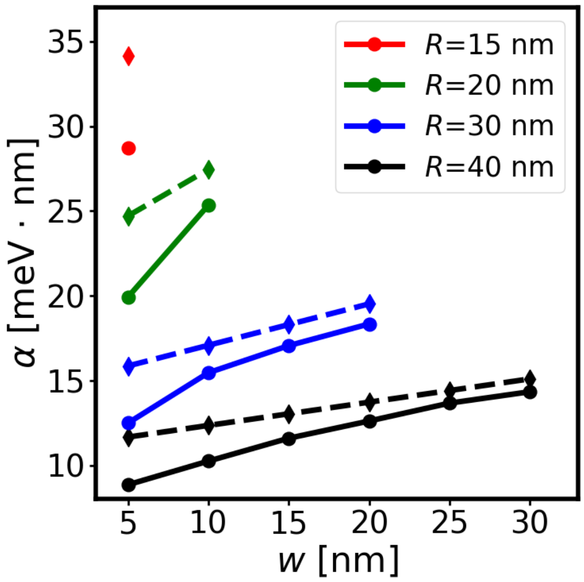

Figure B.1: Spin-orbit coupling of InP/GaSb core-shell nanowires from the Luttinger-Khon effective Hamiltonian Spin-orbit coupling of the highest-energy subbands as a function of GaSb shell thickness w for different wire radii R obtained from the 8-band k·p numerical simulations presented in the main text (full line, dots) and from the effective theory (dashed line, diamonds), calculated using Eq. (B.41) with χ_{12}=χ_{34}=0.3, corresponding to $c_{\text{LH1},1}$=$c_{\text{LH2},4}$=$\sqrt{0.1}$ and $c_{\text{LH1},2}$=$c_{\text{LH2},3}$=$\sqrt{0.9}$ [see Eqs. (B.28) and (B.39)]

with $a = (R/w)\pi$, and

$$\begin{aligned}\chi_{12} &= c_{\text{LH1},1}\, c_{\text{LH3},2}\,,\\ \chi_{34} &= c_{\text{LH1},3}\, c_{\text{LH2},4}\,.\end{aligned} \tag{B.39}$$

Using a Taylor expansion up to first order of $\frac{1}{x-a}$ for $|a| >> |x|$ the integral $\mathcal{I}$ can be approximated as

$$\mathcal{I} \sim -\frac{\pi}{2a} - \frac{\pi^2}{4a^2} + \ldots \tag{B.40}$$

Which gives

$$\alpha_{\text{eff}} = \frac{\gamma_s}{m_0}\hbar^2\sqrt{3}\left(\frac{\chi_{12}+3\chi_{34}}{2}\right)\left(\frac{1}{R}+\frac{w}{2R^2}\right)\,. \tag{B.41}$$

In Fig. (B.1) we show the values of α_{eff} obtained from Eq. (B.41), together with numerical results presented in Fig. 4.3(a), as a function of w for different values of R. We assumed the fixed values $c_{\text{LH1},1}$=$c_{\text{LH2},4}$=$\sqrt{0.1}$ and $c_{\text{LH1},2}$=$c_{\text{LH2},3}$=$\sqrt{0.9}$ for each value of R and w, which is reasonable since the light-hole character dominates in the highest-energy hole states [see Fig. 4.2(b)]. These analytical results are shown together with the numerical ones provided by the 8-band model in Fig. 4.3(a), showing a good agreement.

B.4. Effects of strain in the semiconductor nanowire

It should be noted that in the present derivation we have completely neglected the effect of other subbands which can be close in energy to the first subband pair. A more detailed derivation was performed in Ref. [200] for a system very similar to InP/GaSb core-shell NWs, particularly thin Si/Ge/Si curved quantum wells, but including the effect of strain through the Bir-Pikus Hamiltonian. The authors obtained an effective two-band Hamiltonian that accurately describes the highest-energy hole states of the system through a second-order Schrieffer-Wolff transformation including the effect of the second radial LH subbands as well as the first radial HH subband. Once this two-band Hamiltonian is projected onto the low-energy states $|\mathrm{LH1}\rangle$ and $|\mathrm{LH2}\rangle$, and projected on the radial basis states of Eq. (B.35), with m_j=1/2, they obtain

$$\widetilde{H}^{(\mathrm{s})}_{\mathrm{LK}} \simeq \frac{\hbar^2 k_z^2}{2m_{\mathrm{s}}}\sigma_0 + \alpha_{\mathrm{s}}\sigma_y k_z + \mathcal{O}, \tag{B.42}$$

where

$$\frac{1}{m_{\mathrm{s}}} = \frac{1}{m_0}\left[\gamma_1 + \gamma_{\mathrm{s}}(1+3\tilde{\epsilon}_z) - 3\tilde{\gamma}\right], \tag{B.43}$$

$$\alpha_{\mathrm{s}} = \frac{3}{2}\frac{\hbar^2}{m_0 R}\left[(\gamma_{\mathrm{s}} - \tilde{\gamma}) - (\gamma_1 + \gamma_{\mathrm{s}})\tilde{\epsilon}_z\right], \tag{B.44}$$

and $\mathcal{O}$ includes all the terms that provide the mean energy and the splitting [see Ref. [198, 200]], ignored here for simplicity of the discussion. The definitions of $\tilde{\gamma}$ and $\tilde{\epsilon}_z$ can be found in Ref. [200] as a function of the Luttinger parameters γ_1 and γ_s, and the strain energies along each direction

$$\epsilon_r = |b|\,\varepsilon, \quad \epsilon_r = \frac{w}{2}\left(\frac{R+\frac{\omega}{4}}{\left(R+\frac{\omega}{2}\right)^2}\right)|b|\,\varepsilon, \tag{B.45}$$

being ε the strain coefficient and b the uniaxial deformation potential.

In the absence of strain we have $\varepsilon = 0$ and $\tilde{\epsilon}_z = 0$, and then this Hamiltonian has the same form as the one in Eq. (B.3) and Eq. (B.30). Actually, it provides an estimation for

$$\chi_{12} + 3\chi_{34} \simeq \sqrt{3}\left(1 - \frac{256}{9\pi^2}\frac{1}{10 + 3\gamma_1/\gamma_s}\right) = 1.45, \tag{B.46}$$

that applies to the highest-energy mode. This agrees quantitatively with our numerics, that provide $\chi_{12}+3\chi_{34} = 1.2$ (see above). Since strain typically relaxes sharply at the interface between III-V compound semiconductors in NWs (less than 5 atomic layers), this further justifies the use of Eq. (B.3) for the fitting of the hole SOC α and constitutes another valid method to describe the semiconductor part of the NW.

We can thus legitimately use these results to estimate the effects of strain in the SOC close to the interface where the GaSb shell layer is not relaxed, and it is instead strained by the InP core due to the lattice mismatch $\varepsilon = (a_{\mathrm{GaSb}} - a_{\mathrm{InP}})/a_{\mathrm{GaSb}} \simeq 3.93\%$. This provides $\tilde{\epsilon}_z = 0.07$, and a (detrimental) correction to the SOC of $\sim 20\%$ at the interface.

B.5. Subband splitting in the nanowire

To further evaluate the probability of hosting a topological superconducting (TS) phase in full-shell geometries, we must study the energy splitting between subbands with angular momentum $m_j = 1/2$. These are the only ones capable of hosting a TS phase, as they can effectively wind around a superconducting vortex. It's worth noting that the $m_j = 1/2$ states always appear in pairs, with one pair corresponding to each transverse radial subband. The separation between consecutive

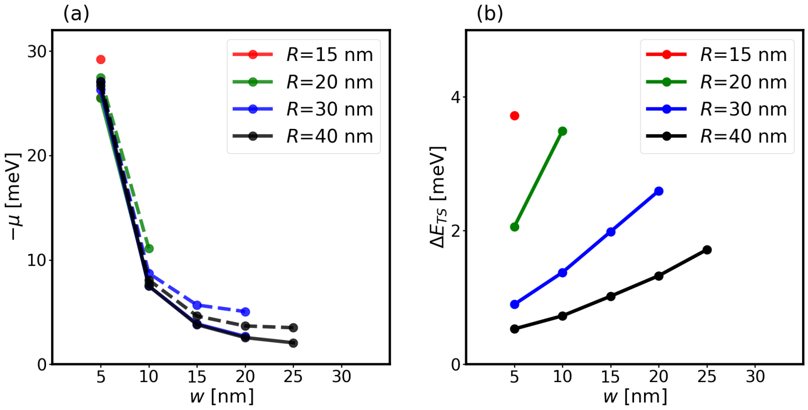

Figure B.2: Topological superconducting window. (a) Crossing points of the chemical potential $-\mu$ with the first (solid lines) and the second (dashed lines) $m_j = 1/2$ highest-energy states vs shell width w for different NW radii R (in different colors). The spacing between the two lines defines the energy window ΔE_{TS} for which a topological superconducting phase is possible, which is plotted in panel (b).

subbands within a pair defines the extent for which a topological superconducting phase is possible and, consequently, the likelihood of encountering Majorana modes at a given fixed chemical potential or doping.

In Fig. B.2(a) we depict the energy position $-\mu$ where the chemical potential cross the highest-energy subband pair with $m_j = 1/2$ vs the shell width w for different wire diameters R. Solid lines indicates the crossing of the first subband of the pair, while dashed lines indicate the crossing with the second one. For simplicity, we display only the first radial mode. In Fig. B.2(b) we explicitly display the topological window ΔE_{TS}, extracted by computing the energy spacing between solid and dashed lines of Fig. B.2(a). Notably, the topological window ranges from approximately 1 to 4 meV across all cases, larger than typical superconducting gaps, e.g., ~ 0.2 meV for Al or ~ 0.5 meV for Sn. While the topological window decreases as the total radius gets bigger, it appears to increase as the shell width increases. This phenomenon can be readily comprehended by examining the analytical equations governing these pairs. Larger shells result in smaller values of R_{av} that lead to a greater level spacing in turn. This agrees with the analytical expression for δE in Eq. (B.30), which is proportional to $R_{\text{av}}^{-2} = (R - \frac{w}{2})^{-2}$, as shown in Ref. [200].

Additionally, we complement this analysis by analyzing the corresponding values of the SOC for these bands, which is shown in Fig. 4.3(a) using the same color coding. Our analysis demonstrates that larger shells yield stronger SOC and wider topological windows. Conversely, smaller diameters also result in enhanced SOC and increased spacing between radial subbands.

C

Appendices for chapter 5

C.1. Nanowire effective model

In this appendix we derive an effective 4×4 Hamiltonian to describe the lowest energy states in InAs-GaSb core-shell nanowires. The nanowire in our model has circular cross section and the electrons move freely in the z-direction. The starting point is the 8-band Kane model, already introduced in Ch. 2, which includes the eight basis states in Eq. (2.65).

From the numerical results obtained in Sec. 5.3 we know that the split-off subbands are well separated in energy from the other bands, hence we neglect the basis states $\left|\frac{1}{2},\pm\frac{1}{2}\right\rangle_{\text{SO}}$ in Eq. (2.65), which results in a six-dimensional basis including the electrons, heavy holes (HHs) and light holes (LHs) Bloch basis states.

$$H_{\text{kp}} = \begin{pmatrix} H_{\text{el}} & H_{\text{el-h}} \\ H_{\text{el-h}}^{\dagger} & H_{\text{LK}} \end{pmatrix} \tag{C.1}$$

where H_{el} describes the s-like conduction band states,

$$H_{\text{el}} = \frac{\hbar^2}{2m^*}(k_x^2 + k_y^2 + k_z^2)\,, \tag{C.2}$$

H_{LK} is the Luttinger-Khon Hamiltonian in axial approximation, Eq. (4.1), and

$$H_{\text{el-h}} = \begin{pmatrix} -\frac{1}{\sqrt{2}}Pk_+ & \sqrt{\frac{2}{3}}Pk_z & \frac{1}{\sqrt{6}}Pk_- & 0 \\ 0 & -\frac{1}{\sqrt{6}}Pk_- & \sqrt{\frac{2}{3}}Pk_z & \frac{1}{\sqrt{2}}Pk_- \end{pmatrix}, \tag{C.3}$$

with $k_\pm = k_x \pm ik_y$, describes the coupling between the conduction band states and the p-like valence band states. As we have done in App. B.3, we rotate the Hamiltonian H_{kp} to a cylindrical coordinate system using the unitary operator $U = e^{-i(\sigma_z \oplus S_z)\varphi}$ and obtain

$$UH_{\text{kp}}U^{\dagger} = \widetilde{H}_{\text{kp}} = \begin{pmatrix} \widetilde{H}_{\text{el}} & \widetilde{H}_{\text{el-h}} \\ \widetilde{H}_{\text{el-h}}^{\dagger} & \widetilde{H}_{\text{LK}} \end{pmatrix}. \tag{C.4}$$

In Eq. (C.4) the matrix element of the rotated Luttinger-Khon Hamiltonian $\widetilde{H}_{\mathsf{LK}}$ are given in Eq. ((B.19)). The remaining rotated blocks In Eq. C.4 are given by

$$\widetilde{H}_{\text{el-h}} = \begin{pmatrix} -\frac{1}{\sqrt{2}}k_+ & \sqrt{\frac{2}{3}}k_z & \frac{1}{\sqrt{6}}k_- & 0 \\ 0 & -\frac{1}{\sqrt{6}}k_+ & \sqrt{\frac{2}{3}}k_z & \frac{1}{\sqrt{2}}k_- \end{pmatrix} + \frac{i\hbar}{\sqrt{2}r}\begin{pmatrix} 1 & 0 & 0 & 0 \\ 0 & 0 & 0 & 1 \end{pmatrix} \tag{C.5}$$

and

$$\widetilde{H}_{\text{el}} = \frac{\hbar^2}{2m^*}\left(k_r^2 + \frac{k_\varphi^2}{r^2} + k_z^2\right)\mathbb{1}_2 - \frac{\hbar^2}{2m^*r^2}k_\varphi\sigma_z\,, \tag{C.6}$$

written in terms of the electron effective mass m^*, the hermitean radial momentum $k_r = -i(\partial_r + 1/2r)$, the orbital angular momentum $k_\varphi = -i\partial\varphi$ and $k_\pm = k_r \pm i\frac{k_\varphi}{r}$.

Analogously to App. B.3, we note that total angular momentum $J_z = p_\varphi + \hbar S_z + \frac{\hbar}{2}\sigma_z$ in the original coordinate system transforms as $U^\dagger F_z U = p_\varphi$ in the rotated frame. As a consequence, p_φ is a good quantum number with quantum numbers $(2l-1)/2$, being $l \in \mathbb{Z}$.

If an electric field $\boldsymbol{E} = E_y\boldsymbol{e}_y$ is present, we need to add the additional energy

$$H_E = -er\,\text{sin}(\varphi)E_x\mathbb{1}_6\,, \tag{C.7}$$

where e is the electron charge and $\mathbb{1}_6$ is a six-dimensional identity matrix.

Now we obtain an effective Hamiltonian that describes the first electron and hole subband pairs with total angular momentum $J_z = \pm 1/2$. To do that, as we have already done in App. B.3, we first split the Hamiltonian $\widetilde{H}_{\mathsf{kp}}$ in two parts as

$$\widetilde{H}_{\mathsf{kp}} = H_0 + H'\,, \tag{C.8}$$

where $H_0 = \widetilde{H}_{\mathsf{kp}}(k_z = 0)$ is the zero-order Hamiltonian, while $H' = \widetilde{H}_{\mathsf{kp}}(k_z) - H_0 + H_E$ is treated as a perturbation.

The eigenstates $|i\rangle$ of the eigenvalue problem $H_0|i\rangle = E_i|i\rangle$ can be written in the form

$$|i_\pm\rangle = \sum_\beta f_{i,\beta}(r)\,|\beta\rangle\,|\pm l\rangle\,. \tag{C.9}$$

where $\beta = 1, ..., 6$ indicates the basis functions of the rotated six-band **k** · **p** Hamiltonian in Eq. (C.4), $|l\rangle$ are eigenstates of the total angular momentum with eigenvalues $p_\varphi|\pm l\rangle = \pm\hbar(l-1/2)|\pm l\rangle$ and $f^\pm_{i,\beta}(r)$ are the corresponding radial components of the envelope function. We consider the first two spinful electron and hole subbands and assume $l = 1$, corresponding to the $J_z = \pm 1/2$ sector, which results in the four-dimensional basis $\{|\text{EL+}\rangle_l\,, |\text{H+}\rangle_l\,, |\text{EL-}\rangle_l\,, |\text{H-}\rangle_l\}$. Explicitly, we have

$$\begin{aligned} |\text{EL+}\rangle_l &= \left(f_{\text{EL}+,1}(r)\,|1\rangle + f_{\text{EL}+,3}(r)\,|3\rangle + f_{\text{EL}+,5}(r)\,|5\rangle\right)|+l\rangle\ , \\ |\text{H+}\rangle_l &= \left(f_{\text{H}+,2}(r)\,|2\rangle + f_{\text{H}+,4}(r)\,|4\rangle + f_{\text{H}+,6}(r)\,|6\rangle\right)|+l\rangle\ , \\ |\text{EL-}\rangle_l &= \left(f_{\text{EL}-,2}(r)\,|2\rangle + f_{\text{EL}-,4}(r)\,|4\rangle + f_{\text{EL}-,6}(r)\,|6\rangle\right)|-l\rangle\ , \\ |\text{H-}\rangle_l &= \left(f_{\text{H}-,1}(r)\,|1\rangle + f_{\text{H}-,3}(r)\,|3\rangle + f_{\text{H}-,5}(r)\,|5\rangle\right)|-l\rangle \end{aligned}\ , \tag{C.10}$$

and we consider only $l = 1$, which corresponds to the $J_z = \pm 1/2$ sector.

It is important to have a look at the symmetry properties of the envelope functions. In particular, for the time reversal operation $\mathcal{T}$ it easy to show that $\mathcal{T}\,|\text{EL+}\rangle_l = |\text{EL-}\rangle_l$, $\mathcal{T}\,|\text{EL-}\rangle_l = -\,|\text{EL+}\rangle_l$, $\mathcal{T}\,|\text{H+}\rangle_l = |\text{H-}\rangle_l$ and $\mathcal{T}\,|\text{H-}\rangle_l = -\,|\text{H+}\rangle_l$, and we use the phase conventions for the envelope functions such that $f_{\text{EL-},2} = f^*_{\text{EL+},1}$, $f_{\text{EL-},4} = f^*_{\text{EL+},5}$, $f_{\text{EL-},6} = f^*_{\text{EL+},3}$ and $f_{\text{H-},1} = -f^*_{\text{H+},2}$, $f_{\text{H-},3} = -f^*_{\text{H+},6}$, $f_{\text{H-},5} = -f^*_{\text{H+},4}$.

The matrix elements of H_0 in the chosen four-dimensional basis yield the eigenenergies of the two subbands at the Γ point $E_{0,\text{EL}}$ and $E_{0,\text{H}}$ separated by an energy splitting $\delta E = E_{0,\text{EL}} - E_{0,\text{H}}$. The matrix element of H', for generic l, are computed as

$$\langle i\pm|H|j\pm\rangle = \frac{1}{2\pi}\int_0^{2\pi} \mathrm{d}\varphi \int_0^R \mathrm{d}r\, r \sum_{\beta,\beta'}^{6} f^*_{i\pm,\beta}(r) e^{\mp i(l-\frac{1}{2})\varphi} H_{\beta\beta'} f_{j\pm,\beta'}(r) e^{\pm i(l-\frac{1}{2})\varphi}\,. \tag{C.11}$$

Note that while the $\widetilde{H}_{\text{kp}}(k_z) - H_0$ in H' only couples states with same angular momentum quantum number, H_E couples states with total angular momentum quantum numbers that differs by one unit. For example, for $l = 1$ we have

$$\langle \text{EL+}|H_E|\text{H-}\rangle = eU_{eh}E_y\,, \tag{C.12}$$

where

$$U_{eh} = -\frac{1}{2i}\int_0^R \mathrm{d}r\, r \sum_{\alpha,\beta}^{6} f^*_{\text{EL}\pm,\alpha}\, r\, f_{\text{H}\mp,\beta} \tag{C.13}$$

Using the symmetry relations on the envelope functions imposed by time-reversal symmetry we also obtain

$$\langle \text{H+}|H_E|\text{EL-}\rangle = -eU_{eh}E_y\,. \tag{C.14}$$

Analogously we have

$$\langle \text{EL+}|H_{\text{kp}}|\text{H+}\rangle = \mathcal{A}k_z\,, \tag{C.15}$$

where

$$\begin{aligned}\mathcal{A} = \sqrt{\frac{2}{3}}&\left[\int_0^R \mathrm{d}r\, r\, P(r)\ \left(f^*_{\text{EL+},1}(r) f_{\text{H+},4}(r) + f_{\text{EL+},5}(r) f_{\text{H+},2}(r)\right)\right]\\ &- \frac{\gamma_s}{m}\hbar^2\sqrt{3}\left[\int_0^R \mathrm{d}r\, r f^*_{\text{E+},3}(r)\left(k_r - i\frac{k_\varphi - 1}{r}\right) f_{\text{H+},4}(r)\right]\\ &- \frac{\gamma_s}{m}\hbar^2\sqrt{3}\left[\int_0^R \mathrm{d}r\, r f^*_{\text{E+},5}(r)\left(-k_r + i\frac{k_\varphi + 1}{r}\right) f_{\text{H+},6}(r)\right]\,.\end{aligned} \tag{C.16}$$

From time-reversal symmetry we also have

$$\langle \text{H-}|H_{\text{kp}}|\text{EL-}\rangle = -\mathcal{A}k_z\,. \tag{C.17}$$

Finally, the Hamiltonian we get has the form

$$\widetilde{H}_4 = \begin{pmatrix} E_{0,\text{EL}} + \frac{\hbar^2 k_z^2}{2m_e} & \mathcal{A}k_z & 0 & eU_{eh}E_y \\ \mathcal{A}^* k_z & E_{0,\text{H}} + \frac{\hbar^2 k_z^2}{2m_h} & -eU_{eh}E_y & 0 \\ 0 & -eU_{eh}E_y & E_{0,\text{EL}} + \frac{\hbar^2 k_z^2}{2m_e} & -\mathcal{A}^* k_z \\ eU_{el\text{-}h}E_y & 0 & -\mathcal{A}k_z & E_{0,\text{H}} + \frac{\hbar^2 k_z^2}{2m_h} \end{pmatrix} \tag{C.18}$$

where we have introduced the effective masses

$$\begin{aligned} m_e &= \frac{m_0}{\bar{\gamma}_e}\,, \\ m_h &= \frac{m_0}{\bar{\gamma}_h}\,, \end{aligned} \tag{C.19}$$

being m_0 the free electron mass and

$$\begin{aligned} \bar{\gamma}_e &= \int_0^R \mathrm{d}r\, r\, \left[\frac{m_0}{m^*(r)}|f_{\text{EL+},1}(r)|^2 - (\gamma_1(r) - 2\gamma_s(r))|f_{\text{EL+},3}(r)|^2 - (\gamma_1(r) + 2\gamma_s(r))\,|f_{\text{EL+},5}(r)|^2\right]\,, \\ \bar{\gamma}_h &= \int_0^R \mathrm{d}r\, r\, \left[\frac{m_0}{m^*(r)}|f_{\text{H+},2}(r)|^2 - (\gamma_1(r) + 2\gamma_s(r))|f_{\text{H+},4}(r)|^2 - (\gamma_1(r) - 2\gamma_s(r))\,|f_{\text{H+},6}(r)|^2\right]\,, \end{aligned} \tag{C.20}$$

taking into account the fact that the electron effective mass m^* and the Luttinger parameters γ_i depend on the radial position r. Using the definitions of the parameters D and B, given in Eqs. (5.15) and (5.16), respectively, as well as

$$\begin{aligned} M &= \frac{E_{0,\text{EL}} - E_{0,\text{H}}}{2}\,, \\ C &= \frac{E_{0,\text{EL}} + E_{0,\text{H}}}{2}\,, \end{aligned} \tag{C.21}$$

and

$$\begin{aligned} \varepsilon(k_z) &= C - Dk_z^2\,, \\ \mathcal{M}(k_z) &= M - Bk_z^2\,, \end{aligned} \tag{C.22}$$

we can rewrite the Hamiltonian in Eq. (C.18) as

$$\widetilde{H}_4 = \varepsilon(k_z)\mathbb{1}_4 + \begin{pmatrix} \mathcal{M}(k_z) & \mathcal{A}k_z & 0 & eU_{eh}E_y \\ \mathcal{A}^*k_z & -\mathcal{M}(k_z) & -eU_{eh}E_y & 0 \\ 0 & -eU_{eh}E_y & \mathcal{M}(k_z) & -\mathcal{A}^*k_z \\ eU_{el\text{-}h}E_y & 0 & -\mathcal{A}k_z & -\mathcal{M}(k_z) \end{pmatrix}\,. \tag{C.23}$$

We see that the electric field induces a direct coupling between basis states $|\text{EL+}\rangle$ and $|\text{H-}\rangle$, as well as between $|\text{EL-}\rangle$ and $|\text{H+}\rangle$. Thus, the effect of this term is to introduce a direct Rashba coupling between electron or holes states with opposite spin. Since this k_z-independent term originates directly from the dipole Hamiltonian H_E at first order, it is expected to dominate at small k_z.

Note that, apart from the term $S_0k_z^2\sigma_y\tau_y$, the form of the Hamiltonian $\widetilde{H}_4$ in Eq. (C.23) is exactly equivalent to the form of the effective Hamiltonian in Eq. (5.19) obtained in Sec. 5.3 starting from the laterally confined two-dimensional quantum well model, as explained in the main text, which, eventually, further supports the results obtained in Ch. 5.

References

[1] Daniel Ramos, Eduardo Gil-Santos, Oscar Malvar, Jose M Llorens, Valerio Pini, Alvaro San Paulo, Montserrat Calleja, and Javier Tamayo. “Silicon nanowires: where mechanics and optics meet at the nanoscale”. In: *Scientific reports* 3.1 (2013), p. 3445.

[2] Li Z Pei and Zheng Y Cai. “A review on germanium nanowires”. In: *Recent Patents on Nanotechnology* 6.1 (2012), pp. 44–59.

[3] Hannah J. Joyce, Qiang Gao, H. Hoe Tan, C. Jagadish, Yong Kim, Jin Zou, Leigh M. Smith, Howard E. Jackson, Jan M. Yarrison-Rice, Patrick Parkinson, and Michael B. Johnston. “III–V semiconductor nanowires for optoelectronic device applications”. In: *Progress in Quantum Electronics* 35.2 (2011), pp. 23–75. ISSN: 0079-6727. DOI: https://doi.org/10.1016/j.pquantelec.2011.03.002. URL: https://www.sciencedirect.com/science/article/pii/S0079672711000036.

[4] A.G.N. Sofiah, M. Samykano, K. Kadirgama, R.V. Mohan, and N.A.C. Lah. “Metallic nanowires: Mechanical properties – Theory and experiment”. In: *Applied Materials Today* 11 (2018), pp. 320–337. ISSN: 2352-9407. DOI: https://doi.org/10.1016/j.apmt.2018.03.004. URL: https://www.sciencedirect.com/science/article/pii/S235294071830060X.

[5] Florian Furtmayr, Jörg Teubert, Pascal Becker, Sonia Conesa-Boj, Joan Ramon Morante, Alexey Chernikov, Sören Schäfer, Sangam Chatterjee, Jordi Arbiol, and Martin Eickhoff. “Carrier confinement in GaN/Al$_x$Ga$_{1-x}$N nanowire heterostructures ($0 < x \leq 1$)”. In: *Phys. Rev. B* 84 (20 Nov. 2011), p. 205303. DOI: 10.1103/PhysRevB.84.205303. URL: https://link.aps.org/doi/10.1103/PhysRevB.84.205303.

[6] Peter Krogstrup, Ronit Popovitz-Biro, Erik Johnson, Morten Hannibal Madsen, Jesper Nygård, and Hadas Shtrikman. “Structural phase control in self-catalyzed growth of GaAs nanowires on silicon (111)”. In: *Nano Lett.* 10.11 (Nov. 2010), pp. 4475–4482. ISSN: 1530-6992. DOI: 10.1021/nl102308k. URL: http://www.ncbi.nlm.nih.gov/pubmed/20932012.

[7] Jerome K Hyun, Shixiong Zhang, and Lincoln J Lauhon. “Nanowire heterostructures”. In: *Annual Review of Materials Research* 43 (2013), pp. 451–479.

[8] M.-E. Pistol and C. E. Pryor. “Band structure of core-shell semiconductor nanowires”. In: *Phys. Rev. B* 78 (11 Sept. 2008), p. 115319. DOI: 10.1103/PhysRevB.78.115319. URL: https://link.aps.org/doi/10.1103/PhysRevB.78.115319.

[9] Xiangfeng Duan, Yu Huang, Yi Cui, Jianfang Wang, and Charles M. Lieber. “Indium phosphide nanowires as building blocks for nanoscale electronic and optoelectronic devices”. In: *Nature* 409.6816 (2001). Cited by: 3353, pp. 66–69. DOI: 10.1038/35051047. URL: https://www.scopus.com/inward/record.uri?eid=2-s2.0-0035804248&doi=10.1038%2f35051047&partnerID=40&md5=93dfb40d1577a7bfe3a13883915b3a73.

[10] H. P. T. Nguyen, S. Zhang, K. Cui, X. Han, S. Fathololoumi, M. Couillard, G. A. Botton, and Z. Mi. “p-Type Modulation Doped InGaN/GaN Dot-in-a-Wire White-Light-Emitting Diodes Monolithically Grown on Si(111)”. In: *Nano Letters* 11.5 (2011). PMID: 21517080, pp. 1919–1924. DOI: 10.1021/nl104536x. eprint: https://doi.org/10.1021/nl104536x. URL: https://doi.org/10.1021/nl104536x.

[11] Jesper Wallentin, Nicklas Anttu, Damir Asoli, Maria Huffman, Ingvar Åberg, Martin H. Magnusson, Gerald Siefer, Peter Fuss-Kailuweit, Frank Dimroth, Bernd Witzigmann, H. Q. Xu, Lars Samuelson, Knut Deppert, and Magnus T. Borgström. “InP Nanowire Array Solar Cells Achieving 13.8% Efficiency by Exceeding the Ray Optics Limit”. In: *Science* 339.6123 (2013), pp. 1057–1060. DOI: 10.1126/science.1230969. eprint: https://www.science.org/doi/pdf/10.1126/science.1230969. URL: https://www.science.org/doi/abs/10.1126/science.1230969.

[12] Yi Cui, Zhaohui Zhong, Deli Wang, Wayne U. Wang, and Charles M. Lieber. “High performance silicon nanowire field effect transistors”. In: *Nano Letters* 3.2 (2003). Cited by: 2031; All Open Access, Green Open Access, pp. 149–152. DOI: 10.1021/nl025875l. URL: https://www.scopus.com/inward/record.uri?eid=2-s2.0-0038161696&doi=10.1021%2fnl025875l&partnerID=40&md5=f5185dfe2c2d510f00318187cd35bc2f.

[13] S. Morkötter, N. Jeon, D. Rudolph, B. Loitsch, D. Spirkoska, E. Hoffmann, M. Döblinger, S. Matich, J. J. Finley, L. J. Lauhon, G. Abstreiter, and G. Koblmüller. “Demonstration of Confined Electron Gas and Steep-Slope Behavior in Delta-Doped GaAs-AlGaAs Core–Shell Nanowire Transistors”. In: *Nano Letters* 15.5 (2015). PMID: 25923841, pp. 3295–3302. DOI: 10.1021/acs.nanolett.5b00518. eprint: https://doi.org/10.1021/acs.nanolett.5b00518. URL: https://doi.org/10.1021/acs.nanolett.5b00518.

[14] Thomas Skotnicki and Frederic Boeuf. “How can high mobility channel materials boost or degrade performance in advanced CMOS”. In: *2010 Symposium on VLSI Technology*. 2010, pp. 153–154. DOI: 10.1109/VLSIT.2010.5556208.

[15] K. N. V. S. Vijaya Lakshmi D. Ajitha and K. Bhagya Lakshmi. “Nanowire Transistors: A Next Step for the Low-Power Digital Technology”. In: *IETE Journal of Research* 69.8 (2023), pp. 5549–5565. DOI: 10.1080/03772063.2021.1972845. eprint: https://doi.org/10.1080/03772063.2021.1972845. URL: https://doi.org/10.1080/03772063.2021.1972845.

[16] Domenic Prete, Elisabetta Dimaggio, Valeria Demontis, Valentina Zannier, Maria Jesus Rodriguez-Douton, Lorenzo Guazzelli, Fabio Beltram, Lucia Sorba, Giovanni Pennelli, and Francesco Rossella. “Electrostatic Control of the Thermoelectric Figure of Merit in Ion-Gated Nanotransistors”. In: *ADVANCED FUNCTIONAL MATERIALS* 31.37 (Sept. 2021). ISSN: 1616-301X. DOI: {10.1002/adfm.202104175}.

[17] Yi Cui, Qingqiao Wei, Hongkun Park, and Charles M. Lieber. “Nanowire Nanosensors for Highly Sensitive and Selective Detection of Biological and Chemical Species”. In: *Science* 293.5533 (2001), pp. 1289–1292. DOI: 10.1126/science.1062711. eprint: https://www.science.org/doi/pdf/10.1126/science.1062711. URL: https://www.science.org/doi/abs/10.1126/science.1062711.

[18] Svenja Mauthe, Yannick Baumgartner, Marilyne Sousa, Qian Ding, Marta D Rossell, Andreas Schenk, Lukas Czornomaz, and Kirsten E Moselund. “High-speed III-V nanowire photodetector monolithically integrated on Si”. In: *Nature communications* 11.1 (2020), p. 4565.

[19] Anas A.M. Alqanoo, Naser M. Ahmed, M.R. Hashim, Munirah A. Almessiere, Sofyan A. Taya, and Samer H. Zyoud. "Silver nanowires assisted porous silicon for high photodetector sensitivity using surface plasmonic phenomena". In: *Sensors and Actuators A: Physical* 347 (2022), p. 113942. ISSN: 0924-4247. DOI: `https://doi.org/10.1016/j.sna.2022.113942`. URL: `https://www.sciencedirect.com/science/article/pii/S0924424722005775`.

[20] Samuele Cornia, Valeria Demontis, Valentina Zannier, Lucia Sorba, Alberto Ghirri, Francesco Rossella, and Marco Affronte. "Calibration-Free and High-Sensitivity Microwave Detectors Based on InAs/InP Nanowire Double Quantum Dots". In: *Advanced Functional Materials* 33.19 (2023), p. 2212517. DOI: `https://doi.org/10.1002/adfm.202212517`. eprint: `https://onlinelibrary.wiley.com/doi/pdf/10.1002/adfm.202212517`. URL: `https://onlinelibrary.wiley.com/doi/abs/10.1002/adfm.202212517`.

[21] Joachim Knoch. "Chapter Eight - Nanowire Tunneling Field-Effect Transistors". In: *Semiconductor Nanowires II: Properties and Applications*. Ed. by Shadi A. Dayeh, Anna Fontcuberta i Morral, and Chennupati Jagadish. Vol. 94. Semiconductors and Semimetals. Elsevier, 2016, pp. 273–295. DOI: `https://doi.org/10.1016/bs.semsem.2015.09.005`. URL: `https://www.sciencedirect.com/science/article/pii/S0080878415000472`.

[22] J. Appenzeller, Y.-M. Lin, J. Knoch, and Ph. Avouris. "Band-to-Band Tunneling in Carbon Nanotube Field-Effect Transistors". In: *Phys. Rev. Lett.* 93 (19 Nov. 2004), p. 196805. DOI: `10.1103/PhysRevLett.93.196805`. URL: `https://link.aps.org/doi/10.1103/PhysRevLett.93.196805`.

[23] J.K. Hyun and S. Zhang. "4 - Growth of nanowire heterostructures and their optoelectronic and spintronic applications". In: *Magnetic Nano- and Microwires*. Ed. by Manuel Vázquez. Woodhead Publishing Series in Electronic and Optical Materials. Woodhead Publishing, 2015, pp. 125–146. ISBN: 978-0-08-100164-6. DOI: `https://doi.org/10.1016/B978-0-08-100164-6.00004-7`. URL: `https://www.sciencedirect.com/science/article/pii/B9780081001646000047`.

[24] P.C. McIntyre and A. Fontcuberta i Morral. "Semiconductor nanowires: to grow or not to grow?" In: *Materials Today Nano* 9 (2020), p. 100058. ISSN: 2588-8420. DOI: `https://doi.org/10.1016/j.mtnano.2019.100058`. URL: `https://www.sciencedirect.com/science/article/pii/S2588842019301270`.

[25] Hua Wang, Minghua Sun, Kang Ding, Martin T. Hill, and Cun-Zheng Ning. "A Top-down Approach to Fabrication of High Quality Vertical Heterostructure Nanowire Arrays". In: *Nano Letters* 11.4 (2011). PMID: 21417458, pp. 1646–1650. DOI: `10.1021/nl2001132`. eprint: `https://doi.org/10.1021/nl2001132`. URL: `https://doi.org/10.1021/nl2001132`.

[26] a RS Wagner and s WC Ellis. "Vapor-liquid-solid mechanism of single crystal growth". In: *Applied physics letters* 4.5 (1964), pp. 89–90.

[27] LJ Lauhon, Mark S Gudiksen, and Charles M Lieber. "Semiconductor nanowire heterostructures". In: *Philosophical Transactions of the Royal Society of London. Series A: Mathematical, Physical and Engineering Sciences* 362.1819 (2004), pp. 1247–1260.

[28] Aneta J. Mieszawska, Romaneh Jalilian, Gamini U. Sumanasekera, and Francis P. Zamborini. "The Synthesis and Fabrication of One-Dimensional Nanoscale Heterojunctions". In: *Small* 3.5 (2007), pp. 722–756. DOI: `https://doi.org/10.1002/smll.200600727`. eprint: `https://onlinelibrary.wiley.com/doi/pdf/10.1002/smll.200600727`. URL: `https://onlinelibrary.wiley.com/doi/abs/10.1002/smll.200600727`.

[29] Ritesh Agarwal. "Heterointerfaces in Semiconductor Nanowires". In: *Small* 4.11 (2008), pp. 1872–1893. DOI: `https://doi.org/10.1002/smll.200800556`. eprint: `https://onlinelibrary.wiley.com/doi/pdf/10.1002/smll.200800556`. URL: `https://onlinelibrary.wiley.com/doi/abs/10.1002/smll.200800556`.

[30] Mark S Gudiksen, Lincoln J Lauhon, Jianfang Wang, David C Smith, and Charles M Lieber. "Growth of nanowire superlattice structures for nanoscale photonics and electronics". In: *nature* 415.6872 (2002), pp. 617–620.

[31] Lincoln J Lauhon, Mark S Gudiksen, Deli Wang, and Charles M Lieber. "Epitaxial core–shell and core–multishell nanowire heterostructures". In: *nature* 420.6911 (2002), pp. 57–61.

[32] Jonas Johansson and Kimberly A. Dick. "Recent advances in semiconductor nanowire heterostructures". In: *CrystEngComm* 13 (24 2011), pp. 7175–7184. DOI: `10.1039/C1CE05821E`. URL: `http://dx.doi.org/10.1039/C1CE05821E`.

[33] Emmanouil Dimakis, Jonas Lähnemann, Uwe Jahn, Steffen Breuer, Maria Hilse, Lutz Geelhaar, and Henning Riechert. "Self-Assisted Nucleation and Vapor–Solid Growth of InAs Nanowires on Bare Si(111)". In: *Crystal Growth & Design* 11.9 (2011), pp. 4001–4008. DOI: `10.1021/cg200568m`. eprint: `https://doi.org/10.1021/cg200568m`. URL: `https://doi.org/10.1021/cg200568m`.

[34] J. Motohisa, J. Noborisaka, J. Takeda, M. Inari, and T. Fukui. "Catalyst-free selective-area MOVPE of semiconductor nanowires on (111)B oriented substrates". In: *Journal of Crystal Growth* 272.1 (2004). The Twelfth International Conference on Metalorganic Vapor Phase Epitaxy, pp. 180–185. ISSN: 0022-0248. DOI: `https://doi.org/10.1016/j.jcrysgro.2004.08.118`. URL: `https://www.sciencedirect.com/science/article/pii/S0022024804010899`.

[35] Bernhard Mandl, Julian Stangl, Thomas Ma, Anders Mikkelsen, Lars Samuelson, Jessica Eriksson, Lisa S Karlsson, and Werner Seifert. "Au-Free Epitaxial Growth of InAs Nanowires". In: *Nano Lett.* 6.8 (2006), p. 1817.

[36] Helmut Feichtinger. "Deep Centers in Semiconductors". In: *Handbook of Semiconductor Technology Set*. John Wiley & Sons, Ltd, 2000. Chap. 4, pp. 167–229. ISBN: 9783527619290. DOI: `https://doi.org/10.1002/9783527619290.ch4`. eprint: `https://onlinelibrary.wiley.com/doi/pdf/10.1002/9783527619290.ch4`. URL: `https://onlinelibrary.wiley.com/doi/abs/10.1002/9783527619290.ch4`.

[37] Chia-Chi Chang, Chun-Yung Chi, Maoqing Yao, Ningfeng Huang, Chun-Chung Chen, Jesse Theiss, Adam W. Bushmaker, Stephen LaLumondiere, Ting-Wei Yeh, Michelle L. Povinelli, Chongwu Zhou, P. Daniel Dapkus, and Stephen B. Cronin. "Electrical and Optical Characterization of Surface Passivation in GaAs Nanowires". In: *Nano Letters* 12.9 (2012). PMID: 22889241, pp. 4484–4489. DOI: `10.1021/nl301391h`. eprint: `https://doi.org/10.1021/nl301391h`. URL: `https://doi.org/10.1021/nl301391h`.

[38] Stefan Funk, Miguel Royo, Ilaria Zardo, Daniel Rudolph, Stefanie Morkötter, Benedikt Mayer, Jonathan Becker, Alexander Bechtold, Sonja Matich, Markus Döblinger, Max Bichler, Gregor Koblmüller, Jonathan J. Finley, Andrea Bertoni, Guido Goldoni, and Gerhard Abstreiter. "High mobility one- and two-dimensional electron systems in nanowire-based quantum heterostructures". In: *Nano Letters* 13 (12 Dec. 2013), pp. 6189–6196. ISSN: 15306984. DOI: `10.1021/nl403561w`.

[39] J Jadczak, Paulina Plochocka, Anatolie Mitioglu, I Breslavetz, Miquel Royo, Andrea Bertoni, Guido Goldoni, T Smolenski, Piotr Kossacki, Andrey Kretinin, et al. "Unintentional high-density p-type modulation doping of a GaAs/AlAs core–multishell nanowire". In: *Nano Letters* 14.5 (2014), pp. 2807–2814.

[40] Jessica L Boland, Gözde Tütüncüoglu, Juliane Q Gong, Sonia Conesa-Boj, Christopher L Davies, Laura M Herz, Anna Fontcuberta i Morral, and Michael B Johnston. "Towards higher electron mobility in modulation doped GaAs/AlGaAs core shell nanowires". In: *Nanoscale* 9.23 (2017), pp. 7839–7846.

[41] Jessica L. Boland, Sonia Conesa-Boj, Patrick Parkinson, Gözde Tütüncüoglu, Federico Matteini, Daniel Rüffer, Alberto Casadei, Francesca Amaduzzi, Fauzia Jabeen, Christopher L. Davies, Hannah. J. Joyce, Laura M. Herz, Anna Fontcuberta i Morral, and Michael B. Johnston. "Modulation Doping of GaAs/AlGaAs Core–Shell Nanowires With Effective Defect Passivation and High Electron Mobility". In: *Nano Letters* 15.2 (2015). PMID: 25602841, pp. 1336–1342. DOI: `10.1021/nl504566t`. eprint: `https://doi.org/10.1021/nl504566t`. URL: `https://doi.org/10.1021/nl504566t`.

[42] Wonjong Kim, Lucas Güniat, Anna Fontcuberta I Morral, and Valerio Piazza. "Doping challenges and pathways to industrial scalability of III-V nanowire arrays". In: *Appl. Phys. Rev.* 8.1 (2021). ISSN: 19319401. DOI: `10.1063/5.0031549`. URL: `https://doi.org/10.1063/5.0031549`.

[43] S. Vaitiekėnas, G. W. Winkler, B. van Heck, T. Karzig, M.-T. Deng, K. Flensberg, L. I. Glazman, C. Nayak, P. Krogstrup, R. M. Lutchyn, and C. M. Marcus. "Flux-induced topological superconductivity in full-shell nanowires". In: *Science* 367.6485 (2020), eaav3392. DOI: `10.1126/science.aav3392`. eprint: `https://www.science.org/doi/pdf/10.1126/science.aav3392`. URL: `https://www.science.org/doi/abs/10.1126/science.aav3392`.

[44] Roman M. Lutchyn, Jay D. Sau, and S. Das Sarma. "Majorana Fermions and a Topological Phase Transition in Semiconductor-Superconductor Heterostructures". In: *Phys. Rev. Lett.* 105 (7 Aug. 2010), p. 077001. DOI: `10.1103/PhysRevLett.105.077001`. URL: `https://link.aps.org/doi/10.1103/PhysRevLett.105.077001`.

[45] Yuval Oreg, Gil Refael, and Felix von Oppen. "Helical Liquids and Majorana Bound States in Quantum Wires". In: *Phys. Rev. Lett.* 105 (17 Oct. 2010), p. 177002. DOI: `10.1103/PhysRevLett.105.177002`. URL: `https://link.aps.org/doi/10.1103/PhysRevLett.105.177002`.

[46] M. T. Deng, S. Vaitiekėnas, E. B. Hansen, J. Danon, M. Leijnse, K. Flensberg, J. Nygård, P. Krogstrup, and C. M. Marcus. "Majorana bound state in a coupled quantum-dot hybrid-nanowire system". In: *Science* 354.6319 (2016), pp. 1557–1562. DOI: `10.1126/science.aaf3961`. eprint: `https://www.science.org/doi/pdf/10.1126/science.aaf3961`. URL: `https://www.science.org/doi/abs/10.1126/science.aaf3961`.

[47] Jason Alicea. “New directions in the pursuit of Majorana fermions in solid state systems”. In: *Reports on Progress in Physics* 75.7 (June 2012), p. 076501. DOI: `10.1088/0034-4885/75/7/076501`. URL: `https://dx.doi.org/10.1088/0034-4885/75/7/076501`.

[48] Andrei Manolescu, Anna Sitek, Javier Osca, Lloren ç Serra, Vidar Gudmundsson, and Tudor Dan Stanescu. “Majorana states in prismatic core-shell nanowires”. In: *Phys. Rev. B* 96 (12 Sept. 2017), p. 125435. DOI: `10.1103/PhysRevB.96.125435`. URL: `https://link.aps.org/doi/10.1103/PhysRevB.96.125435`.

[49] Benjamin D. Woods, Sankar Das Sarma, and Tudor D. Stanescu. “Electronic structure of full-shell InAs/Al hybrid semiconductor-superconductor nanowires: Spin-orbit coupling and topological phase space”. In: *Phys. Rev. B* 99 (16 Apr. 2019), p. 161118. DOI: `10.1103/PhysRevB.99.161118`. URL: `https://link.aps.org/doi/10.1103/PhysRevB.99.161118`.

[50] B. Andrei Bernevig, Taylor L. Hughes, and Shou-Cheng Zhang. “Quantum Spin Hall Effect and Topological Phase Transition in HgTe Quantum Wells”. In: *Science* 314.5806 (2006), pp. 1757–1761. DOI: `10.1126/science.1133734`. eprint: `https://www.science.org/doi/pdf/10.1126/science.1133734`. URL: `https://www.science.org/doi/abs/10.1126/science.1133734`.

[51] Markus König, Steffen Wiedmann, Christoph Brüne, Andreas Roth, Hartmut Buhmann, Laurens W. Molenkamp, Xiao-Liang Qi, and Shou-Cheng Zhang. “Quantum Spin Hall Insulator State in HgTe Quantum Wells”. In: *Science* 318.5851 (2007), pp. 766–770. DOI: `10.1126/science.1148047`. eprint: `https://www.science.org/doi/pdf/10.1126/science.1148047`. URL: `https://www.science.org/doi/abs/10.1126/science.1148047`.

[52] Fanming Qu, Arjan J. A. Beukman, Stevan Nadj-Perge, Michael Wimmer, Binh-Minh Nguyen, Wei Yi, Jacob Thorp, Marko Sokolich, Andrey A. Kiselev, Michael J. Manfra, Charles M. Marcus, and Leo P. Kouwenhoven. “Electric and Magnetic Tuning Between the Trivial and Topological Phases in InAs/GaSb Double Quantum Wells”. In: *Phys. Rev. Lett.* 115 (3 July 2015), p. 036803. DOI: `10.1103/PhysRevLett.115.036803`. URL: `https://link.aps.org/doi/10.1103/PhysRevLett.115.036803`.

[53] Hsiu-Chuan Hsu, Min-Jyun Jhang, Tsung-Wei Chen, and Guang-Yu Guo. “Topological phase transitions in an inverted InAs/GaSb quantum well driven by tilted magnetic fields”. In: *Phys. Rev. B* 95 (19 May 2017), p. 195408. DOI: `10.1103/PhysRevB.95.195408`. URL: `https://link.aps.org/doi/10.1103/PhysRevB.95.195408`.

[54] Shuyang Yang, Derek Dardzinski, Andrea Hwang, Dmitry I. Pikulin, Georg W. Winkler, and Noa Marom. “First-principles feasibility assessment of a topological insulator at the InAs/GaSb interface”. In: *Phys. Rev. Mater.* 5 (8 Aug. 2021), p. 084204. DOI: `10.1103/PhysRevMaterials.5.084204`. URL: `https://link.aps.org/doi/10.1103/PhysRevMaterials.5.084204`.

[55] Kyoichi Suzuki, Yuichi Harada, Koji Onomitsu, and Koji Muraki. “Gate-controlled semimetal-topological insulator transition in an InAs/GaSb heterostructure”. In: *Phys. Rev. B* 91 (24 June 2015), p. 245309. DOI: `10.1103/PhysRevB.91.245309`. URL: `https://link.aps.org/doi/10.1103/PhysRevB.91.245309`.

[56] Shigeru Kaku, Tatsuhito Ando, and Junji Yoshino. “Real Space Imaging of Topological Edge States in InAs/GaSb and InAs/InxGa1–xSb Quantum Wells”. In: *ACS Nano* 13.11 (2019). PMID: 31674762, pp. 12980–12986. DOI: `10.1021/acsnano.9b05611`. eprint: `https://doi.org/10.1021/acsnano.9b05611`. URL: `https://doi.org/10.1021/acsnano.9b05611`.

[57] Manuel Meyer, Tobias Fähndrich, Sebastian Schmid, Adriana Wolf, Sergey Krishtopenko, Benoit Jouault, Gerald Bastard, Frederic Teppe, Fabian Hartmann, and Sven Höfling. “Coexistence of Topological and Normal Insulating Phases in Electro-Optically Tuned InAs/GaSb Bilayer Quantum Wells”. In: *arXiv preprint arXiv:2401.11965* (2024).

[58] J. I. Climente. “Tuning the tunnel coupling of quantum dot molecules with longitudinal magnetic fields”. In: *Applied Physics Letters* 93.22 (Dec. 2008), p. 223109. ISSN: 0003-6951. DOI: `10.1063/1.3040058`. eprint: `https://pubs.aip.org/aip/apl/article-pdf/doi/10.1063/1.3040058/14406395/223109\_1\_online.pdf`. URL: `https://doi.org/10.1063/1.3040058`.

[59] Pawel Wojcik, Andrea Bertoni, and Guido Goldoni. “Tuning Rashba spin-orbit coupling in homogeneous semiconductor nanowires”. In: *PHYSICAL REVIEW B* 97.16 (Apr. 2018). ISSN: 2469-9950. DOI: `10.1103/PhysRevB.97.165401`.

[60] Pawel Wojcik, Andrea Bertoni, and Guido Goldoni. “Enhanced Rashba spin-orbit coupling in core-shell nanowires by the interfacial effect”. In: *APPLIED PHYSICS LETTERS* 114.7 (Feb. 2019). ISSN: 0003-6951. DOI: `10.1063/1.5082602`.

[61] Pawel Wojcik, Andrea Bertoni, and Guido Goldoni. “Anisotropy of the spin-orbit coupling driven by a magnetic field in InAs nanowires”. In: *PHYSICAL REVIEW B* 103.8 (Feb. 2021). ISSN: 2469-9950. DOI: `10.1103/PhysRevB.103.085434`.

[62] Ramdas Ram-Mohan and L Ramdas Ram-Mohan. *Finite element and boundary element applications in quantum mechanics*. Vol. 5. Oxford University Press on Demand, 2002.

[63] Gouri Dhatt, Emmanuel Lefrançois, and Gilbert Touzot. *Finite element method*. John Wiley & Sons, 2012.

[64] M G Burt. “The justification for applying the effective-mass approximation to microstructures”. In: *Journal of Physics: Condensed Matter* 4.32 (Aug. 1992), p. 6651. DOI: `10.1088/0953-8984/4/32/003`. URL: `https://dx.doi.org/10.1088/0953-8984/4/32/003`.

[65] PARTICLE IN A BOX MODEL. “EXACT ENVELOPE FUNCTION EQUATIONS FOR MICROSTRUCTURES AND THE”. In: *Band Structure Engineering in Semiconductor Microstructures* 189 (1989), p. 99.

[66] M. G. Burt. “Direct derivation of effective-mass equations for microstructures with atomically abrupt boundaries”. In: *Phys. Rev. B* 50 (11 Sept. 1994), pp. 7518–7525. DOI: `10.1103/PhysRevB.50.7518`. URL: `https://link.aps.org/doi/10.1103/PhysRevB.50.7518`.

[67] Stefan Birner. “The Multi-Band k⊠ p Hamiltonian for Heterostructures: Parameters and Applications”. In: *Multi-Band Effective Mass Approximations: Advanced Mathematical Models and Numerical Techniques* (2014), pp. 193–244.

[68] Ning Luo, Gaohua Liao, and H. Q. Xu. “K.P Theory of Freestanding Narrow Band Gap Semiconductor Nanowires”. In: *AIP Adv.* 6.12 (2016). ISSN: 21583226. DOI: `10.1063/1.4972987`. arXiv: `1603.00811`.

[69] Bradley A. Foreman. “Elimination of spurious solutions from eight-band **k**·**p** theory”. In: *Phys. Rev. B* 56 (20 Nov. 1997), R12748–R12751. DOI: `10.1103/PhysRevB.56.R12748`. URL: `https://link.aps.org/doi/10.1103/PhysRevB.56.R12748`.

[70] YU Peter and Manuel Cardona. *Fundamentals of semiconductors: physics and materials properties*. Springer Science & Business Media, 2010.

[71] Morten Willatzen and Lok C. Lew Yan Voon. *The k·p Method*. Springer, Berlin, Heidelberg, 2009. ISBN: 978-3-540-92872-0. DOI: `10.1007/978-3-540-92872-0`. URL: `https://doi.org/10.1007/978-3-540-92872-0`.

[72] G. Dresselhaus, A. F. Kip, and C. Kittel. “Cyclotron Resonance of Electrons and Holes in Silicon and Germanium Crystals”. In: *Phys. Rev.* 98 (2 Apr. 1955), pp. 368–384. DOI: `10.1103/PhysRev.98.368`. URL: `https://link.aps.org/doi/10.1103/PhysRev.98.368`.

[73] Bradley A. Foreman. “Effective-mass Hamiltonian and boundary conditions for the valence bands of semiconductor microstructures”. In: *Phys. Rev. B* 48 (7 Aug. 1993), pp. 4964–4967. DOI: `10.1103/PhysRevB.48.4964`. URL: `https://link.aps.org/doi/10.1103/PhysRevB.48.4964`.

[74] John P. Loehr. “Parameter consistency in multienergetic k·p models”. In: *Phys. Rev. B* 52 (4 July 1995), pp. 2374–2380. DOI: `10.1103/PhysRevB.52.2374`. URL: `https://link.aps.org/doi/10.1103/PhysRevB.52.2374`.

[75] J. Los, A. Fasolino, and A. Catellani. “Generalization of the k·p approach for strained layered semiconductor structures grown on high-index-planes”. In: *Phys. Rev. B* 53 (8 Feb. 1996), pp. 4630–4648. DOI: `10.1103/PhysRevB.53.4630`. URL: `https://link.aps.org/doi/10.1103/PhysRevB.53.4630`.

[76] T. Eissfeller and P. Vogl. “Real-space multiband envelope-function approach without spurious solutions”. In: *Phys. Rev. B* 84 (19 Nov. 2011), p. 195122. DOI: `10.1103/PhysRevB.84.195122`. URL: `https://link.aps.org/doi/10.1103/PhysRevB.84.195122`.

[77] Ratko G. Veprek, Sebastian Steiger, and Bernd Witzigmann. “Ellipticity and the spurious solution problem of **k** · **p** envelope equations”. In: *Phys. Rev. B* 76 (16 Oct. 2007), p. 165320. DOI: `10.1103/PhysRevB.76.165320`. URL: `https://link.aps.org/doi/10.1103/PhysRevB.76.165320`.

[78] Bradley A. Foreman. “Choosing a basis that eliminates spurious solutions in **k** · **p** theory”. In: *Phys. Rev. B* 75 (23 June 2007), p. 235331. DOI: `10.1103/PhysRevB.75.235331`. URL: `https://link.aps.org/doi/10.1103/PhysRevB.75.235331`.

[79] Gerard Bastard. *Wave mechanics applied to semiconductor heterostructures*. France: Les Ulis Cedex, 1990.

[80] V. Eyert. “A Comparative Study on Methods for Convergence Acceleration of Iterative Vector Sequences”. In: *Journal of Computational Physics* 124.2 (1996), pp. 271–285. ISSN: 0021-9991. DOI: `https://doi.org/10.1006/jcph.1996.0059`. URL: `https://www.sciencedirect.com/science/article/pii/S0021999196900595`.

[81] D. D. Johnson. “Modified Broyden’s method for accelerating convergence in self-consistent calculations”. In: *Phys. Rev. B* 38 (18 Dec. 1988), pp. 12807–12813. DOI: `10.1103/PhysRevB.38.12807`. URL: `https://link.aps.org/doi/10.1103/PhysRevB.38.12807`.

[82] Sun Lin, Yang Wenwei, Xiang Cailan, Yu Zhiping, and Tian Lilin. "Broyden method for the self-consistent solution of Schrodinger and Poisson equations". In: *2005 6th International Conference on ASIC*. Vol. 2. 2005, pp. 991–994. DOI: `10.1109/ICASIC.2005.1611494`.

[83] David Vanderbilt and Steven G. Louie. "Total energies of diamond (111) surface reconstructions by a linear combination of atomic orbitals method". In: *Phys. Rev. B* 30 (10 Nov. 1984), pp. 6118–6130. DOI: `10.1103/PhysRevB.30.6118`. URL: `https://link.aps.org/doi/10.1103/PhysRevB.30.6118`.

[84] Charles G Broyden. "A class of methods for solving nonlinear simultaneous equations". In: *Mathematics of computation* 19.92 (1965), pp. 577–593.

[85] Ratko G. Veprek and Sebastian Steiger. "Finite Elements for k⊠p Multiband Envelope Equations". In: *Multi-Band Effective Mass Approximations: Advanced Mathematical Models and Numerical Techniques*. Ed. by Matthias Ehrhardt and Thomas Koprucki. Cham: Springer International Publishing, 2014, pp. 129–154. ISBN: 978-3-319-01427-2. DOI: `10.1007/978-3-319-01427-2_4`. URL: `https://doi.org/10.1007/978-3-319-01427-2_4`.

[86] L R Ram-Mohan and K H Yoo. "Wavefunction engineering of layered semiconductors: theoretical foundations". In: *Journal of Physics: Condensed Matter* 18.49 (Sept. 2006), R901. DOI: `10.1088/0953-8984/18/49/R01`. URL: `https://dx.doi.org/10.1088/0953-8984/18/49/R01`.

[87] Jong Chang Yi and Nadir Dagli. "Finite-element analysis of valence band structure and optical properties of quantum-wire arrays on vicinal substrates". In: *IEEE journal of quantum electronics* 31.2 (1995), pp. 208–218.

[88] M. Ogawa, T. Kunimasa, T. Ito, and T. Miyoshi. "Finite-element analysis of quantum wires with arbitrary cross sections". In: *Journal of Applied Physics* 84.6 (Sept. 1998), pp. 3242–3249. ISSN: 0021-8979. DOI: `10.1063/1.368478`. eprint: `https://pubs.aip.org/aip/jap/article-pdf/84/6/3242/10595026/3242\_1\_online.pdf`. URL: `https://doi.org/10.1063/1.368478`.

[89] Xunpeng Ma, Kangwen Li, Zuyin Zhang, Yu Jiang, Yun Xu, and Guofeng Song. "Stable finite element method of eight-band k·p model without spurious solutions and numerical study of interfaces in heterostructures". In: *Journal of Applied Physics* 116.23 (Dec. 2014), p. 235702. ISSN: 0021-8979. DOI: `10.1063/1.4904845`. eprint: `https://pubs.aip.org/aip/jap/article-pdf/doi/10.1063/1.4904845/15154577/235702\_1\_online.pdf`. URL: `https://doi.org/10.1063/1.4904845`.

[90] Chuancheng Jia, Zhaoyang Lin, Yu Huang, and Xiangfeng Duan. "Nanowire Electronics: From Nanoscale to Macroscale". In: *Chem. Rev.* 119.15 (2019), pp. 9074–9135. ISSN: 15206890. DOI: `10.1021/acs.chemrev.9b00164`.

[91] Yunyan Zhang, Jiang Wu, Martin Aagesen, and Huiyun Liu. "III–V nanowires and nanowire optoelectronic devices". In: *J. Phys. D. Appl. Phys.* 48.46 (2015), p. 463001. ISSN: 0022-3727. DOI: `10.1088/0022-3727/48/46/463001`. URL: `http://stacks.iop.org/0022-3727/48/i=46/a=463001?key=crossref.29d426c6e8ac6f8b08d89ae65f5d5ebe`.

[92] Chen Zhang and Xiuling Li. "III-V nanowire transistors for low-power logic applications: A review and outlook". In: *IEEE Trans. Electron Devices* 63.1 (2016), pp. 223–234. ISSN: 00189383. DOI: `10.1109/TED.2015.2498923`.

[93] Steffen Breuer, Carsten Pfüller, Timur Flissikowski, Oliver Brandt, Holger T. Grahn, Lutz Geelhaar, and Henning Riechert. "Suitability of Au- and self-assisted GaAs nanowires for optoelectronic applications". In: *Nano Lett.* 11 (2011), pp. 1276–1279. ISSN: 15306984. DOI: `10.1021/nl104316t`.

[94] Kimberly A. Dick, Jessica Bolinsson, Maria E. Messing, Sebastian Lehmann, Jonas Johansson, and Philippe Caroff. "Parameter space mapping of InAs nanowire crystal structure". In: *J. Vac. Sci. Technol. B, Nanotechnol. Microelectron. Mater. Process. Meas. Phenom.* 29.4 (2011), p. 04D103. ISSN: 2166-2746. DOI: `10.1116/1.3593457`.

[95] Reza R. Zamani, Fredrik S. Hage, Sebastian Lehmann, Quentin M. Ramasse, and Kimberly A. Dick. "Atomic-Resolution Spectrum Imaging of Semiconductor Nanowires". In: *Nano Lett.* 18.3 (2018), pp. 1557–1563. ISSN: 15306992. DOI: `10.1021/acs.nanolett.7b03929`.

[96] Miquel Royo, Marta De Luca, Riccardo Rurali, and Ilaria Zardo. "A review on III – V core – multishell nanowires : growth, properties, and applications". In: *J. Phys. D. Appl. Phys.* 50 (2017), p. 143001. DOI: `https://doi.org/10.1088/1361-6463/aa5d8e`.

[97] Dance Spirkoska, Anna Fontcuberta i Morral, Joseph Dufouleur, Qiushi Xie, and Gerhard Abstreiter. "Free standing modulation doped core-shell GaAs/AlGaAs hetero-nanowires". In: *Phys. Status Solidi - Rapid Res. Lett.* 5.9 (2011), pp. 353–355. ISSN: 18626254. DOI: `10.1002/pssr.201105338`.

[98] N. Isik Goktas, E. M. Fiordaliso, and R. R. Lapierre. "Doping assessment in GaAs nanowires". In: *Nanotechnology* 29.23 (2018). ISSN: 13616528. DOI: `10.1088/1361-6528/aab6f1`.

[99] R. Dingle, H. L. Störmer, A. C. Gossard, and W. Wiegmann. "Electron mobilities in modulation-doped semiconductor heterojunction superlattices". In: *Applied Physics Letters* 33.7 (1978), pp. 665–667. ISSN: 00036951. DOI: `10.1063/1.90457`.

[100] Yoon Jang Chung, K. A. Villegas Rosales, K. W. Baldwin, P. T. Madathil, K. W. West, M. Shayegan, and L. N. Pfeiffer. "Ultra-high-quality two-dimensional electron systems". In: *Nature Materials* 20.5 (2021), pp. 632–637. ISSN: 14764660. DOI: `10.1038/s41563-021-00942-3`. arXiv: `2010.02283`. URL: `http://dx.doi.org/10.1038/s41563-021-00942-3`.

[101] Leila Balaghi, Si Shan, Ivan Fotev, Finn Moebus, Rakesh Rana, Tommaso Venanzi, René Hübner, Thomas Mikolajick, Harald Schneider, Manfred Helm, et al. "High electron mobility in strained GaAs nanowires". In: *Nature communications* 12 (2021), p. 6642.

[102] Andrea Bertoni, Miquel Royo, Farah Mahawish, and Guido Goldoni. "Electron and hole gas in modulation-doped GaAs/Al$_{1-x}$Ga$_x$As radial heterojunctions". In: *Phys. Rev. B* 84 (20 Nov. 2011), p. 205323. DOI: `10.1103/PhysRevB.84.205323`. URL: `https://link.aps.org/doi/10.1103/PhysRevB.84.205323`.

[103] Miquel Royo, Andrea Bertoni, and Guido Goldoni. "Symmetries in the collective excitations of an electron gas in core-shell nanowires". In: *Phys. Rev. B* 89 (15 Apr. 2014), p. 155416. DOI: `10.1103/PhysRevB.89.155416`. URL: `https://link.aps.org/doi/10.1103/PhysRevB.89.155416`.

[104] Miquel Royo, Andrea Bertoni, and Guido Goldoni. "Prediction of inelastic light scattering spectra from electronic collective excitations in GaAs/AlGaAs core-multishell nanowires". In: *Phys. Rev. B* 91 (24 June 2015), p. 245303. DOI: `10.1103/PhysRevB.91.245303`. URL: `https://link.aps.org/doi/10.1103/PhysRevB.91.245303`.

[105] Yasuhiko Ishikawa. “Scanning tunneling microscopy and x-ray photoelectron spectroscopy studies of atomic level structure and Fermi level pinning on GaAs(110) surfaces grown by molecular beam epitaxy”. In: *J. Vac. Sci. Technol. B Microelectron. Nanom. Struct.* 16.4 (1998), p. 2387. ISSN: 0734211X. DOI: `10.1116/1.590179`.

[106] Prokhor A. Alekseev, Mikhail S. Dunaevskiy, George E. Cirlin, Rodion R. Reznik, Alexander N. Smirnov, Demid A. Kirilenko, Valery Yu Davydov, and Vladimir L. Berkovits. “Unified mechanism of the surface Fermi level pinning in III-As nanowires”. In: *Nanotechnology* 29.31 (2018). ISSN: 13616528. DOI: `10.1088/1361-6528/aac480`. arXiv: `1710.06227`.

[107] Fabrizio Buscemi, Miquel Royo, Guido Goldoni, and Andrea Bertoni. “Tailoring the core electron density in modulation-doped core-multi-shell nanowires”. In: *Nanotechnology* 27.19 (2016), p. 195201. ISSN: 0957-4484. DOI: `10.1088/0957-4484/27/19/195201`. URL: `http://dx.doi.org/10.1088/0957-4484/27/19/195201`.

[108] Miquel Royo, Andrea Bertoni, and Guido Goldoni. “Landau levels, edge states, and magnetoconductance in GaAs/AlGaAs core-shell nanowires”. In: *Phys. Rev. B* 87 (11 Mar. 2013), p. 115316. DOI: `10.1103/PhysRevB.87.115316`. URL: `https://link.aps.org/doi/10.1103/PhysRevB.87.115316`.

[109] Miquel Royo, Carlos Segarra, Andrea Bertoni, Guido Goldoni, and Josep Planelles. “Aharonov-Bohm oscillations and electron gas transitions in hexagonal core-shell nanowires with an axial magnetic field”. In: *Phys. Rev. B* 91 (11 Mar. 2015), p. 115440. DOI: `10.1103/PhysRevB.91.115440`. URL: `https://link.aps.org/doi/10.1103/PhysRevB.91.115440`.

[110] Shiyao Wu, Kai Peng, Sergio Battiato, Valentina Zannier, Andrea Bertoni, Guido Goldoni, Xin Xie, Jingnan Yang, Shan Xiao, Chenjiang Qian, Feilong Song, Sibai Sun, Jianchen Dang, Yang Yu, Fabio Beltram, Lucia Sorba, Ang Li, Bei bei Li, Francesco Rossella, and Xiulai Xu. “Anisotropies of the g-factor tensor and diamagnetic coefficient in crystal-phase quantum dots in InP nanowires”. In: *Nano Res.* 12.11 (2019), pp. 2842–2848. ISSN: 19980000. DOI: `10.1007/s12274-019-2522-5`.

[111] G Goldoni, F Rossi, E Molinari, A. Fasolino, R. Rinaldi, and R. Cingolani. “Valence band spectroscopy in V-grooved quantum wires”. In: *Appl. Phys. Lett.* 69.20 (1996), pp. 2965–2967. ISSN: 00036951. DOI: `10.1063/1.117745`.

[112] G. Goldoni, F. Rossi, E. Molinari, and A. Fasolino. “Band structure and optical anisotropy in V-shaped and T-shaped semiconductor quantum wires”. In: *Phys. Rev. B* 55 (11 Mar. 1997), pp. 7110–7123. DOI: `10.1103/PhysRevB.55.7110`. URL: `https://link.aps.org/doi/10.1103/PhysRevB.55.7110`.

[113] V. V. Ravi Kishore, B. Partoens, and F. M. Peeters. “Electronic structure and optical absorption of GaAs$/$Al$_x$Ga$_{1-x}$As and Al$_x$Ga$_{1-x}$As$/$GaAs core-shell nanowires”. In: *Phys. Rev. B* 82 (23 Dec. 2010), p. 235425. DOI: `10.1103/PhysRevB.82.235425`. URL: `https://link.aps.org/doi/10.1103/PhysRevB.82.235425`.

[114] V. V. Ravi Kishore, B. Partoens, and F. M. Peeters. “Electronic structure of InAs/GaSb core-shell nanowires”. In: *Phys. Rev. B* 86 (16 Oct. 2012), p. 165439. DOI: `10.1103/PhysRevB.86.165439`. URL: `https://link.aps.org/doi/10.1103/PhysRevB.86.165439`.

[115] Benny Lassen, Morten Willatzen, R Melnik, and LC Lew Yan Voon. “Electronic structure of free-standing InP and InAs nanowires”. In: *Journal of materials research* 21.11 (2006), pp. 2927–2935.

[116] Ning Luo, Guang-Yao Huang, Gaohua Liao, Lin-Hui Ye, and HQ Xu. "Band-inverted gaps in InAs/GaSb and GaSb/InAs core-shell nanowires". In: *Scientific reports* 6.1 (2016), pp. 1–11.

[117] Andrea Vezzosi, Andrea Bertoni, and Guido Goldoni. "Band structure of n- and p-doped core-shell nanowires". In: *Phys. Rev. B* 105 (24 June 2022), p. 245303. DOI: `10.1103/PhysRevB.105.245303`. URL: `https://link.aps.org/doi/10.1103/PhysRevB.105.245303`.

[118] F. Hecht. "New development in FreeFem++". In: *J. Numer. Math.* 20.3-4 (2012), pp. 251–265. ISSN: 1570-2820. URL: `https://freefem.org/`.

[119] Giulio Ferrari, Guido Goldoni, Andrea Bertoni, Giampaolo Cuoghi, and Elisa Molinari. "Magnetic states in prismatic core multishell nanowires". In: *Nano Letters* 9 (4 Apr. 2009), pp. 1631–1635. ISSN: 15306984. DOI: `10.1021/nl803942p`.

[120] E. A. de Andrada e Silva, G. C. La Rocca, and F. Bassani. "Spin-orbit splitting of electronic states in semiconductor asymmetric quantum wells". In: *Phys. Rev. B* 55 (24 June 1997), pp. 16293–16299. DOI: `10.1103/PhysRevB.55.16293`. URL: `https://link.aps.org/doi/10.1103/PhysRevB.55.16293`.

[121] Danny C Sorensen. "Implicitly restarted Arnoldi/Lanczos methods for large scale eigenvalue calculations". In: *Parallel Numerical Algorithms*. Springer, 1997, pp. 119–165.

[122] Richard B Lehoucq, Danny C Sorensen, and Chao Yang. *ARPACK users' guide: solution of large-scale eigenvalue problems with implicitly restarted Arnoldi methods*. SIAM, 1998.

[123] Till Andlauer. "Optoelectronic and spin-related properties of semiconductor nanostructures in magnetic fields". PhD thesis. Technische Universität München, 2009.

[124] Elizabeth Cuthill and James McKee. "Reducing the bandwidth of sparse symmetric matrices". In: *Proceedings of the 1969 24th national conference*. 1969, pp. 157–172.

[125] Pauli Virtanen, Ralf Gommers, Travis E. Oliphant, Matt Haberland, Tyler Reddy, David Cournapeau, Evgeni Burovski, Pearu Peterson, Warren Weckesser, Jonathan Bright, Stéfan J. van der Walt, Matthew Brett, Joshua Wilson, K. Jarrod Millman, Nikolay Mayorov, Andrew R. J. Nelson, Eric Jones, Robert Kern, Eric Larson, C J Carey, İlhan Polat, Yu Feng, Eric W. Moore, Jake VanderPlas, Denis Laxalde, Josef Perktold, Robert Cimrman, Ian Henriksen, E. A. Quintero, Charles R. Harris, Anne M. Archibald, Antônio H. Ribeiro, Fabian Pedregosa, Paul van Mulbregt, and SciPy 1.0 Contributors. "SciPy 1.0: Fundamental Algorithms for Scientific Computing in Python". In: *Nature Methods* 17 (2020), pp. 261–272. DOI: `10.1038/s41592-019-0686-2`.

[126] I. Vurgaftman, J. R. Meyer, and L. R. Ram-Mohan. "Band parameters for III-V compound semiconductors and their alloys". In: *Journal of Applied Physics* 89.11 (2001), pp. 5815–5875. DOI: `10.1063/1.1368156`. eprint: `https://doi.org/10.1063/1.1368156`. URL: `https://doi.org/10.1063/1.1368156`.

[127] Sadao Adachi. *Properties of semiconductor alloys: group-IV, III-V and II-VI semiconductors*. John Wiley & Sons, 2009.

[128] IA Kokurin. "Electronic states in nanowires with hexagonal cross-section". In: *Semiconductors* 54.14 (2020), pp. 1897–1899.

[129] Gaohua Liao, Ning Luo, Ke-Qiu Chen, and HQ Xu. "Electronic structures of free-standing nanowires made from indirect bandgap semiconductor gallium phosphide". In: *Scientific reports* 6.1 (2016), pp. 1–11.

[130] Gaohua Liao, Ning Luo, Ke-Qiu Chen, and H Q Xu. “Electronic structures of [1 1 1]-oriented free-standing InAs and InP nanowires”. In: *Journal of Physics: Condensed Matter* 28.13 (Mar. 2016), p. 135303. DOI: `10.1088/0953-8984/28/13/135303`. URL: `https://doi.org/10.1088/0953-8984/28/13/135303`.

[131] Moritz Cygorek, Marek Korkusinski, and Pawel Hawrylak. “Atomistic theory of electronic and optical properties of InAsP/InP nanowire quantum dots”. In: *Phys. Rev. B* 101 (7 Feb. 2020), p. 075307. DOI: `10.1103/PhysRevB.101.075307`. URL: `https://link.aps.org/doi/10.1103/PhysRevB.101.075307`.

[132] Anna Sitek, Miguel Urbaneja Torres, and Andrei Manolescu. “Corner and side localization of electrons in irregular hexagonal semiconductor shells”. In: *Nanotechnology* 30 (Aug. 2019). DOI: `10.1088/1361-6528/ab37a1`.

[133] Fausto Rossi and Elisa Molinari. “Coulomb-induced suppression of band-edge singularities in the optical spectra of realistic quantum-wire structures”. In: *Physical Review Letters* 76.19 (1996), pp. 3642–3645. ISSN: 10797114. DOI: `10.1103/PhysRevLett.76.3642`.

[134] Fausto Rossi, Guido Goldoni, Oskar Mauritz, and Elisa Molinari. “Theory of excitonic confinement in semiconductor quantum wires”. In: *J. Phys. Condens. Matter* 11.31 (1999), pp. 5969–5988. ISSN: 09538984. DOI: `10.1088/0953-8984/11/31/306`.

[135] Guido Goldoni and Fausto Rossi. “Optimization of semiconductor quantum devices by evolutionary search”. In: *Optic Letters* 25 (2006).

[136] Guido Goldoni. “Optimal design and quantum limit for second harmonic generation in semiconductor heterostructures”. In: *Journal of Applied Physics* 89.3 (2001), pp. 1755–1758. arXiv: `0011406v1 [arXiv:cond-mat]`.

[137] R. M. Lutchyn, E. P. A. M. Bakkers, L. P. Kouwenhoven, P. Krogstrup, C. M. Marcus, and Y. Oreg. “Majorana zero modes in superconductor–semiconductor heterostructures”. In: *Nature Reviews Materials* 3.5 (May 2018), pp. 52–68. ISSN: 2058-8437. DOI: `10.1038/s41578-018-0003-1`. URL: `https://doi.org/10.1038/s41578-018-0003-1`.

[138] Jay D. Sau, Roman M. Lutchyn, Sumanta Tewari, and S. Das Sarma. “Generic New Platform for Topological Quantum Computation Using Semiconductor Heterostructures”. In: *Phys. Rev. Lett.* 104 (4 Jan. 2010), p. 040502. DOI: `10.1103/PhysRevLett.104.040502`. URL: `https://link.aps.org/doi/10.1103/PhysRevLett.104.040502`.

[139] A Yu Kitaev. “Unpaired Majorana fermions in quantum wires”. In: *Physics-Uspekhi* 44.10S (Oct. 2001), p. 131. DOI: `10.1070/1063-7869/44/10S/S29`. URL: `https://dx.doi.org/10.1070/1063-7869/44/10S/S29`.

[140] Ramón Aguado. “Majorana quasiparticles in condensed matter”. In: *La Rivista del Nuovo Cimento* 40 (11 Nov. 2017), pp. 523–593. DOI: `10.1393/ncr/i2017-10141-9`. URL: `https://www.sif.it/riviste/sif/ncr/econtents/2017/040/11/article/0`.

[141] Jay D. Sau, Roman M. Lutchyn, Sumanta Tewari, and S. Das Sarma. “Generic New Platform for Topological Quantum Computation Using Semiconductor Heterostructures”. In: *Phys. Rev. Lett.* 104 (4 Jan. 2010), p. 040502. DOI: `10.1103/PhysRevLett.104.040502`. URL: `https://link.aps.org/doi/10.1103/PhysRevLett.104.040502`.

[142] Sankar Das Sarma, Michael Freedman, and Chetan Nayak. "Majorana zero modes and topological quantum computation". In: *npj Quantum Information* 1.1 (Oct. 2015), p. 15001. ISSN: 2056-6387. DOI: `10.1038/npjqi.2015.1`. URL: `https://doi.org/10.1038/npjqi.2015.1`.

[143] David Aasen, Michael Hell, Ryan V. Mishmash, Andrew Higginbotham, Jeroen Danon, Martin Leijnse, Thomas S. Jespersen, Joshua A. Folk, Charles M. Marcus, Karsten Flensberg, and Jason Alicea. "Milestones Toward Majorana-Based Quantum Computing". In: *Phys. Rev. X* 6 (3 Aug. 2016), p. 031016. DOI: `10.1103/PhysRevX.6.031016`. URL: `https://link.aps.org/doi/10.1103/PhysRevX.6.031016`.

[144] V. Mourik, K. Zuo, S. M. Frolov, S. R. Plissard, E. P. A. M. Bakkers, and L. P. Kouwenhoven. "Signatures of Majorana Fermions in Hybrid Superconductor-Semiconductor Nanowire Devices". In: *Science* 336.6084 (2012), pp. 1003–1007. DOI: `10.1126/science.1222360`. eprint: `https://www.science.org/doi/pdf/10.1126/science.1222360`. URL: `https://www.science.org/doi/abs/10.1126/science.1222360`.

[145] P Krogstrup, NLB Ziino, W Chang, SM Albrecht, MH Madsen, Erik Johnson, Jesper Nygård, Charles M Marcus, and TS Jespersen. "Epitaxy of semiconductor–superconductor nanowires". In: *Nature materials* 14.4 (2015), pp. 400–406.

[146] Andrey E. Antipov, Arno Bargerbos, Georg W. Winkler, Bela Bauer, Enrico Rossi, and Roman M. Lutchyn. "Effects of Gate-Induced Electric Fields on Semiconductor Majorana Nanowires". In: *Phys. Rev. X* 8 (3 Aug. 2018), p. 031041. DOI: `10.1103/PhysRevX.8.031041`. URL: `https://link.aps.org/doi/10.1103/PhysRevX.8.031041`.

[147] Benjamin D. Woods, Tudor D. Stanescu, and Sankar Das Sarma. "Effective theory approach to the Schrödinger-Poisson problem in semiconductor Majorana devices". In: *Phys. Rev. B* 98 (3 July 2018), p. 035428. DOI: `10.1103/PhysRevB.98.035428`. URL: `https://link.aps.org/doi/10.1103/PhysRevB.98.035428`.

[148] Roman M Lutchyn, Erik PAM Bakkers, Leo P Kouwenhoven, Peter Krogstrup, Charles M Marcus, and Yuval Oreg. "Majorana zero modes in superconductor–semiconductor heterostructures". In: *Nature Reviews Materials* 3.5 (2018), pp. 52–68.

[149] Zhan Cao, Dong E. Liu, Wan-Xiu He, Xin Liu, Ke He, and Hao Zhang. "Numerical study of PbTe-Pb hybrid nanowires for engineering Majorana zero modes". In: *Phys. Rev. B* 105 (8 Feb. 2022), p. 085424. DOI: `10.1103/PhysRevB.105.085424`. URL: `https://link.aps.org/doi/10.1103/PhysRevB.105.085424`.

[150] Zitong Zhang, Wenyu Song, Yichun Gao, Yuhao Wang, Zehao Yu, Shuai Yang, Yuying Jiang, Wentao Miao, Ruidong Li, Fangting Chen, Zuhan Geng, Qinghua Zhang, Fanqi Meng, Ting Lin, Lin Gu, Kejing Zhu, Yunyi Zang, Lin Li, Runan Shang, Xiao Feng, Qi-Kun Xue, Ke He, and Hao Zhang. "Proximity effect in PbTe-Pb hybrid nanowire Josephson junctions". In: *Phys. Rev. Mater.* 7 (8 Aug. 2023), p. 086201. DOI: `10.1103/PhysRevMaterials.7.086201`. URL: `https://link.aps.org/doi/10.1103/PhysRevMaterials.7.086201`.

[151] Elsa Prada, Pablo San-Jose, Michiel WA de Moor, Attila Geresdi, Eduardo JH Lee, Jelena Klinovaja, Daniel Loss, Jesper Nygård, Ramón Aguado, and Leo P Kouwenhoven. "From Andreev to Majorana bound states in hybrid superconductor–semiconductor nanowires". In: *Nature Reviews Physics* 2.10 (2020), pp. 575–594.

[152] D I Pikulin, J P Dahlhaus, M Wimmer, H Schomerus, and C W J Beenakker. “A zero-voltage conductance peak from weak antilocalization in a Majorana nanowire”. In: *New Journal of Physics* 14.12 (Dec. 2012), p. 125011. DOI: `10.1088/1367-2630/14/12/125011`. URL: `https://dx.doi.org/10.1088/1367-2630/14/12/125011`.

[153] Haining Pan and S. Das Sarma. “Physical mechanisms for zero-bias conductance peaks in Majorana nanowires”. In: *Phys. Rev. Res.* 2 (1 Mar. 2020), p. 013377. DOI: `10.1103/PhysRevResearch.2.013377`. URL: `https://link.aps.org/doi/10.1103/PhysRevResearch.2.013377`.

[154] Benjamin D. Woods, Sankar Das Sarma, and Tudor D. Stanescu. “Charge-Impurity Effects in Hybrid Majorana Nanowires”. In: *Phys. Rev. Appl.* 16 (5 Nov. 2021), p. 054053. DOI: `10.1103/PhysRevApplied.16.054053`. URL: `https://link.aps.org/doi/10.1103/PhysRevApplied.16.054053`.

[155] Haining Pan and S. Das Sarma. “Disorder effects on Majorana zero modes: Kitaev chain versus semiconductor nanowire”. In: *Phys. Rev. B* 103 (22 June 2021), p. 224505. DOI: `10.1103/PhysRevB.103.224505`. URL: `https://link.aps.org/doi/10.1103/PhysRevB.103.224505`.

[156] Seongjin Ahn, Haining Pan, Benjamin Woods, Tudor D. Stanescu, and Sankar Das Sarma. “Estimating disorder and its adverse effects in semiconductor Majorana nanowires”. In: *Phys. Rev. Mater.* 5 (12 Dec. 2021), p. 124602. DOI: `10.1103/PhysRevMaterials.5.124602`. URL: `https://link.aps.org/doi/10.1103/PhysRevMaterials.5.124602`.

[157] Haining Pan and Sankar Das Sarma. “On-demand large conductance in trivial zero-bias tunneling peaks in Majorana nanowires”. In: *Phys. Rev. B* 105 (11 Mar. 2022), p. 115432. DOI: `10.1103/PhysRevB.105.115432`. URL: `https://link.aps.org/doi/10.1103/PhysRevB.105.115432`.

[158] Christopher Reeg, Daniel Loss, and Jelena Klinovaja. “Metallization of a Rashba wire by a superconducting layer in the strong-proximity regime”. In: *Phys. Rev. B* 97 (16 Apr. 2018), p. 165425. DOI: `10.1103/PhysRevB.97.165425`. URL: `https://link.aps.org/doi/10.1103/PhysRevB.97.165425`.

[159] Christopher Reeg, Daniel Loss, and Jelena Klinovaja. “Proximity effect in a two-dimensional electron gas coupled to a thin superconducting layer”. In: *Beilstein Journal of Nanotechnology* 9 (2018), pp. 1263–1271. ISSN: 2190-4286. DOI: `10.3762/bjnano.9.118`. URL: `https://doi.org/10.3762/bjnano.9.118`.

[160] Henry F. Legg, Daniel Loss, and Jelena Klinovaja. “Metallization and proximity superconductivity in topological insulator nanowires”. In: *Phys. Rev. B* 105 (15 Apr. 2022), p. 155413. DOI: `10.1103/PhysRevB.105.155413`. URL: `https://link.aps.org/doi/10.1103/PhysRevB.105.155413`.

[161] Bas Nijholt and Anton R. Akhmerov. “Orbital effect of magnetic field on the Majorana phase diagram”. In: *Phys. Rev. B* 93 (23 June 2016), p. 235434. DOI: `10.1103/PhysRevB.93.235434`. URL: `https://link.aps.org/doi/10.1103/PhysRevB.93.235434`.

[162] Olesia Dmytruk and Jelena Klinovaja. “Suppression of the overlap between Majorana fermions by orbital magnetic effects in semiconducting-superconducting nanowires”. In: *Phys. Rev. B* 97 (15 Apr. 2018), p. 155409. DOI: `10.1103/PhysRevB.97.155409`. URL: `https://link.aps.org/doi/10.1103/PhysRevB.97.155409`.

[163] Michael Tinkham. *Introduction to superconductivity*. Courier Corporation, 2004. ISBN: 978-0486435039.

[164] Georg W. Winkler, Andrey E. Antipov, Bernard van Heck, Alexey A. Soluyanov, Leonid I. Glazman, Michael Wimmer, and Roman M. Lutchyn. “Unified numerical approach to topological semiconductor-superconductor heterostructures”. In: *Phys. Rev. B* 99 (24 June 2019), p. 245408. DOI: `10.1103/PhysRevB.99.245408`. URL: `https://link.aps.org/doi/10.1103/PhysRevB.99.245408`.

[165] Pablo San-Jose, Carlos Payá, C. M. Marcus, S. Vaitiek ėnas, and Elsa Prada. “Theory of Caroli–de Gennes–Matricon analogs in full-shell hybrid nanowires”. In: *Phys. Rev. B* 107 (15 Apr. 2023), p. 155423. DOI: `10.1103/PhysRevB.107.155423`. URL: `https://link.aps.org/doi/10.1103/PhysRevB.107.155423`.

[166] Carlos Payá, Samuel D Escribano, Andrea Vezzosi, Fernando Peñaranda, Ramón Aguado, Pablo San-Jose, and Elsa Prada. “Phenomenology of Majorana zero modes in full-shell hybrid nanowires”. In: *arXiv preprint arXiv:2312.11613* (2023).

[167] DE Sidor, GR Savich, and GW Wicks. “Surface leakage mechanisms in III–V infrared barrier detectors”. In: *Journal of Electronic Materials* 45 (2016), pp. 4663–4667.

[168] Dong Liu, Fengjing Liu, Yue Liu, Zhiyong Pang, Xinming Zhuang, Yanxue Yin, Shengpan Dong, Longbing He, Yang Tan, Lei Liao, Feng Chen, and Zai-xing Yang. “Schottky-Contacted High-Performance GaSb Nanowires Photodetectors Enabled by Lead-Free All-Inorganic Perovskites Decoration”. In: *Small* 18.16 (2022), p. 2200415. DOI: `https://doi.org/10.1002/smll.202200415`. eprint: `https://onlinelibrary.wiley.com/doi/pdf/10.1002/smll.202200415`. URL: `https://onlinelibrary.wiley.com/doi/abs/10.1002/smll.202200415`.

[169] W. Chang, S. M. Albrecht, T. S. Jespersen, F. Kuemmeth, P. Krogstrup, J. Nygård, and C. M. Marcus. “Hard gap in epitaxial semiconductor–superconductor nanowires”. In: *Nature Nanotechnology* 10.3 (Mar. 2015), pp. 232–236. ISSN: 1748-3395. DOI: `10.1038/nnano.2014.306`. URL: `https://doi.org/10.1038/nnano.2014.306`.

[170] Thomas Kanne, Mikelis Marnauza, Dags Olsteins, Damon J. Carrad, Joachim E. Sestoft, Joeri de Bruijckere, Lunjie Zeng, Erik Johnson, Eva Olsson, Kasper Grove-Rasmussen, and Jesper Nygård. “Epitaxial Pb on InAs nanowires for quantum devices”. In: *Nature Nanotechnology* 16.7 (July 2021), pp. 776–781. ISSN: 1748-3395. DOI: `10.1038/s41565-021-00900-9`. URL: `https://doi.org/10.1038/s41565-021-00900-9`.

[171] Damon J. Carrad, Martin Bjergfelt, Thomas Kanne, Martin Aagesen, Filip Krizek, Elisabetta M. Fiordaliso, Erik Johnson, Jesper Nygård, and Thomas Sand Jespersen. “Shadow Epitaxy for In Situ Growth of Generic Semiconductor/Superconductor Hybrids”. In: *Advanced Materials* 32.23 (2020), p. 1908411. DOI: `https://doi.org/10.1002/adma.201908411`. eprint: `https://onlinelibrary.wiley.com/doi/pdf/10.1002/adma.201908411`. URL: `https://onlinelibrary.wiley.com/doi/abs/10.1002/adma.201908411`.

[172] Martin Bjergfelt, Damon J Carrad, Thomas Kanne, Martin Aagesen, Elisabetta M Fiordaliso, Erik Johnson, Borzoyeh Shojaei, Chris J Palmstrøm, Peter Krogstrup, Thomas Sand Jespersen, and Jesper Nygård. “Superconducting vanadium/indium-arsenide hybrid nanowires”. In: *Nanotechnology* 30.29 (May 2019), p. 294005. DOI: `10.1088/1361-6528/ab15fc`. URL: `https://dx.doi.org/10.1088/1361-6528/ab15fc`.

[173] Sabbir A. Khan, Charalampos Lampadaris, Ajuan Cui, Lukas Stampfer, Yu Liu, Sebastian J. Pauka, Martin E. Cachaza, Elisabetta M. Fiordaliso, Jung-Hyun Kang, Svetlana Korneychuk, Timo Mutas, Joachim E. Sestoft, Filip Krizek, Rawa Tanta, Maja C. Cassidy, Thomas S. Jespersen, and Peter Krogstrup. "Highly Transparent Gatable Superconducting Shadow Junctions". In: *ACS Nano* 14.11 (2020). PMID: 32396328, pp. 14605–14615. DOI: `10.1021/acsnano.0c02979`. eprint: `https://doi.org/10.1021/acsnano.0c02979`. URL: `https://doi.org/10.1021/acsnano.0c02979`.

[174] Sandip Tiwari and David J. Frank. "Empirical fit to band discontinuities and barrier heights in III–V alloy systems". In: *Applied Physics Letters* 60.5 (Feb. 1992), pp. 630–632. ISSN: 0003-6951. DOI: `10.1063/1.106575`. eprint: `https://pubs.aip.org/aip/apl/article-pdf/60/5/630/7787531/630\_1\_online.pdf`. URL: `https://doi.org/10.1063/1.106575`.

[175] C. Merckling, X. Sun, A. Alian, G. Brammertz, V. V. Afanas'ev, T. Y. Hoffmann, M. Heyns, M. Caymax, and J. Dekoster. "GaSb molecular beam epitaxial growth on p-InP(001) and passivation with in situ deposited Al2O3 gate oxide". In: *Journal of Applied Physics* 109.7 (Apr. 2011), p. 073719. ISSN: 0021-8979. DOI: `10.1063/1.3569618`. eprint: `https://pubs.aip.org/aip/jap/article-pdf/doi/10.1063/1.3569618/15072927/073719\_1\_online.pdf`. URL: `https://doi.org/10.1063/1.3569618`.

[176] K. Miura, Y. Iguchi, and Y. Kawamura. "Type-II InAs/GaSb superlattice grown on InP substrate". In: *Journal of Crystal Growth* 378 (2013). The 17th International Conference on Molecular Beam Epitaxy, pp. 121–124. ISSN: 0022-0248. DOI: `https://doi.org/10.1016/j.jcrysgro.2012.12.090`. URL: `https://www.sciencedirect.com/science/article/pii/S0022024812009748`.

[177] Omer Arif, Valentina Zannier, Ang Li, Francesca Rossi, Daniele Ercolani, Fabio Beltram, and Lucia Sorba. "Growth and Strain Relaxation Mechanisms of InAs/InP/GaAsSb Core-Dual-Shell Nanowires". In: *Crystal Growth & Design* 20.2 (2020), pp. 1088–1096. DOI: `10.1021/acs.cgd.9b01421`. eprint: `https://doi.org/10.1021/acs.cgd.9b01421`. URL: `https://doi.org/10.1021/acs.cgd.9b01421`.

[178] S.J. Bass. "Silicon and germanium doping of epitaxial gallium arsenide grown by the trimethylgallium-arsine method". In: *Journal of Crystal Growth* 47.5 (1979), pp. 613–618. ISSN: 0022-0248. DOI: `https://doi.org/10.1016/0022-0248(79)90002-2`. URL: `https://www.sciencedirect.com/science/article/pii/0022024879900022`.

[179] Matthew Zervos. "Delta-doping of semiconductor nanowires". In: *physica status solidi (RRL) – Rapid Research Letters* 7.9 (2013), pp. 651–654. DOI: `https://doi.org/10.1002/pssr.201307219`. eprint: `https://onlinelibrary.wiley.com/doi/pdf/10.1002/pssr.201307219`. URL: `https://onlinelibrary.wiley.com/doi/abs/10.1002/pssr.201307219`.

[180] Giordano Scappucci, Christoph Kloeffel, Floris A. Zwanenburg, Daniel Loss, Maksym Myronov, Jian-Jun Zhang, Silvano De Franceschi, Georgios Katsaros, and Menno Veldhorst. "The germanium quantum information route". In: *Nature Reviews Materials* 6.6 (2021), pp. 926–943. DOI: `10.1038/s41578-020-00262-z`. URL: `https://doi.org/10.1038/s41578-020-00262-z`.

[181] Hannes Watzinger, Josip Kukučka, Lada Vukušić, Fei Gao, Ting Wang, Friedrich Schäffler, Jian-Jun Zhang, and Georgios Katsaros. “A germanium hole spin qubit”. In: *Nature Communications* 9.1 (Sept. 2018), p. 3902. ISSN: 2041-1723. DOI: `10.1038/s41467-018-06418-4`. URL: `https://doi.org/10.1038/s41467-018-06418-4`.

[182] N. W. Hendrickx, W. I. L. Lawrie, L. Petit, A. Sammak, G. Scappucci, and M. Veldhorst. “A single-hole spin qubit”. In: *Nature Communications* 11.1 (July 2020), p. 3478. ISSN: 2041-1723. DOI: `10.1038/s41467-020-17211-7`. URL: `https://doi.org/10.1038/s41467-020-17211-7`.

[183] N. W. Hendrickx, D. P. Franke, A. Sammak, G. Scappucci, and M. Veldhorst. “Fast two-qubit logic with holes in germanium”. In: *Nature* 577.7791 (Jan. 2020), pp. 487–491. DOI: `10.1038/s41586-019-1919-3`. URL: `https://doi.org/10.1038/s41586-019-1919-3`.

[184] Nico W. Hendrickx, William I. L. Lawrie, Maximilian Russ, Floor van Riggelen, Sander L. de Snoo, Raymond N. Schouten, Amir Sammak, Giordano Scappucci, and Menno Veldhorst. “A four-qubit germanium quantum processor”. In: *Nature* 591.7851 (Mar. 2021), pp. 580–585. ISSN: 1476-4687. DOI: `10.1038/s41586-021-03332-6`. URL: `https://doi.org/10.1038/s41586-021-03332-6`.

[185] Xiao-Jie Hao, Tao Tu, Gang Cao, Cheng Zhou, Hai-Ou Li, Guang-Can Guo, Wayne Y. Fung, Zhongqing Ji, Guo-Ping Guo, and Wei Lu. “Strong and Tunable Spin−Orbit Coupling of One-Dimensional Holes in Ge/Si Core/Shell Nanowires”. In: *Nano Letters* 10.8 (2010), pp. 2956–2960. DOI: `10.1021/nl101181e`. URL: `https://doi.org/10.1021/nl101181e`.

[186] A. P. Higginbotham, F. Kuemmeth, T. W. Larsen, M. Fitzpatrick, J. Yao, H. Yan, C. M. Lieber, and C. M. Marcus. “Antilocalization of Coulomb Blockade in a Ge/Si Nanowire”. In: *Phys. Rev. Lett.* 112 (21 May 2014), p. 216806. DOI: `10.1103/PhysRevLett.112.216806`. URL: `https://link.aps.org/doi/10.1103/PhysRevLett.112.216806`.

[187] R Wang, R S Deacon, J Yao, C M Lieber, and K Ishibashi. “Electrical modulation of weak-antilocalization and spin–orbit interaction in dual gated Ge/Si core/shell nanowires”. In: *Semiconductor Science and Technology* 32.9 (Aug. 2017), p. 094002. DOI: `10.1088/1361-6641/aa7ce6`. URL: `https://dx.doi.org/10.1088/1361-6641/aa7ce6`.

[188] Folkert K. de Vries, Jie Shen, Rafal J. Skolasinski, Michal P. Nowak, Daniel Varjas, Lin Wang, Michael Wimmer, Joost Ridderbos, Floris A. Zwanenburg, Ang Li, Sebastian Koelling, Marcel A. Verheijen, Erik P. A. M. Bakkers, and Leo P. Kouwenhoven. “Spin–Orbit Interaction and Induced Superconductivity in a One-Dimensional Hole Gas”. In: *Nano Letters* 18.10 (2018). PMID: 30192147, pp. 6483–6488. DOI: `10.1021/acs.nanolett.8b02981`. URL: `https://doi.org/10.1021/acs.nanolett.8b02981`.

[189] N. Ares, V. N. Golovach, G. Katsaros, M. Stoffel, F. Fournel, L. I. Glazman, O. G. Schmidt, and S. De Franceschi. “Nature of Tunable Hole g Factors in Quantum Dots”. In: *Phys. Rev. Lett.* 110 (4 Jan. 2013), p. 046602. DOI: `10.1103/PhysRevLett.110.046602`. URL: `https://link.aps.org/doi/10.1103/PhysRevLett.110.046602`.

[190] Matthias Brauns, Joost Ridderbos, Ang Li, Erik P. A. M. Bakkers, and Floris A. Zwanenburg. “Electric-field dependent g-factor anisotropy in Ge-Si core-shell nanowire quantum dots”. In: *Phys. Rev. B* 93 (12 Mar. 2016), p. 121408. DOI: `10.1103/PhysRevB.93.121408`. URL: `https://link.aps.org/doi/10.1103/PhysRevB.93.121408`.

[191] F. N. M. Froning, M. J. Ran či ć, B. Hetényi, S. Bosco, M. K. Rehmann, A. Li, E. P. A. M. Bakkers, F. A. Zwanenburg, D. Loss, D. M. Zumbühl, and F. R. Braakman. “Strong spin-orbit interaction and g-factor renormalization of hole spins in Ge/Si nanowire quantum dots”. In: *Phys. Rev. Res.* 3 (1 Jan. 2021), p. 013081. DOI: `10.1103/PhysRevResearch.3.013081`. URL: `https://link.aps.org/doi/10.1103/PhysRevResearch.3.013081`.

[192] Jie Xiang, A. Vidan, M. Tinkham, R. M. Westervelt, and Charles M. Lieber. “Ge/Si nanowire mesoscopic Josephson junctions”. In: *Nature Nanotechnology* 1.3 (Dec. 2006), pp. 208–213. ISSN: 1748-3395. DOI: `10.1038/nnano.2006.140`. URL: `https://doi.org/10.1038/nnano.2006.140`.

[193] T. W. Larsen, K. D. Petersson, F. Kuemmeth, T. S. Jespersen, P. Krogstrup, J. Nygård, and C. M. Marcus. “Semiconductor-Nanowire-Based Superconducting Qubit”. In: *Phys. Rev. Lett.* 115 (12 Sept. 2015), p. 127001. DOI: `10.1103/PhysRevLett.115.127001`. URL: `https://link.aps.org/doi/10.1103/PhysRevLett.115.127001`.

[194] N. W. Hendrickx, D. P. Franke, A. Sammak, M. Kouwenhoven, D. Sabbagh, L. Yeoh, R. Li, M. L. V. Tagliaferri, M. Virgilio, G. Capellini, G. Scappucci, and M. Veldhorst. “Gate-controlled quantum dots and superconductivity in planar germanium”. In: *Nature Communications* 9.1 (July 2018), p. 2835. ISSN: 2041-1723. DOI: `10.1038/s41467-018-05299-x`. URL: `https://doi.org/10.1038/s41467-018-05299-x`.

[195] Joost Ridderbos, Matthias Brauns, Jie Shen, Folkert K. de Vries, Ang Li, Erik P. A. M. Bakkers, Alexander Brinkman, and Floris A. Zwanenburg. “Josephson Effect in a Few-Hole Quantum Dot”. In: *Advanced Materials* 30.44 (2018), p. 1802257. DOI: `https://doi.org/10.1002/adma.201802257`. eprint: `https://onlinelibrary.wiley.com/doi/pdf/10.1002/adma.201802257`. URL: `https://onlinelibrary.wiley.com/doi/abs/10.1002/adma.201802257`.

[196] Jovian Delaforce, Masiar Sistani, Roman B. G. Kramer, Minh A. Luong, Nicolas Roch, Walter M. Weber, Martien I. den Hertog, Eric Robin, Cecile Naud, Alois Lugstein, and Olivier Buisson. “Al–Ge–Al Nanowire Heterostructure: From Single-Hole Quantum Dot to Josephson Effect”. In: *Advanced Materials* 33.39 (2021), p. 2101989. DOI: `https://doi.org/10.1002/adma.202101989`. eprint: `https://onlinelibrary.wiley.com/doi/pdf/10.1002/adma.202101989`. URL: `https://onlinelibrary.wiley.com/doi/abs/10.1002/adma.202101989`.

[197] Alberto Tosato, Vukan Levajac, Ji-Yin Wang, Casper J. Boor, Francesco Borsoi, Marc Botifoll, Carla N. Borja, Sara Martí-Sánchez, Jordi Arbiol, Amir Sammak, Menno Veldhorst, and Giordano Scappucci. “Hard superconducting gap in germanium”. In: *Communications Materials* 4.1 (Apr. 2023), p. 23. DOI: `10.1038/s43246-023-00351-w`. URL: `https://doi.org/10.1038/s43246-023-00351-w`.

[198] Christoph Kloeffel, Mircea Trif, and Daniel Loss. “Strong spin-orbit interaction and helical hole states in Ge/Si nanowires”. In: *Phys. Rev. B* 84 (19 Nov. 2011), p. 195314. DOI: `10.1103/PhysRevB.84.195314`. URL: `https://link.aps.org/doi/10.1103/PhysRevB.84.195314`.

[199] Christoph Kloeffel, Marko J. Ran či ć, and Daniel Loss. “Direct Rashba spin-orbit interaction in Si and Ge nanowires with different growth directions”. In: *Phys. Rev. B* 97 (23 June 2018),

p. 235422. DOI: `10.1103/PhysRevB.97.235422`. URL: `https://link.aps.org/doi/10.1103/PhysRevB.97.235422`.

[200] Stefano Bosco and Daniel Loss. “Hole Spin Qubits in Thin Curved Quantum Wells”. In: *Phys. Rev. Appl.* 18 (4 Oct. 2022), p. 044038. DOI: `10.1103/PhysRevApplied.18.044038`. URL: `https://link.aps.org/doi/10.1103/PhysRevApplied.18.044038`.

[201] Haining Pan and S. Das Sarma. “Physical mechanisms for zero-bias conductance peaks in Majorana nanowires”. In: *Phys. Rev. Res.* 2 (1 Mar. 2020), p. 013377. DOI: `10.1103/PhysRevResearch.2.013377`. URL: `https://link.aps.org/doi/10.1103/PhysRevResearch.2.013377`.

[202] Seongjin Ahn, Haining Pan, Benjamin Woods, Tudor D. Stanescu, and Sankar Das Sarma. “Estimating disorder and its adverse effects in semiconductor Majorana nanowires”. In: *Phys. Rev. Mater.* 5 (12 Dec. 2021), p. 124602. DOI: `10.1103/PhysRevMaterials.5.124602`. URL: `https://link.aps.org/doi/10.1103/PhysRevMaterials.5.124602`.

[203] Franziska Maier, Jelena Klinovaja, and Daniel Loss. “Majorana fermions in Ge/Si hole nanowires”. In: *Phys. Rev. B* 90 (19 Nov. 2014), p. 195421. DOI: `10.1103/PhysRevB.90.195421`. URL: `https://link.aps.org/doi/10.1103/PhysRevB.90.195421`.

[204] Melina Luethi, Henry F. Legg, Katharina Laubscher, Daniel Loss, and Jelena Klinovaja. “Majorana bound states in germanium Josephson junctions via phase control”. In: *Phys. Rev. B* 108 (19 Nov. 2023), p. 195406. DOI: `10.1103/PhysRevB.108.195406`. URL: `https://link.aps.org/doi/10.1103/PhysRevB.108.195406`.

[205] Katharina Laubscher, Jay D. Sau, and Sankar Das Sarma. *Majorana zero modes in gate-defined germanium hole nanowires*. 2023. arXiv: `2305.14313 [cond-mat.mes-hall]`.

[206] R Winkler, S Papadakis, E De Poortere, and M Shayegan. *Spin-orbit coupling in two-dimensional electron and hole systems*. Vol. 41. Springer, 2003.

[207] Samuel D. Escribano, Alfredo Levy Yeyati, and Elsa Prada. “Improved effective equation for the Rashba spin-orbit coupling in semiconductor nanowires”. In: *Phys. Rev. Research* 2 (3 Aug. 2020), p. 033264. DOI: `10.1103/PhysRevResearch.2.033264`. URL: `https://link.aps.org/doi/10.1103/PhysRevResearch.2.033264`.

[208] AO Rudakov and IA Kokurin. “Electronic states in cylindrical core-multi-shell nanowire”. In: *Semiconductors* 53.16 (2019), pp. 2137–2139.

[209] Sabbir A. Khan, Sara Martí-Sánchez, Dags Olsteins, Charalampos Lampadaris, Damon James Carrad, Yu Liu, Judith Quiñones, Maria Chiara Spadaro, Thomas S. Jespersen, Peter Krogstrup, and Jordi Arbiol. *Epitaxially Driven Phase Selectivity of Sn in Hybrid Quantum Nanowires*. 2023. arXiv: `2212.13314 [cond-mat.mtrl-sci]`.

[210] Aranya Goswami, Sanchayeta R. Mudi, Connor Dempsey, Po Zhang, Hao Wu, Bomin Zhang, William J. Mitchell, Joon Sue Lee, Sergey M. Frolov, and Christopher J. Palmstrøm. “Sn/InAs Josephson Junctions on Selective Area Grown Nanowires with in Situ Shadowed Superconductor Evaporation”. In: *Nano Letters* 23.16 (2023). PMID: 37561818, pp. 7311–7318. DOI: `10.1021/acs.nanolett.3c01320`. eprint: `https://doi.org/10.1021/acs.nanolett.3c01320`. URL: `https://doi.org/10.1021/acs.nanolett.3c01320`.

[211] Tsunehiro Hato, Hiroyuki Akaike, Yoshiaki Takai Yoshiaki Takai, and Hisao Hayakawa Hisao Hayakawa. “Fabrication Process and Properties of Nb-InSb-Nb Planar Junction”. In: *Japanese Journal of Applied Physics* 31.4R (Apr. 1992), p. 1039. DOI: `10.1143/JJAP.31.1039`. URL: `https://dx.doi.org/10.1143/JJAP.31.1039`.

[212] Nicholas A. Güsken, Torsten Rieger, Patrick Zellekens, Benjamin Bennemann, Elmar Neumann, Mihail I. Lepsa, Thomas Schäpers, and Detlev Grützmacher. “MBE growth of Al/InAs and Nb/InAs superconducting hybrid nanowire structures”. In: *Nanoscale* 9 (43 2017), pp. 16735–16741. DOI: `10.1039/C7NR03982D`. URL: `http://dx.doi.org/10.1039/C7NR03982D`.

[213] M. Z. Hasan and C. L. Kane. “Colloquium: Topological insulators”. In: *Rev. Mod. Phys.* 82 (4 Nov. 2010), pp. 3045–3067. DOI: `10.1103/RevModPhys.82.3045`. URL: `https://link.aps.org/doi/10.1103/RevModPhys.82.3045`.

[214] Mengyun He, Huimin Sun, and Qing Lin He. “Topological insulator: Spintronics and quantum computations”. In: *Frontiers of Physics* 14 (2019), pp. 1–16.

[215] B. Andrei Bernevig and Shou-Cheng Zhang. “Quantum Spin Hall Effect”. In: *Phys. Rev. Lett.* 96 (10 Mar. 2006), p. 106802. DOI: `10.1103/PhysRevLett.96.106802`. URL: `https://link.aps.org/doi/10.1103/PhysRevLett.96.106802`.

[216] Chen-Hsuan Hsu, Peter Stano, Jelena Klinovaja, and Daniel Loss. “Helical liquids in semiconductors”. In: *Semiconductor Science and Technology* 36.12 (2021), p. 123003.

[217] Simon Wozny, Karel Vyborny, Wolfgang Belzig, and Sigurdur I. Erlingsson. “Gap formation in helical edge states with magnetic impurities”. In: *Phys. Rev. B* 98 (16 Oct. 2018), p. 165423. DOI: `10.1103/PhysRevB.98.165423`. URL: `https://link.aps.org/doi/10.1103/PhysRevB.98.165423`.

[218] Lukas Kimme, Bernd Rosenow, and Arne Brataas. “Backscattering in helical edge states from a magnetic impurity and Rashba disorder”. In: *Phys. Rev. B* 93 (8 Feb. 2016), p. 081301. DOI: `10.1103/PhysRevB.93.081301`. URL: `https://link.aps.org/doi/10.1103/PhysRevB.93.081301`.

[219] Chaoxing Liu, Taylor L. Hughes, Xiao-Liang Qi, Kang Wang, and Shou-Cheng Zhang. “Quantum Spin Hall Effect in Inverted Type-II Semiconductors”. In: *Phys. Rev. Lett.* 100 (23 June 2008), p. 236601. DOI: `10.1103/PhysRevLett.100.236601`. URL: `https://link.aps.org/doi/10.1103/PhysRevLett.100.236601`.

[220] A.Yu. Kitaev. “Fault-tolerant quantum computation by anyons”. In: *Annals of Physics* 303.1 (2003), pp. 2–30. ISSN: 0003-4916. DOI: `https://doi.org/10.1016/S0003-4916(02)00018-0`. URL: `https://www.sciencedirect.com/science/article/pii/S0003491602000180`.

[221] Sven Marian Albrecht, Andrew P Higginbotham, Morten Madsen, Ferdinand Kuemmeth, Thomas Sand Jespersen, Jesper Nygård, Peter Krogstrup, and CM Marcus. “Exponential protection of zero modes in Majorana islands”. In: *Nature* 531.7593 (2016), pp. 206–209.

[222] Ning Luo, Guang-Yao Huang, Gaohua Liao, Lin-Hui Ye, and HQ Xu. “Band-inverted gaps in InAs/GaSb and GaSb/InAs core-shell nanowires”. In: *Scientific reports* 6.1 (2016), p. 38698.

[223] B Andrei Bernevig. *Topological insulators and topological superconductors*. Princeton university press, 2013.

[224] R. Winkler. “Rashba spin splitting in two-dimensional electron and hole systems”. In: *Phys. Rev. B* 62 (7 Aug. 2000), pp. 4245–4248. DOI: `10.1103/PhysRevB.62.4245`. URL: `https://link.aps.org/doi/10.1103/PhysRevB.62.4245`.

[225] Florinda Viñas Boström, Athanasios Tsintzis, Michael Hell, and Martin Leijnse. “Band structure and end states in InAs/GaSb core-shell-shell nanowires”. In: *Phys. Rev. B* 102 (19 Nov. 2020), p. 195434. DOI: `10.1103/PhysRevB.102.195434`. URL: `https://link.aps.org/doi/10.1103/PhysRevB.102.195434`.

[226] W. Xu, P. A. Folkes, and Godfrey Gumbs. “Self-consistent electronic subband structure of undoped InAs/GaSb-based type II and broken-gap quantum well systems”. In: *Journal of Applied Physics* 102.3 (Aug. 2007), p. 033703. ISSN: 0021-8979. DOI: `10.1063/1.2759873`. eprint: `https://pubs.aip.org/aip/jap/article-pdf/doi/10.1063/1.2759873/13250698/033703\_1\_online.pdf`. URL: `https://doi.org/10.1063/1.2759873`.

[227] Guobin Liu and Shun-Lien Chuang. “Modeling of Sb-based type-II quantum cascade lasers”. In: *Phys. Rev. B* 65 (16 Apr. 2002), p. 165220. DOI: `10.1103/PhysRevB.65.165220`. URL: `https://link.aps.org/doi/10.1103/PhysRevB.65.165220`.

[228] M. Altarelli. “Electronic structure and semiconductor-semimetal transition in InAs-GaSb superlattices”. In: *Phys. Rev. B* 28 (2 July 1983), pp. 842–845. DOI: `10.1103/PhysRevB.28.842`. URL: `https://link.aps.org/doi/10.1103/PhysRevB.28.842`.

[229] I Lapushkin, A Zakharova, S T Yen, and K A Chao. “A self-consistent investigation of the semimetal–semiconductor transition in InAs/GaSb quantum wells under external electric fields”. In: *Journal of Physics: Condensed Matter* 16.26 (June 2004), p. 4677. DOI: `10.1088/0953-8984/16/26/003`. URL: `https://dx.doi.org/10.1088/0953-8984/16/26/003`.

[230] Till Andlauer and Peter Vogl. “Full-band envelope-function approach for type-II broken-gap superlattices”. In: *Phys. Rev. B* 80 (3 July 2009), p. 035304. DOI: `10.1103/PhysRevB.80.035304`. URL: `https://link.aps.org/doi/10.1103/PhysRevB.80.035304`.

[231] Christoph Kloeffel, Mircea Trif, and Daniel Loss. “Strong spin-orbit interaction and helical hole states in Ge/Si nanowires”. In: *Phys. Rev. B* 84 (19 Sept. 2011), p. 195314. DOI: `10.1103/PhysRevB.84.195314`. URL: `https://link.aps.org/doi/10.1103/PhysRevB.84.195314`.

[232] Marcos H. L. de Medeiros, Raphael L. R. C. Teixeira, Guilherme M. Sipahi, and Luis G. G. V. Dias da Silva. “Electric field induced edge-state oscillations in InAs/GaSb quantum wells”. In: *Phys. Rev. B* 104 (19 Nov. 2021), p. 195307. DOI: `10.1103/PhysRevB.104.195307`. URL: `https://link.aps.org/doi/10.1103/PhysRevB.104.195307`.

[233] D G Rothe, R W Reinthaler, C-X Liu, L W Molenkamp, S-C Zhang, and E M Hankiewicz. “Fingerprint of different spin–orbit terms for spin transport in HgTe quantum wells”. In: *New Journal of Physics* 12.6 (June 2010), p. 065012. DOI: `10.1088/1367-2630/12/6/065012`. URL: `https://dx.doi.org/10.1088/1367-2630/12/6/065012`.

[234] and. “Finite size effects on helical edge states in HgTe quantum wells with the spin—orbit coupling due to bulk- and structure-inversion asymmetries”. In: *Chinese Physics B* 23.3 (Jan. 2014), p. 037304. DOI: `10.1088/1674-1056/23/3/037304`. URL: `https://dx.doi.org/10.1088/1674-1056/23/3/037304`.

[235] Lun-Hui Hu, Chao-Xing Liu, Dong-Hui Xu, Fu-Chun Zhang, and Yi Zhou. “Electric control of inverted gap and hybridization gap in type-II InAs/GaSb quantum wells”. In: *Phys. Rev. B* 94 (4 July 2016), p. 045317. DOI: `10.1103/PhysRevB.94.045317`. URL: `https://link.aps.org/doi/10.1103/PhysRevB.94.045317`.

[236] Benjamin D. Woods and Mark Friesen. “Realizing Majorana Kramers pairs in two-channel InAs-Al nanowires with highly misaligned electric fields”. In: *Phys. Rev. B* 108 (15 Oct. 2023), p. 155142. DOI: `10.1103/PhysRevB.108.155142`. URL: `https://link.aps.org/doi/10.1103/PhysRevB.108.155142`.

[237] M P Lopez Sancho, J M Lopez Sancho, J M L Sancho, and J Rubio. “Highly convergent schemes for the calculation of bulk and surface Green functions”. In: *Journal of Physics F: Metal Physics* 15.4 (Apr. 1985), p. 851. DOI: `10.1088/0305-4608/15/4/009`. URL: `https://dx.doi.org/10.1088/0305-4608/15/4/009`.

List of Publications

- Andrea Vezzosi, Andrea Bertoni, and Guido Goldoni. ”Band structure of n- and p-doped core-shell nanowires”. In: *Phys. Rev. B* 105 (2022), p. 245303. DOI:10.1103/PhysRevB.105.245303.

- Carlos Payá, Samuel D Escribano, Andrea Vezzosi, Fernando Peñaranda, Ramón Aguado, Pablo San-Jose, and Elsa Prada. ”Phenomenology of Majorana zero modes in full-shell hybrid nanowires”. In: arXiv preprint arXiv:2312.11613 (2023).

- Vito Clericò, Pawel Wójcik, Andrea Vezzosi, Mirko Rocci, Valeria Demontis, Valentina Zannier, Álvaro Díaz-Fernández, Elena Díaz, Vittorio Bellani, Francisco Domínguez-Adame, Enrique Diez, Lucia Sorba, Andrea Bertoni, Guido Goldoni, and Francesco Rossella. “Spin-Resolved Magneto-Tunneling and Giant Anisotropic g-Factor in Broken Gap InAs-GaSb Core–Shell Nanowires”. In: *Nano Letters* 24.3 (2024). PMID: 38189790, pp. 790–796. DOI: 10.1021/acs.nanolett.3c02559.

- Andrea Vezzosi, Carlos Payá, Pawel Wójcik, Guido Goldoni, Elsa Prada and Samuel D. Escribano. ”Full-shell tubular-core hybrid nanowires with hole bands: a practical proposal for Majorana zero modes”. *Manuscript in preparation*.

- Andrea Vezzosi, Andrea Bertoni and Guido Goldoni. ”A Weyl semimetal state in inverted gap semiconductor nanowires induced by an electric field”. *Manuscript in preparation*.

- Andrea Vezzosi, Andrea Bertoni, Guido Goldoni. ”`nwkp`: A `Python`-package for the self-consistent k·p description of semiconductor nanowires using finite elements”. *Manuscript in preparation*.

- Andrea Vezzosi, Andrea Bertoni, Guido Goldoni. ”Modified envelope function approach for type-II broken gap core-shell nanowires”. *Manuscript in preparation*.